Proceedings

2020 ASPE Spring Topical Meeting

Design and Control of Precision Mechatronic Systems

May 6 - May 8, 2020

Virtual Meeting: hosted via Zoom

American Society for
Precision Engineering

230 Washington Ave. Ext., Suite 101
Albany, NY 12203
518-463-8687

Preface

This book comprises the proceedings of the 2020 ASPE Spring Topical Meeting on the Design and Control of Precision Mechatronic Systems. The contributions reflect the authors' opinions and are published as presented to ASPE, without change. Their inclusion in this publication does not necessarily constitute endorsement by the ASPE, or its editorial staff.

Individual readers of this book and nonprofit libraries acting for them are permitted to make fair use of the material contained in this book to be used in teaching or research; provided they copy said paper in total, as written by the author. Permission is granted to quote excerpts from the scientific or technical works in this book with proper acknowledgement of the source to include: the author's name, the book name, and the ASPE tag line. Reproduction of figures and tables is likewise permitted from the contents of this book, provided that the same acknowledgement of the same source and content is permitted.

Any other type of reproduction, systematic coping, or multiple reproduction of any material in this book is expressly prohibited except with the written permission of the ASPE editorial staff, addressed to the Society's headquarters.

ISBN 978-1-887706-79-7
2020

The American Society for Precision Engineering
230 Washington Ave. Ext., Suite 101
Albany, NY 12203

Contents

Preface i

Table of Contents ii

Foreward iii

ASML 2020 Student Scholarship and Winners iv

Tutorials ..... v - vi

Keynote Speakers ..... vii - viii

Technical, Oral Sessions Index ..... ix - xiii

Technical Extended Abstracts ..... 1 – 146

Author Index 147

Foreword

Welcome to the Sixth ASPE Topical Meeting on **Design and Control of Precision Mechatronic Systems.** The first of these meetings was held in 2001 in Philadelphia; since that time, they have been held on the campus of the Massachusetts Institute of Technology (MIT), as we had planned for this meeting. Of course, plans are *that from which we deviate*, and in this case the coronavirus has thrown all of us a major curve ball, and we are now going to meet in an online virtual conference via Zoom. We welcome all attendees to this new format! We are looking forward to having great papers presented and many opportunities for technical interchanges, albeit in a virtual environment. Thank you to all the presenters and attendees for your adaptability to the new format, and continued interest in this vital topic of precision mechatronics.

The meeting co-chairs and the American Society for Precision Engineering are pleased that you have decided to participate in our 6th Topical Meeting in this series on the precision design and control of mechatronic systems. Mechatronic systems are critical to a wide range of advanced manufacturing and automation processes. The importance of precision mechatronic system control is only expected to rise with the strong push for smarter and more automated manufacturing processes and systems driven by many areas of research and practice, and by the demands of Industry 4.0. Such systems will need to integrate traditional technologies (i.e., mechanical elements, actuators, sensors, drives, and control algorithms) with emerging technologies like cloud computing, big data analytics and artificial intelligence towards achieving high performance. In addition, the multi-domain nature of mechatronic systems requires that designers be able to trade cost and complexity between the mechanical elements, actuators, sensors, drives, and algorithms that constitute a mechatronic system.

The opening tutorials are ***Advanced Feedforward and Iterative Learning Control for Precision Mechatronics and Introduction to Machine Learning and Reinforcement Learning for Precision Engineers.*** These will provide participants with the opportunity to become acquainted with fundamental principles as well as recent developments in the field of mechatronic system design. We have three exciting keynote presentations on topics of great interest to our community, presented by leaders in our field. The many excellent technical papers encompass a wide range of novel progress in precision mechatronics. Enjoy!

Meeting Co-Chairpersons:

Dr. David L. Trumper, Massachusetts Institute of Technology

Prof. Chinedum E. Okwudire, University of Michigan

Dick Laro, MI-Partners

Dr. Wouter B.J. Hakvoort, University of Twente

2020 Scholarships Recipients

ASML Student Scholarships

We are pleased to announce that, with the generous support of the ASML company, 12 student scholarships were awarded to students who submitted and were selected to present a paper at the 2020 ASPE Topical Meeting on Design and Control of Precision Mechatronic Systems. The scholarships cover the cost of conference registration and tutorials for the spring topical meeting.

The ASML student scholarship was offered to students attending university and who are still enrolled at the time of the conference.

Congratulations to our 2020 ASML Student Scholarship Winners:

Paper Title: Low-Cost, High-Dynamic Range Position Sensing Enabled by Oversampling and Averaging
Author: Brij M. Bhushan

Paper Title: Thermally Stable Precision Motion and Positioning Mechanism
Author: Heebum Chun

Paper Title: Heuristically Optimized H-Infinity Synthesis for the Real-time Positioning of a Tip-based Measurement Device
Author: Liam G. Connolly

Paper Title: Vibration Mitigation on Precision Ball-Screw Feed-Drives Through Data-Driven Tuning of Trajectory Pre-Filters
Author: Alper Dumanli

Paper Title: Achieving High-speed and High-precision Extrusion 3D Printing Through Advanced Mechatronic Design and Control
Author: Nosakhare Edoimioya

Paper Title: Design and Control of a Linearly Thermal Actuation System
Author: Chunjie Fan

Paper Title: Variable Resolution FFF Printing Using Variable Orifice Extruder System
Author: Osama Habbal

Paper Title: Closed-loop Suspension and Rotation of A Spherical Permanent Magnetic Dipole Actuator
Author: Tyler T. Hamer

Paper Title: Combined Feedforward Tracking Control and Feedrate Optimization – with Application to a 3-D
Printer
Author: Heejin Kim

Paper Title: Adaptive Feedforward Control of a Flexure Based Hexapod
Author: Sil Spanjer

Paper Title: A Novel Position Sensing System for Bearingless Motors
Author: Benjamin Stone Weinreb

Paper Title: Model and Controller Design for High-speed Atomic Force Microscope Imagine and Autotuning
Author: Fangzhou Xia

Tutorials

AM Tutorial: Wednesday, May 6, 2020 • 8:30 AM – 12:30 PM

Advanced Feedforward and Iterative Learning Control for Precision Mechatronics

Dr. Tom Oomen, Eindhoven University of Technology

Do you also have a system that has the same error in each task? In this tutorial, we investigate advanced feedforward and iterative learning control (ILC) algorithms to improve the performance of your system. The tutorial consists of several topics.

First, traditional ILC algorithms can learn from measured error signals of previous tasks. After just a few iterations, such algorithms can compensate any repeating disturbance perfectly. We will first explore which applications are suitable for ILC, and a very simple test allows you to immediately determine the achievable ILC performance of your system. A complete design framework that resembles standard loop-shaping control techniques is presented, which guarantees fast and safe learning. Essential technical aspects such as robust and monotonic convergence as well as non-causal filtering are explained in an intuitive and directly usable manner. An overview of optimization-based ILC techniques is outlined, as well as their advantages and disadvantages.

Second, advanced feedforward is investigated. Indeed, ILC algorithms achieve exceptional performance for repeating tasks, however, they are far from standard in industrial practice. One of the key reasons is that iterative learning control cannot deal with varying tasks. Even a small variation can lead to disastrous performance deterioration. Many industrial systems perform such very similar yet slightly different tasks, necessitating new concepts for advanced feedforward control, including high-order feedforward (snap, jerk, etc.), input shaping, automated tuning, etc. These new concepts have been developed in recent years, whereas most of these ‘iterative learning control’ (ILC) techniques have been developed in the past two decades and many successful industrial applications have been reported, in particular in precision

mechatronics such as printing systems, additive manufacturing, wafer scanners, pick-and-place machines, etc.

Throughout, extensions of the design framework to multivariable systems are outlined, as well as several recent connections to machine learning techniques. The tutorial is of interest to anyone interested in improving the performance of their control system. It is aimed to attract a broad audience: no prior knowledge of learning control is required and only a basic knowledge of feedforward/feedback control (including block diagrams, frequency domain, etc.) is assumed. The tutorial will also be of interest to experts in the field, since it covers recently developed techniques as well.

PM Tutorial: Wednesday, May 6, 2020 • 1:30 PM – 5:30 PM

Introduction to Machine Learning and Reinforcement Learning for Precision Engineers

Dr. Amir Barati Farimani, Carnegie Mellon University

In this entry-level tutorial, we will explore machine learning techniques with the goal of identifying suitable opportunities to use them in problems related to precision engineering and control engineering. The course assumes no past experience with these techniques and begins with a review of the terminology and differences and similarities between machine learning, reinforcement learning, deep learning, and artificial intelligence tools. With the nomenclature demystified, we will next focus on identifying problems for which these tools can provide a benefit. Some hands-on tutorials with Jupyter Notebooks will be overviewed and practiced. In the second part of the tutorial, we will cover reinforcement learning basics with some classical control examples such as Cart pole, Inverted Pendulum, etc. An introduction to Open AI Gym environment will be given. Finally, we will review case studies of interest to the precision engineers and control with more focus on RL.

Keynote Speakers

Perspectives on Precision Mechatronics

Ton Peijnenburg, Eindhoven University of Technology

Ton Peijnenburg works for VDL Enabling Technologies Group as deputy general manager, with a focus on technology. VDL ETG is a contract development and manufacturing supplier for high-tech equipment industries. In addition, he works as research fellow at the High-Tech Systems Center of Eindhoven University of Technology. He received his MSc in electrical engineering from TU/e in 1992, subsequently joined Philips at the Center for Industrial Technology where he worked on a broad variety of mechatronics projects. Starting in 2002, he served Philips' North America branch as an expat Mechatronics System Manager for five years. In 2008 he became R&D manager for the FEI Phenom desktop electron microscope and in 2010 joined VDL ETG.

Nanomanufacturing Enabled by Precision Systems, In-Situ Metrology and Real-Time Control

Prof. S.V. Sreenivasan, NASCENT Center, The University of Texas at Austin

Prof. S.V. Sreenivasan's research focuses on creating scalable nanofabrication technologies that enable novel devices in electronics, displays, and healthcare sectors. He currently serves as the director of the NSF funded NASCENT Engineering Research Center. He has received several awards for his work including the Technology Pioneer Award from the World Economic Forum, the ASME Leonardo da Vinci Award, the ASME William T. Ennor Award, and the ASME Machine Design Award. He was named a fellow of the National Academy of Inventors in 2017. Dr. Sreenivasan founded Molecular Imprints Inc. (MII), a nanopatterning spin out from UT-Austin that has resulted in commercial products in the semiconductor and display industries. He currently serves as the Chief Technologist of Canon Nanotechnologies, Inc., a company formed as a result of the acquisition of the semiconductor business of MII by Canon Corporation in 2014. The display division of MII was acquired in 2015 by Magic Leap, Inc., a leading augmented/mixed reality company.

Keynote Speakers

Robots with Physical Intelligence

Prof. Sangbae Kim, Biomimetic Robotics Laboratory, Massachusetts Institute of Technology

Sangbae Kim is the director of the Biomimetic Robotics Laboratory and an associate professor of Mechanical Engineering at MIT. His research focuses on bio-inspired robot design achieved by extracting principles from animals. Kim's achievements include creating the world's first directional adhesive inspired by gecko lizards and a climbing robot named Stickybot that utilizes the directional adhesive to climb smooth surfaces. TIME Magazine named Stickybot one of the best inventions of 2006. One of Kim's recent achievements is the development of the MIT Cheetah, a robot capable of stable running outdoors up to 13 mph and autonomous jumping over obstacles at the efficiency of animals. Kim is a recipient of best paper awards from the ICRA (2007), King-Sun Fu Memorial TRO (2008) and IEEE/ASME TMECH (2016). Additionally, he received a DARPA YFA (2013), an NSF CAREER award (2014), and a Ruth and Joel Spira Award for Distinguished Teaching (2015).

ASPE 6th Design and Control of Precision Mechatronic Systems
Topical Meeting Oral Sessions

Session Chairs:
David L. Trumper (Massachusetts Institute of Technology),
Chinedum Okwudire (University of Michigan),
Dick Laro (MI-Partners),
Wouter B.J. Hakvoort (University of Twente)

Session 1 – Industry 4.0 and Learning Control
Thursday, May 7, 2020, 9:30 AM - 11:00 AM

1. **How Learning Control Supports Industry 4.0 in Semiconductor Manufacturing**
   Van der Veen, G.; Stokkermans, J. (Equipment & Automation Technologies Nexperia); Mooren, N.; Oomen T. (Eindhoven University of Technology) 1

2. **Advanced Feedforward Control as a Service from the Cloud**
   Okwudire, C. E. (University of Michigan)..... 6

3. **Procedure Control of Nano Materials Design via Reinforcement Learning Control**
   Wang, Y.; Cao, Z. (Department of Mechanical Engineering); Farimani, A. B. (Department of Mechanical Engineering; Carnegie Mellon University) 12

4. **Long-range Piezo-stepper Actuators: Towards Nanoscale Accuracy Through Commutation-angle Iterative Learning**
   Aarnoudse, L.; Strijbosch, N. (Eindhoven University of Technology); Verschueren, E. (Thermo Fisher Scientific); Oomen T. (Eindhoven University of Technology) 16

Session 2 – Advances in Motors
Thursday, May 7, 2020, 11:30 AM - 12:45 PM

1. **Harness the Lag: Precision Positioning with Hysteresis Motors**
   Zhou, L. (Mitsubishi Electric Research Laboratories); Trumper, D. L. (Massachusetts Institute of Technology)..... 21

2. **Design and Measurement of a 6-Phase Combined Winding Bearingless Synchronous Reluctance Slice Motor**
   Gruber, W.; Enengl, P. (Institute of Electrical Drives and Power Electronics Johannes Kepler University Linz); Sokolov, M. (Aalto University School of Electrical Engineering) 27

3. **Decoupled, Closed-loop, Multi-DoF Suspension of a Spherical Permanent Magnetic Dipole Actuator**
   Hamer, T. T. (Massachusetts Institute of Technology); Chabot, J. (MIT Lincoln Laboratory); Trumper, D. L. (Massachusetts Institute of Technology) 31

4. **A Novel Position Sensing System for Bearingless Motors**
   Weinreb, B. S. (Massachusetts Institute of Technology; The Charles Stark Draper Laboratory, Inc.); Fyler, D. (The Charles Stark Draper Laboratory, Inc.); Trumper, D. L. (Massachusetts Institute of Technology) 37

Session 3 – Advances in Autotuning and Feedforward Control
Thursday, May 7, 2020, 1:30 PM - 3:00 PM

1. **Auto-Tuning of Precision Servo Controllers Suffering from Large Mass Ratio Induced Vibrations**
   Dumanli, A. (Oregon State University); Lowe, J.; Badrawy, S. (Moore Nanotechnology Systems); Sencer, B. (Oregon State University) 43

2. **Combined Feedforward Tracking Control and Feedrate Optimization – with Application to a Precision XY Stage**
   Kim, H.; Okwudire, C. E. (University of Michigan) 49

3. **Feedforward Spectral Tuning and Using Iterative Learning Control for Automated Parameter Fitting**
   Jabben, L.; Luijten, F. (MI-Partners) 54

4. **Adaptive Feedforward Control of a Flexure Based Hexapod**
   Spanjer, S. T.; Hakvoort, W. B. J. (University of Twente) 58

Session 4 – Advances in Mechatronic Design I
Thursday, May 7, 2020, 3:00 PM - 4:00 PM

1. **Vacuum Compatible Contactless Active Magnetic Linear Bearings for High Cleanliness Robotic Applications**
   Baade, R. (Eindhoven University of Technology); Peijnenburg, T. (VDL Enabling Technology Group); Steinbuch, M. (Eindhoven University of Technology) 63

2. **Variable Resolution Fused Filament Fabrication (FFF) Printing Using a Variable Orifice Extruder System**
   Habbal, O.; Pannier, C (University of Michigan-Dearborn) 69

3. **Design and Control of a Thermal Actuation System**
   Fan, C.; Hastings, D. J.; Smith, S. T. (The University of North Carolina at Charlotte) 73

Session 5 – Advances in Sensing and Feedback Control I
Friday, May 8, 2020, 9:30 AM - 11:00 AM

1. **Low-cost, High Dynamic Range Position Sensing Enabled by Oversampling and Averaging**
   Bhushan, B. M.; Trumper, D. L. (Massachusetts Institute of Technology) 77

2. **Improved Current Control of Inverter Fed Two-phase Bipolar Stepper Motors Using Repetitive Control**
   Kramer, B. (ACS Motion Control) 82

3. **Dynamics and Control of the PTB Nanometer Comparator**
   Köchert, P.; Köning, R.; Weichert, C.; Flügge, J. (Physikalisch-Technische Bundesanstalt); Manske, E. (Ilmenau University of Technology) 87

4. **Heuristically Optimized H-Infinity Synthesis for the Real-time Positioning of a Tip-based Measurement Device**
   Connolly, L. G.; Dibua, O. G.; Cullinan, M. (The University of Texas at Austin) ..... .93

Session 6 – Advances in Sensing and Feedback Control II
Friday, May 8, 2020, 11:30 AM - 12:45 PM

1. **Model and Controller Design for High-speed Atomic Force Microscope Imaging and Autotuning**
   Fangzhou, X.; Yang, C.; Wang, Y.; Youcef-Toumi, K. (Massachusetts Institute of Technology) 99

2. **Implementation of Length Control of an Optical Cavity Using Second-order Transverse Modes**
   Fernández-Galiana, A. (Massachusetts Institute of Technology); Arnbak, J. (The Technical University of Denmark); Evans, M.; Mavalvala, N. (Massachusetts Institute of Technology) 105

3. **Active Optical Mode Matching for Quantum Squeezing Cavaties and Upcoming LIGO Upgrades**
   Noh, M. (LIGO Laboratory, Massachusetts Institute of Technology) (The British University of Technology); Cao, T. C.; Ng, S. (The University of Adelaide); Srivastava, V. (Syracuse University); Jia, W.; Mansell, G. (LIGO Laboratory, Massachusetts Institute of Technology); Griffith, D.; Torrie, C.; Abbott, R.; Brooks, A. (LIGO Laboratory); Ballmer, S. (Syracuse University); Veitch, P. (The University of Adelaide); Fritschel, P. (LIGO Laboratory, Massachusetts Institute of Technology); Matichard, F. (LIGO Laboratory, Massachusetts Institute of Technology) 110

Session 7 – Modeling and Control of Precision Machines
Friday, May 8, 2020, 1:30 PM - 3:00 PM

1. **Reduced Thermo-mechanical Model of a Rotary Table of a 5-axis Precision Machine Tool**
   Hernández-Becerro, P. (Inspire AG Technoparkstrasse; Institute of Machine Tools and Manufacturing); Mayr, J. (Inspire AG Technoparkstrasse); Wegener, K. (Institute of Machine Tools and Manufacturing) 113

2. **Loop-shaping Controller Design in the Development of the High-Dynamic Double-Crystal Monochromator for Sirius Light Source**
   Caliari, R. M. (Brazilian Synchrotron Light Laboratory); Geraldes, R. R. (Brazilian Synchrotron Light Laboratory; Eindhoven University of Technology); Moraes, M. A. L. (Brazilian Synchrotron Light Laboratory); Witvoet, G. (Eindhoven University) 119

3. **Dynamic Error Budgeting in the Development of the High-Dynamic Double-Crystal Monochromator for Sirius Light Source**
   Geraldes, R. R. (Brazilian Synchrotron Light Laboratory; Eindhoven University of Technology); Moraes, M. A. L. (Brazilian Synchrotron Light Laboratory); Caliari, R. M. (Brazilian Synchrotron Light Laboratory); Witvoet, G. (Eindhoven University) ... 125

4. **The FPGA Control Implementation of the High-Dynamic Double-Crystal Monochromator at Sirius Light Source**
Moraes, M. A. L.; Caliari, R. M. (Brazilian Synchrotron Light Laboratory); Geraldes, R. R. (Brazilian Synchrotron Light Laboratory; Eindhoven University of Technology) 131

Session 8 – Advances in Mechatronic Design II
Friday, May 8, 2020, 3:00 PM - 3:45 PM

1. **Delta Robot Combining Millimetre Travel with Nanometre Performance**
Kelly, J. H. (Harwell Science Campus) 137

2. **Thermally-stable Precision Motion and Positioning Mechanism**
Chun, H. (Texas A&M University); Kim, H. Y. (Korea Institute of Industrial Technology); Lee, C. (Texas A&M University) 141

HOW LEARNING CONTROL SUPPORTS INDUSTRY 4.0 IN SEMICONDUCTOR MANUFACTURING

Gijs van der Veen[1], Joep Stokkermans[1], Noud Mooren[2], and Tom Oomen[2]
[1]Equipment & Automation Technologies
Nexperia
Nijmegen, The Netherlands
[2]Department of Mechanical Engineering, Control Systems Technology Group
Eindhoven University of Technology
Eindhoven, The Netherlands

INTRODUCTION

Successful smart manufacturing implementations bring tremendous cost and quality benefits in the semiconductor industry. Instead of optimizing single-system performance, production is optimized at factory level. High-accuracy and reliable servo performance at machine level are must-be qualities [1]. Data-based concepts such as machine learning and performance prediction can only work reliably if similar systems behave and perform similarly. This is also required to enable portability of process programs across a scalable number of machines. Classical feedforward control no longer suffices to achieve flawless motion performance over the life-cycle of a machine, independent of its maintenance condition and valid over various generations of equipment.

Semiconductor assembly machines, such as die bonders and pick-and-place machines, have many precision servo axes that operate in a point-to-point fashion with a precision in the order of micrometers. The point-to-point motions have very short durations of tens of milliseconds, making the axes largely dependent on feedforward control for decent tracking performance. In order for a process to start as soon as possible, the axis must quickly settle at the final position. Even with a good feedforward controller, the optimal feedforward parameters differ between machines due to manufacturing tolerances, wear and cost constraints. This provides an opportunity for a robust, real-time tuning strategy that can maintain optimal performance over time.

Since many machine axes perform (almost) repeating tasks, iterative learning control [2] (ILC) can potentially improve performance by learning from reproducible errors. In Nexperia's die bonding equipment, the critical axes rely on camera-assisted trajectory planning. For instance, a point-to-point trajectory of a pickup head may be adjusted by several micrometers each time to account for observed offsets in product positions. The consequence is that no two trajectories are identical. While conventional ILC deals with perfectly reapeating setpoints, ILC with basis functions [3] has been developed to handle varying trajectories. Basis-function ILC essentially results in an online feedforward tuning algorithm, which is parameterized using the reference and tunable parameters.

The aim of this paper is to implement basis function ILC [2] on several axes of the Nexperia ADAT3-XF die bonder platform, leading to significant performance improvements. Axes with different combinations of dominant characteristics such as Coulomb friction, viscous friction, and stiffness are considered. In each case, the ILC algorithm performs reliably with little tuning effort, leading to smaller tracking errors, faster and improved settling at the final position, and reduced performance variation. The learning can be active during production, meaning that representative production cycles are used to learn. To run the ILC algorithm alongside the machine cycle which runs in excess of 72000 products per hour, updates must be computed within a fraction the 50ms cycle time. For this reason, an efficient implementation based on the FFT is used. The implementation relies on inexpensive frequency response measurements of the system.

This paper discusses the potential of ILC in several modules of Nexperia's die bonder. Furthermore, an efficient implementation is developed, that is essential for industrial deployment of the solution.

DIE BONDER MACHINE ARCHITECTURE

Nexperia's ADAT (Automatic Die ATtach) die bonder (Fig. 1) is a versatile semiconductor assembly

platform. It is mostly aimed at assembly of small discrete (diode, transistor, logic) semiconductor packages ranging in size from 200 µm to 1 mm. The platform is intended for high-speed (more than 48000 units per hour) and high-accuracy (better than 10 µm 1σ placement accuracy) assembly.

FIGURE 1. The Nexperia ADAT3-XF assembly platform.

The basic assembly process is shown in Fig 2. After wafer production (1) and cutting (2), the first step is to select and pick up the product (3). The wafer is handled by a wafer stage (3). The products are picked up by a vacuum nozzle (3) that can move in vertical direction. The vacuum nozzle attaches the product to a substrate (4) that is handled by a substrate handler. The substrate handler is an interchangable module that permits handling of copper lead frame strips, reel-based lead frames, plastic strips, real-based tapes and RFID/NFC substrates depending on the particular semiconductor device. Subsequently, the products are molded (5) and electrically tested (6).

In this work we consider two motion axes that are critical to the quality of the assembly process.

Axis 1: Product handler logitudinal movement
The first axis is the product handler X-axis, which is involved in accurately positioning the substrate before assembly. This positioning must happen with a fast settling at the final position so that the machine speed is not hampered.

Axis 2: Pickup head radial movement
The second axis is involved in the motion of the pickup head. Each pickup head can move in axial direction in order to pick up products from the wafer and place them onto a substrate. This axis is involved in handling the semiconductor dies and accurate control results in predictable forces on the products.

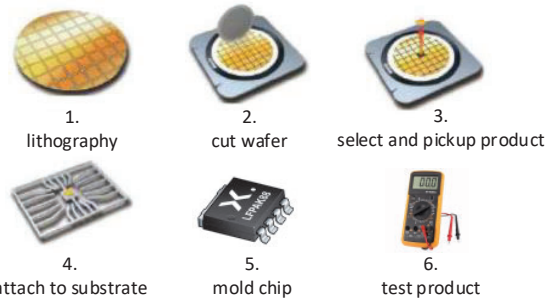

FIGURE 2. The basic semiconductor assembly process.

IMPLEMENTATION OF BASIS FUNCTION ILC

Standard ILC generates a feedforward signal that attempts to eliminate the reproducible errors for a specific perfectly repeating task. To be robust to changes in tasks and task durations, model-based feedforward is combined with learning control. This leads to basis function ILC [3].

Controller structure

The control structure is shown in Fig. 3. The feedback controller C(z) is a standard PID controller with optional filters, operating at an 8 kHz sample rate. The feedforward model structure includes jerk (k_j), inertia (k_a), viscous friction (k_v), Coulomb friction (k_C), stiffness (k_s) and spring offset (k_{so}) feedforward, according to Eq. 1:

$$f_j = k_j \dddot{r}_j + k_a \ddot{r}_j + k_v \dot{r}_j + k_C \operatorname{sign}(\dot{r}_j) + k_s r_j + k_{so}. \quad (1)$$

In this model, the derivatives of r_j are precomputed and implemented following the considerations in [4]. The index j refers to the j-th task.

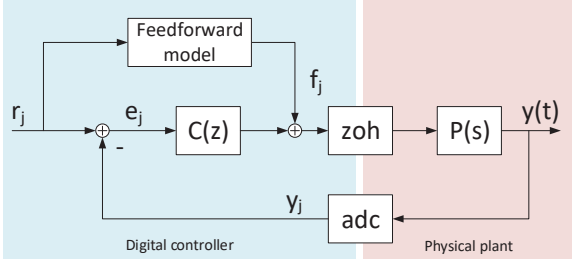

FIGURE 3. Controller structure.

Basis function ILC

Based on Fig. 3, the error in task j is given by [6]:

$$e_j = Sr_j - PSf_j,$$

with $S = \frac{1}{1+PC}$ and P the plant. For a constant reference signal, it follows that:

$$e_{j+1} = e_j - PS(f_{j+1} - f_j). \tag{2}$$

In our implementation of basis function ILC the feedforward signal f_j is linearly parameterized as:

$$f_j = \Psi_j \theta_j \tag{3}$$

Specifically, for the structure in (1):

$$\Psi_j = \begin{bmatrix} \dddot{r}_j & \ddot{r}_j & \dot{r}_j & \text{sign}(\dot{r}_j) & r_j & \mathbf{1} \end{bmatrix}$$
$$\theta_j = \begin{bmatrix} k_J & k_a & k_v & k_C & k_s & k_{so} \end{bmatrix}^T$$

For a norm-optimal ILC solution the following objective function is minimized [2, 3]:

$$\mathcal{J}(\theta_{j+1}) = \|e_{j+1}\|^2_{W_e} + \|\theta_{j+1} - \theta_j\|^2_{W_{\Delta\theta}}, \tag{4}$$

in which $e_j \in \mathbb{R}^N$ is the error signal in the j-th task of N samples, $W_e \in \mathbb{R}^{N\times N}$ is a (diagonal) matrix imposing a temporal weight on the error signal and $W_e \in \mathbb{R}^{n\times n}$ is a (diagonal) matrix weighing the rate of change of the feedforward parameters.

Substituting (2) and (3) into (4) it can be shown [3, 9] that the update of the feedforward parameters is given by:

$$\theta_{j+1} = Q\theta_j + Le_j, \tag{5}$$

with:

$$Q = \left(\Psi_j^T J^T W_e J \Psi_j + W_{\Delta\theta}\right)^{-1} \left(\Psi_j^T J^T W_e J \Psi_j + W_{\Delta\theta}\right),$$
$$L = \left(\Psi_j^T J^T W_e J \Psi_j + W_{\Delta\theta}\right)^{-1} \Psi_j^T J^T W_e,$$

in which J is the Toeplitz matrix corresponding to the process sensitivity PS (i.e.the lifted representation).

Efficient implementation

Although the update (5) involves inversion of small matrices (i.e. n-by-n matrices with n the number of feedforward parameters), the construction of these matrices relies on forming the product $J\Psi_j$, where J is an $N \times N$ Toeplitz matrix containing the impulse response of the process sensitivity PS. Hence, the product $J\Psi_j$ is identical to filtering the columns in Ψ_j with the process sensitivity. To speed up computation, use is made of the fact that this filtering in the time domain, equivalent to a linear convolution, can be executed efficiently in the frequency domain. To achieve a linear convolution, zero-padding must be performed. Suppose m samples of the impulse response of PS are available. Then, the impulse response and the vectors in Ψ_j must both be zero-padded to a length of $N+m-1$ samples (or the next power of two). These sequences can be transformed to the frequency domain (using the fast Fourier transform (FFT)), where the convolution translates into a point-wise multiplication. The result is transformed back to the discrete time domain (using the inverse FFT).

The FFT-based algorithm involves $2Nn(\log(N)+1)$ operations compared to the $nN(N+1)$ operations for the full matrix product.

The impulse response is the inverse FFT of a frequency response function (FRF) measurement of PS, which is readily obtained from an experiment in which noise is injected on the feedforward input and its effect on the error signal is measured.

RESULTS

This section reports the results of applying basis function ILC to the two machine modules mentioned earlier.

Axis 1: Product handler

The product handler is a linear stage with preloaded bearings and a linear motor. It is affected by friction. The feedforward model includes the terms k_a, k_v and k_C.

In the experiments, the product handler makes steps of 1 mm with a uniformly distributed variation of 10 µm. Fig. 4 shows the results with feedforward with fixed parameters. The mean error is indicated in solid black, and indicates the reproducible portion of the servo error. Fig. 5 confirms that the mean error across the tasks is indeed reduced significantly with basis function ILC. Fig. 6 shows that after enabling ILC, the performance already improves within 10 tasks.

Axis 2: Pickup head

The pickup head is a small leaf-spring mechanism, driven by a brushless motor via a pulley and cable assembly. The whole mechanism is affected by friction and stiffness. The feedforward model includes the terms k_a, k_v, k_C, k_s and k_{so}. The spring offset term is essential since the axis not equipped with an integrator to remove offsets.

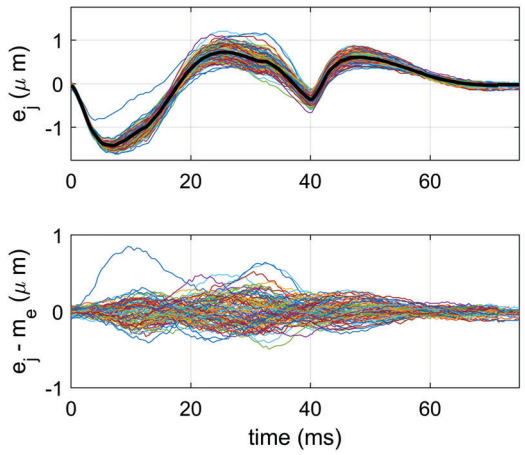

FIGURE 4. Product handler position error with standard feedforward. The mean error m_e is shown in black. The bottom plot shows the deviations from the mean error.

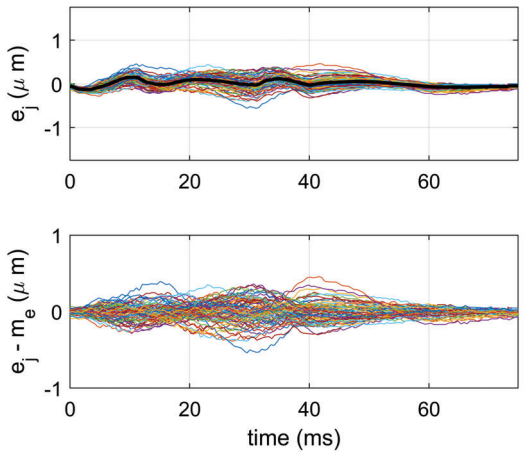

FIGURE 5. Product handler position error with basis function ILC. The mean error m_e (black) has been reduced significantly. The non-reproducible component of the error is similar to that of Fig. 4

In the experiments, the pickup head makes resetting movements of $1\,\mathrm{mm}$. Fig. 7 shows that with a fixed feedforward model the errors are significant but highly reproducible. With basis function ILC (Fig. 8) a small error remains. Interestingly, the remaining errors are still largely reproducible, but of an oscillatory nature caused by machine vibrations. These errors cannot be accounted for by the basis functions. Input shaping could be considered to improve performance [8].

CONCLUDING REMARKS

Basis function ILC is demonstrated to lead to significant performance improvements on two important machine axes of the ADAT die bonding platform. The algorithm improves servo performance in a few cycles and maintains performance when slight variations in the dynamics occur, such as a position-dependent friction or force constant. These characteristics have the potential to make the performance of the machine more robust and consistent over time. If this succeeds, smart manufacturing systems can allocate different manufacturing processes to a group of machines at will, relying on the fact that they perform predictably and identically (so-called process portability).

Remaining work includes the definition of safe limits on feedforward parameters adapted by the ILC algorithm. These limits should ensure that the module is functionally sound. Furthermore, as parameters tend towards one of the limits, this can serve as an indication of machine health or the need for maintenance.

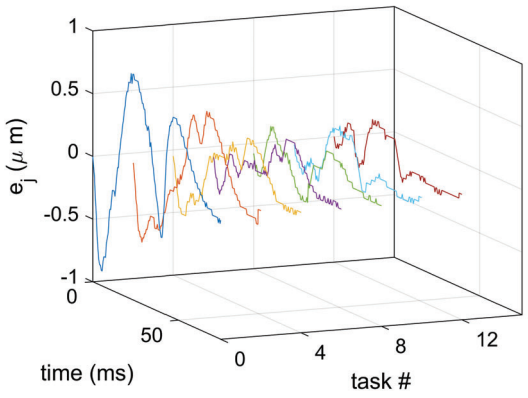

FIGURE 6. When basis function ILC is enabled, performance is improved within about 10 tasks.

ACKNOWLEDGMENTS

The authors would like to thank Abhishek Bareja and Thijs Kniknie for their suggestions. This work was made possible by funding from ECSEL-2016-1 under grant agreement number 737453 (I-MECH).

REFERENCES

[1] Kano N, Seraku N, Takahashi F, Tsuji S. Attractive Quality and Must-Be Quality. Journal of the Japanese Society for Quality Control. 1984; 41: 39-48.

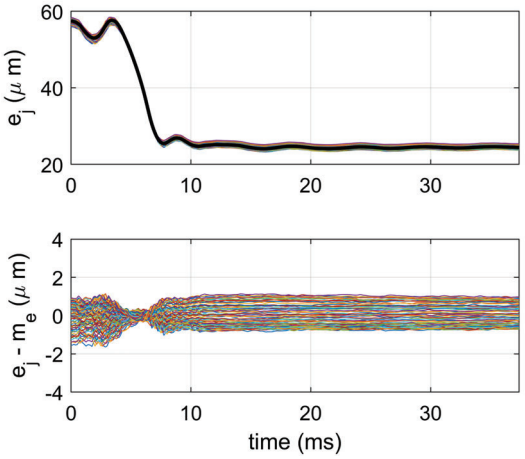

FIGURE 7. Pickup head position error with standard feedforward. The mean error m_e is shown in black.

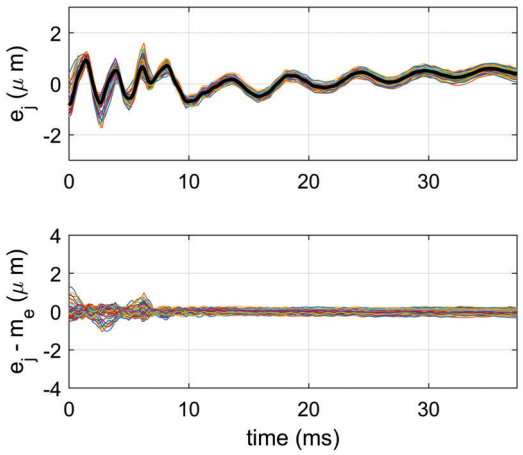

FIGURE 8. Pickup head position error with basis function ILC. The mean error m_e (black) has been reduced significantly. Even the non-reproducible component of the error has been reduced compared to Fig. 7

[2] Bristow D A, Tharayil M, Alleyne A G. A survey of iterative learning control. IEEE Control Systems Magazine. 2006; 26(3): 96-114.

[3] van de Wijdeven J, Bosgra O H. Using basis functions in iterative learning control: analysis and design theory. International Journal of Control. 2010; 23: 661-675.

[4] Lambrechts P, Boerlage M, Steinbuch M. Trajectory planning and feedforward design for electromechanical motion systems. Control Engineering Practice. 2005; 13(2): 145-157.

[5] Franklin G F, Powell J D, Emami-Naeini, A. Feedback control of dynamic systems. Pearson Education. 2006.

[6] Oomen T. Learning for Advanced Motion Control. International Workshop on Advanced Motion Control, Agder, Norway, 2020

[7] Boeren F, Bareja A, Kok T, Oomen T. Frequency-Domain ILC Approach for Repeating and Varying Tasks: With Application to Semiconductor Bonding Equipment. IEEE/ASME Transactions on Mechatronics. 2016; 21(6): 1083-4435.

[8] Boeren F, Bruijnen D, van Dijk N, Oomen T. Joint Input Shaping and Feedforward for Point-to-Point Motion: Automated Tuning for an Industrial Nanopositioning System. Mechatronics. 2014; 24(2): 572-581.

[9] Bolder J, Oomen T, Steinbuch M. Exploiting rational basis functions in iterative learning control. IEEE Conference on Decision and Control. 2013.

ADVANCED FEEDFORWARD CONTROL AS A SERVICE FROM THE CLOUD

Chinedum E. Okwudire
Department of Mechanical Engineering
University of Michigan
Ann Arbor, MI

OVERVIEW

Control as a Service (CaaS) is an emerging paradigm where low-level control of a device is moved from a local controller to the cloud, and is provided to the device as an on-demand service. CaaS gives the device access to advanced control algorithms which may not be executable on a local controller due to computational limitations. It also provides other benefits like ease of controller upgrade and machine-to-machine learning, to mention but a few. This paper summarizes efforts at University of Michigan's Smart and Sustainable Automation Lab to develop a CaaS platform for advanced feedforward control of manufacturing machines from the cloud, with initial deployment on desktop 3D printers. Preliminary results on a cloud-controlled desktop 3D printer demonstrate the potential benefits and challenges of this concept. Ongoing and future work is outlined.

INTRODUCTION

Control as a Service (CaaS) is an idea that has been growing in popularity over the past few years [1]-[10]. In CaaS, low-level control functionalities of a device are moved out of a local controller to the cloud, where they are remotely accessed on-demand (i.e., as a service). Just like Netflix and similar video streaming services have displaced Blockbuster for video content distribution, we envision CaaS as the future of manufacturing machine (MM) control. Some potential benefits of CaaS are ([1]-[10]):

- With CaaS, a MM can be controlled using advanced algorithms that may not be executable on a local controller with limited computational resources; CaaS thus holds the potential to significantly improve the performance of MMs without need for costly upgrades to powerful onboard computers.
- With CaaS, upgrading the controller of a machine will become much easier, involving little or no hardware changes. This will reduce the problem of frequent obsolescence of MMs due to outdated control hardware.
- CaaS will allow a user to opt for only the control algorithms they need, when they need it, thus slashing costs.
- CaaS could lead to an "app marketplace" for control algorithms, where control engineers and researchers can develop and easily share new control algorithms.
- Due to the connected infrastructure provided by CaaS, data analytics can be used to improve the performance of control algorithms (e.g., fine-tune controller parameters) based on feedback from several machines running the algorithms.
- Computer aided design (CAD), computer aided manufacturing (CAM), computer aided process planning (CAPP) and other upstream software relevant to precision machine control are transitioning to the cloud. CaaS, which can be considered as a form of cloud-based computer numerical control (CNC), could be fully integrated with CAD, CAM and CAPP in the cloud, allowing for seamless information transfer, which has eluded the industry for decades.

Some potential challenges with CaaS include ([1]-[10]):

- Cybersecurity and privacy. These are valid concerns raised against virtually all cloud-based services, and often slows down adoption of cloud solutions [11]. However, companies (like Amazon) which provide platforms for cloud-based applications are able to guarantee close to 100% security [12]. Hence, security-critical applications (like banking) are increasingly adopting cloud solutions. Techniques, like those used for cloud banking, can be used in cloud manufacturing.
- Sending real-time control signals over the Internet introduces safety and reliability risks due to time delays, dropped packets, and similar Internet quality of service (QoS)

issues. This problem is particularly acute for MMs, for which the timing of control signals is very strict and critical.

In this paper, we present a vision being pursued at University of Michigan's Smart and Sustainable Automation Laboratory to create a platform for explorating the promise of CaaS.

OVERARCHING CAAS VISION

Manufacturing machines often make use of feedback (FB) and feedforward (FF) control. Both require very strict timing of control commands (typically at sampling rates of 1 ms or less). Delivering FB control over the internet at 1 ms intervals is infeasible based on the prevailing internet connection technology. However, it is feasible to deliver FF signals at 1 ms sampling intervals because FF control can benefit from look ahead and buffering which relax timing restrictions.

There are several advanced FF control algorithms, like model-based FF compensation, iterative learning control, reinforcement learning, model-based feed rate optimization, etc., that hold potential to boost the control performance of MMs. However, several of these algorithms are computationally expensive and cannot run on existing control hardware. Offloading these algorithms to the cloud could help alleviate this issue. Some advanced FF algorithms require FB updates. For instance, iterative learning control requires FB updates after every iteration of applying a set of control commands. Model-based FF compensation may need periodic or occasional FB to update model parameters. However, the intervals for obtaining these FB updates are typically greater than 1 s, and are, therefore, feasible over the internet. This leads to the first feature of our CaaS vision:

Feature 1: Focus CaaS on transitioning advanced FF control algorithms (with slow FB updates) to the cloud, while leaving fast FB loops in the local controller.

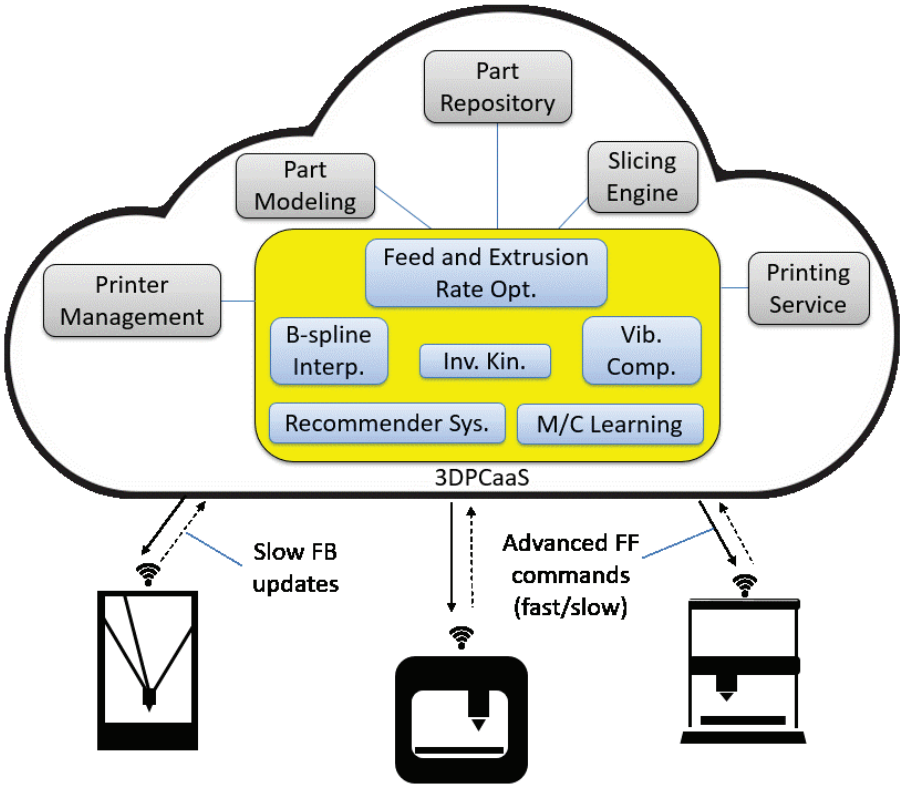

FIGURE 1: Our vision of CaaS for 3D printers (i.e., 3DPCaaS) integrated with various components of the existing cloud-based 3D printing ecosystem

CaaS (also known as cloud-based CNC, or C-CNC [10]) is beneficial to a wide range of industrial-grade MMs; e.g., machine tools, robots, precision motion stages, etc. However, a major impediment to realizing CaaS on industrial-grade MMs – from a researcher's standpoint – is that they are typically closed systems. Significant changes to their control system architecture is needed to enable implementation of CaaS, but industrial-grade MMs do not permit such modifications. Moreover, most of the users of industrial-grade MMs are very sensitive to cybersecurity and privacy. This poses a major cultural barrier to implementing CaaS on industrial-grade MMs.

On the other hand, a thriving community has formed around desktop 3D printers. It revels in open platforms and welcomes cloud-based software. Platforms like 3DPrinterOS, Astroprint and Octoprint are commonly employed by desktop 3D printer users to perform high-level control of their desktop 3D printers. By high-level control, we mean sending Gcode over the internet to control 3D printers remotely. A recent article [13] reports that over the last five years, 95,000 users have generated over three million CAD designs and machine codes, and produced more than one million physical parts on 32,000 manufacturing machines in 100 countries using the 3DPrinterOS cloud platform. Therefore, we see desktop 3D printer users as promising early adopters of CaaS. This leads to the second feature of our vision:

Feature 2: Focus initial deployment and testing of CaaS on desktop 3D printers, and integrate CaaS with other cloud-based software used for desktop 3D printing.

Figure 1 summarizes our CaaS vision comprising features 1 and 2 discussed above. It is termed 3DPCaaS (which stands for 3D printer CaaS) to represent its initial emphasis on desktop 3D printers. Some advanced FF algorithms under consideration for 3DPCaaS include B-spline interpolation, model-based feed rate and extrusion rate optimization, inverse kinematics for non-Cartesian machines, model-based vibration compensation, iterative and reinforcement learning based controllers and servo parameter recommender systems. 3DPCaaS will input Gcode, compute advanced FF commands in the cloud and send them via the internet to a variety of 3D printers connected to the platform. Moreover, 3DPCaaS will be integrated with cloud-based: part repositories (e.g., Thingiverse); part modelling (CAD) and part slicing (CAM) software; as well as printer management and printing service platforms.

INITIAL PROTOTYPE OF CAAS ON A DESKTOP 3D PRINTER ([9][10])

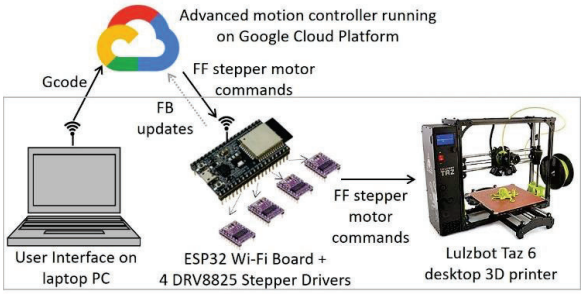
Advanced motion controller running on Google Cloud Platform
Gcode
FF stepper motor commands
FB updates
FF stepper motor commands
User Interface on laptop PC
ESP32 Wi-Fi Board + 4 DRV8825 Stepper Drivers
Lulzbot Taz 6 desktop 3D printer

FIGURE 2. Experimental Set up

Figure 2 shows an experimental set up used for initial prototyping of 3DPCaaS. It consists of a standard virtual machine (cloud computer) from Google Cloud Platform, and an ESP32 Wi-Fi board connected to four DRV8825 stepper motor drivers. The stepper motor drivers are used to separately drive the X, Y, and Z-axes and E (extruder) motors of a Lulzbot Taz 6 3D. An advanced cloud controller runs on a virtual machine and calculates low-level FF control signals in the form of commands for each stepper motor. The FF signals are delivered to the ESP 32 board (which serves as the local machine) via public Internet connection. The local machine buffers the FF signals received from the cloud controller and transmits them in real-time at 20 kHz to the 3D printer via the stepper motor drivers. The size of the buffer is limited by the memory available on the local machine.

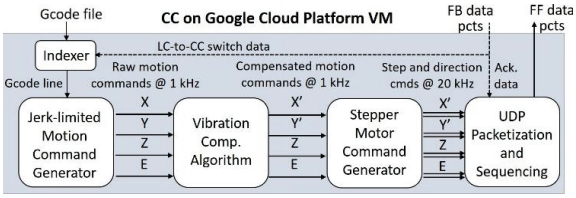

FIGURE 3. Contents of advanced CC on the Google Cloud Platform.

Figure 3 shows the contents of the advanced cloud controller which runs on Google Cloud Platform's n1-standard-1 VM (having 1 vCPU, 3.75 GB memory and Linux OS). It consists of:

(i) an indexer to select the Gcode line from which printing starts or continues; (ii) a jerk-limited motion command generator which generates motion commands at 1 kHz for the X and Y axes of the printer; (iii) an advanced vibration compensation algorithm which convert the X- and Y-axis commands into modified commands (X' and Y') that minimize the vibration of the printer; and (iv) a stepper motor command generator which converts the respective axis commands into equivalent stepper motor commands at 20 kHz frequency. The stepper commands are placed in FF data packets, sequenced in chronological order, and transmitted via user datagram protocol (UDP) to the local machine (i.e., ESP 32 board) as detailed in [9]. FB data packets, comprising acknowledgement (ack) data, are returned by the local machine to the cloud controller to ensure the accuracy and completeness of the transmitted data. Note that, due to their relatively slow motions, the Z and E axis do not need jerk-limited motion nor vibration compensation [9]. For more details of the cloud controller and its execution see [9][10].

To compare the cloud-based controller to the local controller, a Medieval Castle is printed at a feedrate of 75 mm/s using the default acceleration limit of the local controller (i.e., 0.5 m/s^2), as well as using the cloud-based controller at 10 m/s^2 acceleration limit. The reason for the 20x difference in acceleration limits between the local and cloud-based controllers is mostly because of the benefits of the advanced vibration compensation algorithm, as demonstrated in [9]. The 3D printer is located in Ann Arbor, MI, while the cloud controller is hosted in South Carolina and Australia. The results are shown in Figure 4. The local controller completes the print in 19 hours 26 minutes while the advanced cloud-based controller in South Carolina and Australia both complete it in 8 hours 47 minutes, without any pauses throughout the prints.

In terms of printing accuracy, the prints by the local and cloud-based controllers are very similar. Notice that the local and cloud-based controllers alike failed in printing a few features at the top of some towers of the castle, highlighted by dashed yellow rectangles in Figure 4. Those features broke off during printing due to very delicate support structures, and may need to be printed at feedrates much lower than 75 mm/s on both the local and cloud-based controllers. However, printing just those delicate portions at lower feedrates is not likely to affect overall printing time very significantly.

However, some preliminary work reported in [10][14] has shown potential for quality and speed issues caused by excessive internet latency. For example, the same Medieval Castle model as in Figure 4 was printed from a cloud controller stationed in Mumbai, India (with the printer still in Ann Arbor, MI [14]). Excessive latency was experienced during the print job. As

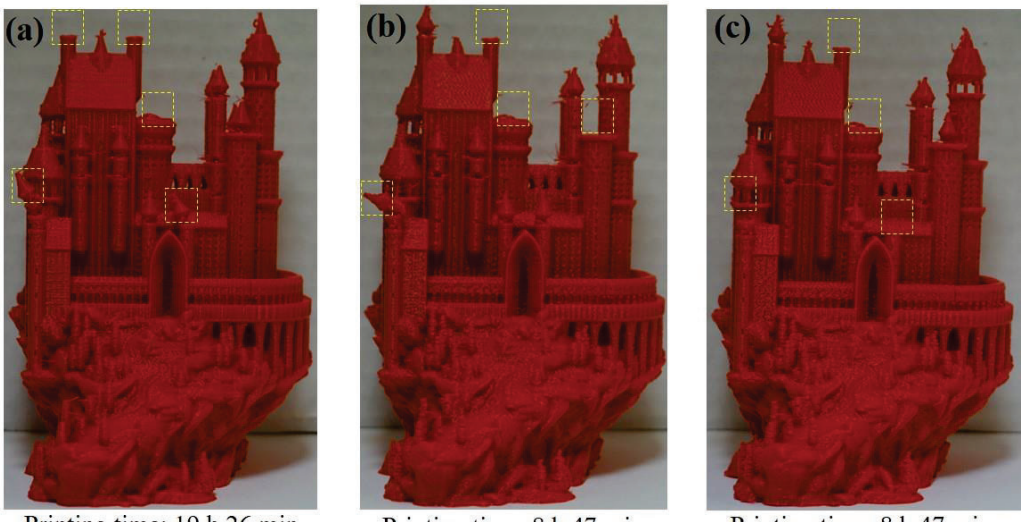

FIGURE 4: Prints of Medieval Castle (height 114.25 mm) using: (a) local controller (Marlin); (b) cloud-based controller in South Carolina and (c) cloud-based controller in Australia. The portions of the prints highlighted in dashed rectangles failed (broke off) during printing due to their very delicate support structures.

a result, the buffer on the ESP32 board would sometimes become empty, resulting in pauses during printing. While the printer was paused to refill the buffer, extra molten filament would ooze out from the nozzle causing blobs on the surface of printed part. Both the print quality and speed were adversely affected.

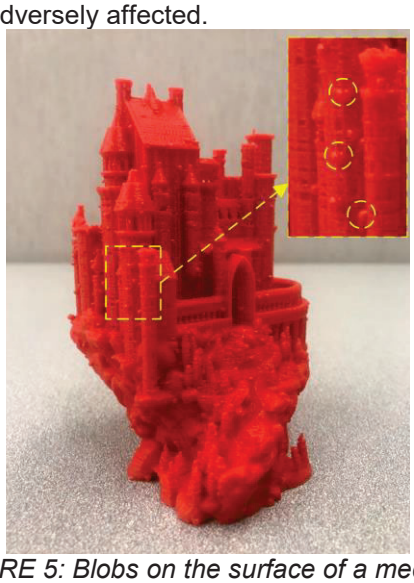

FIGURE 5: Blobs on the surface of a medieval castle model printed using an advanced cloud-based controller stationed in Mumbai, India, due to excessive internet latency. Printing time: 10 h 1 min.

CONCLUSIONS

We have presented a vision for CaaS built on provisioning advanced FF control algorithms from the cloud over internet connections, together with slow FB updates back to the cloud. Furthermore, we have made a case for initial deployment of CaaS on desktop 3D printers. Our reasoning for focusing on advanced FF control in CaaS is because it relaxes the timing requirements for precision control by leveraging look-ahead and buffering. Moreover, we believe that advanced FF control algorithms have a lot to offer to precision manufacturing machines in terms of control performance benefits. The reason for initial deployment of CaaS on desktop 3D printers is because they provide a lower barrier for entry and exploration of this new concept compared to industrial manufacturing machines. Desktop 3D printers can, therefore, serve as a launch pad for deployment of CaaS on industrial-grade manufacturing machines in the form of cloud-based CNC (or C-CNC) [10]. Initial prototyping of CaaS on a desktop 3D printer shows that it is feasible but could introduce issues in control performance due to internet transmission delays and reliability.

ONGOING AND FUTURE WORK

We are currently building a 3DPCaaS platform at the University of Michigan to be hosted at www.3dpcaas.org. The ESP 32 board which was used in our initial prototype will be replaced by a Raspberry Pi minicomputer that will receive the low-level control signals from the cloud. It will interface with desktop 3D printers via USB connection. Furthermore, we are developing a variety of advanced FF control algorithms (shown in Figure 1) for the platform. Interested desktop 3D printer users would be able to connect their printers to the platform and deploy the control algorithms of their choice to obtain enhanced control performance of their printers. Moreover, we anticipate that interested control engineers or researchers would be able to develop new FF control algorithms and deploy them on the platform for the benefit of the 3D printing community.

REFERENCES

[1] A. Verl et al., An approach for a cloud-based manufacturing machine control, *Procedia CIRP*, vol. 7, 2013, pp. 682-687.

[2] O. Givehchi, H. Trsek, and J. Jasperneite, Cloud computing for industrial automation systems—A comprehensive overview, *IEEE 18th Conference on Emerging Technologies and Factory Automation (ETFA)*, 2013, pp. 1-4.

[3] A. Vick et al., Robot control as a service—towards cloud-based motion planning and control for industrial robots, *10th International Workshop on Robot Motion and Control (RoMoCo)*, 2015, pp. 33-39.

[4] T. Hegazy and M. Hefeeda, Industrial automation as a cloud service, *IEEE Transactions on Parallel and Distributed Systems*, vol. 26, no. 10, 2015, pp. 2750-2763.

[5] C. Horn and J. Krüger, Feasibility of connecting machinery and robots to industrial control services in the cloud, *IEEE 21st International Conference on Emerging Technologies and Factory Automation (ETFA)*, 2016, pp. 1-4.

[6] S. Mubeen et al., Delay mitigation in offloaded cloud controllers in industrial IoT, *IEEE Access*, vol. 5, 2017, pp. 4418-4430.

[7] J. Schlechtendahl et al., Extended study of network capability for cloud based control systems, *Robotics and Computer-Integrated Manufacturing*, vol. 43, 2017, pp. 89-95.
[8] Z. Sang and X. Xu, The framework of a cloud-based CNC system, *Procedia CIRP*, vol. 63, 2017, pp. 82-88.
[9] C. Okwudire et al., Low-Level Control of 3D Printers from the Cloud: A Step toward 3D Printer Control as a Service, *Inventions*, vol. 3, no. 3, 2018, pp. 56.
[10] C.E. Okwudire et al., A three-tier redundant architecture for safe and reliable cloud-based CNC over public internet networks, *Robotics and Computer-Integrated Manufacturing*, Vol. *62*, 2020, p.101880.
[11] B. Buckholtz, I. Ragai, and L. Wang, Cloud manufacturing: current trends and future implementations, *Journal of Manufacturing Science and Engineering*, vol. 137, no. 4, 2015,
[12] G. Adamson et al., Cloud manufacturing–a critical review of recent development and future trends, *International Journal of Computer Integrated Manufacturing*, vol. 30, no. 4-5, 2017, pp. 347-380.
[13] A. Vedeshin, et al., A Digital Ecosystem for Personal Manufacturing: An Architecture for Cloud-based Distributed Manufacturing Operating Systems. In *Proceedings of the 11th International Conference on Management of Digital EcoSystems* (pp. 224-228). 2019.
[14] X. Lu, G. Kumaravelu and C.E Okwudire, An Evaluation of Data Size Reduction Techniques for Improving the Reliability of Cloud-based Control of a 3D Printer, *47th North American Research Conference (NAMRC 2019)*, June 10-14, 2019, Erie, PA.

PROCEDURE CONTROL OF NANO MATERIALS DESIGN VIA REINFORCEMENT LEARNING

Yuyang Wang[1], Zhonglin Cao[1] and Amir Barati Farimani[1,2]
[1]Department of Mechanical Engineering
[2]Machine Learning Department
Carnegie Mellon University
Pittsburgh, PA, USA

INTRODUCTION

The scarcity of fresh, drinkable water has grown to be much more severe than it was decades ago. Approximately 1.8 billion people will be affected by water scarcity by the time of 2025, estimated by the United Nations. Currently, water desalination is regarded as a effectively method to alleviate water scarcity caused by physical reasons such as lack of access to fresh water source. Reverse osmosis (RO), which involves applying pressure on saline water against a porous membrane to filter out undesired ions, is the most prevailing technology in the domain of water desalination. The geometry of pore and membrane material can significantly influence the efficiency of reverse osmosis process, by determining the two major performance indicators including water flux and ion rejection rate. For the ideal case of water desalination, the membrane should be able to maximize the water flux allowed from the pore while maintaining high level of ion rejection rate. Therefore, precise design of the porous structure of membranes can potentially increase the energy-efficiency of RO water desalination. However, due to the large quantity and variety of atoms contained in a membrane, as well as the time-consuming nature of molecular dynamics simulations to obtain water flux or ion rejection rate of a specific membrane, it is infeasible to find the optimal design of nanoporous structure by exhaustion of experiments.

One possible solution to expedite the designing process of optimal pore geometry for RO membrane is reinforcement learning. Some explanation of why reinforcement learning is useful in this case, with a figure to introduce the pipeline of reinforcement learning.

In this work, we demonstrate that the water flux and ion rejection of a membrane can be accurately predicted by machine learning models (CNN, LightGBM), and reinforcement learning can successfully balance the trade-off between water flux and ion rejection rate thus generate novel design of porous membrane for RO water desalination.

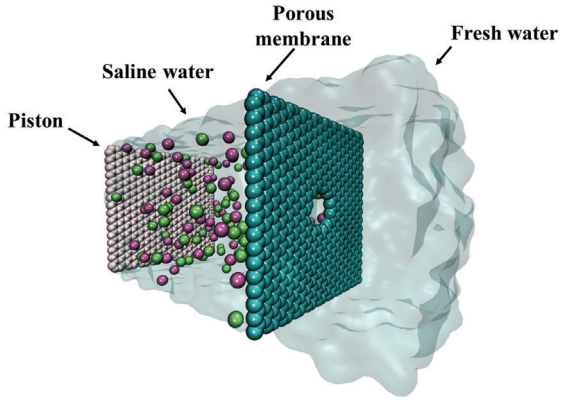

FIGURE 1. Typical schematic of reverse osmosis water desalination: A piston as source of hydraulic pressure; Saline water section; Membrane with nanopore as filter; And a fresh water section

DATA COLLECTION

Simulation

Molecular dynamics (MD) simulation was used for generating necessary data for the training of machine learning model to predict the water flux and ion rejection rate of a given membrane. In order to eliminate the effect of material type and focus on the influence of pore geometry to membrane performance, we conducted our study with one specific material: single-layer graphene (circular pore in Fig. 1, other pore variations simulated shown by Figure 2) which has been proven to be an outstanding candidate for water desalination because of its Angstrom level thickness[1]. Initially, nanopores were created by artificially removing atoms from the center of graphene membrane using Visual Molecular Dynamics (VMD) [4]. MD simulations were then conducted using LAMMPS package. The dimension of a typical simulation system was approximately 4 nm x 4 nm x 13 nm in x, y, and z direction. In each simu-

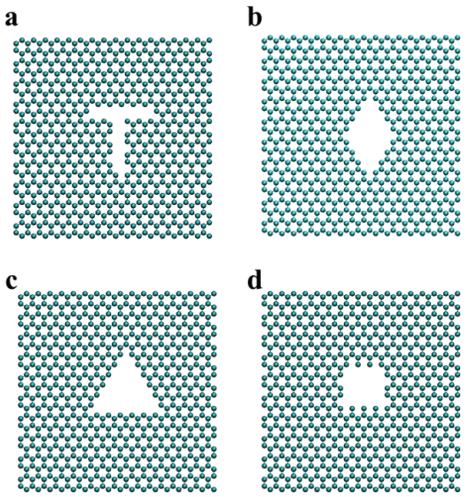

FIGURE 2. Various shapes of graphene pore geometry simulated in this work: a. T-shape b.Rhombus c. Triangle and d. Square

lation, the entire system was minimized for 10,000 iterations for the purpose of reducing internal energy. After minimization, the piston constantly applied 100 MPa hydraulic pressure on the saline water section against the porous membrane for 10 nanoseconds. The trajectories of atoms were collected every 5 picoseconds for the calculation of water flux and ion rejection rate.

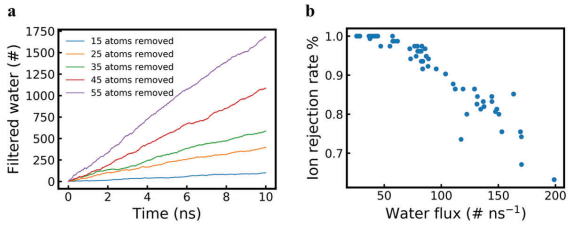

FIGURE 3. a. Filtered water with respect to simulation time curve for sample membranes b. Ion rejection and water flux for over 500 samples in the dataset

Water flux was computed by fitting the slope of the number of filtered water molecules with respect to time curve (Figure 3a), and the ion rejection was calculated by dividing the number of ions on the fresh water section by the total number of ions at the end of simulation (part of the samples shown by Figure 3b). Besides membrane with large enough pore to allow visible water flux, we also created some membrane with very small pore (less than 10 atoms removed) which allow zero water flux to increase data variety.

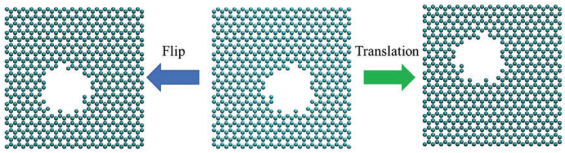

FIGURE 4. Two methods for data augmentation include: 1. Flipping (create a mirrored replication of original membrane) and 2. Translation (create replication of original membrane with translated pore)

Data Agumentation

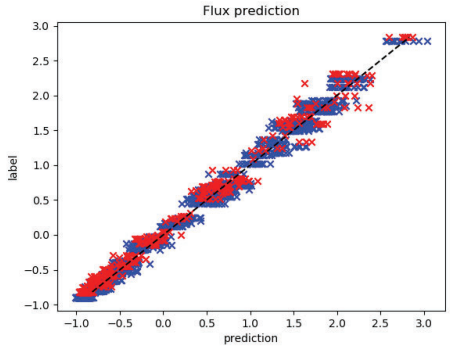

(a) Adaboosting ResNet18 on flux prediction

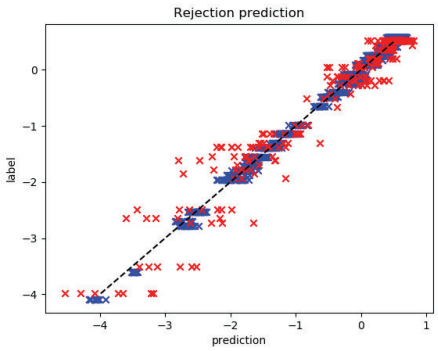

(b) Adaboosting ResNet18 on ion rejection prediction

FIGURE 5. Adaboosting on pre-trained Resnet18, where the blue crossings indicate training set and red crossings indicate test set

Due to the high computational cost of MD simulations, data augmentation was crucial to enlarge the size of dataset. For each membrane simulated, several other membrane with exactly the same pore could be generated by translating or flipping the pore (Figure 4). Membrane generated by data augmentation should have the same water flux and ion rejection as the original mem-

brane. The utilization of data augmentation expanded the dataset to over 1600 samples from 203 unique simulated membranes.

METHOD

GRAPHENE PROPERTY PREDICTION

Since molecular simulation can be time-consuming which is infeasible in an online controlling process. We propose to use machine learning to learn a "pseudo" simulator which predicts water flux and ion rejection rate under certain conditions. We use image-based convolutional neural network (CNN) as well as RDkit-based shallow machine learning. In detail, the former is built upon a pre-trained ResNet18 model with the figure of graphene as input. Also ensemble technique, like adaboost, is introduced to enhance the prediction accuracy, as shown in Fig. 5. The former generates features concerning the chemical information of different graphen structures and shallow machine learning model like LighGBM is implemented on the RDkit features, as shown in Fig. 6. Notice that to make the model training more smooth, all flux and ion rejections are standardized before feed into the learning-based model.

REINFORCEMENT LEARNING CONTROLLER

Reinforcement learning (RL) is introduced to accelerate precise design of optimal nanoporous and currently Deep Q-network (DQN) [3] is utilized. As shown in Fig. 7, the DQN agent takes input of current structure of the nanoporus and determine the atom to remove at each time step. Meanwhile, current graphene structure is fed into the property prediction model to obtain the flux f_t and ion rejection rate i_t. Let assume the initial flux and ion rejection is f_0 and i_0 respectively, the reward function R_t is computed as given in Eq. 1

$$R_t = 0.02 \times (f_t - f_0) - 200 \times (i_t - i_0)^2. \quad (1)$$

The reward is conveyed to the RL agent, in our case, a DQN model to make prediction of next action, namely the atom to remove. In each episode during training, the RL learns to design the structure of the pore in the graphene to maximize the expectation of accumulated reward. Eventually, the RL agent is intended to learn an energy-efficient nanoporous structure which possess both high water flux with reasonable ion rejection rate.

Illustrated in Fig. 8 is the evolution of graphene in one episode controlled by the RL agent. The

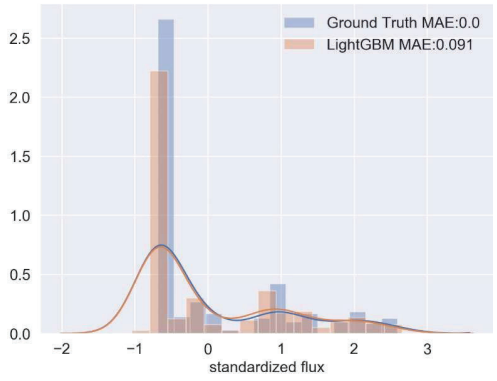

(a) LightGBM on flux

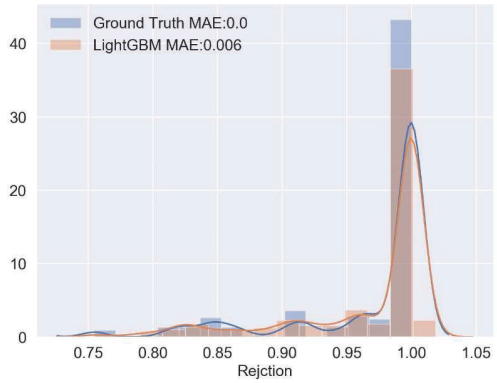

(b) LightGBM on ion rejection

FIGURE 6. LightGBM test results

pore in the graphene learns to grow to a specific geometry so that the accumulated reward, which measures the combination of flux and ion rejection rate, is maxmized.

REFERENCES

[1] Cao, Zhonglin, Vincent Liu, and Amir Barati Farimani. "Water Desalination with Two-Dimensional Metal–Organic Framework Membranes." Nano letters 19.12 (2019): 8638-8643.

[2] Xie, Tian, and Jeffrey C. Grossman. "Crystal graph convolutional neural networks for

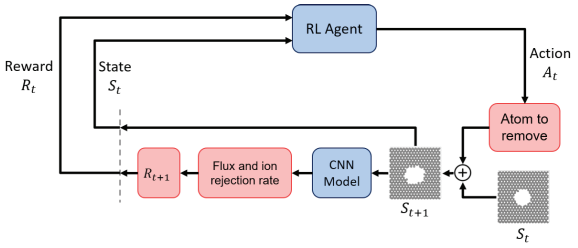

FIGURE 7. Pipeline of combination of property predictor and RL controller for graphene design

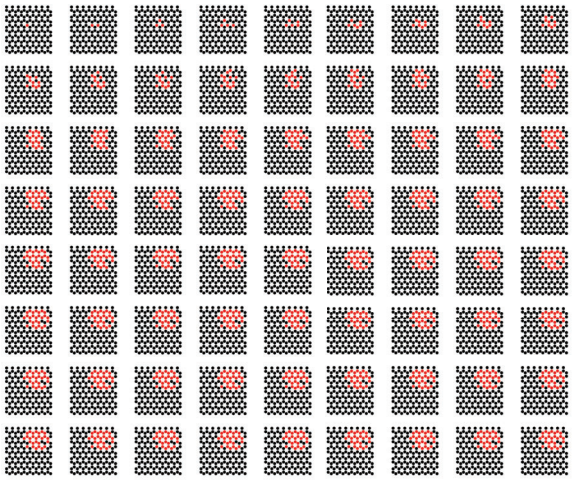

FIGURE 8. Evolution of nanoporous of different time step using RL

an accurate and interpretable prediction of material properties." Physical review letters 120.14 (2018): 145301.

[3] Mnih, Volodymyr, et al. "Human-level control through deep reinforcement learning." Nature 518.7540 (2015): 529-533.

[4] Humphrey, W.; Dalke, A.; Schulten, K. Vmd: Visual MolecularDynamics.J. Mol. Graphics1996,14,3338.

LONG-RANGE PIEZO-STEPPER ACTUATORS: TOWARDS NANOSCALE ACCURACY THROUGH COMMUTATION-ANGLE ITERATIVE LEARNING CONTROL

Leontine Aarnoudse[1], Nard Strijbosch[1], Edwin Verschueren[2], and Tom Oomen[1]

[1]**Control Systems Technology, Eindhoven University of Technology, Eindhoven, The Netherlands**

[2] **Thermo Fisher Scientific, Eindhoven, The Netherlands**

BACKGROUND

Piezo-stepper actuators have major benefits in nano-positioning applications, including scanning-probe microscopy [1]. The actuators, illustrated in Figure 1, retain the high precision and high stiffness properties of the piezo elements, while achieving an infinite stroke of the mover through a walking motion. Periodic waveforms are used to map a commutation angle α to the input voltages of the piezo elements.

Engagement and release between the piezo-elements and the mover during the walking motion lead to disturbances [2]. These disturbances are directly related to the actuating waveforms, and are repeating in the commutation-angle or α-domain. Consequently, for varying velocities, the error profile caused by these disturbances is varying in the temporal domain.

Iterative Learning Control (ILC) can compensate repeating disturbances completely by modifying a feedforward signal based on preceding experiments [3]. The disturbances for a piezo-stepper actuator are repeating in the temporal domain for a constant velocity, but for varying velocities the disturbances are varying. The aim of this paper is to develop and implement an ILC approach that is applicable to long-range piezo-stepper actuators with varying velocities, by exploiting the observation that the disturbance is repeating in the α-domain.

This paper is organized as follows. First, the commutation-angle based control of a piezo-stepper actuator is explained. Then, the disturbances caused by the walking motion are analyzed. A commutation-angle iterative learning control approach is proposed to compensate these disturbances. After that, the implementation of this approach is explained and the approach is experimentally validated. In the final section, conclusions are given.

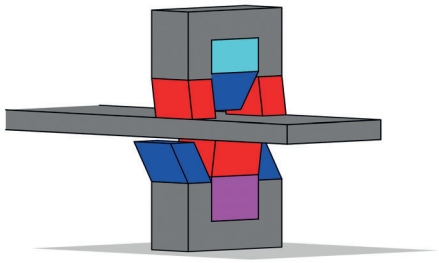

FIGURE 1. Schematic representation of a piezo-stepper actuator with clamp elements 1 (—) and 2 (—) and shear groups 1 (—) and 2 (—) indicated.

COMMUTATION-ANGLE CONTROL

In this section, the functioning and control of a piezo-stepper actuator are explained and the actuator is modeled.

The piezo-stepper actuator considered in this work consists of two groups of longitudinal and shear piezo elements, as shown in Figure 2b. When the longitudinal element or clamp of one group is elongated, the corresponding shear elements are in contact with the mover. The mover follows the position of the connected shear elements. A walking motion is obtained by alternating the connected piezo group.

The walking motion of the piezo-stepper actuator is implemented using waveforms that map a commutation angle $\alpha \in [0, 2\pi)$ [rad] to the input voltages of the piezo elements, as shown in Figure 2a. The waveforms can be divided into four phases: takeover phases 1 and 3 and reset phases 2 and 4, as shown in Figure 2.

1. Takeover phase: the clamp of group 1 is extending while that of group 2 is retracting, such that the mover is taken over by group 1. Both sets of shear elements are moving with equal velocity.

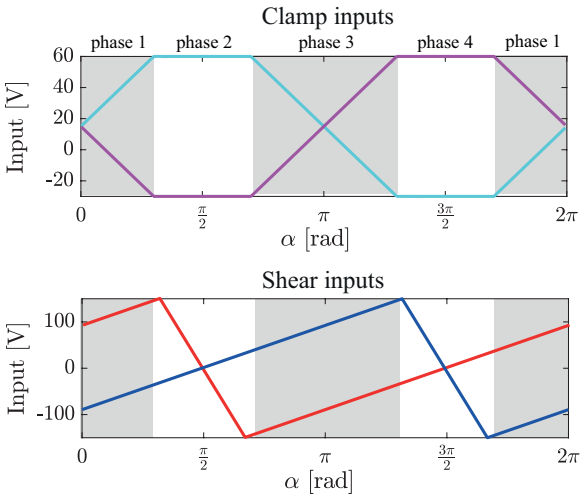

(a) Piezo-stepper actuator waveforms.

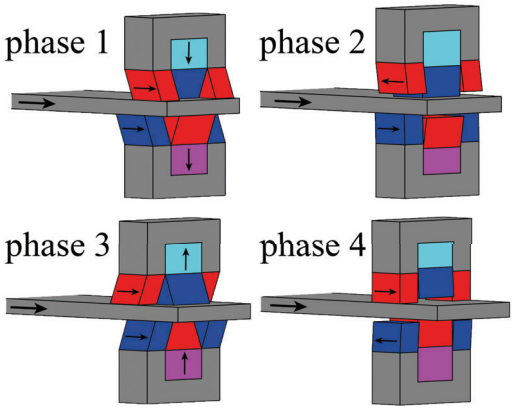

(b) Phases in a step of a piezo-stepper actuator.

FIGURE 2. The waveforms (a) map the commutation angle α to the input for the piezo elements: clamp elements 1 (—) and 2 (—) and shear groups 1 (—) and 2 (—). A step of a piezo-stepper actuator is divided into four phases, indicated in (a) and illustrated in (b). Note that in takeover phases 1 and 3, both groups may be in contact with the mover. In these phases the inputs of the shear groups have equal derivatives, such that the elements move with equal velocity.

2. Reset phase: once the clamp of group 2 is fully retracted, the shear elements of this group are reset. The shear elements of group 1 continue displacing the mover.
3. Takeover phase: the clamp of group 1 is retracting while that of group 2 is extending, such that the mover is taken over by group 2. Both sets of shear elements are moving with equal velocity.
4. Reset phase: once the clamp of group 1 is fully retracted, the shear elements of this group are reset. The shear elements of group 2 continue displacing the mover.

The piezo-stepper actuator is modeled in the α-domain as a gain with a lumped disturbance $d_\alpha(\alpha)$ [m]. The disturbance $d_\alpha(\alpha)$ is assumed to be related to the commutation angle and is analyzed in the next section. The position of the mover y [m] during a single step is described by

$$y(\alpha) = cu_s(\alpha) + d_\alpha(\alpha), \quad \alpha \in [0, 2\pi), \tag{1}$$

where c [m V^{-1}] is a positive piezo constant and u_s [V] is a combination of the inputs to the shear elements. The inputs to the two groups of shear elements are denoted by u_{s1} [V] and u_{s2} [V]. Because the derivatives of the connected shear elements are always equal, as shown in Figure 2a, the input that influences the mover can be written as a single signal $u_s(\alpha)$ for modeling. For $u_s(\alpha)$, the following holds:

$$\frac{\delta u_s(\alpha)}{\delta \alpha} = \begin{cases} \frac{\delta u_{s1}(\alpha)}{\delta \alpha} & \text{in phase 2} \\ \frac{\delta u_{s2}(\alpha)}{\delta \alpha} & \text{in phase 4} \\ \frac{\delta u_{s1}(\alpha)}{\delta \alpha} = \frac{\delta u_{s2}(\alpha)}{\delta \alpha} & \text{otherwise.} \end{cases} \tag{2}$$

Note that in this model, rate-dependent effects such as creep and hysteresis are assumed to be negligible, since these effects can be compensated, for example, by using separate feedforward [4, ch. 2,11].

The commutation angle $\alpha(t)$ is a function of time and depends on the drive frequency $f_\alpha(t)$ [Hz]. The number of steps per second is equal to the drive frequency. For each step of duration T [s], the commutation angle increases from $\alpha(0) = 0$ to $\alpha(T) = 2\pi$. The commutation angle is given by

$$\alpha(t) = 2\pi \int_0^t f_\alpha(\tau)\, \mathrm{d}\tau. \tag{3}$$

The system is modeled in terms of α for a single step. During this step, the sign of $f_\alpha(t)$ is constant and $\alpha(t) \in [0, 2\pi)$ is monotonically increasing, i.e., there is no change in direction. The time-dependency of α is omitted for brevity.

DISTURBANCE ANALYSIS

In this section, the disturbances for a piezo-stepper actuator are analyzed in the temporal and the commutation-angle domain.

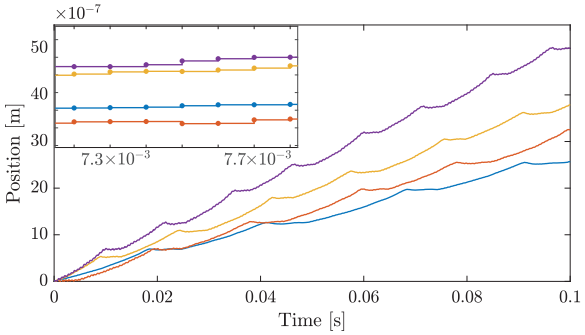

(a) Position as a function of time.

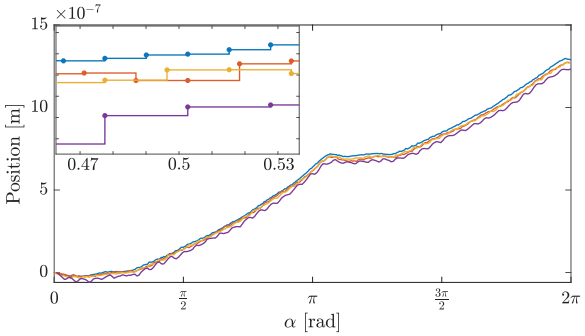

(b) Position as a function of the commutation angle.

FIGURE 3. Positions for a piezo-stepper for drive frequencies 20 Hz *(—),* 25 Hz *(—),* 30 Hz *(—) and* 40 Hz *(—). In the temporal domain (a) the sampling is equidistant but the disturbance is varying. In the α-domain (b) the sampling is non-equidistant for varying velocities, but the disturbances are similar.*

During walking experiments, disturbances in the position of the piezo-stepper actuator are observed. The desired behavior for the actuator is that for a constant drive frequency, the mover velocity is also constant. However, due to disturbances this desired behavior is not obtained, as is shown for multiple drive frequencies in Figure 3a.

Although the disturbances are varying in the temporal domain for varying drive frequencies, they are largely repeating in the commutation-angle or α-domain. This is shown in Figure 3b, where the position of the mover during a single step is plotted as a function of α for varying drive frequencies. The disturbances could be explained by considering physical sources: misalignment between the piezo elements and the mover or contact dynamics.

The central idea is to exploit the repetitiveness in the α-domain to compensate the position disturbances for the piezo-stepper actuator. To this end, an approach for commutation-angle or α-domain ILC is developed that is used to design a disturbance-compensating input as an addition to the existing waveforms.

COMMUTATION-ANGLE ITERATIVE LEARNING CONTROL

In this section, a new framework for α-domain iterative learning control is introduced. ILC can exactly compensate repeating disturbances by learning a compensating input over a series of experiments, known as iterations, while it typically amplifies non-repeating disturbances [3]. Typically, ILC is applied to systems with repetitive behavior in the temporal domain. To compensate the repeating disturbances for a piezo-stepper actuator, an α-domain approach is proposed, where each step is considered to be one iteration.

For varying drive frequencies, the number of samples per step in the α-domain is varying and samples are non-equidistant, as shown in Figure 3b. Since the sampling is iteration-varying, ILC cannot be applied directly to the sampled signals. This is resolved by parameterizing the sampled input and error signals using basis functions. ILC is then applied to the resulting continuous signals.

ILC is applied to a system that is continuous in α, given by

$$y_j(\alpha) = c(u_s(\alpha) + u_j(\alpha)) + d_\alpha(\alpha) \tag{4}$$
$$e_j(\alpha) = y_d(\alpha) - y_j(\alpha), \tag{5}$$

with disturbance-compensating input $u_j(\alpha)$, error $e_j(\alpha)$ and reference $y_d(\alpha)$ for iteration j. The error and input are parameterized such that

$$u_j(\alpha) = \psi^\top(\alpha)\theta_j^u \tag{6}$$
$$e_j(\alpha) = \psi^\top(\alpha)\theta_j^e, \tag{7}$$

where it is assumed that the basis functions can be scaled to describe the error exactly. The basis function vector ψ, containing M basis functions, and the parameter vector θ_j^u are given by

$$\psi(\alpha) = \begin{bmatrix}\psi_1(\alpha) & \psi_2(\alpha) & \dots & \psi_M(\alpha)\end{bmatrix}^\top \tag{8}$$
$$\theta_j^u = \begin{bmatrix}\theta_{1,j}^u & \theta_{2,j}^u & \dots & \theta_{M,j}^u\end{bmatrix}^\top. \tag{9}$$

The steps to implement α-domain ILC are outlined in Algorithm 1 for n iterations and explained below.

Algorithm 1 Approach to α-domain ILC

Choose a basis ψ (see next section)
for $j = 1 : n$
1: Perform an experiment of one step using u_j
2: Compute θ_j^e by determining the least squares optimal fit of the sampled error
3: Update the input parameters θ_{j+1}^u according to (10)
4: Update the input: $u_{j+1} = \psi^\top \theta_{j+1}^u$
5: Divide u_{j+1} into waveforms for the shear elements
end

Each iteration consists of five steps. First, an experiment consisting of one step of the piezo-stepper actuator is performed, resulting in an output and error according to (4) and (5). The error is parameterized according to (7), using a least squares optimal fit to find the parameter vector θ_j^e. The parameter vector for the input of the next iteration θ_{j+1}^u depends only on the previous error and input parameter vectors and is given by

$$\theta_{j+1}^u = Q_\psi \theta_j^u + L_\psi \theta_j^e, \tag{10}$$

where Q_ψ and L_ψ are optimal learning matrices. The input signal for the next iteration is determined according to (6). Extended derivations for Q_ψ and L_ψ are available as [5]. The implementation of the input signal is explained in the next section.

IMPLEMENTATION

In this section, the selection of suitable basis functions and the implementation of the input signals using waveform enhancement are explained.

The first step mentioned in Algorithm 1 is the selection of a basis ψ. This basis should be selected such that it can describe the measured error well. In this case, a set of 30 linearly independent inverse quadratic radial basis functions is used, see [6, ch.5]. The functions are of the form

$$\psi_k(\alpha) = \frac{1}{1 + (\|\alpha - c_k\|)^2}, \; k = 1, 2, ..., 30 \tag{11}$$

where the centerpoints c_k are divided equidistantly over the domain $[0, 2\pi)$. An example of a fit of an error signal with 1000 samples using this set of basis functions is shown in Figure 4.

Using the update law of (10) results in a continuous input signal $u_j(\alpha)$ for each iteration j.

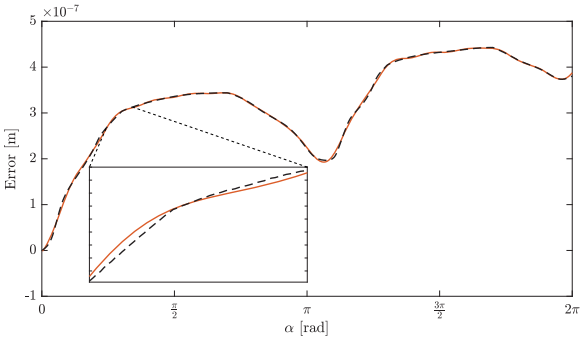

FIGURE 4. Fit (—) of the sampled error at 1000 points (- -) using 30 inverse quadratic radial basis functions.

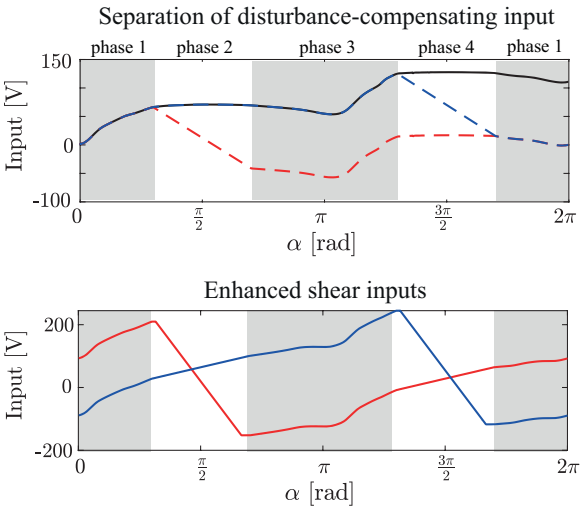

FIGURE 5. Waveform enhancement for disturbance compensation. The disturbance compensating input $u_j(\alpha)$ (—) is divided into waveforms for shear groups 1 (- -) and 2 (- -), such that the waveforms for both shear groups have equal derivatives in phases 1 and 3, where both groups may be in contact with the mover. The compensating waveforms are added to the existing shear inputs of Figure 2a, resulting in enhanced waveforms for shear group 1 (—) and 2 (—).

This single input signal cannot be implemented directly, since the input to the actuator consists of two separate shear input signals. Therefore, the disturbance-compensating input $u_j(\alpha)$ is separated into two shear input signals, such that (2) is satisfied. These signals are then added to the existing shear inputs. This procedure is illustrated in Figure 5.

EXPERIMENTAL RESULTS

The developed ILC framework is applied to a piezo-stepper actuator walking at varying

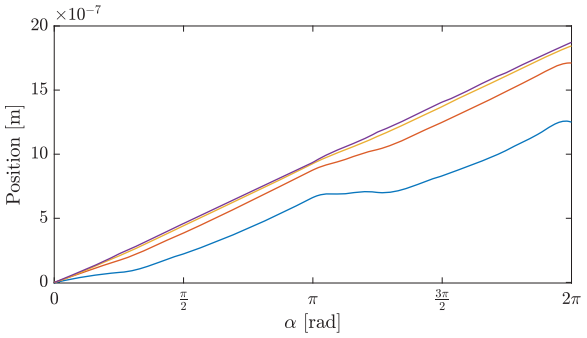

FIGURE 6. Improvements in the position of the piezo-stepper actuator for one step between iterations 1 (—), 4 (—), 8 (—) and 16 (—) using the proposed α-domain ILC framework.

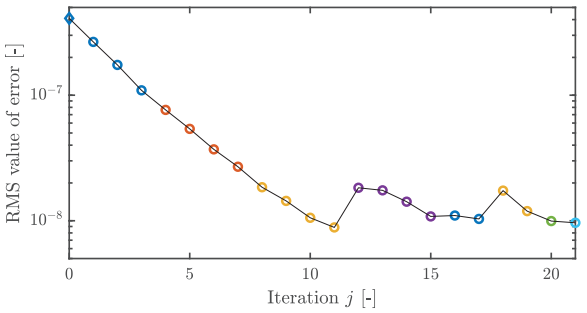

FIGURE 7. The RMS value of the error converges over iterations with iteration-varying drive frequencies: 30 Hz*(o),* 35 Hz*(o),* 25 Hz*(o),* 28 Hz*(o),* 22 Hz*(o) and* 20 Hz*(o).*

velocities for experimental validation. The desired mover position is given by the reference $y_d(\alpha) = 3 \times 10^{-7}\alpha$. The iteration-varying drive frequencies range from 20 to 35 Hz.

During the experiments, the influence of the repeating part of the disturbance is reduced significantly over iterations, as shown in Figure 6. In Figure 7 it is shown that the RMS value of the error converges to a bounded region over iterations.

Note that part of the error reduction as shown in Figure 6 and 7 is caused by convergence of the slope of the mover position to that of the reference signal. The improvements with regard to the repeating disturbance are also shown in Figure 8, where the detrended error signal before and after learning a disturbance-compensating input are compared. The experiments show that learning a disturbance-compensating signal using α-domain ILC leads to significant improvements in the positioning accuracy and jogging smoothness of the actuator.

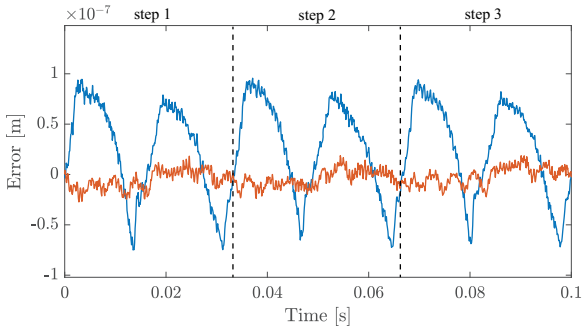

FIGURE 8. Comparsion between the detrended error for three steps at 30 Hz *before (—) and after (—) learning a disturbance compensating input.*

CONCLUSION

A new approach for iterative learning control in the commutation-angle domain is developed that can fully compensate the repeating disturbance for a piezo-stepper actuator. The approach is used to learn a disturbance-compensating input over iterations, which improves the positioning accuracy and jogging smoothness significantly. Experimental results show that the error is reduced significantly after several iterations.

REFERENCES

[1] Den Heijer M, Fokkema V, Saedi A, Schakel P, Rost MJ. Improving the accuracy of walking piezo motors. Rev Sci Instrum. 2014;85(5).

[2] Strijbosch N, Tacx P, Verschueren E, Oomen T. Commutation angle iterative learning control: Enhancing piezo-stepper actuator Waveforms. In: 8th IFAC Symp. Mechatron. Syst. Vienna, Austria; 2019. p. 1451–1456.

[3] Bristow DA, Tharayil M, Alleyne AG. A survey of iterative learning control. IEEE Control Syst. 2006;26(3):96–114.

[4] Fleming AJ, Leang KK. Design, Modeling and Control of Nanopositioning Systems. Springer; 2014.

[5] Aarnoudse L, Strijbosch N, Verschueren E, Oomen T. Commutation-Angle Iterative Learning Control for Intermittent Data: Enhancing Piezo-Stepper Actuator Waveforms. In: IFAC 21st World Congr. Berlin, Germany; 2020. .

[6] Schaback R, Wendland H. Kernel techniques: From machine learning to meshless methods. Acta Numer. 2006;15(2006):543–639.

HARNESS THE LAG: PRECISION MOTION WITH HYSTERESIS MOTORS

Lei Zhou[1], David L. Trumper[2]
[1] **Mitsubishi Electric Research Laboratories, Cambridge, MA, USA**
[2] **Massachusetts Institute of Technology, Cambridge, MA, USA**

INTRODUCTION

In precision motion systems, hysteresis in actuators is typically a detrimental effect, and a number of research efforts have studied methods to compensate it. However, the hysteresis effect is not always harmful. When building motors with secondaries made of magnetically semi-hard materials, the hysteresis effect of the secondaries can generate a spacial lag between the secondary's magnetization and the external magnetic field, and thus generate thrust force/torque. Such motors are called hysteresis motors. In recent years, the hysteresis motor is receiving increasing research attention due to its advantages of simple construction, vibration-free operation, constant torque/force in transient, and self-starting [1]. The most distinct feature of a hysteresis motor is that its secondary can be made of a monolithic piece of magnetically semi-hard alloy, which has high strength, stiffness, and thermal robustness. This fact makes the hysteresis motor attractive to many special precision devices, such as in-vacuum drives [2], miniature pumps [3], high-temperature/high-speed drives [4], and space devices [5].

In contrast to the motor's good potential, the research on hysteresis motors until today remains limited. To our knowledge, hysteresis motors are typically operated in open-loop, and there was no developed method to control the motor's torque or position with high bandwidth before our work. As a result, the hysteresis motor has been almost ignored in precision applications in the past. This gap between the motor's great potential and the existing technology motivated our study for methods to control the hysteresis motors with high bandwidth, and therefore enable them for precision applications in the future.

This paper introduces the research efforts at the Precision Motion Control Lab at MIT on the precision positioning using hysteresis motors. The paper includes two parts. In the first part, we introduce the modeling and field-oriented control (FOC) for hysteresis motors, and presents the experimental tests of the proposed method on three rotary hysteresis motors with different rotor materials. Test results show that all three motors can reach a position control bandwidth of 130 Hz with the proposed methods. The second part briefly introduces the design, building, and testing of a magnetically-levitated linear stage driven by linear hysteresis motors, targeting at the in-vacuum transportation application in semiconductor manufacturing systems. To the best of our knowledge, our work demonstrates the first experimental study on position control for hysteresis motors, and the first linear version of hysteresis motors. It also first demonstrates the use of hysteresis motor in precision motion stages.

POSITION CONTROL FOR ROTATY HYSTERESIS MOTORS

Hysteresis Motor Operating Principle

In this section we briefly discuss the operating principle of hysteresis motors. We first limit our discussion to rotary hysteresis motors. A hysteresis motor consists of a regular poly-phase stator and a rotor made of solid semi-hard magnetic material. The magnetic hysteresis effect of the rotor material causes a lag angle between the rotor magnetic field and the air-gap magnetic field, and a hysteresis torque can be generated. Hysteresis motors can be operated either synchronously or asynchronously. When the motor is under asynchronous operation, eddy current is induced in the rotor, which also contribute to the motor's torque generation. Under this operation mode, the motor can be regarded as a hysteresis-induction-hybrid motor. When the motor is operated synchronously, the motor behaves like a weak permanent magnet motor. When operated synchronously, the rotors of hysteresis motors are often pre-magnetized or over-excited for torque and efficiency improvement [6].

Rotor Field Orientation Estimation

The challenge of controlling a hysteresis motor is because the magnetization can move on the ro-

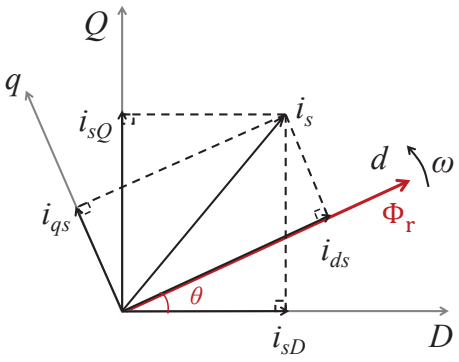

FIGURE 1. Hysteresis motor field-oriented control vector diagram.

tor surface. Fig. 2 shows a vector diagram of the hysteresis motor's field-oriented control. Here, D-Q is the stationary two-phase frame, d-q is the rotor flux-oriented frame, where the d-axis is aligned with the rotor flux linkage. Vector i_s represents the stator phase currents, and Φ_r is the rotor flux vector. Under this case, the motor's torque is proportional to i_{qs}. It can be seen that the key of hysteresis motor's control is to achieve an accurate estimation to rotor flux vector's orientation, i.e. the field angle θ. With such field orientation information, one can control a hysteresis motor in the same way with a PM machine. In the rest of this section, we discuss two different rotor field orientation estimation methods for both synchronously- and asynchronously-operated hysteresis motors.

Asynchronous Operation

For asynchronously-operated hysteresis motors, we propose to use a model-based rotor flux observer for real-time field-orientation estimation. A model that describes the hysteresis motor's transient-time dynamics is required to construct such estimator. The challenge of constructing such model for hysteresis motors is mainly due to the fact that the hysteresis effect and the eddy current effect need to be modeled in different coordinate frames. Fig. 2 shows such separation in reference frames. In a hysteresis motor, the hysteresis effect of the rotor generates a constant lag angle between the rotor flux and the air-gap flux, and this relationship should be modeled in the stator-fixed frame. On the other hand, the eddy current effect should be modeled in the rotor-fixed frame, since the eddy currents are generated in conductors fixed on the rotor. This fact prevents us from modeling the rotor flux using unified variables as in an induction motor model.

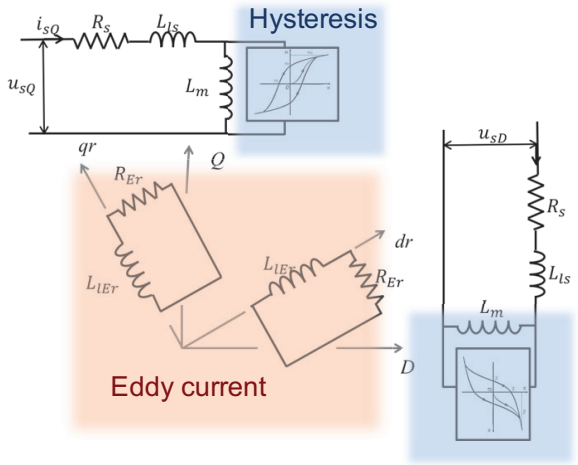

FIGURE 2. Hysteresis motor circuit diagram with hysteresis effect and eddy current effect in different coordinate systems.

In this work, we developed a transient-time dynamic model for hysteresis motors with eddy current effect considered. The model is based on the elliptical hysteresis loop assumption [7], where the the B-H curve of the rotor material is approximated by an ellipse, as $B = B_m \cos\theta$, $H = (B_m/\mu)\cos(\theta + \delta)$, where B_m is the maximum flux density amplitude, μ is the rotor material permeability, and δ is the lag angle between B and H. This model considers only the fundamental harmonics for B- and H-fields. Based on such simplified hysteresis model, we listed the motor's eddy current and hysteresis dynamic dquations in their different coordinates, and selected a set of state variables as $x = [i_{sD}, i_{sQ}, \Phi_{HrD}, \Phi_{HrQ}, \Phi_{ErD}, \Phi_{ErQ}]^\top$, a state-space model for the hysteresis motor can be derived. For more details about the hysteresis motor model, see equations (9-14) in [8].

Given the hysteresis motor state space model, a full-order Luenberger state observer can be designed to estimate the rotor's field orientation. The derived hysteresis motor model is fully observable even when the motor is operating at zero speed, and therefore asymptotically converging observer designs are available. This flux observer method provides good rotor flux angle estimation accuracy over a large speed range. Note that the estimation performance of this method significantly depend on the model parametric accuracy.

Synchronous Operation

For synchronously-operated hysteresis motors with or without pre-magnetization, one can use model-free methods to estimate the rotor's field

orientation for control purpose, as discussed in the following:

(a) Approximate with Rotor Mechanical Angle: The most simple method for estimating the rotor flux angle is to directly use the measured rotor angular position. This method assumes that the magnetization is fixed on the rotor surface. Pre-magnetizing the rotor by a large d-axis current can help improve the performance of this flux angle estimation method.

(b) Back-EMF method: The second method uses the back-electromotive force (EMF) in the stator coils to estimate the rotor flux orientation. When the magnetized rotor is rotating, the change of the rotor field induces voltages in the stator windings, which is the back-EMF. The back-EMF in the stationary D-Q frame can be calculated as

$$e_D = u_{sD} - R_s i_{sD} - L_{ls}\dot{i}_{sD}, \quad (1)$$

$$e_Q = u_{sQ} - R_s i_{sQ} - L_{ls}\dot{i}_{sQ}. \quad (2)$$

An estimate for the flux linkage in the stationary two-phase frame can be calculated by

$$\hat{\Phi}_{rD} = \int e_D \mathrm{d}t, \;\; \hat{\Phi}_{rQ} = \int e_Q \mathrm{d}t. \quad (3)$$

Finally the estimated flux angle $\hat{\theta}$ can be calculated. This method provides good rotor flux orientation estimation performance when the motor speed is relatively high. However, when the motor is standing still or operating at low speed, the back-EMF signals are small and therefore the angle estimation is not accurate.

(c) Combination of Mechanical Angle and Back-EMF Methods: To improve the rotor field orientation estimation performance over a large motor speed range, we can use a combination of using back-EMF based estimation when the rotor speed is high, and using rotor's mechanical angle when the rotor speed is low. One implementation of the combined flux orientation estimation is

$$\hat{\theta} = (1 - S(|\omega_r| - \omega_r^{sw}))\theta_r + S(|\omega_r| - \omega_r^{sw})\hat{\theta}_{EMF},$$

where ω_r is the rotor speed, ω_r^{sw} is a threshold rotor speed for estimation method switching, $\hat{\theta}_{EMF}$ is the back-EMF method estimated angle, θ_r is the rotor's mechanical angle, and $\hat{\theta}$ is the resultant rotor flux angle estimation. $S(x) = 1/(1+e^{-x})$ is the sigmoid function, which is a smooth transition function from 0 to 1 at $x = 0$.

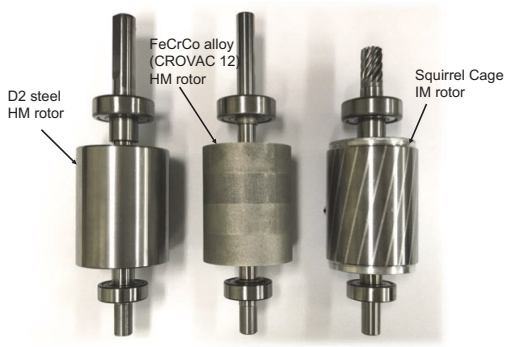

FIGURE 3. Custom-made rotors for hysteresis motors. Left: D2 hysteresis rotor for Motor I. Middle: FeCrCo alloy hysteresis rotor for Motor II. Right: the original squirrel cage rotor for the induction motor.

Rotary Hysteresis Motor Tests

Three different rotary hysteresis motors are tested to validate the proposed control method. Motor I and Motor II are custom-made hysteresis motors, which are fabricated by replacing the squirrel cage rotor in a regular three-phase induction motor with rotors made of different semi-hard magnetic materials. Motor I has a rotor made of D2 tool steel, and Motor II has a rotor of FeCrCo alloy. Fig. 3 shows the custom-made rotors for Motor I and II and the original rotor for the induction motor. The third hysteresis motor being tested, Motor III, is a commercial hysteresis motor from Elinco Inc.

The proposed field-oriented control scheme is tested with all three hysteresis motors. For Motor I and Motor II, the full-order state observer method is used for the rotor flux orientation estimation. For Motor III, rotor flux orientation is estimated through the combination of the mechanical angle and back-EMF method. Fig. 4 shows the measured plant frequency responses of the position control plant for the three hysteresis motors, where the input signal is the q-axis current, and the output signal is the measured rotor angular position. Fig. 4 shows that all three measured Bode plots demonstrate -2 (or -40 dB/dec) slope at high frequency, which follows the torque-to-position relationship in a motor. This observation indicates that the q-axis current is roughly proportional to the torque of the motor. The three plots in Fig. 4 all demonstrate zero slope at low frequency, which is due to the spring-like behavior of bearing friction.

Fig. 5 shows the measured close-loop Bode plots

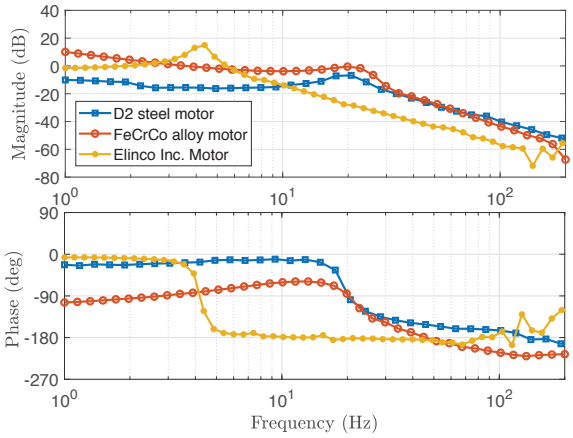

FIGURE 4. Measured Closed-loop Bode plots for three hysteresis motors. Input: reference position; output: measured position. The -3 dB in magnitude plot is shown as the dashed line.

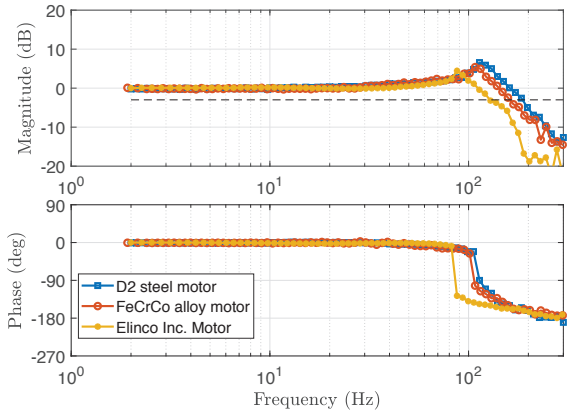

FIGURE 5. Measured Closed-loop Bode plots for three hysteresis motors. Input: reference position; output: measured position. The -3 dB in magnitude plot is shown as the dashed line.

for the position control systems for the hysteresis motors. Fig. 5 demonstrates that the position control for all three hysteresis motors are successful with a bandwidth of above 130 Hz.

HYSTERESIS MOTOR DRIVEN MAGNETICALLY LEVITATED LINEAR STAGE

The second part of this paper discusses the design and tests of a magnetically-levitated linear stage driven by linear hysteresis motors. The target application of this linear stage is for the in-vacuum transportation in semiconductor manufacturing systems, for example reticle transportation in EUV photolithography scanners. Hysteresis motors do not require permanent magnets (PM) on the moving stage. This feature of the motors is highly-desirable for in vacuum environment, since the magnets can out-gas in vacuum

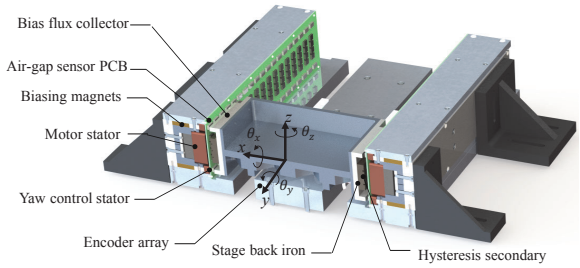

FIGURE 6. Cross-section CAD model of the hysteresis-motor-driven magnetically-levitated linear stage.

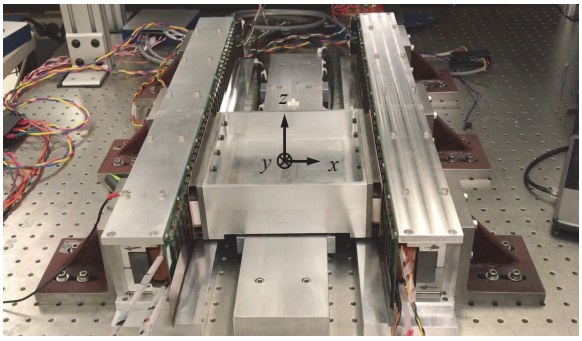

FIGURE 7. Photograph of the magnetically-levitated linear stage prototype.

and thus need to be encapsulated. Using motor secondaries made of solid magnetically-semi-hard steel will allow a much simpler stage design. The major disadvantage of using hysteresis motor is that their thrust force is relatively low compared to other motor types. However, this is acceptable for the reticle transportation application, since its acceleration requirement is relatively low and is achievable with linear hysteresis motors. To our knowledge, this work demonstrates the first linear version of hysteresis motors.

Fig. 6 shows a cross-section CAD model for the linear stage design, and Fig. 7 shows a photograph of the linear stage prototype. The coordinate system is also shown in Fig. 6 and Fig. 7. Here, the stage is driven along the y-axis via linear hysteresis motors, and is magnetically levitated in all other degrees of freedoms. Here, the stage is passively suspended in the z-, θ_x-, and θ_y-directions via the reluctance forces between the stage and stator assemblies using a linear bearingless slice motor design, and is levitated actively using feedback control in the x- and θ_z-DOFs.

Fig. 8 shows the magnetic fluxes and the suspension forces/torques generation principle for our linear stage. There are three kinds of magnetic

fluxes in the system. The black lines in Fig. 8a and Fig. 8b show the PM bias magnetic fluxes, which generate passive suspension force/torque in the z-, θ_x-, and θ_y-DOFs. The blue lines in Fig. 8a and Fig. 8b represent the yaw control fluxes, which are distributed approximately sinusoidally in the air gaps, and is synchronous with respect to the moving stage. This flux steers the PM bias flux (black lines) for yaw (θ_z) suspension control torque generation. The red lines in Fig. 8a and Fig. 8c show the motor fluxes. The common-mode of the two motor fluxes generates thrust force on the stage in the y-direction by interacting with the hysteresis secondaries on the moving stage. The differential of the two motor fluxes generates lateral-directional reluctance forces, which is used to control the stage's levitation in the x-direction. With all three magnetic fluxes, we are able to stabilize all five suspension DOFs of the moving stage, either actively or passively. More detailed suspension force/torque generation mechanism as well as the hardware system design are discussed in [9].

The thrust force generation of our linear stage uses short-secondary linear hysteresis motors, where D2 tool steel is used as the motor secondary material. We operate the linear motors synchronously with the secondaries pre-magnetized to improve the thrust force capability of the linear stage. The linear hysteresis motors are operated synchronously for two reasons: First, reluctance force can be generated in the motor due to the end effects, which is oscillatory if the motor is driven asynchronously and thus generate an undesirable vibration. Second, synchronous operation of the motors reduces hysteresis and eddy current losses in the secondaries. This is especially important for in-vacuum operation, since cooling of the moving stage is challenging when the stage is in vacuum, where conduction and convection heat transfer are not possible.

The position control of our linear stage uses the field-oriented control method assuming the secondary's magnetization fixed in the stage coordinate. Fig. 9 shows the measured closed-loop step response of the moving stage's position in the motion direction. Here the 10%-90% rise time of the step response is 0.012 s, which corresponds to a position control bandwidth of 30 Hz. Fig. 10 shows the measured tracking performance of the stage to a second-order polyno-

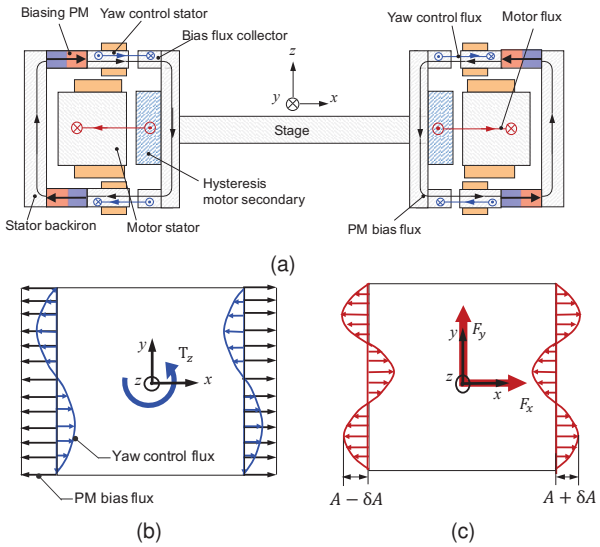

FIGURE 8. Magnetic fluxes and the suspension forces/torques generation in the magnetically-levitated linear stage. (a) Cross section diagram of the stage. (b) Top view of the permanent magnet bias fluxes (black) and the yaw control fluxes (blue) in the air gaps. (c) Top view of the motor fluxes (red) in the air gaps.

mial reference trajectory, including the reference and measured position (top plot), y-directional tracking error (middle plot), and the stage's x- and θ_z-directional displacements (bottom plot). The trajectory's maximum acceleration and velocity are $500\ \mathrm{mm/s^2}$ and $250\ \mathrm{mm/s}$, respectively, which are the acceleration and velocity requirements for the reticle transportation application in EUV photolithography scanners. The middle plot in Fig. 10 shows that the maximum position control tracking error is about $50\ \mu\mathrm{m}$, and the tracking error demonstrates a periodic pattern, where the spatial period of the tracking error matches with the motor stator tooth pitch. To our understanding, this error is caused by the cogging force in the pre-magnetized linear hysteresis motors. The bottom plot in Fig. 10 shows that the stage's maximum deviation from center in the x-direction is also approximately $50\ \mu\mathrm{m}$. Such data show that the stage's active magnetic suspension are successful during the stage in transportation.

CONCLUSIONS AND FUTURE WORK

In this work, we discussed the position control method for rotary hysteresis motors, and a case study of using linear hysteresis motors in magnetically-levitated linear stages. Experiments show the proposed field-oriented control method is able to achieve high-bandwidth position servo

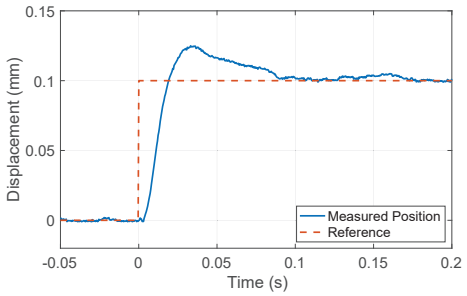

FIGURE 9. Measured closed-loop position step response of the linear stage in the y-axis motion direction.

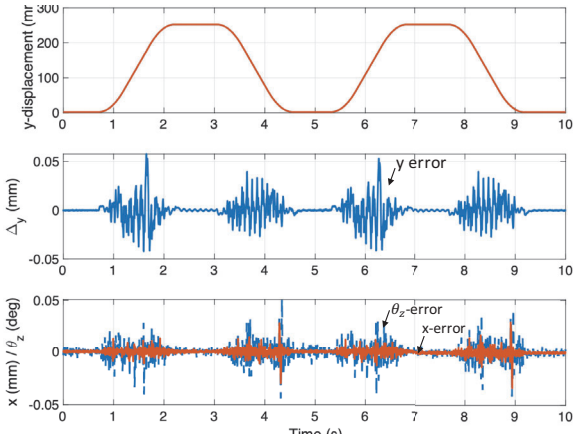

FIGURE 10. Measured tracking performance of the stage while tracking an S-shaped trajectory with $a_{max} = 500$ mm/s^2 and $v_{max} = 250$ mm/s. Top plot: reference and measured stage displacement. Middle plot: position tracking error. Bottom plot: measured stage displacements in x- and θ_z-directions.

for hysteresis motors, and the linear motor is able to demonstrate satisfactory performance for the in-vacuum transportation stage. To this point, it is fair to say that this series of work has enabled the hysteresis motors for being used in precision motion systems for special applications.

Given the hysteresis motors' good potential, future work should consider further use of these motors in precision mechatronic devices. The study on vector hysteresis models with improved accuracy is also suggested to further improve the motor's performance.

ACKNOWLEDGMENT

The authors thank ASML for supporting this work. We thank Dr. Ruvinda Gunawardana and Dr. Minkyu Kim at ASML for valuable discussions throughout the project. We thank Dr. Wolfgang Gruber and Gereon Goldbeck at JKU, Linz, Austria for their help with the hysteresis property measurements.

REFERENCES

[1] Rahman MA, Osheiba AM. Steady-state performance analysis of polyphase hysteresis-reluctance motors. IEEE Trans on Industry applications. 1985;22(3):659–663.

[2] Zhou L, Trumper D. Magnetically levitated linear stage for in-vacuum transportation tasks. In: 33 Annual Conference of American Society of Precision Engineering. ASPE; 2018. p. 1–6.

[3] Noh M, Gruber W, Trumper DL. Hysteresis bearingless slice motors with homopolar flux-biasing. IEEE/ASME Trans on mechatronics. 2017;22(5):2308–2318.

[4] Galluzzi R, Tonoli A, Amati N. Magnetic hysteresis machines for next-generation electric turbochargers. In: 2017 International Conference of Electrical and Electronic Technologies for Automotive. IEEE; 2017. p. 1–5.

[5] Zhou L, Nejad MI, Trumper DL. One-axis hysteresis motor driven magnetically suspended reaction sphere. Mechatronics. 2017;42:69–80.

[6] Galluzzi R, Amati N, Tonoli A. Modeling, Design and Validation of Magnetic Hysteresis Motors. IEEE Transactions on Industrial Electronics. 2019;.

[7] Miyairi S, Kataoka T. A basic equivalent circuit of hysteresis motor. Electrical Engineering Japan. 1965;85(10):41.

[8] Zhou L, Gruber W, Trumper DL. Position Control for Hysteresis Motors: Transient-time Model and Field-oriented Control. IEEE Trans on Ind Appl. 2018;54(4):3197–3207.

[9] Zhou L. Magnetically levitated hysteresis motor driven linear stage for in-vacuum transportation tasks. Department of Mechanical Engineering, Massachusetts Institute of Technology; 2019.

DESIGN AND MEASUREMENT OF A 6-PHASE COMBINED WINDING BEARINGLESS SYNCHRONOUS RELUCTANCE SLICE MOTOR

Wolfgang Gruber[1], Patrick Enengl[1], and Maksim Sokolov[2]
[1]Institute of Electrical Drives and Power Electronics
Johannes Kepler University Linz
A-Linz, Austria
[2]Department of Electrical Engineering and Automation
Aalto University School of Electrical Engineering
FI-00076 Aalto, Espoo, Finland

INTRODUCTION

Bearingless (or self-bearing) motors combine torque and suspension force generation in one common unit [1]. Over the time, nearly all standard drive topologies also got their bearingless counterparts, generating radial suspension forces to stabilize the rotor radially inside stator and allowing contact-free and, hence, wear-less operation. Using combined winding systems and disk-shaped rotors led to very compact bearingless motors. A combined winding is able to generate both, drive torque and suspension forces, while a separated winding creates either torque or force [2]. Combined windings are easier to manufacture, need less space and feature lower copper losses, but demand a more complex control scheme to decouple force and torque generation. A disk-shaped rotor allows to stabilize certain degrees of freedom (the axial deflection and the two tilting directions) passively, when the magnetic air-gap field is properly biased [3]. Such bearingless slice motors are typically used with a rotor impeller wheel in ultra-pure pump and mixing applications in the semiconductor, biomedical or pharmaceutical industry.

Recently, high-temperature surroundings, economic issues and demand for environmental sustainability restrict the use of permanent magnets, which are typically used in the rotor of these systems. Hence, a few years ago first bearingless slice motor concepts without permanent magnets in the rotor emerged [4], [5].

BEARINGLESS SYNCHRONOUS RELUCTANCE SLICE MOTOR

Previously, we have developed one of the first bearingless synchronous slice motors [6], [7] with combined winding system. The prototype is shown in Fig. 1 and features only six concentric coils connected in double star, leaving four independent stator currents to influence the four degrees of freedom air-gap bias flux, drive torque and suspension forces in perpendicular x- and y-direction. The geometric key values of the system are summarized in Table 1.

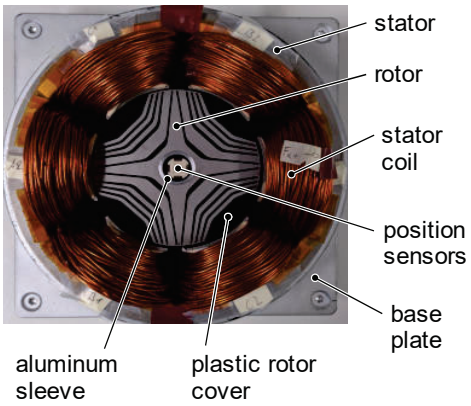

FIGURE 1. Bearingless synchronous switched reluctance slice motor prototype.

TABLE 1. Geometric prototype dimensions.

Description	Value
outer rotor diameter	80mm
inner rotor diameter	18mm
outer stator diameter	160mm
inner stator diameter	82mm
magnetic air gap	1mm
mechanic air gap	0.5mm
axial height of lamination stack	10mm
salient rotor poles	4

MOTOR MODEL

It is well known, that torque in synchronous reluctance motors obeys

$$T=\frac{m}{2}p_z\left(L_{sd}-L_{sq}\right)i_{sd}i_{sq}\,, \qquad (1)$$

where i_{sd} and i_{sq} are the common rotor-fixed current components generating a magnetic field in the air gap, that features the same number of magnetic polepairs p_z as salient rotor polepairs. m represents the motor phase number, while L_{sd} and L_{sq} are the stator inductances in the rotor-fixed coordinate frame.

Often, the flux generated from i_{sd} is called magnetization flux, as it can be seen as an air-gap bias flux. This flux strongly influences the stabilizing passive axial and tilting stiffness values as well as the destabilizing passive radial stiffness.

Additionally, [1] shows in chapter 12.2, that stator-fixed suspension forces F_x and F_y are created by

$$\begin{pmatrix} F_x \\ F_y \end{pmatrix} = \begin{pmatrix} M'_{sd} i_{sd} & -M'_{sq} i_{sq} \\ M'_{sq} i_{sq} & M'_{sd} i_{sd} \end{pmatrix} \begin{pmatrix} i_{sx} \\ i_{sy} \end{pmatrix}, \qquad (2)$$

where i_{sx} and i_{sy} create either two more or two less magnetic poles in the air gap compared to the salient rotor poles. Notice that constant i_{sx} and i_{sy} will not create rotor-fixed magnetic air-gap fields, while constant i_{sd} and i_{sq} do. Magnetic fields generated from constant i_{sx} and i_{sy} rotate either faster (when featuring two magnetic poles less) or slower (when featuring two magnetic poles more) than the rotor. The ratio of the rotating speeds equals the fields' poles ratio.

However, a separated winding bearingless motors features two different winding sets creating two by one different pole pair numbers p_z and $p_z \pm 1$ in the air gap, one for drive torque generation (energized with i_{sd} and i_{sq}) and one for suspension force generation (energized by i_{sx} and i_{sy}). Thereby, often Parks inverse transformation is used to map the rotating orthogonal 2-phase components into stator-fixed 3-phase components.

In a combined winding bearingless motor only one winding set exists. Stator-fixed phase currents now need to be found to achieve the same field generation as in the separate winding set for the current components i_{sd}, i_{sq}, i_{sx} and i_{sy}. Here, a generalized Park transformation

$$\begin{pmatrix} i_{s\lambda} \\ i_{s\mu} \end{pmatrix} = \mathbf{R}(\varphi)^T \mathbf{C}_k \begin{pmatrix} i_{s1} & i_{s2} & \cdots & i_{sm} \end{pmatrix}^T, \qquad (3)$$

with the generalized Clarke transformation

$$\mathbf{C}_k = \sqrt{\frac{2}{m}} \begin{pmatrix} 1 & \cos\left(\frac{2\pi k}{m}\right) & \cdots & \cos\left(\frac{2\pi (m-1) k}{m}\right) \\ 0 & \sin\left(\frac{2\pi k}{m}\right) & \cdots & \sin\left(\frac{2\pi (m-1) k}{m}\right) \end{pmatrix}$$

and the 2D rotation matrix $\mathbf{R}(\varphi)$, can be used to map the m stator-fixed components of a multi-phase system into rotating orthogonal λμ-coordinates featuring different pole pair numbers (in dependence on the two variables k and m).

Table 2 shows the model parameters obtained from 2D finite element simulations.

TABLE 2. Electromagnetic model data.

Variable name	Value
m	6
L_{sd}	18mH
L_{sq}	6.5mH
M'_{sd}	13.2H/m
M'_{sq}	2H/m

CONTROL SCHEME

The implemented control scheme is illustrated in Fig. 2. It depends on a generalized field-oriented control approach with the announced generalized Park transformation. The reference magnetization current i_{sd} is chosen and the reference i_{sq} component is computed by

$$i_{sd} = \frac{2T}{m p_z \left(L_{sd} - L_{sq}\right) i_{sd}}, \qquad (4)$$

while the reference i_{sx} and i_{sy} are determined by

$$\begin{pmatrix} i_{sx} \\ i_{sy} \end{pmatrix} = \begin{pmatrix} M'_{sd} i_{sd} & -M'_{sq} i_{sq} \\ M'_{sq} i_{sq} & M'_{sd} i_{sd} \end{pmatrix}^{-1} \begin{pmatrix} F_x \\ F_y \end{pmatrix}. \qquad (5)$$

These currents are impressed into the m phases by nested P or PI current controllers. The generalized Park transformation is used to calculate the force-current vector $\mathbf{i}_{sf}=(i_{sx}\ i_{sy})^T$ (with k=2) and the torque-current vector $\mathbf{i}_{st}=(i_{sd}\ i_{sq})^T$ (with k=1) from the measured phase currents. The referring rotation is conducted with the measured electrical rotor angle. The outer PID position controller in x- and y-direction stabilize the rotor in centered position, while the PI speed controller sets the necessary torque.

PROTOTYPE DESIGN

The prototype is already shown in Fig. 1, but Fig. 3 additionally presents a sectional view of the motor construction.

The stator lamination stack is mounted on a base plate. This base plate also bears the sensor bracket for the four 90°-shifted eddy current position sensors, located in the center of the rotor. As target for these sensors the rotor is equipped with an aluminum sleeve on the inside. Below the sleeve under the rotor an axially

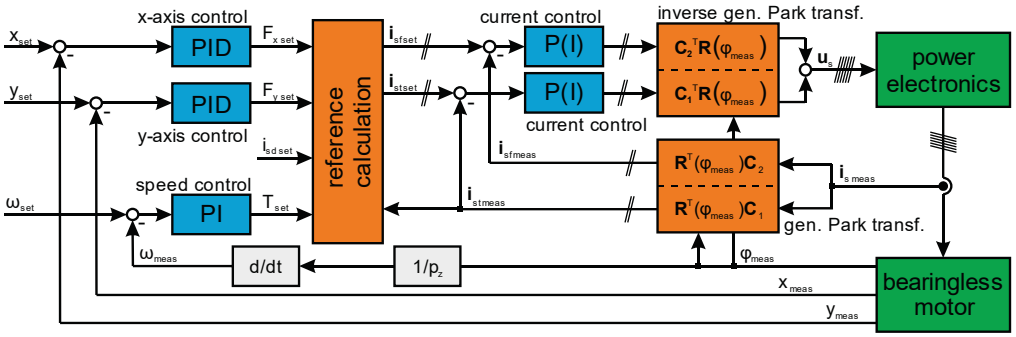

FIGURE 2. Control scheme of the six-phase four-pole synchronous reluctance slice motor prototype.

magnetized permanent magnet ring is glued. Its magnetic field is used to determine the rotor angle by four 90°-shifted Hall sensors. All the sensors are connected to a sensor evaluation printed circuit board in close proximity under the base plate.

The rotor is surrounded by a plastic rotor cover, which protects the rotor and also acts as radial auxiliary bearing.

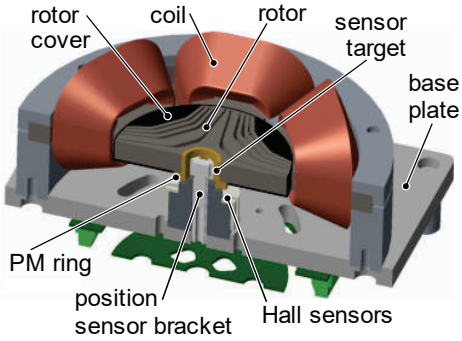

FIGURE 3. Cut through the bearingless motor construction.

MEASUREMENT RESULTS

Only recently, the motor was put into full bearingless operation. Additionally, it was mounted on a special test rig (shown in Fig. 4) to measure its characteristics. This test bench features a dividing head holding the rotor, a x-y-z cross table to move the rotor versus the stator and a rotor-fixed load cell to measure the passively and actively generated forces and torque. When necessary, instead of dividing head and load cell a load machine can be linked to the rotor to set the operating point of the bearingless drive regarding speed and torque.

Even though the motor is mechanically supported, this test setup is very flexible and allows numerous measurements, like the determination of passive stiffness values, active force and torque characteristics and also drive efficiency and loss performance.

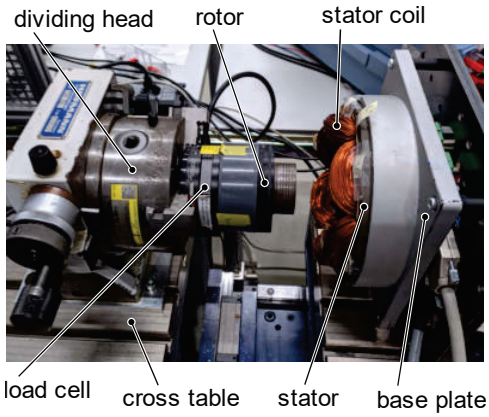

FIGURE 4. Test rig used for measurements.

A static measurement is shown in Fig. 5 presenting a force orbit. The six stator phases are set to create a rotating force vector of constant amplitude. Additionally, also the rotor is turned with the force vector. The measurement was conducted for two different force amplitudes. However, the ideal output-force curves should be circles, but measurements show a relatively strong fluctuation in the amplitude. This results from the fact, that the created air-gap fluxes are not purely sinusoidal due to slotting effects. So, formally in reality the variables M'_{sd} and M'_{sq} in (2) are not constants but depend on the rotor angle. However, while the obtained data showed that the force amplitude varies, the direction of the force vector is hardly affected. This means that cross coupling between x- and y-force generation remains small.

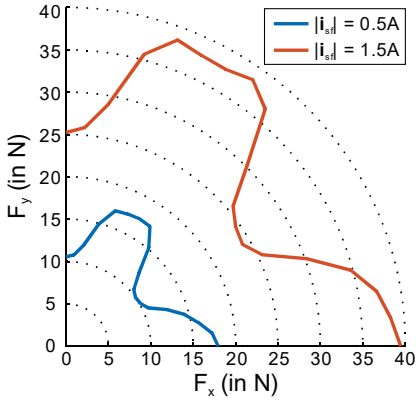

FIGURE 5. Measured force response to rotating constant force-current vectors at i_{sd}=2A. The rotor angle moves along with the force vector.

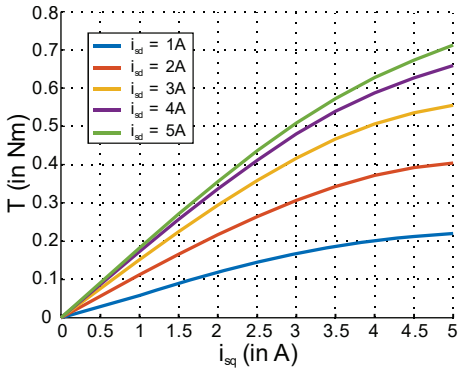

FIGURE 6. Measured torque response for increasing torque current i_{sq} at constant rotor angle for different constant i_{sd}.

Additionally, in Fig. 6 the measured torque characteristic over i_{sq} is shown for various constant i_{sd} values. For small currents the expected linear relationship according to (1) is fulfilled, but for higher i_{sq} (over 2.5A) saturation effects become considerable. Saturation effects are also noticed from higher i_{sd} currents (over 2.5A) as the steepness of the torque characteristic increases significantly less for higher i_{sd} current values.

FUTURE WORK

The feasibility of a bearingless synchronous reluctance slice motor with combined windings has been proven.

First measurements show the expected results regarding force and torque generation. However, compensation methods for angle dependent force and torque variations might need to be developed. Further consideration has to be given to the interaction of drive torque (with i_{sq}) and suspension force generation. Up to now, bearingless operation was only tested under no load torque, while higher torque generation was only tested with mechanical bearings. Finally, efficiency measurements and a separation of losses (into iron, windage and copper losses) need to be conducted in the future.

From the first experience, bearingless synchronous reluctance slice motors seem to be very flexible as the magnetization can be changed easily by i_{sd} (thereby influencing stiffness values, resonances and active force and torque generation). However, small air-gap sizes are necessary for efficient operation of these drives.

ACKNOWLEDGEMENT

This work has been supported by Linz Center of Mechatronics GmbH within the COMET-K2 “Center for Symbiotic Mechatronics” funded by the Austrian and Upper Austrian government.

REFERENCES

[1] Chiba A, Fukao T, Ichikawa O, Oshima M, Takemoto M, Dorrell D G. Magnetic Bearings and Bearingless Drives. Elsevier. 2005.

[2] Raggl K, Kolar J W, Nussbaumer T. Comparison of Winding Concepts for Bearingless Pumps. 7th International Conference on Power Electronics, Daegu, South Korea, 2007, 1013-1020.

[3] Barletta N, Schöb R. Design of a Bearingless Blood Pump, 3rd International Symposium on Magnetic Suspension Technology, Tallahassee, USA,1995, 265-274.

[4] Noh M, Trumper D L. Homopolar Bearingless Slice Motor with Flux-biasing Halbach Arrays. IEEE Transactions on Industrial Electronics, 2019, early access.

[5] Gruber W, Briewasser W, Rothböck M, Schöb R. Bearingless Slice Motor Concepts without Permanent Magnets in the Rotor. IEEE International Conference on Industrial Technology, Cape Town, South Africa, 2013, 259–265.

[6] Sokolov M, Gruber W, Saarakkala S E, Hinkkanen M. Modeling of a Bearingless Synchronous Reluctance Motor with Combined Windings. IEEE Energy Conversion Congress and Exposition, Baltmore, USA, 2019, 7084-7090.

[7] Holenstein T, Nussbaumer T, Kolar J W. A Bearingless Synchronous Reluctance Slice Motor with Rotor Flux Barriers. International Power Electronics Conference, Niigata, Japan, 2018, 3619-3626.

DECOUPLED, CLOSED-LOOP, MULTI-DOF SUSPENSION OF A SPHERICAL PERMANENT MAGNETIC DIPOLE ACTUATOR

Tyler T. Hamer[1], Joshua Chabot[2], and David L. Trumper[1]
[1]Department of Mechanical Engineering
Massachusetts Institute of Technology
Cambridge, MA, USA
[2]MIT Lincoln Laboratory
Lexington, MA, USA

INTRODUCTION

Multiple actuators, such as reaction wheels, control moment gyroscopes (CMGs) or thrusters, typically form a spacecraft's attitude control system (ACS) for rotating the spacecraft in 3 degrees of freedom (DoFs). An ACS's quality is commonly judged on SWaP (Size, Weight, and Power), torque generation, momentum storage, pointing stability, and reliability. CMG based ACSs often struggle with size and weight, whereas reaction wheel based ACSs suffer from low torque generation and low momentum storage. Further, mechanical bearings, a potential source of pointing jitter and a common failure point, are commonly used in reaction wheels and CMGs. Thruster based ACSs consume finite onboard propellant, thus limiting mission duration.

Reaction spheres rotate a spacecraft about an arbitrary axis with an equal-and-opposite torque about their rotation axis when accelerated about that axis, similar to reaction wheels, or with an equal-and-opposite gyroscopic torque from reorienting their rotation axis, similar to CMGs. Thus reaction sphere based ACSs have potentially lower SWaP from utilizing a single actuator over multiple actuators and highly efficient torque generation when operated similar to CMG based ACSs. Lastly, reaction spheres typically use magnetic levitation over mechanical bearings, resulting in increased momentum storage, pointing accuracy, and ACS life.

While NASA first proposed reaction spheres over a half century ago, limitations with previous designs have kept the technology from commercialization [1, 2]. Recently, reaction spheres with a dipole permanent magnet as the rotor have appeared promising due to their mechanical simplicity and simple modeling despite their inherent underactuation [3, 4]. Torque cannot be generated about the rotor's axis of magnetization. Specifically, Figure 1 depicts a bench-level prototype for a reaction sphere with a dipole permanent magnet as the rotor that has been modeled, designed, and vertically suspended [5]. Having implemented decoupling commutation laws and multi-DoF-translation and-orientation sensing [6], this paper continues the work from [5, 6], presenting multi-DoF angular velocity estimation, a decoupled controller for multi-DoF suspension, and decoupled, closed-loop, multi-DoF suspension of the bench-level prototype.

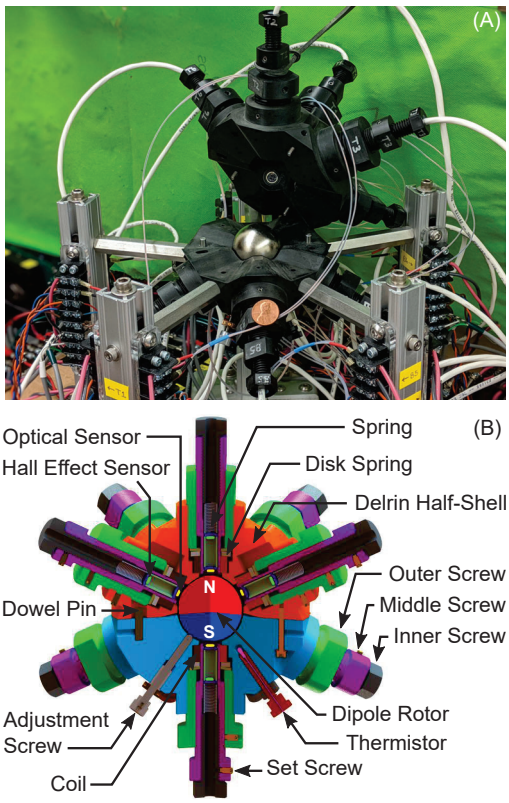

FIGURE 1. A permanent magnetic dipole reaction sphere (a) fully-wired and-assembled, bench-level prototype with (b) label cross section from [5, 6].

DISTRIBUTION STATEMENT A. Approved for public release. Distribution is unlimited.
This material is based upon work supported under Air Force Contract No. FA8702-15-D-0001. Any opinions, findings, conclusions or recommendations expressed in this material are those of the author(s) and do not necessarily reflect the views of the U.S. Air Force.

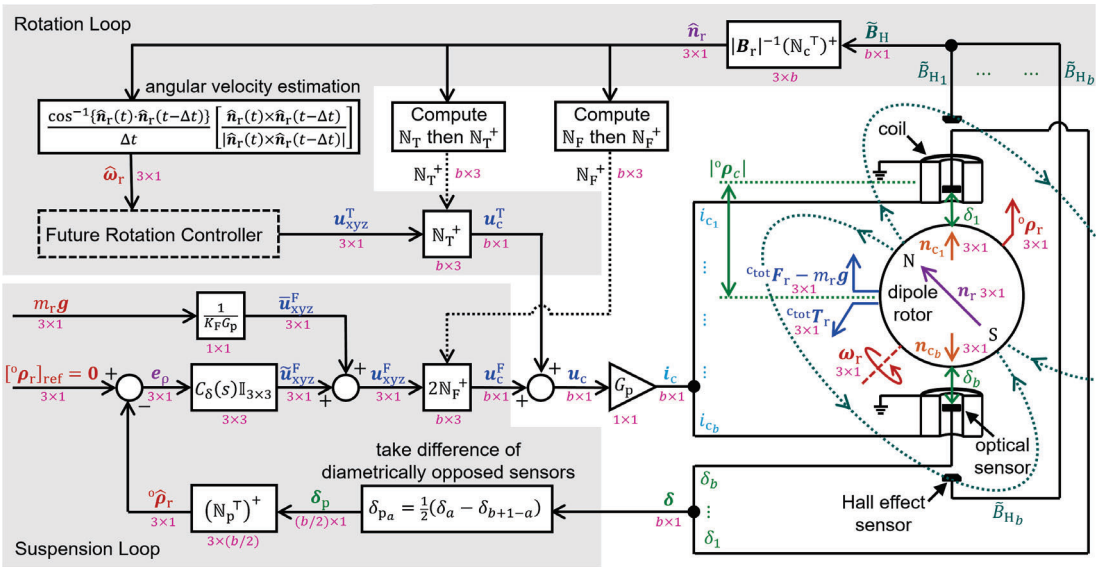

FIGURE 2. Control scheme for simultaneous decoupled, closed-loop, 3-DoF suspension and decoupled, open-loop, 2-DoF rotation of the dipole rotor. Real-time force $\mathbb{N}_F^+$ and torque $\mathbb{N}_T^+$ commutation laws decouple the rotor's dynamics allowing each DoF, except rotation about the rotor's magnetization axis, to be controlled independently. 3 identical SISO translation controllers $C_\delta(s)$ control the rotor's 3 dimensional (3D) position ${}^{\mathrm{o}}\boldsymbol{\rho}_{\mathrm{r}}$ relative to the center of the stator's spherical pocket O from the difference between the rotor's desired position $[{}^{\mathrm{o}}\boldsymbol{\rho}_{\mathrm{r}}]_{\mathrm{ref}}$ and the estimate of the rotor's position ${}^{\mathrm{o}}\widehat{\boldsymbol{\rho}}_{\mathrm{r}}$ as measured by the surrounding optical sensors $\boldsymbol{\delta}$. The rotor's 3D angular velocity $\boldsymbol{\omega}_{\mathrm{r}}$, which is estimated $\widehat{\boldsymbol{\omega}}_{\mathrm{r}}$ from an estimate $\widehat{\boldsymbol{n}}_r$ of the rotor's magnetization axis $\boldsymbol{n}_r$ as measured by the surrounding Hall effect sensors $\widetilde{\boldsymbol{B}}_{\mathrm{H}}$, is open loop controlled by directly setting the rotation control effort $\boldsymbol{u}_{\mathrm{xyz}}^{\mathrm{T}}$. The torque commutation law drives the rotor's magnetization axis into a plane normal to the rotation control effort, allowing the rotor to rotate about arbitrarily directed rotation control effort.

MULTI-DOF CONTROL SCHEME

A surrounding radial array of 12 equidistant coils, one centered on each face of the bench-level prototype's dodecahedron stator, closed-loop suspends the prototype's rotor, a 38.1 mm (1.5 in) diameter, spherical NdFeB (Grade 42) permanent magnet (K&J Magnetics SX8). Current driven through each coil by a linear amplifier is controlled by the decoupled, multi-input, multi-output (MIMO) control scheme shown in Figure 2. A surrounding radial array of 12 optical sensors (Fairchild QRE1113GR), each coaxially placed within a coil, measures the rotor's 3×1 translational position ${}^{\mathrm{o}}\boldsymbol{\rho}_{\mathrm{r}}$ relative to the center of the stator's spherical pocket O with a theoretical standard deviation of 0.05 µm, while a surrounding radial array of 12 Hall effect sensors (Allegro A1308KUA-1-T), each also coaxially placed within a coil, measures the rotor's 3×1 magnetization axis $\boldsymbol{n}_{\mathrm{r}}$ with a theoretical standard deviation of 190 µrad.

Force $\mathbb{N}_F^+$ and torque $\mathbb{N}_T^+$ commutation laws, constructed in real-time from an estimate of the rotor's magnetization axis $\widehat{\boldsymbol{n}}_{\mathrm{r}}$, decouple the rotor's dynamics, mapping control effort corresponding to forces along and torques about the X-, Y-, and Z-axes to the currents driven through each coil [6]. Since the rotor is underactuated, torque cannot be generated about the rotor's magnetization axis, the desired torque's component about the rotor's magnetization axis maps to zero current distributed among the coils. However, the remaining mapped torque components, which are about an axis normal to the rotor's magnetization axis, reorient the rotor such that the rotor's magnetization axis is normal to the desired torque. Thus despite the rotor's underactuation, the rotor can be commanded to rotate about an arbitrary inertial axis.

Additionally, an estimate $\widehat{\boldsymbol{\omega}}_{\mathrm{r}}$ of the rotor's 3×1 angular velocity $\boldsymbol{\omega}_{\mathrm{r}}$ about the X-, Y-, and Z-axes is constructed from the current estimate $\widehat{\boldsymbol{n}}_{\mathrm{r}}(t)$ at time t and the previous estimate $\widehat{\boldsymbol{n}}_{\mathrm{r}}(t-\Delta t)$ of the rotor's magnetization axis separated by the control loop execution time Δt as depicted in Figure 3:

$$\widehat{\boldsymbol{\omega}}_{\mathrm{r}} = |\widehat{\boldsymbol{\omega}}_{\mathrm{r}}|\,\widehat{\boldsymbol{n}}_{\omega} \tag{1a}$$

$$|\widehat{\boldsymbol{\omega}}_{\mathrm{r}}| = \cos^{-1}\left[\widehat{\boldsymbol{n}}_{\mathrm{r}}(t)\cdot\widehat{\boldsymbol{n}}_{\mathrm{r}}(t-\Delta t)\right]\Delta t^{-1} \tag{1b}$$

$$\widehat{\boldsymbol{n}}_{\omega} = \frac{\widehat{\boldsymbol{n}}_{\mathrm{r}}(t)\times\widehat{\boldsymbol{n}}_{\mathrm{r}}(t-\Delta t)}{|\widehat{\boldsymbol{n}}_{\mathrm{r}}(t)\times\widehat{\boldsymbol{n}}_{\mathrm{r}}(t-\Delta t)|}. \tag{1c}$$

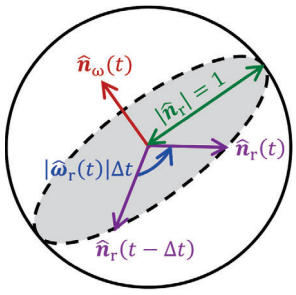

FIGURE 3. Estimation of the rotor's angular velocity $|\widehat{\boldsymbol{\omega}}_{\mathrm{r}}|\,\widehat{\boldsymbol{n}}_{\omega}$ from the current $\widehat{\boldsymbol{n}}_{r}\,(t)$ and previous $\widehat{\boldsymbol{n}}_{r}\,(t-\Delta t)$ rotor's magnetization axis estimations.

Similar to when estimating derivatives via the backwards Euler method, the gain of Equation (1) increases with frequency, causing high-frequency noise in the estimates of the rotor's magnetization axis to generate large, undesirable variations in the rotation control effort when fed back on. Specifically, this method estimates the rotor's angular velocity with a theoretical standard deviation of 7.26 rpm without filtering. Thus the angular velocity estimate or the resulting rotational control effort must be filtered for closed-loop control.

However, to simply control the rotor's rotation in open-loop, the 3×1 rotation control effort $\boldsymbol{u}^{\mathrm{T}}_{\mathrm{xyz}}$ can be directly set as

$$\boldsymbol{u}^{\mathrm{T}}_{\mathrm{xyz}} = G_{\mathrm{p}}\boldsymbol{i}^{\mathrm{T}}_{\mathrm{xyz}}, \quad \boldsymbol{i}^{\mathrm{T}}_{\mathrm{xyz}} = K_{\mathrm{T}}^{-1}\left[{}^{\mathrm{c_{tot}}}\boldsymbol{T}_{\mathrm{r}}\right]_{\mathrm{ref}}, \qquad (2)$$

where G_{p} is the nominal power amplifier gain, K_{T} is the reaction sphere's single-coil torque constant for a centered (${}^{\mathrm{o}}\boldsymbol{\rho}_{\mathrm{r}} = \boldsymbol{0}$) rotor, $\boldsymbol{i}^{\mathrm{T}}_{\mathrm{xyz}}$ is the effective 3×1 rotation control current, and $\left[{}^{\mathrm{c_{tot}}}\boldsymbol{T}_{\mathrm{r}}\right]_{\mathrm{ref}}$ is the 3×1 desired total torque applied to the rotor by the coils.

As the rotor's position is closed-loop controlled, the 3×1 suspension control effort $\boldsymbol{u}^{\mathrm{F}}_{\mathrm{xyz}}$ given by

$$\boldsymbol{u}^{\mathrm{F}}_{\mathrm{xyz}} = G_{\mathrm{p}}\boldsymbol{i}^{\mathrm{F}}_{\mathrm{xyz}}, \qquad (3)$$

where $\boldsymbol{i}^{\mathrm{F}}_{\mathrm{xyz}}$ is the effective 3×1 suspension control current, is generated by 3 identical single-input single-output (SISO) controllers $C_{\delta}\,(s)$, one for each translational DoF, from the error between the rotor's desired position $\left[{}^{\mathrm{o}}\boldsymbol{\rho}_{\mathrm{r}}\right]_{\mathrm{ref}}$ and the estimate of the rotor's position ${}^{\mathrm{o}}\widehat{\boldsymbol{\rho}}_{\mathrm{r}}$:

$$\boldsymbol{e}_{\rho} = \left[{}^{\mathrm{o}}\boldsymbol{\rho}_{\mathrm{r}}\right]_{\mathrm{ref}} - {}^{\mathrm{o}}\widehat{\boldsymbol{\rho}}_{\mathrm{r}}. \qquad (4)$$

Initially, the SISO vertical suspension controller from [5] was used to suspend the rotor in all 3-DoF. With the rotor suspended, the 3×3 frequency matrix of the rotor's (plant's) dynamics, provided in Figure 4 and discussed in a later section, was measured to directly design a more robust suspension controller from. For suspension, a proportional-integral-derivative (PID) controller with a second order low pass filter is used to crossover at a predicted $[\omega_{\mathrm{c}}]_{\mathrm{calc}}$ = 60 Hz with a predicted phase margin $[\phi_{\mathrm{M}}]_{\mathrm{calc}}$ = 30°:

TABLE 1. SISO Suspension Controller Parameters.

Symbol	Value	Symbol	Value
K_{p}	51.6	τ_{i}	13.3 ms
α	13.9	τ_{d}	0.711 ms
ω_{lp}	1885 rad/s	ζ_{lp}	$\sqrt{2}$

$$C_{\delta}(s) = K_{\mathrm{p}}\frac{\tau_{\mathrm{i}}s+1}{\tau_{\mathrm{i}}s}\cdot\frac{\alpha\tau_{\mathrm{d}}s+1}{\tau_{\mathrm{d}}s+1}\cdot\frac{\omega_{\mathrm{lp}}^2}{s^2+2\zeta_{\mathrm{lp}}\omega_{\mathrm{lp}}s+\omega_{\mathrm{lp}}^2} \qquad (5)$$

whose values are given in Table 1.

SUSPENSION FREQUENCY RESPONSE

To evaluate decoupled, 3-DoF suspension of the rotor in the frequency domain, the rotor's desired position is varied sinusoidally along the X-, Y-, and Z-axes each, with an amplitude of 50 µm over 90 frequencies from 1 Hz to 1 kHz while zero rotation control effort is applied to the rotation loop. At each of these frequencies, the following 3×3 MIMO frequency response matrices are measured: (1) the rotor's (plant's) translational dynamics $\mathbb{P}(s)$ given by

$${}^{\mathrm{o}}\boldsymbol{P}_{\mathrm{r}} = \mathbb{P}(s)\boldsymbol{I}_{\mathrm{xyz}}, \qquad (6)$$

where ${}^{\mathrm{o}}\boldsymbol{P}_{\mathrm{r}}$ and $\boldsymbol{I}_{\mathrm{xyz}}$ are the Laplace transformations of the rotor's position and the effective suspension control current respectively, (2) the MIMO suspension controller $\mathbb{C}(s)$ given by

$$\boldsymbol{E}_{\rho} = \mathbb{C}(s)\boldsymbol{U}_{\mathrm{xyz}} \qquad (7a)$$

$$\mathbb{C}(s) = C_{\delta}(s)\mathbb{I}_{3\times3}, \qquad (7b)$$

where $\boldsymbol{E}_{\rho}$ and $\boldsymbol{U}_{\mathrm{xyz}}$ are the Laplace transformations of the error in the rotor's position and the suspension control effort respectively and $\mathbb{I}_{3\times3}$ is the 3×3 identity matrix, (3) the return ratio $\mathbb{RR}(s)$ given by

$${}^{\mathrm{o}}\boldsymbol{P}_{\mathrm{r}} = \mathbb{RR}(s)\boldsymbol{E}_{\rho} \qquad (8a)$$

$$\mathbb{RR}(s) = \mathbb{P}(s)G_{\mathrm{p}}\mathbb{C}(s), \qquad (8b)$$

and (4) the closed loop dynamics given by

$${}^{\mathrm{o}}\boldsymbol{P}_{\mathrm{r}} = \mathbb{CL}(s)\left[{}^{\mathrm{o}}\boldsymbol{P}_{\mathrm{r}}\right]_{\mathrm{ref}} \qquad (9a)$$

$$\mathbb{CL}(s) = \left(\mathbb{I}_{3\times3} + \mathbb{RR}\right)^{-1}\mathbb{RR}. \qquad (9b)$$

Figure 4 displays the measured frequency responses as Bode Plots. The on-diagonal frequency responses of the plant and controller are compared against the plant model for vertical suspension of the rotor with a single coil from [5] and Equation (5)

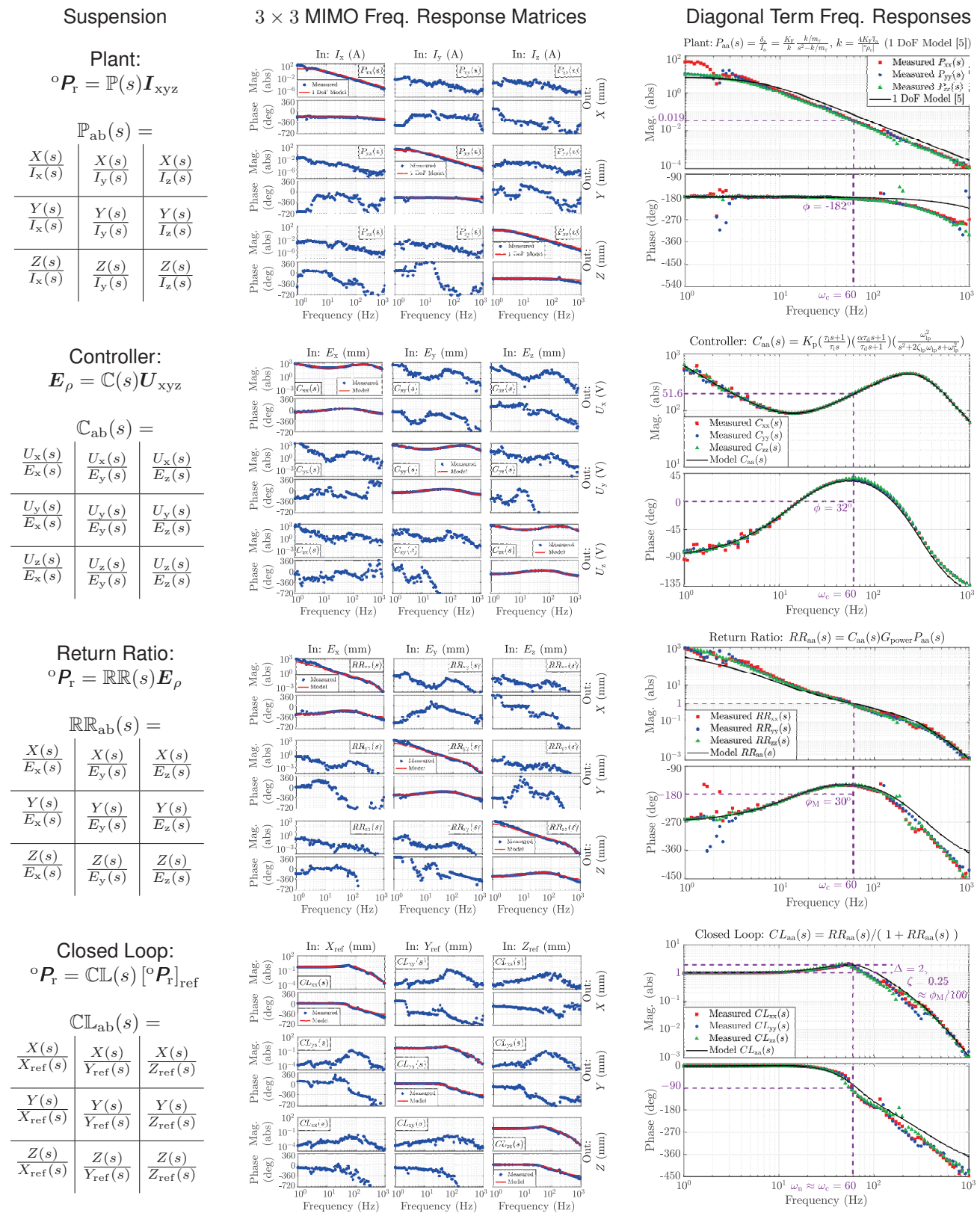

FIGURE 4. Suspension frequency responses: (middle column) 3×3 MIMO frequency response matrices and (right column) on-diagonal frequency responses for (1st row) the plant, (2nd row) the controller, (3rd row) the return ratio, and (4th row) the closed loop. On-diagonal frequency responses are 2-3 orders greater in magnitude than off-diagonal frequency responses supporting that the commutation laws decouple the rotor's dynamics.

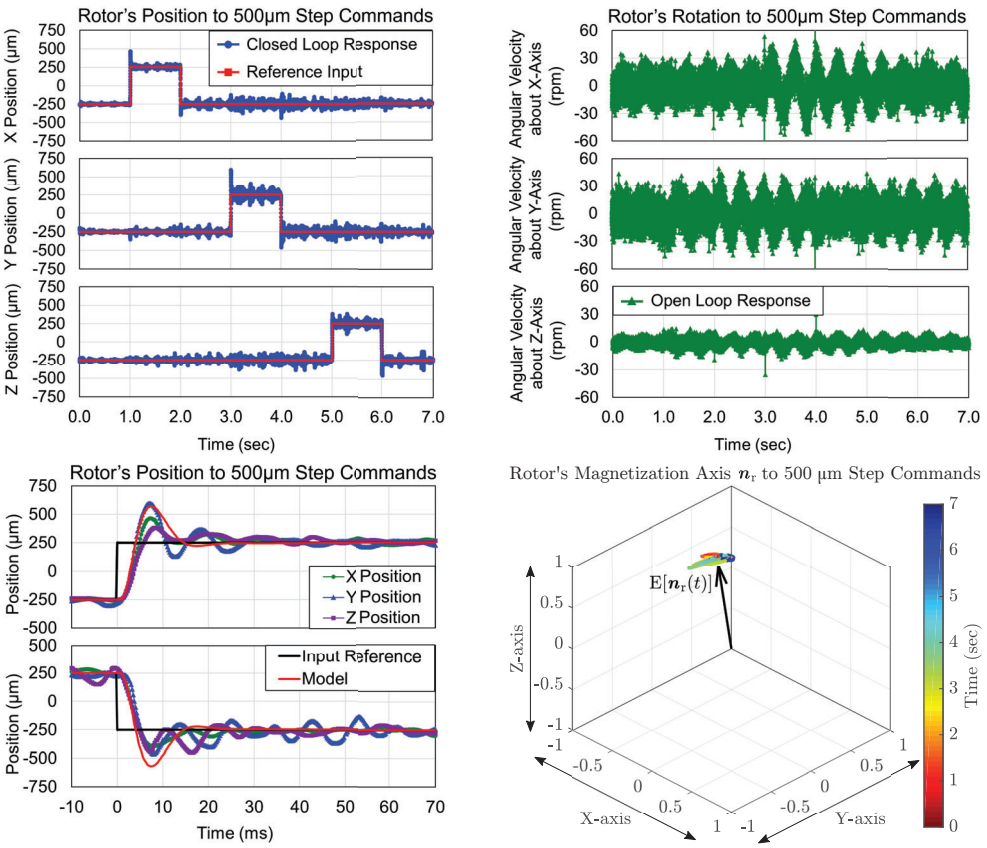

FIGURE 5. Time response of (upper-left) the rotor's 3D position, (upper right) 3D angular velocity, and (lower right) magnetization axis's direction for commanded 500 µm *position steps. (lower left) Position time responses are overlaid against the modeled decoupled, closed loop position time response.*

respectively. The on-diagonal frequency responses of the return ratio and closed loop are compared against Equations (8) and (9) based on the model from [5], respectively.

Below crossover, the on-diagonal components of each MIMO frequency response matrix are 2-3 orders greater in magnitude than the off-diagonal components, supporting that the force commutation law successfully decouples the rotor's translation DoFs. Further, the on-diagonal frequency responses of the rotor's translational dynamics are decently predicted by [5]'s plant model, especially above the model's instability frequency of 6.1 Hz. Below that frequency, the rotor's dynamics along the X-axis appear to be closer to that of a free mass.

Such a discrepancy cannot be explained by gravity as the dynamics along the Z-axis would deviate from the other two axes. Instead the following is hypothesized. The noise level of the Fairchild QRE1113GR optical sensors used for translational feedback has been shown to be very sensitive to the surface finish of the target [7]. When the target rotates, the target's surface finish with respect to the optical sensors appears to roughen, increasing the noise level. Below the model's instability frequency where the rotor's translational dynamics have the highest gain, the little remaining cross-coupling with the rotational DoFs could also be greatest. Thus when the rotor's translational dynamics are measured at low frequencies, slight rotations are introduced which increases noise in the measurement of the rotor's translation, causing artifacts in the frequency response. Such noise increases in the measurement of the rotor's position are seen in the time response of the closed loop in the following section. Further, to verify, the suspension frequency response matrices can be retaken after closed-loop rotation control is implemented to prevent rotation from cross-coupling.

The on-diagonal frequency responses of the controller, return ratio, and closed loop agree well with the model predictions. The controller's on-diagonal frequency responses have a magnitude of 51.6 and a phase of 32° at 60 Hz which, combined with the plant's on-diagonal frequency response's mag-

nitude of 0.019 and phase of -182° at 60 Hz, result in unity gain of the return ratio's on-diagonal frequency responses at a measured crossover of $[\omega_c]_{meas}$ = 60 Hz with a measured phase margin $[\phi_M]_{meas}$ = 30° as predicted. Further, the closed loop on-diagonal frequency responses have a natural frequency approximately equal to crossover and a peak magnitude of 2, corresponding to a phase margin slightly below 30°.

SUSPENSION TIME RESPONSE

To evaluate decoupled, 3-DoF suspension of the rotor in the time domain, the rotor's desired position is stepped 500 µm and back along the X-, Y-, and Z-axes each while zero rotation control effort is applied to the rotation loop. Figure 5 shows these time responses of the rotor's 3 translational DoFs against the predicted step response of the suspension closed loop (Equation (9)), the cross-coupled response of the 3 rotational DoFs represented as the rotor's angular velocity, and the orbit of the rotor's magnetization axis.

The rotor's position successfully steps 500 µm and back, peaking in 7.25 – 8.25 ms versus a predicted 7.5 ms. These peak times correspond to a measured natural frequency 62 – 72 Hz versus a predicted 68 Hz, close to the designed and measured crossover of ω_c = 60 Hz. Additionally, steps in the rotor's position along a specific DoF produce only minor deviations in the rotor's position along the other translation DoFs and only minor rotation of the rotor. The minor translational cross-coupling is difficult to estimate due to increased noise in the rotor's position from the minor rotation of the rotor induced after stepping. Noise in the rotor's position is greatest from 3 – 5 ms when oscillations in the rotor's measured angular velocity are greatest.

CONCLUSION

Reaction sphere based ACSs have potentially lower SWaP (Space, Weight, and Power) and potentially higher torque generation, momentum storage, pointing stability, and reliability than reaction wheel, CMG, or thruster based ACSs. This paper continues the work from [5, 6] on a permanent magnetic dipole reaction sphere for an ACS. Specifically multi-DoF angular velocity estimation, a decoupled controller for multi-DoF suspension, and decoupled, closed-loop multi-DoF suspension of a bench-level prototype were presented.

Commutation laws decoupled the rotor's dynamics, allowing the rotor's 3-DoF suspension to be controlled by 3 identical SISO controllers, one for each translational DoF, and the rotor's 2-DoF rotation to be driven open loop by directly specifying a rotation control effort. Filtered PID controllers were implemented for each SISO controller allowing the suspension loop to crossover at a measured 60 Hz with a measured phase margin of 30° as predicted. The rotor's 3×3 suspension frequency response matrices were measured and found to have on-diagonal components 1-2 orders greater in magnitude than the off-diagonal components, supporting decoupling of the rotor's translation DoF. The rotor's translational step response with estimations of the rotor's angular velocity showed the rotational DoFs to also be well decoupled from the translational DoFs.

REFERENCES

[1] Zhu L, Guo J, Gill E. Review of reaction spheres for spacecraft attitude control. Progress in Aerospace Sciences. 2017 May;91:67–86.

[2] Zhang J, Yuan L, Chen SL, Liang Y, Huang X, Zhang C, et al. A survey on design of reaction spheres and associated speed and orientation measurement technologies. ISA transactions. 2020 April;99:417–431.

[3] Wang J, Jewell GW, Howe D. Analysis, design and control of a novel spherical permanent-magnet actuator. IEE Proceedings - Electric Power Applications. 1998 January;145(1):61–71.

[4] Chabot J. A Spherical Magnetic Dipole Actuator for Spacecraft Attitude Control [Master's Thesis]. Aerospace Engineering Sciences, University of Colorado. Boulder, CO, USA; 2015.

[5] Hamer TT, Noh M, Zhou L, Chabot J, Trumper DL. A Magnetically Suspended, Spherical Permanent Magnetic Dipole Actuator. In: Proceedings of The Thirty-Third Annual Meeting of the American Society for Precision Engineering, Las Vegas, NV, USA. ASPE; 2018. p. 70–75.

[6] Hamer TT, Chabot J, Trumper DL. Sensing And Commutation Of A Spherical Permanent Magnetic Dipole Actuator. In: Proceedings of the Thirty-Fourth Annual Meeting of the American Society for Precision Engineering, Pittsburgh, PA, USA. ASPE; 2019. p. 115–120.

[7] Noh M, Gruber W, Trumper DL. Hysteresis Bearingless Slice Motors With Homopolar Flux-Biasing. IEEE/ASME Transactions on Mechatronics. 2017;22(5):2308–2318.

A NOVEL POSITION SENSING SYSTEM FOR BEARINGLESS MOTORS

Benjamin S. Weinreb[1,2], Donald C. Fyler[2], and David L. Trumper[1]
[1]Department of Mechanical Engineering
Massachusetts Institute of Technology
Cambridge, MA, USA
[2]The Charles Stark Draper Laboratory, Inc.
Cambridge, MA, USA

INTRODUCTION

Bearingless motors are electric machines with torque and force generating windings on a single stator, combining the function of a torque motor and a magnetic bearing. Many variants of bearingless motors have been developed since they were first introduced in the 1980's [1]. Bearingless motors enable contact-free rotation and levitation of a rotor and eliminate the need for mechanical bearings. Thus, they been used in extreme temperature, high purity, and vacuum pumping applications among others.

Magnetic suspension systems such as bearingless motors typically exhibit a negative stiffness along one or more degrees of freedom, thus closed-loop feedback control is often required to achieve stable leviation of the rotor [2]. As such, bearingless motors require sensors, power electronics, and a control system. The design of each of these subsystems must be considered to optimize the cost, performance, and functionality of a bearingless motor. Particularly, the sensing system must have sufficient resolution and bandwidth as well as be easily packaged into the stator assembly.

In this paper, we present the design, construction, and testing of a novel position sensing system for use in bearingless motors with relatively large airgap magnetic flux density. This system utilizes an array of Hall elements installed on a circuit board to provide an angular position estimate and differential pairs of reflective optical sensors to provide a radial position estimate. We first explain the motivation for this new sensing system. Next, we provide a brief overview of the position sensing system and explain the basic operating principle. Then, we describe the design of the sensor conditioning electronics and processing algorithms. Finally, we present experimental results from resolution characterization and sensitivity calibration tests and present our conclusions.

BACKGROUND AND MOTIVATION

The motivation for a new bearingless motor position sensing system arose from our design of a new bearingless motor rotor. The new rotor contains permanent magnets that generate a dipole magnetic field. It was designed to be driven by a modified version of the of the stator developed by Noh et al. [3]-[5], which was originally developed to drive a reluctance rotor for extracorporeal life support (blood pumping) applications. The sensing system developed by Noh [5] for the reluctance motor was not suitable for the permanent magnet based rotor, as the large airgap magnetic flux produced by the the permanent magnets would saturate the commericial Hall effect sensors.

SENSOR SYSTEM OVERVIEW

A 3-D rendering of the sensing system installed in the stator is shown in Figure 1. Two annular ring shaped printed circuit boards (PCBs), used to sense the rotor angular and axial position, are installed above and below the stator teeth. Four reflective optical sensors, used to sense the rotor radial position, are installed in differential pairs between the stator teeth.

Each of the ring PCBs, pictured in Figure 2, contains an array of six Hall elements, six precision current source circuits to power each Hall element, and six instrumentation amplifiers to amplify the output signal. The Hall elements are evenly spaced around the circumfrence of the stator above and below every other stator tooth, and are oriented to sense the fringing Z-component of the airgap magnetic field. The output signals from the Hall elements on each board are sampled by an analog-to-digital converter (ADC) and processed by an FPGA to yield an angular position estimate for use in torque and force commutation. The signals from the top and bottom

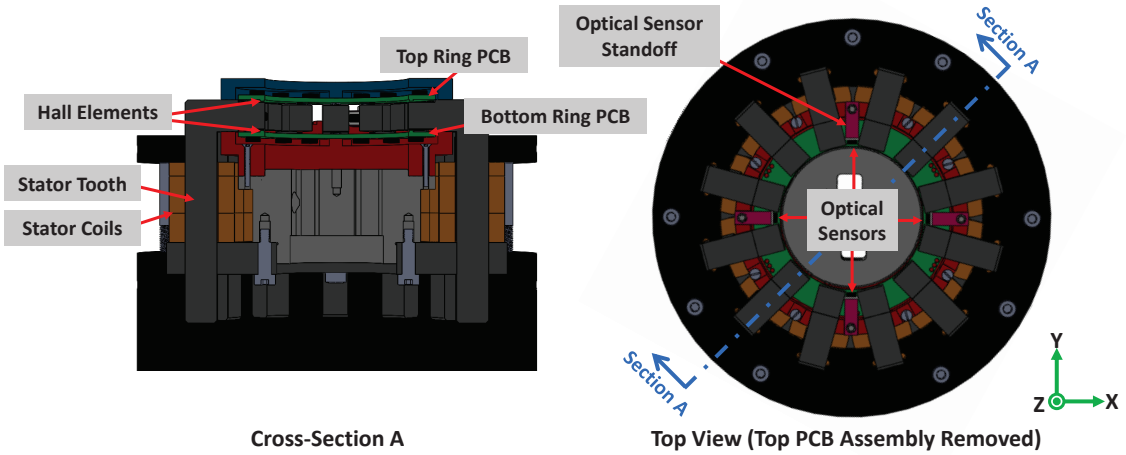

FIGURE 1. Diagram of the sensing system

boards are also compared to yield an estimate of the rotor's axial (Z) position.

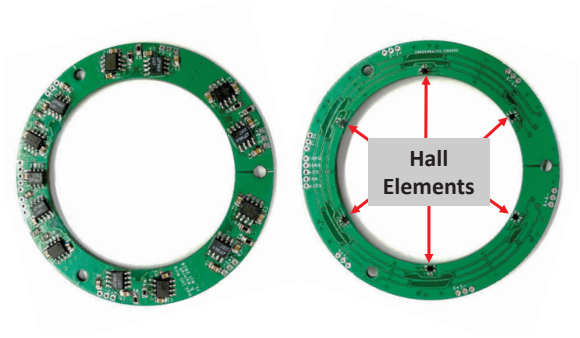

FIGURE 2. Top view (right) and bottom view (left) of the Hall element ring PCB

The optical sensors are attached to aluminum standoffs and installed in a retaining structure between the stator teeth. The sensors are wired to a prototyping breadboard which provides the required supply voltages and readout electronics. The sensor output signals are sampled by the ADC and processed on the FPGA to yield rotor radial position estimates for use in radial position feedback control.

SENSOR SYSTEM DESIGN

In this section, we describe the design of the interface electronics for both the Hall elements and the optical sensors, as well as the processing algorithms used to yield position estimates from the sensor signals.

Hall Element Operating Principle

Hall elements are devices that measure the strength of a magnetic field using the Hall effect. Hall elements consist of a thin rectangular strip of semiconductor material with four leads, one attached to each side. A current is supplied between two leads on opposite sides of the rectangular strip. When a magnetic field is a applied perpendicular to the plane of the rectangular strip, a voltage is produced across the other two leads. This voltage, referred to as the Hall voltage, is proportional to the magnetic field, applied current, and an inherent gain of the system. Thus, by applying a constant current, the magnetic field strength can be deduced by the response voltage. The Hall voltage is typically very small, and thus amplification is required prior to the ADC.

Off-the-shelf Hall effect sensors typically contain a Hall element, current-source electronics, and an output amplification stage. While this packaging is convenient, we have observed that off the shelf sensors are typically only rated for magnetic fields on the order of 50-100mT, limited by either the output amplification stage rails or nonlinear properties of the semiconductor material in the Hall element. In our application, we expect to see fields on the order of 150mT or above. Thus, we have elected to use gallium arsendide (GaAs) Hall elements (HG-176A from AKM Semiconductor), and design our own current source and amplification stage around them. These Hall elements produce a linear Hall voltage output with linearity error less than 2% for magnetic fields up to 0.5T [6].

Hall Element Interface Electronics

A schematic of the interface circuit for a single Hall element is shown in Figure 3. A precision voltage source (LT1021DCS8-5 from Analog Devices) and a low-noise operational amplifier (OP27G from Analog Devices) are used to provide a precise 1mA current source to the Hall element. The Hall element is configured with the current supply leads connected between the output and inverting input of the op-amp. The 5V supply is connected to the non-inverting input, and a 4.99kΩ resistor is placed between the inverting input and ground. The op-amp will drive it's output such that the inverting and non-inverting inputs are at the same voltage. Thus, there will be 5 volts at the inverting input, and by Ohm's law, 1mA through the Hall element ($i_{out} = V_-/R_1 = 5V/4.99k\Omega = 1mA$).

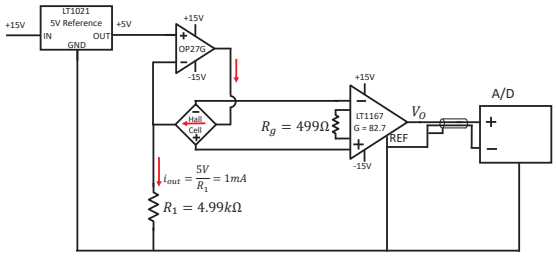

FIGURE 3. Single Hall element interface electronics schematic

The Hall element output is amplified by an instrumentation amplifier (LT1167 from Analog Devices). The LT1167 gain is set by a single resistor, R_g such that the output will span the full +/-10V ADC range with the expected +/-150mT magnetic field range. Each ring PCB contains six Hall elements, each requiring their own current supply and output amplification stage as described in Figure 3. Only one precision 5V reference chip is used per board, with the output routed to the non-inverting inputs of each of the six low noise op-amps.

Angular Position Sensing Algorithm

In this section, we describe the algorithms used to process the ring board PCB sensor signals to yield angular position and axial position estimates. To develop and evaluate these algorithms, we used 2-D electromagnetic finite element simulations. A top-view diagram of the sensor configuration is shown in Figure 4.

The dipole rotor produces a radial magnetic field pattern in the airgap that repeats once per revolution. We define the rotor angle, ϕ, as the angle between the rotor's axis of magnetization (the d-axis) and the stator X-axis. The Hall element voltage V_i due to the first spatial harmonic component of the magnetic field present on the i^{th} sensor is a function of the rotor angle ϕ, sensor location $\gamma(i-1)$, the first harmonic amplitude B, and the sensor scale factor K. This can be expressed as:

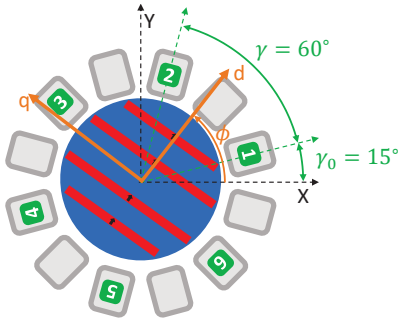

FIGURE 4. Layout of Hall elements with respect to stator and rotor axes

$$V_i = KBcos(\gamma_0 + \gamma(i-1) - \phi) \tag{1}$$

Using trigonometric identities, this expression can equivalently be written as:

$$V_i = KBcos(\gamma_0 + \gamma(i-1))cos(\phi) + KBsin(\gamma_0 + \gamma(i-1))sin(\phi) \tag{2}$$

The expressions for the six Hall elements can be combined in a linear matrix equation of the form shown in Equation 3. Here, A is a 6-by-2 matrix containing the known sensor angular location information (Equation 4), b is a 6-by-1 column vector containing the Hall element voltages (Equation 5), and x is a 2-by-1 column vector containing the unknown first harmonic amplitude and rotor angle information (Equation 6).

$$Ax = b \tag{3}$$

$$A = \begin{bmatrix} cos(\gamma_0) & sin(\gamma_0) \\ cos(\gamma_0+\gamma) & sin(\gamma_0+\gamma) \\ cos(\gamma_0+2\gamma) & sin(\gamma_0+2\gamma) \\ cos(\gamma_0+3\gamma) & sin(\gamma_0+3\gamma) \\ cos(\gamma_0+4\gamma) & sin(\gamma_0+4\gamma) \\ cos(\gamma_0+5\gamma) & sin(\gamma_0+5\gamma) \end{bmatrix} \tag{4}$$

$$b = \begin{bmatrix} V_1 & V_2 & V_3 & V_4 & V_5 & V_6 \end{bmatrix}^T \quad (5)$$

$$x = \begin{bmatrix} KBcos(\phi) & KBsin(\phi) \end{bmatrix}^T \quad (6)$$

To estimate the rotor angle, we first compute the least squares solution to Equation 3 with:

$$\hat{x} = \begin{bmatrix} \hat{KBcos}(\phi) & \hat{KBsin}(\phi) \end{bmatrix}^T = (A^T A)^{-1} A^T b \quad (7)$$

From $\hat{x}$, we compute the rotor angle with the inverse tangent:

$$\hat{\phi} = atan2(\hat{KBsin}(\phi), \hat{KBcos}(\phi)) \quad (8)$$

The matrix $(A^T A)^{-1} A^T$, which is equivalent to the pseudo-inverse of A, can be pre-computed once offline. This reduces the computing resources required on the FPGA.

Axial Position Sensing Algorithm

We also process the Hall element signals to yield an estimate of the rotor axial position. While this is not required for feedback control, as the rotor is passively stable along the Z-axis, it is useful to characterize the dynamics along this degree of freedom. Defining the i^{th} Hall element signal on the top ring PCB as V_{iT}, the i^{th} Hall element signal on the bottom ring PCB as V_{iB}, and a constant scale factor C, we can estimate the Z-position with:

$$\hat{Z} = C \sum_{i=1}^{6} |V_{iT}| - C \sum_{i=1}^{6} |V_{iB}| \quad (9)$$

Optical Sensor Operating Principle

We use four reflective optical sensors (QRE1113 from ON Semiconductor) to produce rotor radial position estimates. This sensor configuration has been used by several others in the Precision Motion Control Lab (PMCL) at MIT for radial position feedback in magnetic suspension systems [5, 7, 8]. Each sensor package contains a infrared (IR) light emitting diode (LED) and a phototrasistor. The phototransistor collector-emitter current varies in response to the amount of IR light reflected back from the LED. We apply white electrical tape is to the rotor outer diameter to improve the surface reflectivity.

Optical Sensor Interface Electronics

A schematic of the interface electronics for a single optical sensor is shown in Figure 5. The 200 Ω resistor, R_D is placed in series with the LED to limit the forward current to 20 mA. The 10$k\Omega$ potentiometer and resistor are placed in series with the phototransistor such that a voltage V_{OUT} proportional to the phototransistor current is generated at the high side of the resistor. An ADC (NI9205 from National Instruments) is used to measure this voltage. The 10$k\Omega$ potentiometer is adjusted such that the peak output voltage is 10V, thus taking advantage of the full range of the ADC.

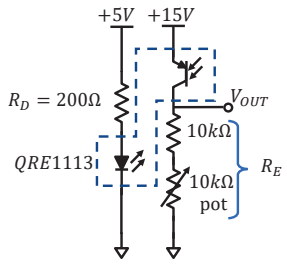

FIGURE 5. Optical sensor interface schematic

Radial Position Sensing Algorithm

The output of an individual optical sensor varies nonlinearly with the distance between the sensor and rotor. However, we can calculate a linear estimate of the rotor radial position by using the sensors in differential pairs. The sensors are arranged along the X and Y stator axes in diamterically opposed pairs. The signals from each diametrically opposed pair are subtracted from eachother to yield X-position and Y-position estimates.

EXPERIMENTAL RESULTS

In this section, we present experimental results from the calibration and characterization of the sensing system. To calibrate the sensor system, we install the rotor on a rotation stage (RP005 from Thorlabs) which is installed on an XYZ stage (562-XYZ from Newport). We install the stator upside-down on a platform above the rotor such that the rotor sits within the stator bore. This set-up is shown in Figure 6. The XYZ stage is equipped with micrometers with 10 micron graduations, and the rotation stage has 2 degree graduations. The optical sensors and Hall element ring PCB signals are sampled by three ADC modules (NI9205 from National Instruments) installed in a

real-time controller chassis (cRIO-9057 from National Instruments) equipped with an FPGA. All processing is performed on the FPGA.

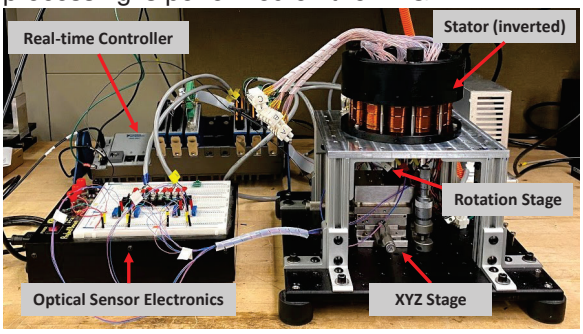

FIGURE 6. Sensor calibration set-up

Angular Position Calibration

To calibrate the Hall element ring boards, the rotor is centered within the stator bore and the rotation stage is indexed in 10 degree increments. Angle estimates from the top and bottom Hall element ring PCBs, processed using the algorithms described above, are recorded at each increment. The results from this calibration sequence are shown in Figure 7.

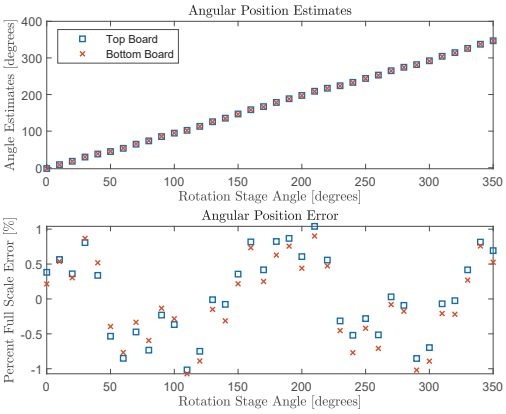

FIGURE 7. Angular position calibration data

As shown in the top plot, the resulting angular estimates from the top and bottom boards are in good agreement. In the bottom plot, we calculate the percent full scale error by taking the difference between each estimate and a linear least squares fit to the average of the top and bottom board estimates, then dividing by the full scale of 360 degrees. We use a linear least squares (LLS) fit to the average of the top and bottom board estimates as the truth measurement to remove the misalignment between the rotor axis of magnetization and the rotation stage 0 degree marking, which in this case is about 3 degrees. We see a 2x harmonic component in the error which we suspect arises from the 2x harmonic salient iron features in the rotor. The maximum observed error is -1.7%.

To measure the angular position resolution, we sample 50,000 data points from the Hall element board signals with the ADC modules at 20 kHz. The signals are processed to produce an angular position estimate on the FPGA running at a 20kHz loop rate. The angular estimates are then sampled on the real-time processor at 5kHz and noise statistics calculations are performed. From this dataset, we calculate that our system achieves an angular position resolution of 0.018 degrees at a 20kHz bandwidth.

Radial Position Calibration

To calibrate the radial position sensitivity, we first adjust the potentiometer in series with each phototransistor such that the maximum output voltage observed is 10V. Then, we center the rotor along one axis, index it in 0.1mm increments along the perpedincular axis, and record the differential voltage at each position.

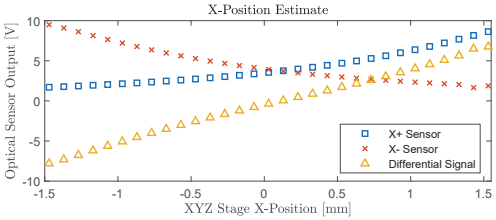

FIGURE 8. X-position calibration data

A plot of the data set from X-motion calibration is shown in Figure 8. The sensitivity is calculated as the slope of a LLS fit to the points within a +/- 0.5mm range. The X-axis sensitivity was determined to be 4.23 V/mm and the Y-axis sensitivity was determined to be 4.43 V/mm. The difference in sensitivities can be attributed to slightly different spacing between the pairs of sensors along the X and Y axes.

The radial position resolution was measured using the same method as described for the angular position resolution, except that the sensor signals are sampled and processed at 31.25 kHz on the ADC and FPGA. We calculate that both the X-position and Y-position resolution are 0.17 $\mu\mathrm{m}$ at a 31.25 kHz bandwidth, which is sufficient for closed-loop levitation control for our blood pumping application.

Axial Position Calibration

We measure the rotor axial position (Z-motion) sensitivity by indexing the XYZ stage Z-axis in 0.1mm increments and recording the Z-position estimate as calculated from the Hall element signals using Equation 9. We performed this calibration sequence for multiple rotor angular positions. The resulting data is shown in Figure 9.

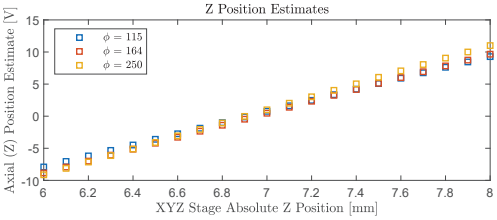

FIGURE 9. Axial position calibration data

The Z-position sensitivity at each radial position is calculated as the slope of a least squares linear fit. We calculate sensitivities of 9.27 V/mm, 8.63 V/mm, and 10.11 V/mm for the 164 degree, 115 degree, and 250 degree radial positions. We suspect that the angular dependence of the sensitivity arises from the orientation of the rotor axis of magnetization with respect to the angular sensors. At 164 degrees the rotor axis of magnetization is centered on a stator tooth that does not have Hall elements above or below it. At 115 degrees the axis of magentizaton is between two teeth. At 250 degrees the axis of magnetization is centered on a tooth that does have Hall elements above and below it. In the future, we plan to further study the Z-motion sensitivity dependence on rotor angle such that we can reliably determine the Z-position.

CONCLUSIONS AND FUTURE WORK

In this paper, we presented the design, construction, and testing of a novel position sensing system for use in bearingless motors. This sensing system achieves 0.018 degree angular position resolution at a 20 kHz bandwidth and 0.17 $\mu\mathrm{m}$ radial position resolution at 31.25 kHz bandwidth. While thus far only tested with one specific permanent magnet rotor, this sensing system could be utilized in other surface permanent magnet or interior permanent magnet rotor configurations. Particularly, the angular sensing system is useful for rotors which produce higher airgap fluxes than can be sensed with off the shelf Hall sensors. Future work will focus on levitation and rotation of the new rotor, further characterization of the Z-motion, and processing of the Hall element signals to yield radial position estimates.

ACKNOWLEDGEMENT

We thank the Charles Stark Draper Laboratory, Inc. for funding the first author's graduate studies through the Draper Fellow Program.

REFERENCES

[1] Chiba A, Fukao T, Ichikawa O, Oshima M, Takemoto M, Dorrell DG. Magnetic bearings and bearingless drives. Amsterdam London: Elsevier/Newnes; 2005. 381 p.

[2] Schweitzer G, Maslen EH, editors. Magnetic bearings: theory, design, and application to rotating machinery. Dordrecht; New York: Springer; 2009. 535 p.

[3] Noh M, Trumper DL. Homopolar Bearingless Slice Motor with Flux-biasing Halbach Arrays. IEEE Transactions on Industrial Electronics. 2019;1–1.

[4] Noh M, Gruber W, Speakman J, Gartner MJ, Trumper DL. Homopolar Bearingless Slice Motors Driving Reluctance Rotors. In: Proceedings of the 16th International Symposium on Magnetic Bearings. Beijing, China; 2018.

[5] Noh M. Homopolar Bearingless Slice Motors with Magnet-free Rotors for Extracorporeal Life Support [Doctoral Thesis]. [Cambridge, MA, USA]: Massachusetts Institute of Technology; 2018.

[6] HG-176A GaAs Hall Element Datasheet. AKM Semiconductor.

[7] Zhou L. Magnetically Levitated Hysteresis Motor Driven Linear Stage for In-Vacuum Transportation Tasks.

[8] T. T. Hamer, J. Chabot, and D. L. Trumper, "Sensing and commutation of a spherical permanent magnetic dipole actuator," in Proceedings of the 34th Annual Meeting of the American Society for Precision Engineering, Pittsburgh, PA, USA. American Society for Precision Engineering, 2019.

AUTO-TUNING OF PRECISION SERVO CONTROLLERS SUFFERING FROM LARGE MASS RATIO INDUCED VIBRATIONS

Alper Dumanli[1], Jeff Lowe[2], Sinan Badrawy[2], Burak Sencer[1]
[1]School of Mechanical, Industrial and Manufacturing Engineering
Oregon State University
Corvallis, Oregon, USA
[2]Moore Nanotechnology Systems
Swanzey, New Hampshire, USA

INTRODUCTION

This paper presents an automated controller tuning strategy for precision servo positioning systems suffering from large inertial load ratio induced vibrations. Typical industrial ulta-precision feed drive systems are designed based on direct driven linear motor systems and controlled by PID controllers tuned based on nominal inertia. When large loads are attached on the feed drive, robustness of the PID controller may not suffice, and feedback control loop may suffer from unwanted vibrations [1]. This vibratory behavior originates mainly from shrinking stability margins of the servo control system and potentially causes instability [2]. Moreover, varying load inertia hinders accuracy of feedforward (FF) compensators, which are typically designed based on the inverse of the nominal system [3]. This paper considers dynamics of ultra-precision feed drive systems and presents an auto-tuning algorithm to stabilize feedback controllers considering attached load inertia. The auto-tuning strategy is based on on-machine measured frequency response function (FRF). The PID controller is augmented with a simple feedback filter whose parameters are automatically tuned to attain desired phase and gain margins. In addition, a trajectory pre-filter is designed and iteratively tuned to further improve the tracking performance. Effectiveness of the proposed strategy is verified on an actual ultra-precision machine tool (Nanotech 650FG-v[2] freeform generator) shown in Fig. 1.a.

Overall block diagram of the proposed strategy is given in Fig. 2. Proposed control system consists of three key components: (1) a PID controller *K(z)* to meet cross-over frequency and phase margin requirements, (2) a low pass filter *H(z)* to suppress higher order dynamics and ensure stability, and finally (3) a Trajectory Pre-Filter *P(z)* to modify the reference trajectory in order to increase tracking bandwidth.

MODELING OF PRECISION SERVO MECHANISMS WITH LARGE LOAD INERTIA

In typical industrial applications, servo-drives are modeled as a rigid body with a moment of inertia of J_D [kgm^2]. With a load/workpiece attached, the overall model of the system becomes:

$$\frac{\theta}{\tau} = G = \frac{1}{(J_D + J_L)s^2 + bs} \qquad (1)$$

where G is the rigid body transfer function (TF). θ and τ are the measured angular displacement and motor torque input. J_L is the inertia of the load (workpiece), and b is the equivalent viscous friction coefficient.

a) Experimental setup with large load inertia

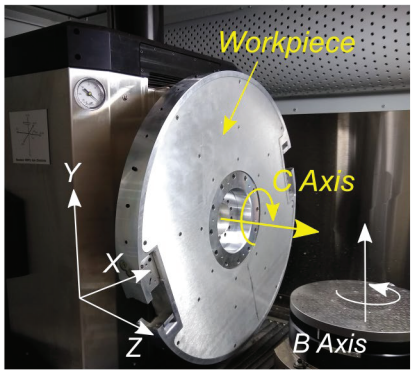

b) Open Loop FRFs of C-Axis

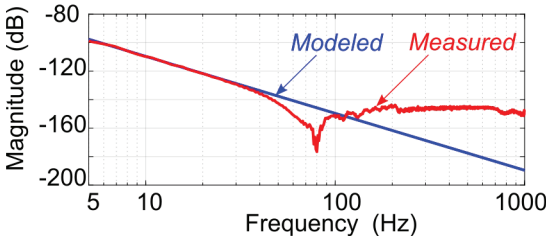

FIGURE 1: Experimental setup (a) and FRFs(b).

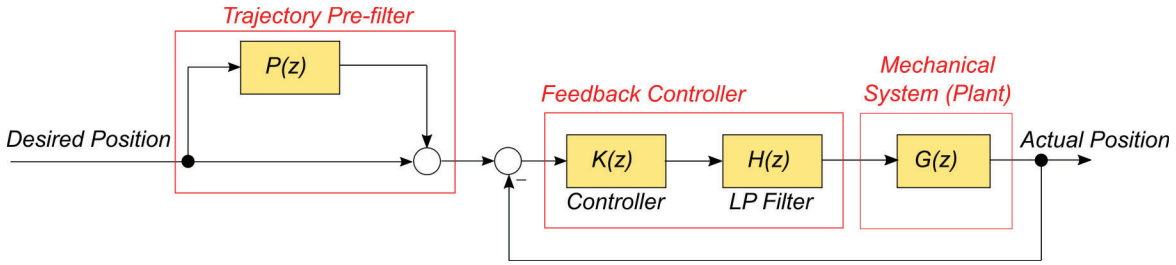

FIGURE 2: Block diagram of the proposed control scheme.

This model captures the system dynamics for typical applications. However, if the load inertia J_L increases excessively, i.e. $J_L>>J_D$, higher order dynamics invalidates the modeling accuracy of G, and measured and modeled FRFs differ significantly (see Fig. 1.b). Thus, closed loop controllers designed by using G may not provide robust stability. In order to retain stability of the servo-loop, a PID controller is designed based on G, and the controller is augmented by a low-pass filter designed considering the measured FRF of the servo positioning system G_{FRF}. Design of these two components are described in the following.

CLOSED LOOP CONTROLLER DESIGN

The closed loop PID controller is designed in order to ensure that the loop transmission TF, $L=KG$, has the desired cross-over frequency and phase margin, where K is defined in discrete frequency-domain as:

$$K(z)=K_P\left(1+K_I\left(\frac{T_s z}{z-1}\right)\right)+K_D\left(\frac{z-1}{T_s z}\right) \quad (2)$$

with K_P, K_I and K_P being the PID controller gains, and z is the discrete frequency (z-Transform) variable. The acceptable value of the cross-over frequency is determined by examining the discrepancy between modeled (G) and measured (G_{FRF}) FRFs. First, the smallest frequency at which G_{FRF} deviates from G more than +3[dB] is determined. This frequency is denoted as ω_{lim}. Next, to ensure robust avoidance of modeling mismatches, cross-over frequency (ω_c) is selected as: $\omega_c=0.2\omega_{lim}$. On the experimental setup shown in Fig 1.a, this corresponds to $\omega_{lim}=115$[Hz] and $\omega_c=23$[Hz]. This guarantees that the controller only acts on the portion of the system with significantly high modeling accuracy. The phase-margin is selected as 65[deg], which is typical for industrial applications. The PID gains are determined to meet the cross-over frequency and phase margin requirements as described in the following.

First, the integral gain is calculated as $K_I=0.1\omega_c$ to ensure that the phase lag introduced by numerical integration does not influence the loop phase in the vicinity of ω_c. Next, K_P and K_D gains are determined to meet the cross-over frequency (ω_c) and phase margin (PM) requirements given by:

$$\begin{aligned} L_{\text{Re}} &= K_{\text{Re}}G_{\text{Re}} - K_{\text{Im}}G_{\text{Im}} = \cos\left(180^o + PM\right) \\ L_{\text{Im}} &= K_{\text{Re}}G_{\text{Im}} + K_{\text{Im}}G_{\text{Re}} = \sin\left(180^o + PM\right) \end{aligned} \quad (3)$$

where $L_{Re}=Re\{L(e^{j\omega cTs})\}$ and $L_{Im}=Im\{L(e^{j\omega cTs})\}$. Notice that Eq. (3) poses a simple linear system of equations, and K_P and K_D can be obtained as:

$$\begin{bmatrix} K_P \\ K_D \end{bmatrix} = \Omega^{-1}\begin{bmatrix} \cos\left(180^o + PM\right) \\ \sin\left(180^o + PM\right) \end{bmatrix}, \text{ where:}$$

$$\Omega = \begin{bmatrix} K_{\text{Re}}^{(1)}G_{\text{Re}} - K_{\text{Im}}^{(1)}G_{\text{Im}} & K_{\text{Re}}^{(2)}G_{\text{Re}} - K_{\text{Im}}^{(2)}G_{\text{Im}} \\ K_{\text{Re}}^{(1)}G_{\text{Im}} + K_{\text{Im}}^{(1)}G_{\text{Re}} & K_{\text{Re}}^{(2)}G_{\text{Im}} + K_{\text{Im}}^{(2)}G_{\text{Re}} \end{bmatrix} \quad (4)$$

$$K^{(1)} = 1 + \frac{\omega_c}{10}\left(\frac{T_s e^{j\omega_c T_s}}{e^{j\omega_c T_s} - 1}\right),\ K^{(2)} = \frac{e^{j\omega_c T_s} - 1}{T_s e^{j\omega_c T_s}}$$

where T_s is the sampling period. The designed PID controller is implemented utilizing the Delta-Tau servo-driver on board with the ultra-precision machine tool. Modeled (L) and measured (L_{FRF}) loop transmission FRFs are shown in Fig. 3.

As seen, desired crossover frequency and phase margin are achieved. At high frequencies, i.e. $\omega>\omega_{lim}$, L_{FRF} deviates from L significantly, and instability occurs at ~1.2[kHz] with a -8.64[dB] gain margin. In order to mitigate this model-measurement deviation and retain closed loop stability, an optimal low pass filter design strategy is proposed in the following section.

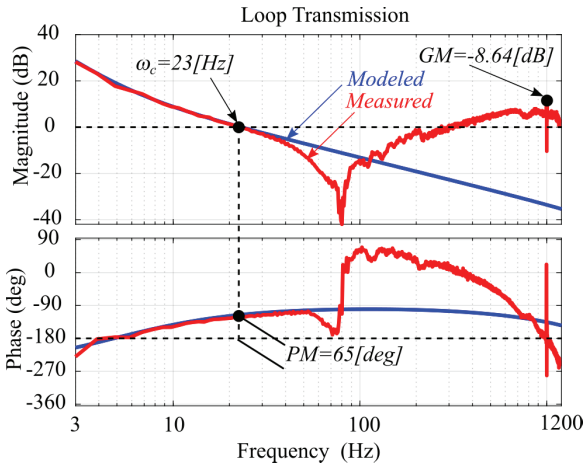

FIGURE 3: Loop transmission FRFs with PID controller. Note that PID controller by itself cannot prevent high frequency instability.

OPTIMAL LOW PASS FILTER DESIGN

This section describes the low pass filter design procedure in order to eliminate closed loop stability issues caused by modelling inaccuracies. Low pass filter H (see Fig. 2) is designed in continuous Laplace (s) domain as:

$$H(s)=\frac{1}{c_2 s^2+c_1 s+c_0} \tag{5}$$

where $c_0 \ldots c_2$ are the design parameters. The low pass filter is then converted into discrete (z) domain for implementation. The purpose of H is to ensure that loop transmission magnitude do not increase after the desired crossover frequency is achieved. This objective is expressed as an optimization problem as:

$$\begin{aligned} &\min_{H(s)} \left| L\left(e^{j\omega T_s}\right)H(j\omega)-L\left(e^{j\omega T_s}\right)\right| \\ &\text{subject to:} \\ &\left|L_{FRF}\left(e^{j\omega T_s}\right)H(j\omega)\right| \le \alpha, \text{ for } \omega \ge \omega_{\text{lim}} \\ &H(s) \text{ is stable.} \end{aligned} \tag{6}$$

where α is the maximum allowable loop transmission magnitude for frequencies higher than ω_{lim}. Notice that the magnitude operator, i.e. $|.|$, is used in both the objective function and the inequality constraints of Eq. (6). This nonlinearity causes the optimization problem to be nonconvex, and thus the solution suffers from local minima, numerical inefficiency and inaccuracy. To circumvent this, Eq. (6) is modified to pose a convex optimization problem. This is done by substituting the magnitude operator by the two norm, $\|.\|_2$, acting on the real and imaginary parts of the TFs. Additionally, H is substituted by H^{-1} to ensure that the decision variables $c_0 \ldots c_2$ appear linearly in the optimization objective and constraints. The modified optimization problem is written as:

$$\min_{H^{-1}(s)} \left(\begin{aligned} &\left\| \text{Re}\left\{ L\left(e^{j\omega T_s}\right)H^{-1}(j\omega)-L\left(e^{j\omega T_s}\right)\right\}\right\|_2^2 \cdots \\ &+\left\| \text{Im}\left\{ L\left(e^{j\omega T_s}\right)H^{-1}(j\omega)-L\left(e^{j\omega T_s}\right)\right\}\right\|_2^2 \end{aligned} \right)$$

subject to:

$$\left.\begin{aligned} &\text{Re}\left\{H^{-1}(j\omega)\right\} \le -\left|\text{Re}\left\{L_{FRF}\left(e^{j\omega T_s}\right)\right\}\right|\frac{1}{\alpha} \\ &\text{Im}\left\{H^{-1}(j\omega)\right\} \ge \left|\text{Im}\left\{L_{FRF}\left(e^{j\omega T_s}\right)\right\}\right|\frac{1}{\alpha} \end{aligned}\right\} \text{for } \omega \ge \omega_{\text{lim}} \tag{7}$$

$H(s)$ is stable.

Notice that Eq. (7) minimizes real and imaginary parts of *(L(z)H(s)-L(z))/H(s)*, instead of the magnitude of *L(z)H(s)-L(z)* as in Eq. (6). Since H has small magnitude at high frequencies (imposed by inequality constraints), division by H does not change the objective function significantly. Conversion of the inequality constraints from Eq. (6) to Eq. (7) follows from:

$$\begin{aligned} &\left|L_{FRF}\left(e^{j\omega T_s}\right)H(j\omega)\right| \le \alpha \rightarrow \left|H^{-1}(j\omega)\right| \ge \frac{1}{\alpha}\left|L_{FRF}\left(e^{j\omega T_s}\right)\right| \\ &\text{Re}\left\{H^{-1}(j\omega)\right\}^2+\text{Im}\left\{H^{-1}(j\omega)\right\}^2 \ge \cdots \\ &\qquad \frac{1}{\alpha^2}\left(\text{Re}\left\{L(j\omega)\right\}^2+\text{Im}\left\{L(j\omega)\right\}^2\right) \end{aligned} \tag{8}$$

$$\begin{aligned} &\text{Re}\left\{H^{-1}(j\omega)\right\}^2 \ge \frac{1}{\alpha^2}\text{Re}\left\{L(j\omega)\right\}^2 \\ &\text{Im}\left\{H^{-1}(j\omega)\right\}^2 \ge \frac{1}{\alpha^2}\text{Im}\left\{L(j\omega)\right\}^2 \end{aligned} \tag{9}$$

Eq. (8) is derived from the inequality constraint of Eq. (6). Taking the square root of both sides of Eq. (9) gives the inequality constraints in Eq. (7). Notice that in Eq. (7), real part of the inequality constraints is imposed to be negative, and the imaginary part is imposed to be positive. This enforces *H(s)* to have a phase angle within the interval [-90°, -180°] for $\omega > \omega_{lim}$, and guarantees that the filter suppresses the magnitude of its input in this frequency region. Eq. (7) poses a linear least squares minimization problem with linear inequality constraints. It is convex and can be solved to global optimality efficiently. Finally, it is put in matrix-vector form to obtain the parameters of H, $(c_0 \ldots c_2)$, as shown in Eq. (10) at the top of the next page. Notice that the inequality constraint $\mathbf{x} \ge 0$ in Eq. (10) ensures stability of *H(s)*, and the equality constraint $c_0=1$ imposes unity gain at "zero"

frequency, and therefore the low pass filter does not introduce additional gain to the loop.

$$\min_{c_0,c_1,c_2} \|\mathbf{Ax}-\mathbf{b}\|_2^2$$

subject to: $\mathbf{Cx} \le \mathbf{d}$, $\mathbf{x} \ge 0$ and $c_0 = 1$

where: $\mathbf{x} = [c_2 \quad c_1 \quad c_0]$

$$\mathbf{A} = \begin{bmatrix} -\omega_1^2 \mathrm{Re}\left\{L\left(e^{j\omega_1 T_s}\right)\right\} & -\omega_1 \mathrm{Im}\left\{L\left(e^{j\omega_1 T_s}\right)\right\} & 1 \\ \vdots & \vdots & \vdots \\ -\omega_N^2 \mathrm{Re}\left\{L\left(e^{j\omega_N T_s}\right)\right\} & -\omega_N \mathrm{Im}\left\{L\left(e^{j\omega_N T_s}\right)\right\} & 1 \\ -\omega_1^2 \mathrm{Im}\left\{L\left(e^{j\omega_1 T_s}\right)\right\} & \omega_1 \mathrm{Re}\left\{L\left(e^{j\omega_1 T_s}\right)\right\} & 0 \\ \vdots & \vdots & \vdots \\ -\omega_N^2 \mathrm{Im}\left\{L\left(e^{j\omega_N T_s}\right)\right\} & \omega_N \mathrm{Re}\left\{L\left(e^{j\omega_N T_s}\right)\right\} & 0 \end{bmatrix}$$

$$\mathbf{b} = \begin{bmatrix} \mathrm{Re}\left\{L\left(e^{j\omega_1 T_s}\right)\right\} \\ \vdots \\ \mathrm{Re}\left\{L\left(e^{j\omega_N T_s}\right)\right\} \\ \mathrm{Im}\left\{L\left(e^{j\omega_1 T_s}\right)\right\} \\ \vdots \\ \mathrm{Im}\left\{L\left(e^{j\omega_N T_s}\right)\right\} \end{bmatrix}, \quad \mathbf{C} = \begin{bmatrix} -\omega_{\mathrm{lim}}^2 & 0 & 1 \\ \vdots & \vdots & \vdots \\ -\omega_N^2 & 0 & 1 \\ 0 & -\omega_{\mathrm{lim}} & 0 \\ \vdots & \vdots & \vdots \\ 0 & -\omega_N & 0 \end{bmatrix}$$

$$\mathbf{d} = \begin{bmatrix} -\left|\mathrm{Re}\left\{L_{FRF}\left(e^{j\omega_{\mathrm{lim}} T_s}\right)\right\}\right| \\ \vdots \\ -\left|\mathrm{Re}\left\{L_{FRF}\left(e^{j\omega_N T_s}\right)\right\}\right| \\ -\left|\mathrm{Im}\left\{L_{FRF}\left(e^{j\omega_{\mathrm{lim}} T_s}\right)\right\}\right| \\ \vdots \\ -\left|\mathrm{Im}\left\{L_{FRF}\left(e^{j\omega_N T_s}\right)\right\}\right| \end{bmatrix} \tag{10}$$

Once *H(s)* is designed in continuous domain, it is discretized (*H(z)*) and implemented in the control loop as shown in Fig 2. Comparison of loop transmission performance with and without *H* is given by Fig 4. As seen, the low pass filter *H* suppresses higher order dynamics at high frequencies and retains closed loop stability without altering frequency domain design specifications (crossover frequency and phase margin).

TRAJECTORY PRE-FILTER DESIGN

The closed loop controller designed in the previous section provides a command tracking bandwidth (ω_{BW}) close to the crossover frequency $\omega_{BW} \cong \omega_c$. In high-speed industrial applications, reference trajectories contain rapidly varying acceleration/deceleration segments, and thus they may have frequency components in their spectra that are beyond ω_c. As a result; inertial forces, low pass filter dynamics and high frequency modeling errors may cause large tracking errors due to insufficient tracking bandwidth. To increase the tracking bandwidth, a trajectory pre-filter *P* is proposed as shown in Fig. 2.

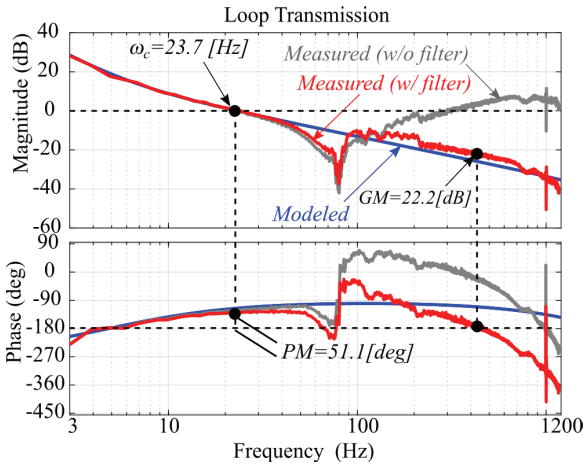

FIGURE 4: Comparison of loop transmission FRFs with and without the optimally designed low pass filter.

The filter structure is selected in order to achieve near-perfect tracking as:

$$\frac{\theta}{\theta_R} = (1+P)\frac{KHG}{1+KHG} \cong 1 \rightarrow P = \frac{1}{KHG} \tag{11}$$

where θ_R is the reference angular displacement command. *K* and *H* are known by design. However, mismatch between *G* and G_{FRF} may lead to a sub-optimal implementation of *P* as given in Eq. (11). To ensure that *P* is designed optimally, its parameters are identified iteratively through on-site measured data as described in the following.

First, *P* is optimized by assuming *K* and *G* dominate the closed loop dynamics. This assumption is valid for lower frequencies, since *H* starts influencing loop transmission TF for frequencies higher than ω_{lim}. By assuming *H*=1, tracking error ($e=\theta_R-\theta$) dynamics in continuous frequency and time domains are written as:

$$\frac{e}{\theta_R} = \frac{Js^3 + bs^2}{Js^3 + (K_D + b)s^2 + K_P s + K_P K_I}$$
$$\ddot{e} = \ddot{\theta}_R - \frac{1}{J}\left((K_D + b)\dot{e} + K_P e + K_P K_I \int_0^t e d\tau - b\dot{\theta}_R\right) \tag{12}$$

where $J=J_D+J_L$. Notice that Eq. (12) contains critical parameters that are useful for identifying *P* such as *J* and *b*. Controller parameters K_P, K_D

and K_I are already known by design. However, J and b may not be accurately identified through frequency domain-based (FRF) identification. To circumvent this, J and b values are estimated through a simple back-and-forth trajectory tracking experiment. The position data recorded by this experiment is utilized to form the following optimization problem derived by Eq. (12):

$$\min_{J_e, b_e} \left\| \Phi\Lambda - \Psi \right\|_2^2, \text{ subject to: } J_e \geq 0 \text{ and } b_e \geq 0$$

$$\Phi = \begin{bmatrix} \ddot{e}(0) & \dot{e}(0) & e_i(0) & -\dot{\theta}_R(0) \\ \ddot{e}(T_s) & \dot{e}(T_s) & e_i(T_s) & -\dot{\theta}_R(T_s) \\ \vdots & \vdots & \vdots & \vdots \\ \ddot{e}(MT_s) & \dot{e}(MT_s) & e_i(MT_s) & -\dot{\theta}_R(MT_s) \end{bmatrix} \quad (13)$$

$$\Psi = \begin{bmatrix} \ddot{\theta}_R(0) - e(0) \\ \ddot{\theta}_R(T_s) - e(T_s) \\ \vdots \\ \ddot{\theta}_R(MT_s) - e(MT_s) \end{bmatrix}, \Lambda = \begin{bmatrix} K_D + b \\ K_P \\ K_P K_I \\ b \end{bmatrix}$$

where M is the number of samples for the trajectory following experiment, and e_i is the numerically integrated error signal. J_e and b_e are the estimated inertia and viscous friction coefficient. Notice that Eq. (13) is a convex optimization problem, and thus its globally optimal solution can be obtained efficiently. Once Eq. (13) is solved, the "rough" pre-filter P_1 (without including H) is implemented in discrete domain as:

$$P_1 = \frac{J_e\left(\frac{z-1}{T_s z}\right)^2 + b_e\left(\frac{z-1}{T_s z}\right)}{K_P\left(1 + K_I\left(\frac{T_s z}{z-1}\right)\right) + K_D\left(\frac{z-1}{T_s z}\right)} \quad (14)$$

By implementing this trajectory pre-filter, tracking performance can be increased greatly. Fig. 5 shows an example trajectory following experiment with a total displacement of 2 [deg]. Maximum velocity and acceleration of the reference trajectory are selected as 5 [deg/sec] and 50 [deg/sec^2]. As seen, tracking error peaks reach up to 4 [mdeg] without the pre-filter. With the pre-filtered trajectory, maximum tracking error peak is reduced to ~570 [μdeg].

Although the error reduction shown in Fig. 5 is significant, there are still some residual error peaks when P_1 is used. These errors are attributed to the phase lag introduced by the low pass filter and power electronics circuitry as well as high frequency dynamics of the mechanical system. In order to eliminate these remaining errors, the pre-filter structure is augmented by second order finite impulse response filter (FIR) dynamics as:

$$P = P_1\left(n_0 + n_1 z^{-1} + n_2 z^{-2}\right) \quad (15)$$

The new set of parameters for P ($n_0 \ldots n_2$) are identified through machine-in-the-loop optimization, by minimizing the trajectory tracking errors as:

$$\min_{n_0, n_1, n_2}\left(J_{\text{Cost}} = \frac{1}{2}\|\mathbf{e}\|_2^2\right) \quad (16)$$

where $\mathbf{e}$ is the vector of tracking error data obtained by the tracking experiment shown in Fig. 5.

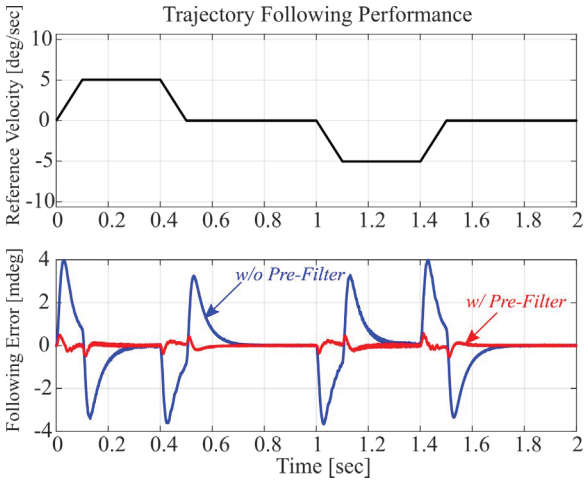

FIGURE 5: Trajectory tracking performance with and without "rough" pre-filter.

Eq. (16) is a convex optimization problem, and thus utilizing the gradient ∇J_{Cost} and Hessian $\nabla^2 J_{Cost}$ of its cost function enables us to rapidly and safely guide the parameter search to global optimum. Note that, $\mathbf{e}$ is already available from the trajectory following experiment, and its gradient $\nabla\mathbf{e}$ is obtained as:

$$e = \left(\frac{1 - PG_{FRF}KH}{1 + G_{FRF}KH}\right)\theta_R$$

$$\nabla e = \begin{bmatrix} \frac{\partial e}{\partial n_0} \\ \frac{\partial e}{\partial n_1} \\ \frac{\partial e}{\partial n_2} \end{bmatrix} = -\nabla P \underbrace{\left(\frac{G_{FRF}KH}{1 + G_{FRF}KH}\right)\theta_R}_{\theta} \quad (17)$$

$$\nabla P = -\begin{bmatrix} 1 \\ z^{-1} \\ z^{-2} \end{bmatrix} P_1$$

Notice that the actual angular displacement (θ) appears in Eq. (17), which is obtained experimentally. Therefore, the error gradient $\nabla\mathbf{e}$ can be calculated in a complete data-driven fashion, without requiring any system model. The calculated gradient is then used to guide the machine-in-the-loop parameter search using Newton's second order iteration scheme as:

$$\begin{bmatrix} n_0 \\ n_1 \\ n_2 \end{bmatrix}^{k+1} = \begin{bmatrix} n_0 \\ n_1 \\ n_2 \end{bmatrix}^{k} - \eta\left(\nabla\mathbf{e}^T\nabla\mathbf{e}\right)^{-1}\left(\mathbf{e}^T\nabla\mathbf{e}\right) \quad (18)$$

where η is the learning rate. It can be shown that $0 \le \eta \le 1$ guarantees monotonic convergence to global optimum [4], and η is selected as 1.

Fig. 6.a shows trajectory tracking performance of the system with the augmented pre-filter *P*. Trapezoidal velocity reference given by Fig. 5 is used in machine-in-the-loop experiments as well. Fig. 6.b shows convergence performance of the machine-in-the-loop optimization scheme. Iteration "0" corresponds to the case without any pre-filter. Iteration "1" shows the performance with the initial design of the pre-filter P_1 given by Eq. (14). Iterations "2" and "3" show two consecutive iterations where the pre-filter *P* given by Eq. (15) is used, and filter parameters are updated based on Eq. (18) at each iteration. As seen, convergence is achieved in only two iterations and the maximum tracking error peak is reduced to ~215 [μdeg].

CONCLUSIONS

In this paper, we presented an auto-tuning strategy for ultra-precision servo-drives suffering from largely varying load mass inertia. First, a PID controller is tuned based on the experimentally obtained frequency response function of the servo-drive. A safe cross-over frequency for PID tuning is automatically determined based on the modeling accuracy of the open loop system. Stability issues caused by higher order modes induced by large load inertia is prevented by an optimally designed low pass filter. Trajectory tracking bandwidth is expanded by a trajectory pre-filter. Pre-filter parameters are obtained through data-driven machine-in-the-loop iterations.

REFERENCES

[1] Varanasi K. K. 2002. On the Design of a Precision Machine for Closed-Loop Performance. PhD Thesis. MIT.

[2] Erkorkmaz K, Gordon D. J. 2013. Accurate control of ball screw drives using pole-placement vibration damping and a novel trajectory prefilter. Precision Engineering 37(2):308-322.

[3] Dumanli A, Sencer B. 2018. Optimal high-bandwidth control of ball-screw drives with acceleration and jerk feedback. Precision Engineering 54:254-268.

[4] Dumanli A, Sencer B. 2019. Pre-compensation of servo tracking errors through data-based reference trajectory modification. CIRP Annals 68(1):397-400.

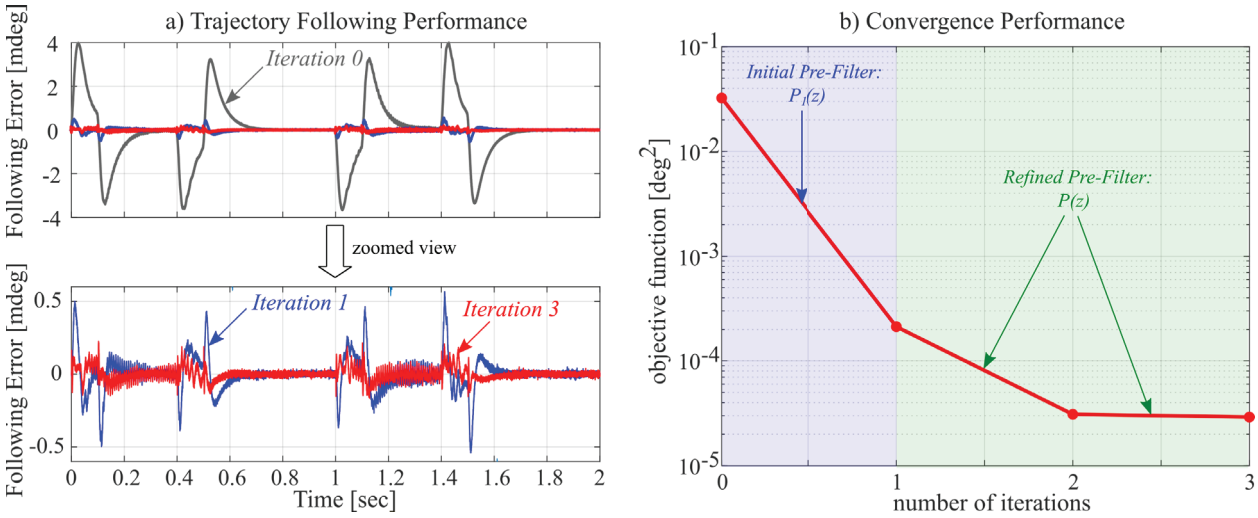

FIGURE 6: Trajectory tracking and convergence performance of the proposed iteratively optimized trajectory pre-filter scheme.

COMBINED FEEDFORWARD TRACKING CONTROL AND FEEDRATE OPTIMIZATION WITH APPLICATION TO A PRECISION XY STAGE

Heejin Kim[1] and Chinedum E. Okwudire[1]
[1]Department of Mechanical Engineering
University of Michigan
Ann Arbor, MI

OVERVIEW

Servo error pre-compensation (i.e., feedforward tracking control) and feedrate optimization are often performed independently to improve the accuracy and speed of precision motion stages. However, this independent approach leads to unnecessary trade-offs between productivity and quality in manufacturing or metrology where such stages are commonly used. This paper proposes a novel linear programming approach for combined servo error pre-compensation and feedrate optimization, subject to contour error (tolerance) and kinematic constraints. The incorporation of servo error pre-compensation into feedrate optimization allows for faster motions without violating tolerance constraints. Experiments on a precision XY stage are used to demonstrate 53% reduction in cycle time without compromising part quality using the proposed compared to the independent approach.

INTRODUCTION

Precision manufacturing and metrology machines typically use motion stages powered by computer numerical control (CNC) to generate motion commands. Two critical requirements for manufacturing and metrology are productivity and quality, which often involve a trade-off between speed and accuracy of precision motion stages [1]. This trade-off is typically handled, in practice, by maximizing speed so long as a pre-specified accuracy (tolerance) level is not violated.

Major source of inaccuracy in precision motion stages are servo errors caused by commanded motion, i.e., motion-induced servo errors. They are very important in determining the trade-off between speed and accuracy because servo controllers always have limited bandwidth. One way of reducing motion-induced servo errors is through pre-compensation (i.e., feedforward compensation). Knowledge of the machine's servo dynamics is used to modify the motion commands offline or online in the CNC interpolator to reduce servo errors [2-7]. However, available SEP approaches focus on reducing or minimizing servo error without trying to maximize feedrate subject to tolerance constraints.

On the other hand, there are numerous works on feedrate optimization (FO) subject to tolerance constraints. Traditionally, tolerance constraints are introduced implicitly into FO by imposing velocity, acceleration and jerk limits [8,9]. Some works have explicitly added tracking or contouring accuracy constraints to FO [10,11]. In practice, SEP and FO are combined by first performing FO and then applying the optimized results to SEP for error minimization, as shown by the one-way arrow between FO and SEP in Fig. 1(a). However, this independent (or sequential) approach could lead to sub optimality, as FO does not benefit from the reduction of error provided by SEP in maximizing feedrate. A better approach is to incorporate information from SEP into FO, as shown by the two-way arrow between FO and SEP in Fig. 1(b). To our best knowledge, such a combined technique for FO and SEP has not been explored in the open literature.

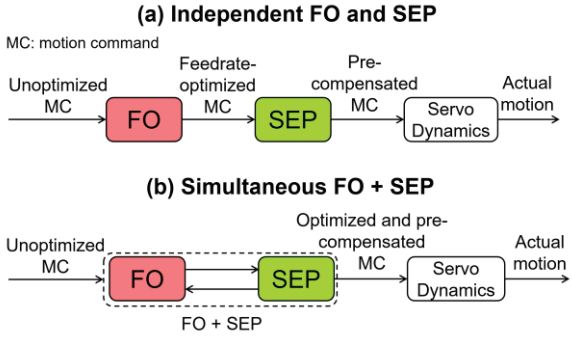

FIGURE 1. Comparison of (a). independent FO and SEP – standard practice – and (b). proposed concept of simultaneous FO and SEP (i.e., FO+SEP).

This paper proposes a novel linear programming (LP) approach for simultaneous FO and SEP. The systematic incorporation of SEP into FO expands the feasible region for FO, thus allowing for faster motions without violating tolerance constraints. In addition, the use of LP makes the proposed method computationally efficient and mathematically elegant.

TIME-BASED LP FOR FEEDRATE OPTIMIZATION

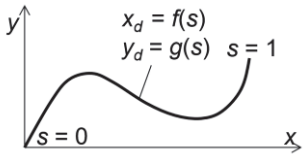

FIGURE 2. Parametric planar curve as function of path variable, s

Fig. 2 illustrates an arbitrary, curved path in the *x*-*y* plane with path parameter $s \in [0,1]$. Note that *s* is a function of time *t* (i.e., $s = s(t)$). Let $x_d = f(s)$ and $y_d = g(s)$ denote a pair of parametric equations in *s*, representing the *x* and *y* components of desired position, respectively.

The time-based LP approach for FO, adapted from the model predictive contour control framework proposed by Lam et al. [12], is formulated as follows. Assuming that $s(t)$ is discretized with fixed sampling interval, T_s, and expressed as a vector $\boldsymbol{s} = \{s(0), s(1), \ldots, s(N-1)\}^T$, FO can be written as:

$$\min_{\boldsymbol{s}} \sum_{k=0}^{N-1} -s(k) \tag{1}$$

$$\text{s.t. } s(k-1) \le s(k) \le 1 \;\; \forall\, k = 1, 2, \ldots, N-1$$

The idea of Eq. (1) is that to minimize total time, the sum of $s(k)$ over *N* time steps must be maximized – i.e., the path from $s(0) = 0$ to $s(N-1) = 1$ should be traversed as fast as possible, while satisfying the monotonicity and endpoint constraints on $\boldsymbol{s}$ in Eq. (1). In addition, it should satisfy kinematic constraints F_{max}, A_{max}, and J_{max} on feedrate, axis acceleration and axis jerk, respectively:

$$L\frac{D[\boldsymbol{s}]}{T_s} \le \boldsymbol{F}_{max} \tag{2}$$

$$\left|\frac{D^2[\hat{\boldsymbol{x}}_d]}{{T_s}^2}\right|, \left|\frac{D^2[\hat{\boldsymbol{y}}_d]}{{T_s}^2}\right| \le \boldsymbol{A}_{max}$$

$$\left|\frac{D^3[\hat{\boldsymbol{x}}_d]}{{T_s}^3}\right|, \left|\frac{D^3[\hat{\boldsymbol{y}}_d]}{{T_s}^3}\right| \le \boldsymbol{J}_{max}$$

Here, *D* denotes finite difference operator and *L* the total path length, while $\boldsymbol{F}_{max}$, $\boldsymbol{A}_{max}$, and $\boldsymbol{J}_{max}$ are vectorized representations of the corresponding kinematic limits. The terms $x_d = f(s)$ and $y_d = g(s)$ are generally nonlinear in *s*. Thus, at each time step *k*, they are linearized with linearization points $s^e(k)$ estimated from an initial unoptimized trajectory as:

$$\hat{x}_d(k) = \left.\frac{\partial f(s)}{\partial s}\right|_{s=s^e(k)} \cdot (s(k) - s^e(k)) + f(s^e(k)) \tag{3}$$

$\hat{y}_d(k)$ is obtained by linearizing $g(s)$ in the same manner; $\hat{\boldsymbol{x}}_d$ and $\hat{\boldsymbol{y}}_d$ are vectorized versions of $\hat{x}_d(k)$ and $\hat{y}_d(k)$, respectively, similar to $\boldsymbol{s}$. This notation is maintained hereinafter.

FRAMEWORK OF SIMULTANEOUS FO AND SEP USING TIME-BASED LP

Fig. 3 shows a block diagram of the proposed simultaneous SEP and FO. The idea is to impose contour error (tolerance) constraints on FO taking SEP into account. However, because the proposed approach uses LP, contour errors must be estimated using linear dynamics. To do this, linearized desired *x*-axis position, $\hat{x}_d$, is used to generate modified position command $\hat{x}_{dm}$ using a SEP process represented by C_x. A linear model, $\hat{G}_x$, of the actual servo dynamics, G_x, is used to estimate the *x*-axis position as $\hat{x}$ and tracking error as $\hat{e}_x = \hat{x}_d - \hat{x}$. A similar process is followed to obtain $\hat{e}_y = \hat{y}_d - \hat{y}$, using C_y and $\hat{G}_y$. The contour error $\hat{\varepsilon}_c$ can be estimated from the axis tracking errors using a linear approximation [13] as:

$$\begin{aligned}\hat{\varepsilon}_c(k) = &-\sin(\theta(k))\underbrace{(1 - \hat{G}_x C_x)\hat{x}_d(k)}_{=\hat{e}_x(k)} \\ &+\cos(\theta(k))\underbrace{(1 - \hat{G}_y C_y)\hat{y}_d(k)}_{=\hat{e}_y(k)}\end{aligned} \tag{4}$$

where $\theta(k)$ is the angle of incline of the curve $(\hat{x}_d, \hat{y}_d)$ at time step *k*. The linear approximation of contour error $\hat{\varepsilon}_c$ (including the effects of SEP using C_x and C_y) is imposed as an additional constraint on the time-based LP formulation of as:

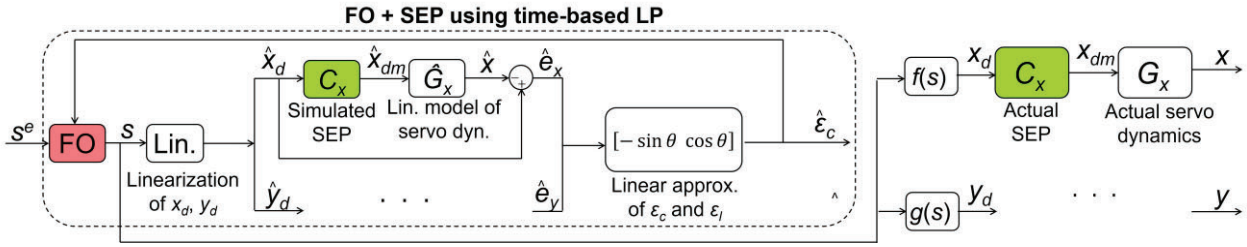

FIGURE 3. Block diagram of the proposed FO+SEP using time-based LP (Note: y-component of SEP and servo dynamics omitted for simplicity)

$$|\hat{\varepsilon}_c| = -\sin(\boldsymbol{\theta})\left(\mathbf{I} - \hat{\boldsymbol{G}}_x\boldsymbol{C}_x\right)\hat{\boldsymbol{x}}_d + \cos(\boldsymbol{\theta})\left(\mathbf{I} - \hat{\boldsymbol{G}}_y\boldsymbol{C}_y\right)\hat{\boldsymbol{y}}_d \le \boldsymbol{E}_{max} \quad (5)$$

where $\boldsymbol{E}_{max}$ is the vectorized form of the maximum allowable contour error E_{max}; $\boldsymbol{C}_x$, $\hat{\boldsymbol{G}}_x$, $\boldsymbol{C}_y$ and $\hat{\boldsymbol{G}}_y$ are matrix (lifted) versions of the corresponding system dynamics; and $\mathbf{I}$ is the identity matrix. The implication is that a model of SEP is incorporated into FO, yielding FO+SEP. The optimized x_d and y_d from FO+SEP are then applied to the actual servo dynamics, G_x and G_y, pre-compensated using C_x and C_y, respectively. Note that if $C_x = C_y = 1$, then it means that no SEP is considered.

REALIZATION OF SEP IN FO+SEP USING FILTERED B SPLINES

It is worth pointing out that C_x and C_y can be any SEP (feedforward tracking control) method, e.g., [2-7], as long as it is linear. However, among the available SEP methods, the filtered B spline (FBS) approach [6,7] stands out because of its effectiveness and versatility in handling any type of linear system dynamics [7]. Therefore, it is selected for SEP in this paper.

The FBS approach parameterizes modified command $\boldsymbol{x}_{dm}$ using B splines as $\boldsymbol{x}_{dm} = \boldsymbol{N}_x\boldsymbol{p}_x$, where $\boldsymbol{N}_x$ is the basis function matrix and $\boldsymbol{p}_x$ is a vector of n control points. Accordingly, the system output is expressed as $\boldsymbol{x} \approx \hat{\boldsymbol{G}}_x\boldsymbol{x}_{dm} = \tilde{\boldsymbol{N}}_x\boldsymbol{p}_x$, where $\tilde{\boldsymbol{N}}_x = \hat{\boldsymbol{G}}_x\boldsymbol{N}_x$ (i.e., $\boldsymbol{N}_x$ filtered by $\hat{\boldsymbol{G}}_x$). Hence, the tracking error is modeled as $\boldsymbol{e}_x = \boldsymbol{x}_d - \boldsymbol{x} \approx \boldsymbol{x}_d - \tilde{\boldsymbol{N}}_x\boldsymbol{p}_x$. The least-squares solution for minimizing $\boldsymbol{e}_x$ yields optimal coefficients $\boldsymbol{p}_x^* = \tilde{\boldsymbol{N}}_x^{\dagger}\boldsymbol{x}_d$, where $\tilde{\boldsymbol{N}}_x^{\dagger}$ represents the pseudo-inverse of $\tilde{\boldsymbol{N}}_x$. Thus, the optimal modified command can be expressed as $\boldsymbol{x}_{dm} = \boldsymbol{N}_x\boldsymbol{p}_x^* = \boldsymbol{N}_x\tilde{\boldsymbol{N}}_x^{\dagger}\boldsymbol{x}_d$, which leads to $\boldsymbol{C}_x = \boldsymbol{N}_x\tilde{\boldsymbol{N}}_x^{\dagger}$. The same process is applied to $\boldsymbol{y}_d$. Accordingly, $\boldsymbol{C}_x = \boldsymbol{N}_x\tilde{\boldsymbol{N}}_x^{\dagger}$ and $\boldsymbol{C}_y = \boldsymbol{N}_y\tilde{\boldsymbol{N}}_y^{\dagger}$ are substituted into Eq. (5) to realize FO+SEP using the FBS approach.

EXPERIMENTAL RESULTS

For experimental validation, a biaxial linear-motor-driven motion stage (Aerotech ALS 25010) is used, as shown in Fig. 4. The optimization algorithms are implemented on dSPACE DS1103 real-time control board running at 1 kHz sampling rate, connected to Soloist CP controller/drive. Each axis is controlled by pre-tuned closed-loop P-PI controller and velocity feedforward. The XY stage is equipped with optical linear encoders with resolution 0.1 μm to provide position feedback on each axis.

To execute FO and FO+SEP with error constraints, the x and y axis vibration dynamics of the stage must be measured in the form of frequency response functions (FRFs) and modeled, via curve fitting, as $\hat{G}_x$ and $\hat{G}_y$. Fig. 5 shows the measured and modeled FRFs of x- and y-axes of the stage. The input of each FRF are position commands constructed by swept sine acceleration to the servomotor, and output is the position measured by encoders on each axis.

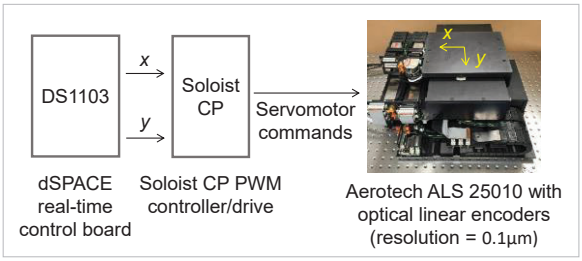

FIGURE 4. Experimental Set up

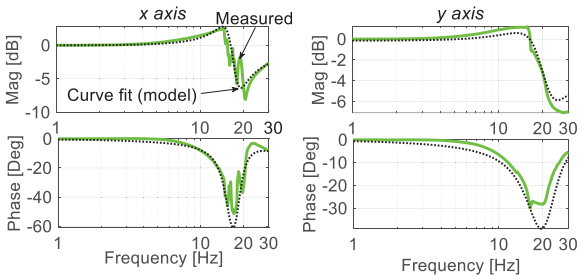

FIGURE 5. Measured and curve fitted FRFs of x and y axes of XY stage

BENCHMARKING TO DETERMINE ERROR TOLERANCE

Unoptimized position commands generated using the industry-standard trapezoidal acceleration profile (TAP) [5] are used for benchmarking to determine suitable error tolerance limit to traverse a circle of 5 mm radius.

Fig. 6(a) shows the TAP feedrate profile generated using conservative kinematic limits of F_{max} = 40 mm/s, A_{max} = 0.4 m/s^2, J_{max} = 4 m/s^3; the acceleration and jerk profiles are omitted for the sake of brevity. Fig. 6(b) shows simulated and measured contour error profiles of the TAP position commands applied to the XY stage. The simulations are performed using the curve fit linear dynamic model of Fig. 5. The conservative TAP yields maximum contour errors of 13 µm and 50 µm in simulations and experiments, respectively. The reason for the discrepancy between the simulated and measured contour errors is due to dynamics like friction and geometric errors not included in the linear model, as well as the approximations involved in the linear model. The contouring accuracy of the conservative TAP is considered to be satisfactory. Therefore, E_{max} = 13 µm is selected as the tolerance limit for optimization (using the linear model), to help keep contour errors close to the target 50 µm in experiments.

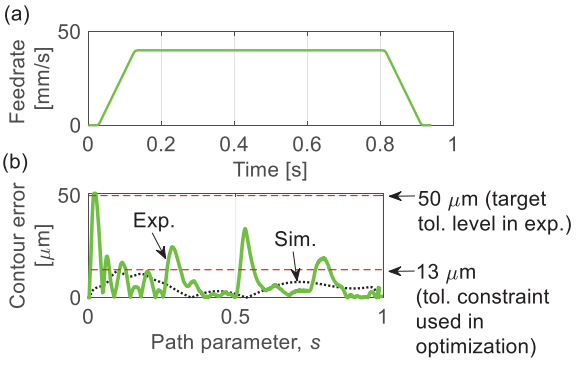

FIGURE 6. Commanded feedrate and (b) simulated and measured contour error profiles of TAP motion commands

OPRIMIZATION RESULTS USING FO AND FO+SEP

We compare FO and the proposed FO+SEP with a goal to achieve similar accuracy as Conservative TAP in Fig. 6(b) with the shortest cycle time. To do this, aggressive kinematic limits are imposed on both FO and FO+SEP as: F_{max} = 80 mm/s, A_{max} = 8 m/s^2, J_{max} = 8,000 m/s^3. In addition, a tolerance limit of E_{max} = 13 µm using Eq. (5). For FO, $\boldsymbol{C}_x$ = $\boldsymbol{C}_y$ = **I** (i.e., tolerance constraints are imposed without SEP) is imposed. However, for FO+SEP, $\boldsymbol{C}_x$ and $\boldsymbol{C}_y$ are generated via the FBS approach [7] using a 5th degree B-spline with uniform knot vector and n = 30 control points. Both cases are initialized using unoptimized TAP trajectories.

Fig. 7 shows the commanded feedrate, acceleration, and jerk profiles of FO and FO+SEP. Fig. 8 shows the simulated and measured contour error profiles. Both FO and FO+SEP enforce the tolerance in simulations, leading to the system staying close to the target error level in experiments. However, FO has to slow down because it hits the contour error limit while FO+SEP is able to stay very close to the maximum speed throughout the motion. As a

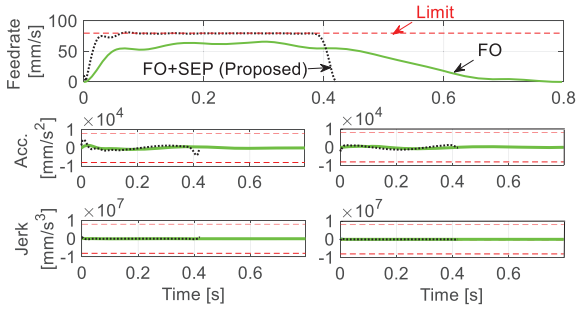

FIGURE 7. Feedrate, acceleration and jerk profiles of trajectories generated by FO and FO+SEP using aggressive kinematic limits and Emax = 13 µm

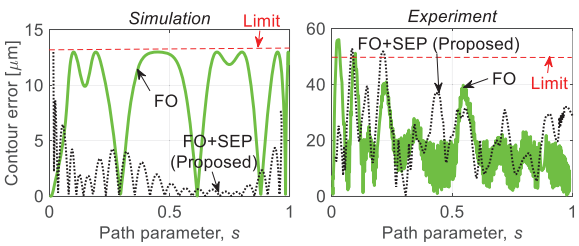

FIGURE 8. Simulated and measured contour error profiles of FO and FO+SEP

result, FO+SEP completes the motion in 0.42 s, which is 47% faster than FO at 0.79 s. Notice that the cycle time of FO is only 0.15 s (i.e., 16.0%) faster than the conservative TAP because the error constraint does not allow FO much room to travel faster than the conservative TAP. Implementing SEP after FO (i.e., independent approach) would not lower the cycle time of FO; it would only reduce the contour error, which has little or no practical value if the desired tolerance has already been met. The computation time for FO+SEP is 0.04 s; FO's is higher at 0.12 s because it is operating very close to the error constraint.

CONCLUSIONS

This paper has introduced a new concept of simultaneous FO and SEP (i.e., FO+SEP), and proposed a novel approach for realizing FO+SEP using time-based LP. Compared to the standard practice of performing FO and SEP independently, FO+SEP relaxes the error tolerance constraints imposed on FO, allowing shorter cycle times without violating tolerance constraints. Experiments carried out on a XY stage yielded up to 47% reduction in cycle time using FO+SEP compared to FO, subject to the same tolerance and kinematic constraints.

Future work will explore limited-preview (windowing) [7,9] into FO+SEP to enable its application to longer trajectories. Incorporation of actuator (e.g., torque) limits into FO+SEP will also be explored to help expand its performance benefits over FO.

ACKNOWLEDGEMENT

This work is funded by the National Science Foundation's award #1825133: Boosting the Speed and Accuracy of Vibration-Prone Manufacturing Machines at Low Cost through Software.

REFERENCES

[1] Altintas Y, Verl A, Brecher C, Uriarte L, Prtischow G. Machine Tool Feed Drives. CIRP Annals 2011; 60(2): 779-796.

[2] Tomizuka M. Zero Phase Error Tracking Algorithm for Digital Control. 1987.

[3] Altintas Y, Khoshdarregi MR. Contour Error Control of CNC Machine Tools with Vibration Avoidance. CIRP Annals 2012; 61(1): 335-338.

[4] Yang S, Ghasemi AH, Lu X, Okwudire CE. Pre-Compensation of Servo Contour Error Using a Model Predictive Control Framework. International Journal of Machine Tools and Manufacture 2015; 98: 50-60.

[5] Gordon DJ, Erkorkmaz K. Accurate Control of Ball Screw Drives Using Pole-Placement Vibration Damping and a Novel Trajectory Prefilter. Precision Engineering 2013; 37(2): 308-322.

[6] Okwudire C, Ramani K, Duan M. A Trajectory Optimization Method for Improved Tracking of Motion Commands Using CNC Machines That Experience Unwanted Vibration. CIRP Annals 2016; 65(1): 373-376.

[7] Duan M, Yoon D, Okwudire CE. A Limited-Preview Filtered B-Spline Approach to Tracking Control-With Application to Vibration-Induced Error Compensation of a 3D Printer. Mechatronics 2018; 56: 287-296.

[8] Fan W, Gao XS, Lee CH, Zhang K, Zhang Q. Time-Optimal Interpolation for Five-Axis CNC Machining along Parametric Tool Path Based on Linear Programming. The International Journal of Advanced Manufacturing Technology 2013; 69(5-8): 1373-1388.

[9] Erkorkmaz K, Chen QGC, Zhao MY, Beudaert X, Gao XS. Linear Programming and Windowing Based Feedrate Optimization for Spline Toolpaths. CIRP Annals 2017; 66(1): 393-396.

[10] Guo J, Zhang Q, Gao XS, Li H. Time Optimal Feedrate Generation with Confined Tracking Error based on Linear Programming. Journal of Systems Science and Complexity 2015; 28(1): 80-95.

[11] Zhang Y, Ye P, Zhao M, Zhang H. Dynamic Feedrate Optimization for Parametric Toolpath with Data-Based Tracking Error Prediction. Mechanical Systems and Signal Processing 2019; 120: 221-233.

[12] Lam D, Manzie C, Good MC. Model Predictive Contouring Control for Biaxial Systems. IEEE Transactions on Control Systems Technology 2012; 21(2): 552-559.

[13] Koren Y, Lo CC. Variable-Gain Cross-Coupling Controller for Contouring. CIRP Annals 1991; 40(1): 371-374.

FEEDFORWARD TUNING AND USING ITERATIVE LEARNING CONTROL FOR AUTOMATED PARAMETER FITTING

Leon Jabben[1], Fons Luijten[1]
[1]MI-Partners, Veldhoven, The Netherlands

INTRODUCTION

For accurate stage positioning after a point-to-point movement, it is paramount that the required force is generated as much as possible through feedforward control ([1]). In many applications the reference trajectory and its higher derivatives can be calculated a priori, which can be used to calculate the feedforward profile. The problem definition can then be split in two:

1. How to design the reference trajectory and feedforward profile
2. How to minimize the tracking error in practice.

Setpoint generation

For a point-to-point motion (e.g. in pick and place applications), the following phases can be distinguished: an acceleration phase, a phase with constant velocity (often) and a deceleration phase. Together these phases may be referred to as the move phase. After the move phase the system may require a certain settling time to allow damping of internal dynamics (settle phase) followed by a phase where the accuracy required by the process is achieved (process phase).

In [2] the setpoint is calculated by setting a desired step size and bounds on the maxima of the higher derivatives, while minimizing the move time. The bounds on the derivative's maxima are limited by the properties of the system.

To maximize the throughput, both the move time and the settling time should be minimized. To realize the latter, excitation of the dynamics should be prevented. One approach is to adapt the trajectory by filtering. In [3], two filtering techniques are suggested: 1) time domain filtering with a FIR or IIR filter, or 2) input shaping which involves convolution of the generated reference trajectories and feedforward profile with a series of impulses (see also [4]).

In this paper a method is proposed to reduce the excitation of the resonances by minimizing the energy of the setpoint at those frequencies.

Minimizing the tracking error in practice

Once the trajectory and feedforward profiles have been generated, the resulting error in practice is usually bigger than expected. This is due to either inaccuracies in model parameters like actuator gain, damping and time delay or because of un-modelled effects like friction and cogging.

An extremely effective technique to deal with these model inaccuracies is Iterative Learning Control (ILC). Key feature of ILC is that a feedforward profile is improved iteratively in a number of trial experiments performed on the physical system, see [5]. As long as the error has repeating components it can be improved upon, leading to a vastly improved performance.

The main drawback of ILC, and the reason why it is hardly applied in industry, is that whenever the setpoint is changed, the learned feedforward signal is rendered useless. To address this drawback, the ILC scheme can be adapted by using basis-functions, which will be discussed in the second part of this paper.

SPECTRAL TRAJECTORY ANALYSIS

Second order trajectory

Consider a second order trajectory, with an acceleration profile as given in FIGURE 1. The Fourier transform of the acceleration phase only (i.e. a block pulse with amplitude A and width T_a, starting at t=0), is given by:

$$a(f) = A\,T_a\,\mathrm{sinc}(\pi f T_a)\,e^{-i2\pi f \frac{1}{2}T_a} \qquad (1)$$

where the part left of the exponential function is the Fourier transform of the block pulse centered around t=0 (unnormalized sinc function), and the exponential function itself is the Fourier transform of a time delay of $\frac{1}{2}T_a$ to make the pulse causal. Notice that the sinc function is zero for each frequency $f = k/T_a$, with k an integer ≥1.

The Fourier transform of the deceleration pulse is the same sinc function, but delayed with an additional T_v+T_a, with T_v the duration of the constant velocity phase. The Fourier transform of the total trajectory then becomes:

$$a(f) = AT_a\mathrm{sinc}(\pi f T_a)e^{-i2\pi f \frac{1}{2}T_a}\left(1 - e^{-i2\pi f(T_a+T_v)}\right) \qquad (2)$$

The first part is exactly as (1), while the second part adds additional frequencies with zero amplitude (short: zero frequencies), namely

whenever $f = k/(T_a + T_v)$, with *k* an integer ≥0. A physical interpretation is that, for a system with an undamped resonance, the response to the deceleration pulse is equal, but opposite in sign to the acceleration pulse, so these cancel each other whenever the period of the resonance frequency equals $(T_a + T_v)/k$.

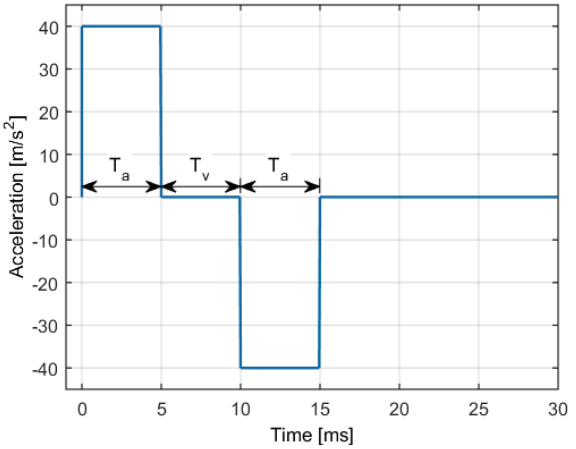

FIGURE 1. Example of an acceleration profile of a second order setpoint.

Third Order Trajectory

A third order acceleration profile can be generated from a second order profile, by convolution with a pulse having a duration equal to the desired jerk time and an area equal to one. FIGURE 2 shows the resulting acceleration profile. Convolution in time domain corresponds to multiplication in frequency domain, hence (2) becomes:

$$a(f) = A(T_a + T_j)\mathrm{sinc}\left(\pi f(T_a + T_j)\right) \mathrm{sinc}(\pi f T_j) e^{-i2\pi f \frac{1}{2}(T_a+T_j)} \left(1 - e^{-i2\pi f(T_a+T_v+2T_j)}\right) \quad (3)$$

with the additional sinc function representing the jerk pulse, and other changes can be derived by inspecting FIGURE 2.

The Fourier amplitudes are given in FIGURE 3, which clearly shows the multiplication effect, with the additional zero frequencies due to the jerk at multiples of 625 Hz (jerk time: 1.6 ms).

Higher Order Trajectories

Higher order trajectories can be constructed in the same manner as the third order; through subsequent convolution with pulses of desired periods. To calculate the zero frequencies, one should take into account the durations of these pulses, as is shown in TABLE 1. Here the fourth and fifth derivative are denoted snap and crackle, and are referred to by their first letter.

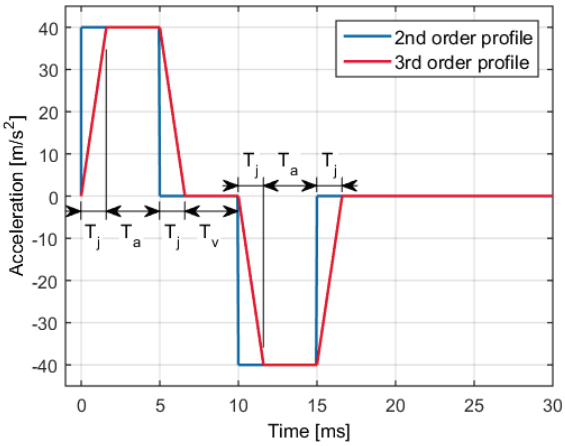

FIGURE 2. Example of acceleration profiles of second and third order setpoints.

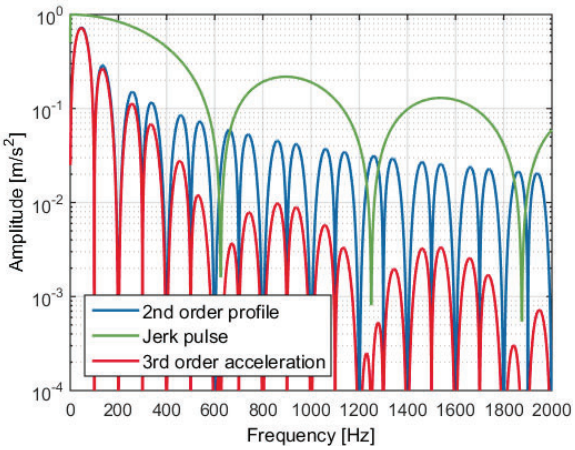

FIGURE 3. Fourier amplitudes of second and third order acceleration profiles

A SPECTRAL SETPOINT GENERATOR

With the found durations of the phases, one can construct the trajectory following the approach of [1]: first the highest derivative trajectory is constructed (a block shaped profile, like the acceleration profile for a second order trajectory) and then the lower derivative signals are found through subsequent integration steps. The first integration step is done through a cumulative sum of the trajectory, which does not introduce a Zero-Order-Hold (ZOH) type of delay because of the block shape. Subsequent integration steps use trapezoidal numerical integration in order to prevent these delays in each integration step. For the final integration step (velocity to position) the cumulative sum is again used, which yields a much more accurate result (error in the order of 10^{-18}) when simulating with a discrete-time simple

TABLE 1. Overview of the calculation of the frequencies with zero energy content

Zeros at $f=k/T_X$, due to constant:		***2nd order trajectory***	***3rd order trajectory***	***4th order trajectory***	***5th order trajectory***
Velocity;	$T_X =$	T_v+T_a	$T_v+T_a+2T_j$	$T_v+T_a+2T_j+4T_s$	$T_v+T_a+2T_j+4T_s+8T_c$
Acceleration;	$T_X =$	T_a	T_a+T_j	$T_a+T_j+2T_s$	$T_a+T_j+2T_s+4T_c$
Jerk;	$T_X =$	NA	T_j	T_j+T_s	$T_j+T_s+2T_c$
Snap;	$T_X =$	NA	NA	T_s	T_s+T_c

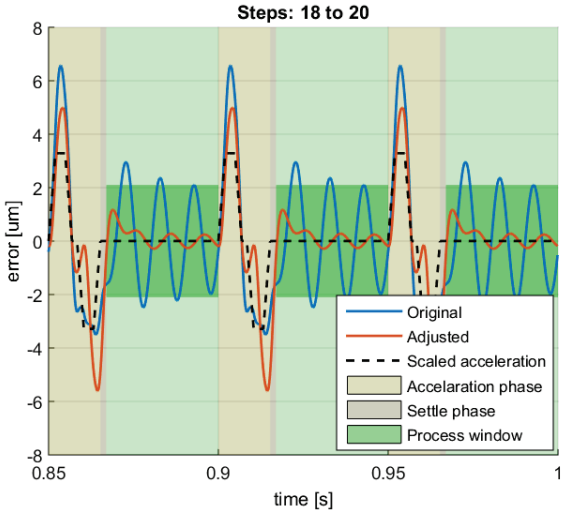

FIGURE 4: Simulation of tracking errors.

mass system. As a result, the position trajectory is half a time sample delayed w.r.t. the higher orders, and to synchronize one has to do an interpolation step.

To illustrate the effect of spectral setpoint generation, a model of a wafer positioning machine is used. The machine is capable of indexing up to 1 mm steps with a frequency of 20 Hz. In the first prototype that was built by MI-Partners, a dynamic mode caused a phase jump of about 7 degrees at 100 Hz. Because 100 Hz is a relative low harmonic of the indexing frequency, the mode had such an impact that the error requirement of 2.1 µm was not met (FIGURE 4).

The original setpoint has its first zero at about 120 Hz, but with the found insights the first zero frequency could be shifted to 100 Hz. In FIGURE 5 the original and adjusted acceleration profiles are shown and the resulting tracking error is also shown in FIGURE 4 (now within specification).

BASIS FUNCTIONS ILC

Having obtained a well-designed setpoint profile, we can use so-called Basis Functions Iterative Learning Control (BF-ILC) to minimize the tracking error on a physical system. With BF-ILC,

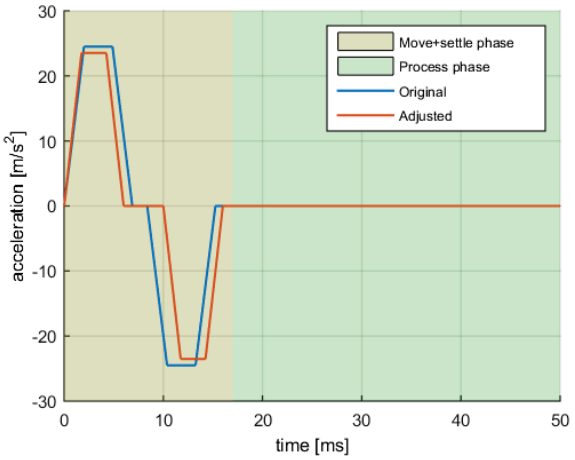

FIGURE 5. Comparing acceleration profiles.

the feedforward signal is parameterized using basis functions, refer to [6] for a detailed description. Usually the set of basis functions contains the acceleration, velocity, and position profile. The associated parameters then represent the mass (and actuator gain), damping, and stiffness of the system, respectively. Also higher order profiles (jerk and snap) can be included to better represent a stage with a mass decoupling. Friction can be compensated for (to a limited degree), by making the sign of the velocity profile a basis function. Because of the parametrization, updating feedforward signal after a change of setpoint is done with limited loss of performance. Furthermore, it can be readily implemented in industrial controllers.

EXPERIMENTAL RESULTS

To test the feasibility of BF-ILC, it was applied to a simple rotational motor with a rigidly mounted mass. Two sets of BFs were considered, the first set containing the profiles for acceleration, velocity and the sign of the velocity. The second set adds six position dependent cogging terms to the first set. These are sine and cosine functions for three spatial frequencies (related to the pole

and magnet pitch). Each cogging function is then evaluated over the trajectory, to obtain a basis function as function of time. In FIGURE 6 the first five basis functions are shown.

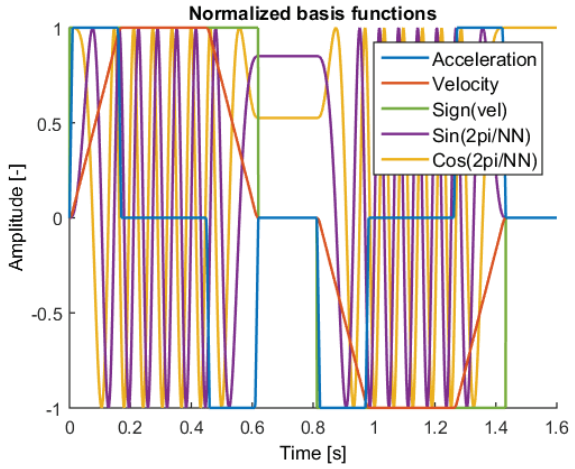

FIGURE 6. First five of total nine basis functions.

For the first iteration the already tuned inertia/gain term was used, resulting in an RMS tracking error (calculated over the whole trajectory) of 13 mrad. After six iterations a different setpoint is applied. In total four different setpoint profiles were applied, differing in position, velocity and acceleration. The generated feedforward profiles are given in FIGURE 7, (indirectly) showing the differences in the setpoints. From FIGURE 8 it can be seen that compensating for the cogging improves the performance significantly. Moreover, the degradation in performance right after a setpoint change is quite small!

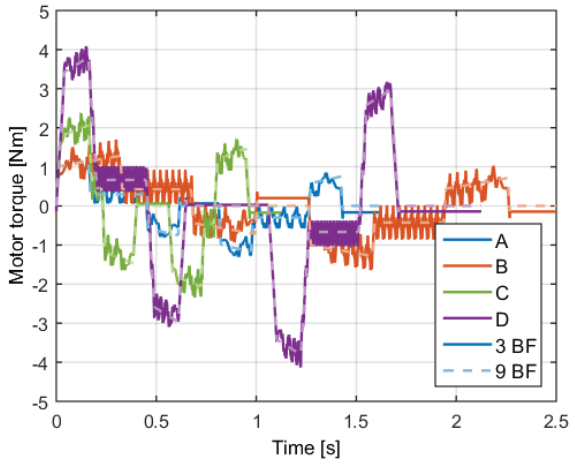

FIGURE 7. Generated feedforward profiles.

CONCLUSIONS

A method to generate setpoints that minimizes the energy at desired (zero) frequencies during synthesis is described. The method might be

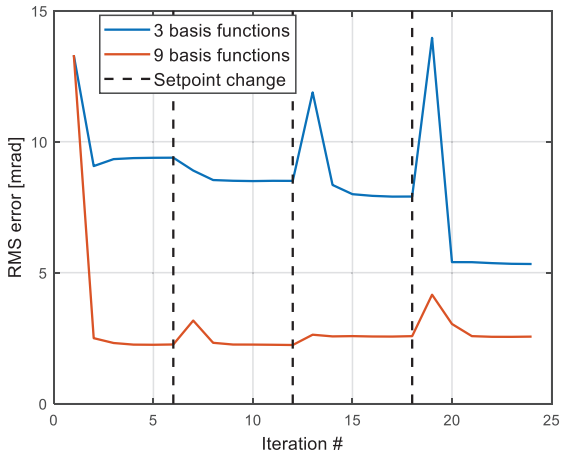

FIGURE 8. Tracking error vs iteration number.

especially beneficial if the desired zero frequency is relatively close to the inverse of the move time and the increase of the move time is to be minimized.

When applying the found setpoint in practice, the tracking error can be minimized using BF-ILC to adapt the feedforward profile. Because the feedforward profile is parameterized, updating this profile after a setpoint change can readily be done with minimal deterioration of the performance, as was shown in this paper.

REFERENCES

[1] Boerlage M, Steinbuch M, Lambrechts P, van de Wal M. Model-Based Feedforward for Motion Systems. Proc. IEEE Conf. on Control Applications. 2003; 2:1158-1163

[2] Lambrechts P, Boerlage M, Steinbuch M. Trajectory Planning and Feedforward Design for High Performance Motion Systems. Proc. American Control Conf. 2004; 5:4637-4642.

[3] Singer N, Singhose W, Seering W. Comparison of Filtering Methods for Reducing Residual Vibration. European Journal of Control. 1999; 5(2-4):208-218.

[4] Singer N, and Seering W. Preshaping Command Inputs to Reduce System Vibration. Journal of Dyn. Systems, Meas. and Control. 1990; 112(1): 76–82.

[5] Bristow D, Tharayil M, Alleyne A. A Survey of Iterative Learning Control. IEEE Control Systems Magazine. 2006; 26(3):96-114.

[6] Meulen S. van der, Tousain R, Bosgra O. Fixed Structure Feedforward Controller Design Exploiting Iterative Trials : Application to a Wafer Stage and a Desktop Printer. Journal of Dynamic Systems, Meas. and Control. 2008; 130(5): 051006

ADAPTIVE FEEDFORWARD CONTROL OF A FLEXURE BASED HEXAPOD

S.T. Spanjer[1], **W.B.J. Hakvoort**[1]
[1]**Precision engineering,**
University of Twente,
Enschede, the Netherlands

INTRODUCTION

The use of flexure hinges in manipulators offers excellent tracking and repeatability properties due to the lack of friction and backlash. Recently, a large stroke spherical hinge was developed [1]. This has been used to design a 6-Degree of Freedom (DoF) precision manipulator. The manipulator is shown in figure 1. This manipulator covers a workspace of 5.5 dm^3, has an intended repeatability of 100 nm, and allows for accelerations beyond 5g. Frameless direct drive permanent magnet motors are used to actuate the system [2]. Proper motion control is required to unleash the full potential of the manipulator in terms of accuracy and repeatability.

First, the paper considers feedback control, which is aimed at realising high repeatability. Thereafter, the paper considers feedforward control, which is aimed at at realising the high tracking performance. This is followed by the experimental results and the paper ends with conclusions and future research topics.

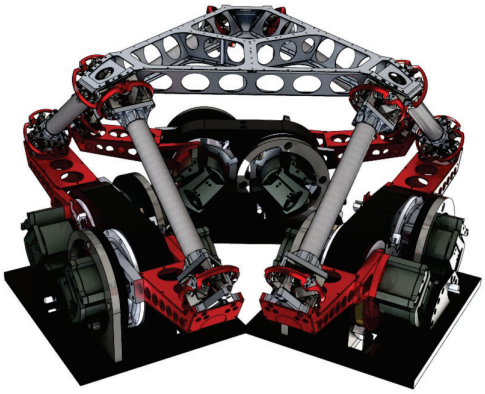

FIGURE 1. T-Flex - Large range of motion flexure-based hexapod.

FEEDBACK CONTROL

High repeatability is allowed by the absence of friction. On the other hand, the lack of self-locking friction results in a small position error by the noise on the actuator current. H_2 controller synthesis is used to minimize the effect of the input noise on the position in a mean square sense. Effectively, the controller tries to increase the control bandwidth as much as allowed by the sampling delays in the controller. Figure 2 shows the open loop transfer functions of the proposed H_2 controller. This figures shows a high phase margin. The cumulative power spectral density of the remaining position noise at standstill is shown in figure 3. The measured angle is translated to a position with the typical transfer ratio of $0.1\mathrm{m/rad}$

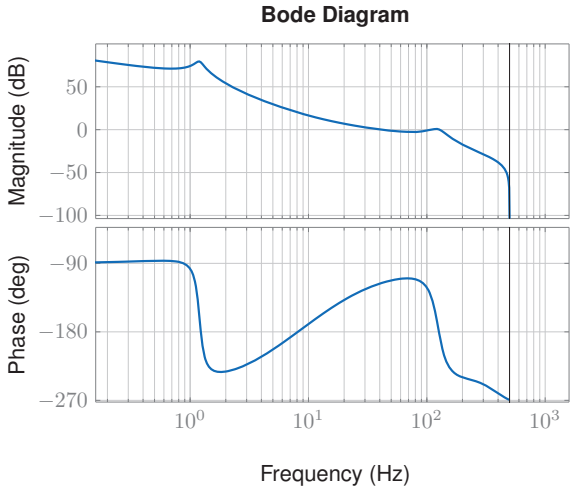

FIGURE 2. Open loop response for H_2 control.

ADAPTIVE FEEDFORWARD CONTROL

The deterministic system allows high accuracy tracking performance. High tracking performane can be realised by feedforward control if the system dynamics are accurately know. An adaptive feedforward controller is developed to be able to track even the slightest change in the system dynamic's parameters. This adaptive feedforward controller uses an estimate of the inverse dynamics of the system to exactly compute the required feedforward signal. The estimate of the inverse dynamic's parameters is determined online. The model equations are formulated for the 6-DoF setup, and reduced to the 1-DoF setup for experimental validation.

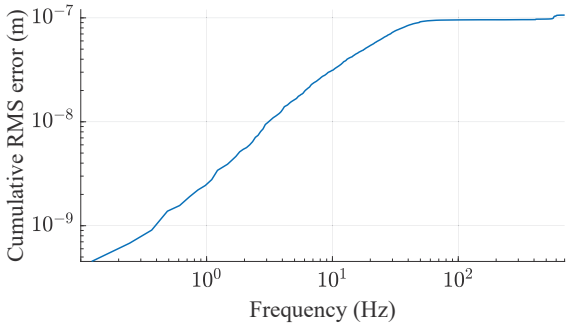

FIGURE 3. Cumulative power spectral density of the position noise with H_2 control.

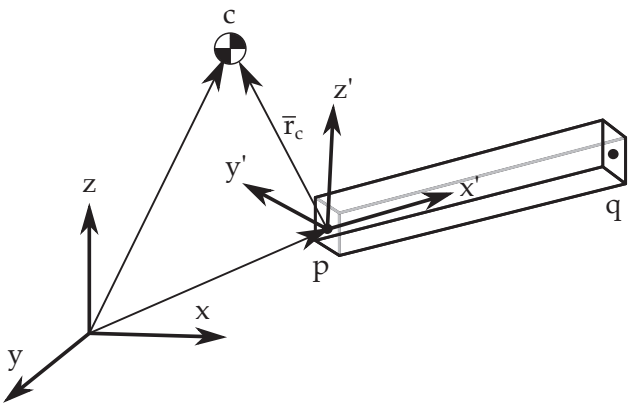

FIGURE 4. Rigid beam model with the center of gravity located in an arbitrary position. The pose of the rigid beam is specified by the position and orientation of nodes p and q. The centre of gravity c is located at $\bar{r}_c$ from the local coordinate system $\mathrm{x'y'z'}$ in node p

Inverse dynamics model

The structure of the 6-DoF manipulator suggests that the dominant natural frequencies are due to the elasticity in the joints. Therefore a model that uses rigid links and lumped elasticity in the joints provides a good low frequent approximation to the manipulator. The elasticities in the joints are modeled as linear rotational springs.

The equation of motion of the system can be written as

$$\boldsymbol{M}(\boldsymbol{q})\ddot{\boldsymbol{q}} + \boldsymbol{C}(\boldsymbol{q},\dot{\boldsymbol{q}})\dot{\boldsymbol{q}} + \boldsymbol{N}(\boldsymbol{q},\dot{\boldsymbol{q}}) = \boldsymbol{\tau} \qquad (1)$$

where $\boldsymbol{q}$ are the coordinates of the degrees of freedom, $\boldsymbol{M}(\boldsymbol{q})$ is the mass matrix, $\boldsymbol{C}(\boldsymbol{q},\dot{\boldsymbol{q}})$ the velocity dependent inertia matrix and $\boldsymbol{N}(\boldsymbol{q},\dot{\boldsymbol{q}})$ the position dependent forces due to gravity, stiffness and damping. $\boldsymbol{\tau}$ are the applied forces and torques. These matrices can be written in a linear in parameter form [3]. For this purpose, a multi body finite element formulation is used [4].

To illustrate the procedure of writing the system linear in the parameters, consider the following expression for the mass matrix

$$\boldsymbol{M}(\boldsymbol{q}) = \boldsymbol{\mathcal{F}}(\boldsymbol{q})_{,\boldsymbol{q}}^{T}\bar{\boldsymbol{M}}(\boldsymbol{x})\boldsymbol{\mathcal{F}}(\boldsymbol{q})_{,\boldsymbol{q}} \qquad (2)$$

where $\boldsymbol{\mathcal{F}}(\boldsymbol{q})_{,\boldsymbol{q}}$ are the first order geometric transfer functions which are the derivative of the functions that map the generalized coordinates $\boldsymbol{x}$ to the degrees of freedom. These functions capture the kinematic non-linearity of the equation of motion. The matrix $\bar{\boldsymbol{M}}$ for a rigid beam in the global coordinate frame, as displayed in figure 4, can be written as

$$\bar{\boldsymbol{M}}_l = \begin{bmatrix} m\boldsymbol{I} & -2m\boldsymbol{R}^p\tilde{\bar{\boldsymbol{r}}}_c\check{\boldsymbol{\Lambda}}^p & \boldsymbol{\mathcal{O}} \\ 2m\check{\boldsymbol{\Lambda}}^{pT}\tilde{\bar{\boldsymbol{r}}}_c\boldsymbol{R}^{pT} & 4\check{\boldsymbol{\Lambda}}^{pT}\bar{\boldsymbol{J}}^p\check{\boldsymbol{\Lambda}}^p & \boldsymbol{\mathcal{O}} \\ \boldsymbol{\mathcal{O}} & \boldsymbol{\mathcal{O}} & \boldsymbol{\mathcal{O}} \end{bmatrix} \qquad (3)$$

where the bar indicates the body fixed frame. The orientation of node p is described by rotation matrix $\boldsymbol{R}^p$

$$\boldsymbol{R}^p = \boldsymbol{\Lambda}\check{\boldsymbol{\Lambda}}^T = \left[-\boldsymbol{\lambda},\ \lambda_0\boldsymbol{I} + \tilde{\boldsymbol{\lambda}}\right]\left[-\boldsymbol{\lambda},\ \lambda_0\boldsymbol{I} - \tilde{\boldsymbol{\lambda}}\right]^T \qquad (4)$$

where $[\lambda_0,\ \boldsymbol{\lambda}]$ is the vector of Euler parameters. The mass and inertia parameters in the body fixed frame are m and $\bar{\boldsymbol{J}}$ respectively. $\tilde{\bar{\boldsymbol{r}}}_c$ is the skew symmetric matrix with the coordinates of the center of gravity in the body fixed frame. The entries of this vector appear linearly in the body fixed mass matrix.

With equation 2 and 3 it can be concluded that the mass matrix of the i^{th} rigid beam is linear in the parameters

$$\boldsymbol{\theta}_{i,RB} = \left[m_i,\ col(\bar{\boldsymbol{J}}_i)^T,\ m_i\bar{\boldsymbol{r}}_{i,c}^T\right]^T, \qquad (5)$$

where $col(\bar{\boldsymbol{J}}_i)$ stacks the elements of matrix $\bar{\boldsymbol{J}}_i$ into a column vector.

Derivations similar to the one described above can be applied to the velocity dependent inertia

matrix. The position dependent forces can be partitioned as a gravity dependent part and a stiffness dependent part which are linear in the inertia parameters and the stiffness parameters respectively.
This yields 10 parameters to describe each rigid beam element. The stiffness and damping of each spatial hinge are described by 6 parameters. The complete system consists of 13 rigid beams with mass and 18 spatial hinges. This yields 238 parameters that describe the lumped elasticity, rigid body dynamics.

Actuator dynamics

It has been observed that the relation between the input current to the drives and the torque on the actuator deviates from the ideal linear relation. To compensate for this deviation, the rigid body model is extended with an additional actuator dynamics model.
The observed deviation can be divided into two parts, the cogging and the hysteresis part. The cogging effect is modeled as a set harmonics. The base frequency of these harmonics is the greatest common divisor of the number of poles and the number of magnets of the permanent magnet motor. The hysteresis effect is modeled as a reset integrator [5]. The output of the reset integrator model is determined by integrating the velocity V_r of hinge rotation up to a threshold p_0 and is linear in its amplitude. It uses an additional state p according to

$$\begin{aligned} \dot{p} &= 0 \quad \begin{cases} V_r > 0 \text{ and } p \geq p_0 \\ V_r < 0 \text{ and } p \leq p_0, \end{cases} \\ \dot{p} &= V_r \quad -p_0 < p < p_0, \\ \tau_{i,h} &= K \int \dot{p}, \end{aligned} \tag{6}$$

where $\tau_{i,h}$ is the current offset generated by the hysteresis model.
Please note that the amplitude of the offset is not dependent on the velocity. The optimal value for p_0 is found offline by solving a suitable optimization problem with a gradient descent based approach.
Including the reset integrator and 5 harmonics in the cogging model yields the model fit displayed in figure 5 with a total of 11 linear parameters per actuator. The cogging can be recognized as the ripple in the current. The hysteresis is the offset between both sides of the loop.

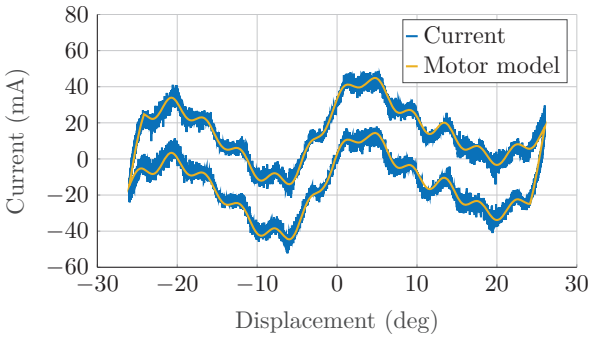

FIGURE 5. Measured current for a 1/20 Hz sine trajectory, compensated for the stiffness and gravity by means of a least squares fit. Current averaged over 10 repetitions.

Parameter estimation

The rigid body dynamics and the actuator model for all elements and actuators can be captured in

$$\boldsymbol{\tau}_i = \boldsymbol{\Phi}\boldsymbol{\theta} \tag{7}$$

in which the regressor matrix $\boldsymbol{\Phi} \in \mathbb{R}^{n \times m}$ consists of the model equations normalized with respect to the parameters vector $\boldsymbol{\theta}$, which consists of all linear parameters of the system. $\boldsymbol{\tau}_i$ is the input current to the drives. This system has 304 parameters in total.
Several of these 304 parameters are unobservable yielding a null space in the parameter estimation problem. A robust approach to find the basis for the null space is the Singular Value Decomposition (SVD) [3]. The regressor matrix is decomposed as

$$\boldsymbol{\Phi} = \boldsymbol{U}\boldsymbol{\Sigma}\boldsymbol{V}^T \tag{8}$$

where the orthonormal matrices $\boldsymbol{U} \in \mathbb{R}^{n \times n}$ and $\boldsymbol{V} \in \mathbb{R}^{m \times m}$ contain the right and left singular vectors respectively. The diagonal matrix $\boldsymbol{\Sigma}$ contains the singular values and a null matrix

$$\boldsymbol{\Sigma} = \begin{bmatrix} \boldsymbol{S} \\ \boldsymbol{\mathcal{O}} \end{bmatrix}. \tag{9}$$

$\boldsymbol{S} = diag(\sigma_1, \sigma_2, ..., \sigma_m)$ contains the singular values of $\boldsymbol{\Phi}$ in descending order. The SVD can be truncated by choosing a suitable r such that the matrices $\boldsymbol{U}$, $\boldsymbol{S}$ and $\boldsymbol{V}$ are partitioned as

$$\boldsymbol{U} = \begin{bmatrix} \boldsymbol{U}_1 & \boldsymbol{U}_2 \end{bmatrix}, \boldsymbol{S} = \begin{bmatrix} \boldsymbol{S}_1 & \boldsymbol{\mathcal{O}} \\ \boldsymbol{\mathcal{O}} & \boldsymbol{S}_2 \end{bmatrix}, \boldsymbol{V} = \begin{bmatrix} \boldsymbol{V}_1 & \boldsymbol{V}_2 \end{bmatrix}, \tag{10}$$

with $\boldsymbol{S}_1 \in \mathbb{R}^{r\times r}$, $\boldsymbol{S}_2 \in \mathbb{R}^{(m-r)\times(m-r)}$, $\boldsymbol{U}_1 \in \mathbb{R}^{n\times r}$, $\boldsymbol{U}_2 \in \mathbb{R}^{n\times(m-r)}$, $\boldsymbol{V}_1 \in \mathbb{R}^{m\times r}$ and $\boldsymbol{V}_2 \in \mathbb{R}^{m\times(m-r)}$.
The singular values can be used to truncate the system to a suitable dimensionality. With this truncation the regressor is split into an essential parameter space and a null space. Choosing r such that $\sigma_{r+1} = \sigma_{r+2} = ... = \sigma_m = 0$ corresponds to defining the null space to match the unobservable states.
The matrix containing the right singular vectors can be interpreted geometrically as a rotation matrix. The truncated rotation matrix is used to map the parameters into an essential parameter space, where all the parameters are linearly independent. This yields

$$\boldsymbol{\Phi}\boldsymbol{V}_1 \approx \boldsymbol{U}_1\boldsymbol{S}_1 = \hat{\boldsymbol{\Phi}} \tag{11}$$

The essential parameters yield good estimation results in a sense that they minimize the mean square difference between the measured and the estimated current. However, they often fail to be physical convincing, e.g. negative mass. As a counter measure, the null space can be used to minimize the difference between the essential parameters and an a priori estimate of the parameters.

The set of previous equations form a basis in the essential parameter space. To find the optimal set of parameters a Kalman filter is used [6]. In the Kalman filter approach, the change in parameters are assumed to be independent Gaussian processes. This enables tracking of changes in the parameters.
The projection of the system onto the essential parameter space assumes that the system can be described according to the model. When this is not the case this can lead to biases in the parameters and non-optimal prediction of the feedforward current. Due to the linear structure of the parameter estimation problem, the basis of the essential parameter space can be expanded with arbitrary functions.

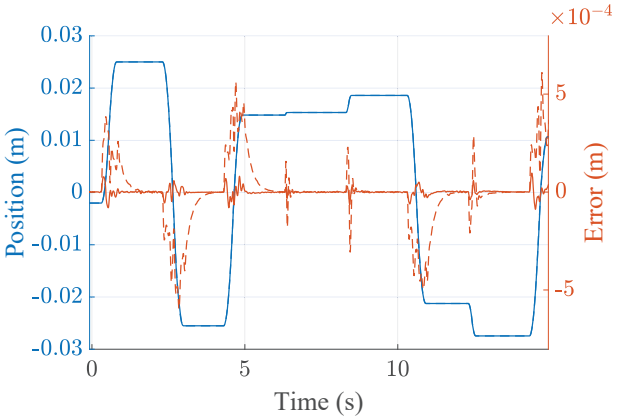

FIGURE 6. Tracking error for a random setpoint trajectory. The dashed line is the error with only the feedback control, the solid line with both feedback and adaptive feedforward.

EXPERIMENTAL VALIDATION

The proposed method yields the parameters for an approximate of the inverse dynamics. These inverse dynamics are used for calculation of a feedforward torque of a single base joint of the T-Flex.
For the validation, a set of random setpoint is generated. The setpoints are connected with a transient profile to limit the maximal acceleration. In this early testing stage, the setpoints are limited to halve of the maximum stroke and the acceleration to $0.2\mathrm{g}$. For testing, a PID controller with a crossover of $25\mathrm{Hz}$ and phase margin of $45°$ has been used.
The used electronics are listed in table 1. The electric motor has a peak torque of 41Nm, the motor drive can provide a continues current of $3\mathrm{A}$ and a peak current of $9\mathrm{A}$. The encoder measures the absolute position with a resolution of $2{\cdot}10^{-9}\mathrm{m}$.
Figure 6 shows the tracking error after convergence of the adaptive feedforward controller. This error is compared to the error of the same profile with the feedback controller only. The RMS error of the system is reduced with a factor of 10 by the adaptive feedforward controller.
In figure 7 the delivered current is decomposed in the feedforward and the feedback part. It can be seen that the feedforward generates the majority of the current. To quantify this, around 95% of the RMS current is provided by the feedforward controller.
The residue in the torque still has components under the cross-over frequency. This indicates that there is room for improvement in the adaptive feedforward controller. This improvement can

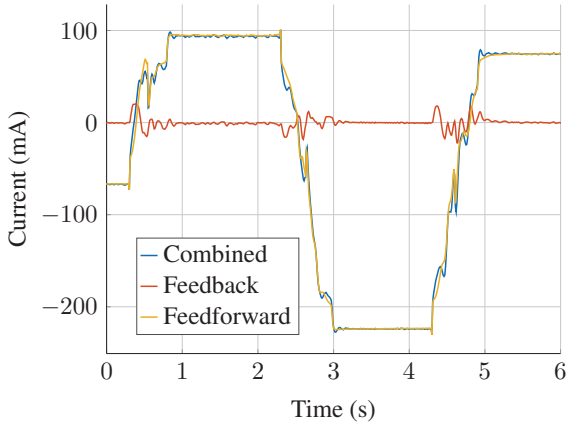

FIGURE 7. Current decomposition random set-point trajectory.

	Manufacturer	Product name
Electric Motor	Tecnotion	QTR-A-133-60
Motor drive	Kollmorgen	AKP-P00306
Encoder	Heidenhain	LIC 4007-411
Target PC	Speedgoat	Baseline

TABLE 1. Electronics T-flex

most likely be found in an extension of the actuator model.

CONCLUSION

This paper considers control design for an elastic 6DoF manipulator with potentially high repeatability and tracking accuracy. The feedback controller is designed to minimize the position error at stand-still. H_2 controller synthesis yields a stand-still RMS error of 106 nm. In the eventual 6 DoF system the standstill error will be reduced further to about 50 nm by doubling the inertia for balancing purposes. On top of the feedback controller an adaptive feedforward controller is implemented to improve tracking by accurate parameter estimations. This feedforward controller reduced the maximal tracking error with a factor 10. Current research considers further reduction of the tracking error integrating the H_2 controller with the adaptive feedforward controller, as well as by extending the actuator model and application of the method to the 6-DoF setup.

ACKNOWLEDGEMENTS

The authors would like to thank the following companies for their support and technical advice in this project; Tecnotion B.V., Almelo, The Netherlands; Heidenhain Netherlands B.V., Ede, Netherlands, SigmaControl B.V., Barendrecht, The Netherlands.

REFERENCES

[1] Naves, M., Aarts, R. G. K. M., Brouwer, D. M. Large stroke high off-axis stiffness three degree of freedom spherical flexure joint. Precision engineering 562 2019; 422-431.

[2] Naves, M., Nijenhuis, M., Hakvoort, W. B. J., Brouwer, D. M. Design of a large stroke flexure-based suspension for an iron core torque motor. In 19th EUSPEN International Conference & Exhibition, ICE. EUSPEN. 2019; 52-55

[3] Waiboer, R., Aarts, R. G. K. M., and Jonker, B. Modelling and identification of a six axes industrial robot. ASME 2005 International Design Engineering Technical Conferences and Computers and Information in Engineering Conference. American Society of Mechanical Engineers Digital Collection, 2005.

[4] Jonker, J. B., Meijaard, J. P. SPACAR—Computer program for dynamic analysis of flexible spatial mechanisms and manipulators. In Multibody systems handbook. Springer, Berlin, Heidelberg. 1990; 123-143

[5] Haessig Jr, D. A., Friedland, B. On the modeling and simulation of friction. 1991; 354-362

[6] Ninness, B., Gómez, J. C.. Frequency domain analysis of tracking and noise performance of adaptive algorithms. IEEE transactions on signal processing. 1998; 46.5: 1314-1332.

VACUUM COMPATIBLE CONTACTLESS ACTIVE MAGNETIC LINEAR BEARINGS FOR HIGH CLEANLINESS ROBOTIC APPLICATIONS

Rick Baade[1], Ton Peijnenburg[2], and Maarten Steinbuch[1]
[1]Department of Mechanical Engineering
Eindhoven University of Technology
Eindhoven, Netherlands
[2]VDL Enabling Technologies Group
Eindhoven, Netherlands

MOTIVATION & INTRODUCTION

Requirements on both particulate and molecular contamination are becoming increasingly stringent in many industrial robotic applications, and substrate handling robotics in particular. Examples are semiconductor-, MEMS-, flat panel and solar industry. This holds for both atmospheric and in-vacuum operating robots. Conventionally these robots are constructed as SCARA or double SCARA structures where rigid links are connected by rotational joints. Considering the workspace and required degrees of freedom, kinematic structures containing prismatic joints can potentially improve performance.

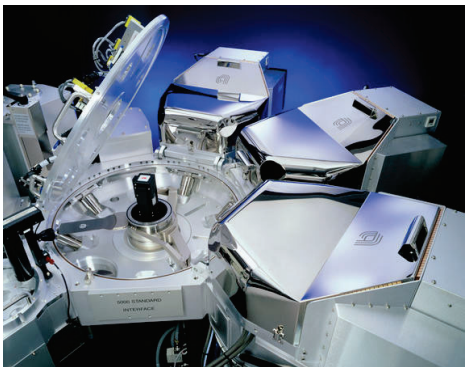

FIGURE 1. Semiconductor manufacturing equipment: CVD cluster tool Applied Materials

In robotic systems, or motion systems in general, mechanical joints between moving bodies are often the main source of contamination. The joints typically contain rolling element bearings and contamination seals to prevent contamination from reaching the clean process environment. Examples of such contamination seals are ferrofluid-, labyrinth- and differentially pumped gas purged seals. The seals significantly contribute to the mass, cost and complexity of the system. Sealing of long stroke linear joints is more difficult than sealing rotational joints, especially for in-vacuum applications. Commercially available linear contamination seals, which meet semiconductor industry performance requirements,have not been found.

Active magnetic linear bearings could provide an advantageous alternative to conventional rolling element bearings [1]. Since magnetic bearings are contactless, there is no mechanical friction and thus little particle generation. Moreover, there is no need for lubrication which enables in-vacuum operation without significant outgassing. These aspects make that contamination seals can be omitted.

The main challenges of applying magnetic bearings in high-tech in-vacuum systems lie in minimization of heat generation in the coils, implementation of a stable position feedback-control loop and linearization of the typically non-linear characteristics in case of non-linear actuators.

STATE OF THE ART

A significant amount of research has been done by a number of institutions on the design and control of linear motors, magnetic bearings and magnetic levitation systems for high-tech manufacturing equipment. Most of this research is driven by increasingly demanding requirements on positioning accuracy, stability and increasing velocities and accelerations (throughput). Examples are the work of Trumper [2] at MIT on a high performance linear actuator and a long stroke magnetically levitated stage. At the University of British Columbia, Lu and Usman [3] developed a 6 DoF motion stage. In 2009, Laro, Spronk and van Eijk [4] designed an electromagnetically suspended slider for optical disk mastering. At Philips Applied Technologies, de Klerk et al. [5] developed a stage based on e-core reluctance actuators for e-beam inspection tools.

RESEARCH OBJECTIVES

This work describes the design of a magnetically suspended linear guide for a substrate handling robotics application. The research objective differs from the state of the art in the sense that the focus is on a cost effective, high reliability solution while minimizing contamination. Position accuracy requirements are less stringent and corresponding to conventional rolling element bearings, in the order of $1\,\mu m$ reproducibility at the end of stroke. Three main cost drivers of magnetic levitated systems are identified, namely the motor drives, position sensors and the actual hardware such a coils and mechanics. All are evaluated to be cost efficient at the desired performance levels.

BEARING PRINCIPLE

We can distinguish two types of linear electromagnetic actuators, namely Lorentz and reluctance type. Table 1 shows a high level comparison. From this table can be concluded that reluctance actuators are more efficient given the higher steepness and force density, at the cost of increased control complexity due to the non-linearity and negative stiffness.

Given the proposed operation of the electromagnetic actuators in a linear bearing application with constant gap setpoint, the non-linear dependence of the reluctance force to the air gap can be linearized around the gap setpoint. Position stability requirements corresponding to conventional rolling element bearings, in the order of 1 to $10\,\mu m$, are believed to be feasible with reluctance based actuators.

Single bearing module

The reluctance bearing modules are based on the bearings proposed in [5] and [7]. A single magnetic bearing module is shown schematically in figure 2 and consists of a moving e-core assembly (1) and a static back iron (2). The e-core assembly consists of a laminated e-core (3), where a permanent magnet (4) is mounted on the central tooth and a coil (5) is wound around the central tooth. The static back iron is placed at a distance g_1 from the e-core assembly. This system defines a low reluctance path where the resulting magnetic flux density in the air gap will yield a gap dependent attraction force between the e-core and the back iron. The magnetic flux density in the air gap can either be magnified or reduced, based on the direction and magnitude of the current running through the coil, thereby controlling the magnitude of the attraction force. Note that this system can only generate an attraction force and no repelling force between the e-core and back iron. Preloading opposite to the attraction force is required for bi-directional actuation.

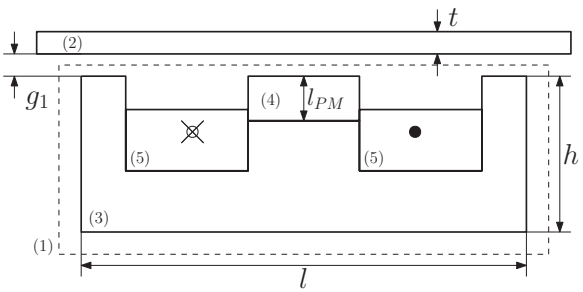

FIGURE 2. Schematic representation of a single reluctance bearing module

Parameter		***Lorentz***	***Reluctance***
Linearity	$[N/A]$	High	Non-linear in current and airgap
Force density	$[N/m^3]$	Low	High
Steepness	$[N^2/W]$	Low	High
Negative stiffness	$[N/m]$	Low	High
Bi-directional actuation	$[-]$	Yes	No
Stroke	$[mm]$	Long	Short

TABLE 1. Linear actuators: Lorentz vs reluctance [6]

MAGNETIC CIRCUIT MODELLING

Given the micrometer level positioning requirement, feedback control is based only on position or air gap sensors without additional flux sensors [8]. A typical feedback control scheme is shown in figure 3. An inverse model of the electromagnetic system (P_{em}^{-1}) that maps the actuator force as function of air gap length and current is needed to calculate the current setpoint. Several analytical models are evaluated and compared to finite element modeling simulations and actual measurements.

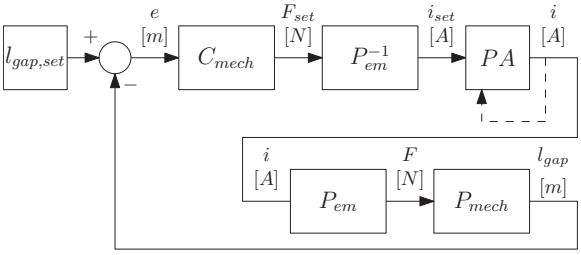

FIGURE 3. Feedback control loop

Figure 4 shows an example of an electrical equivalent circuit [9]. The left branch describes the most basic reluctance model of a bearing module. This model contains the coil, permanent magnet, e-core, twice an air gap and the metal counter part. The reluctance values are calculated analytically. It was found that the most basic model deviates significantly from measurements and simulations. When flux leakage is included in the model (right hand side of figure 4), the results between measurements and models are within 5 percent (figure 5). The reluctance value of the leakage path is extracted from finite element model simulations, at the nominal air gap value without current flowing through the coils.

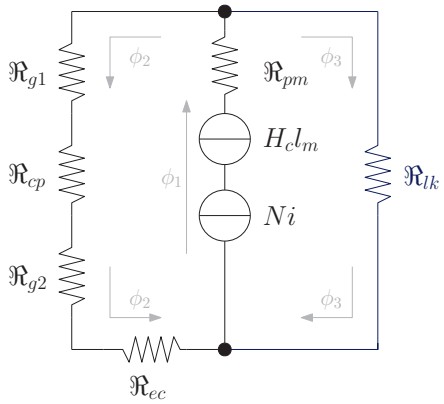

FIGURE 4. Electrical equivalent circuit including flux leakage

A measurement setup is created to validate these results. Static measurements are performed to map the attraction force as function of current and gap. The e-core is fixed to a Newport optical table. Shim plates are used to maintain a defined air gap. A PI linear actuator (M-235.5DG) is used to pull the counter plate from the e-core in a repeatable manner. A Kistler 9203 force sensor is used to measure the attraction force, with a sensitivity of $1.3\,\mathrm{N\,V^{-1}}$ and linearity of $\pm\ 0.5\,\mathrm{N}$ over the measurement range. A Siglab data acquisition box is used to log the force sensor output.

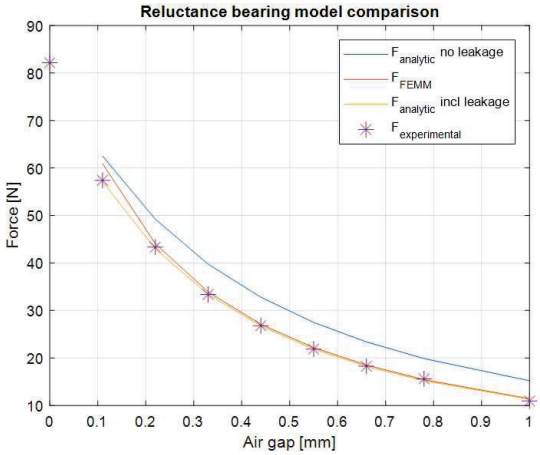

FIGURE 5. Static bearing force as function of air gap (current = 0 [A]), model vs. measurement

System dimensioning

The models of the of the electromagnetic system are used to dimension the parameters of the magnetic bearing modules. Parameters are chosen such that energy dissipation in the coils is minimized. A number of parameters are preselected such as the width of the e-core, coils and permanent magnets. These dimensions are chosen as large as possible within the allowed volume claim. Two parameters, the magnitude of preload force and the steady-state flux density, are varied over a range of values. A number of system parameter follow for each combination. All scenarios are calculated and the option with the lowest energy dissipation is selected. Several boundaries are set on maximum allowed dimensions within the volume claim, such as e-core length. Other boundaries are applied to assure as physically feasible design, for example a minimal wire diameter for the coil is set to $50\,\mu\mathrm{m}$. Magnetic system parameters are optimized following this procedure for each degree of freedom.

LINEAR GUIDE DESIGN

One bearing module described in the previous sections is able to constrain or control a single degree of freedom. By combining multiple bearing modules, a linear guide is created as shown in figure 6. The linear guide design described in this sections serves as a proof of principle before it is implemented in a more elaborate substrate handling robot design.

The linear guide design consists of a carriage (1) which is able to move along a beam (2) in x-direction. All other degrees of freedom are constrained by magnetic bearing modules. Two SCARA type arms (3) are used to feed electrical power and sensor signals to the carriage in a clean manner, and to drive the carriage in x-direction similar to a slider-crank mechanism.

Degree's of freedom

The magnetic bearing modules are mounted to the moving carriage, as depicted in figure 7 where a top view of the carriage is shown with the blue body partly transparent.

The out-of-plane degrees of freedom (z, ϕ and ψ) are constrained by bearing modules $(1, 2$ and $3)$ which are preloaded by the weight of the carriage. Modules (1) and (2) support the weight of the carriage and module (3) constraints rotation around the x-axis.

The in-plane degrees of freedom (y and θ) are constrained by two sets of two opposing bearing modules. Modules (4) and (5) from a set, where both modules generate a constant preload force. Additional to the preload force, module (4) is able to generate a force in positive y-direction and module (5) is able to generate a force in negative y-direction. In a similar fashion, modules (6) and (7) form a set.

A membrane (8) located at connection of the SCARA arm with the carriage releases the z, ϕ and ψ degrees of freedom to prevent overconstraining.

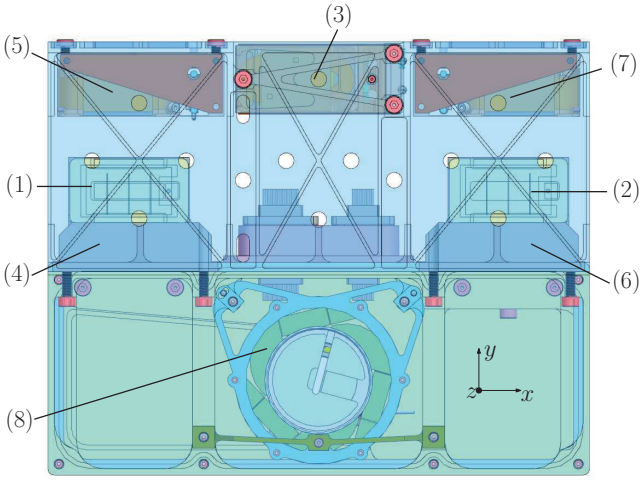

FIGURE 7. Top view of carriage, blue body transparent to show placement of bearing modules

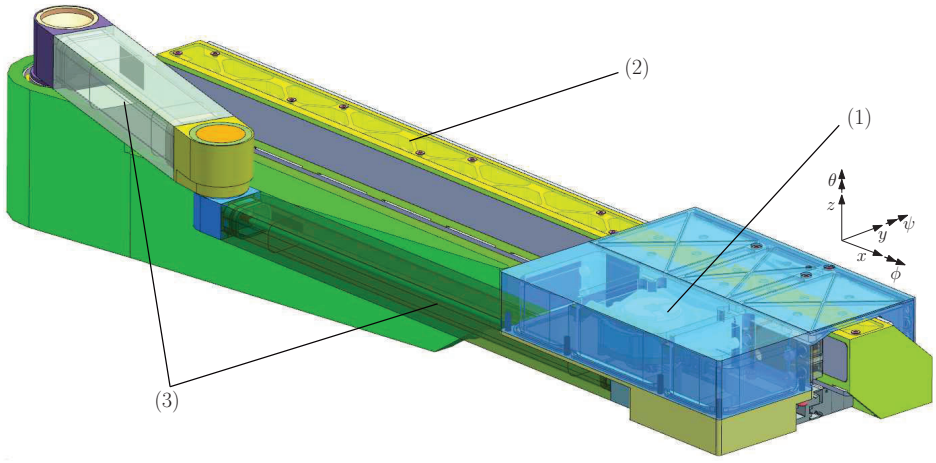

FIGURE 6. Design of the linear guide

Adjustment mechanism

The bearing modules that constrain the out-of-plane degrees of freedom are preloaded by the weight of the carriage. To minimize energy dissipation, i.e. heat generation, the steady-state forces, required to counteract the weight of the carriage, are generated by permanent magnets. Any mismatch between the static forces generated by the permanent magnets and the forces required to counteract the weight will require a current through the coils to correct the force balance and maintain the position setpoint. This wil in turn lead to additional heat generation in the vacuum environment. This mismatch, for example due to tolerances on permanent magnet parameters can be compensated for by adjusting the air gap setpoint such that steady-state currents approach zero. To level the carriage, each degrees of freedom has a mechanical adjustment mechanism as depicted in figure 8. consisting of two parallel leaf springs (1) with a setscrew (2). The mechanism is designed to have a stroke of $\pm$ 0.2 mm and an expected sensitivity of 10 µm.

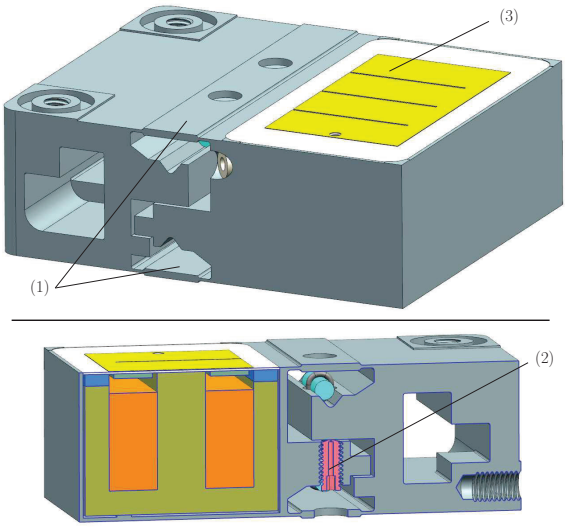

FIGURE 8. Single bearing module including adjustment mechanism and capacitive sensor

Gap sensing

The magnetic bearing system is operated in closed-loop position control, where the air gap is measured and controlled to the desired setpoint. Contactless gap sensing is preferred. The sensor requires a measurement range of approximately 1 mm with an accuracy of 0.5 µm. The operating environment of the sensor is under vacuum and close to relatively strong magnetic fields. Therefore a sensing principle insensitive to magnetic fields and which requires minimal active electronic components for low heat dissipation and outgassing is desired. Capacitive displacement sensors meet these requirements. To minimize Abbe measurement errors, the gap measurement should coincide with the acting point of the magnetic bearing force i.e., the center of the magnetic bearing module.

Commercially available capacitive sensors are generally cylindrical or flat shaped, with a typical minimal thickness of 4 mm. These shapes makes it difficult to integrate the sensor with the magnetic bearing module and meet the Abbe criterium stated above. Moreover, each sensor requires one (often triaxial) cable for shielding, measurement signals and guard signals [10]. These cables need to be fed from the base, through the SCARA arm and the three corresponding rotary joints to the moving carriage. The amount of cables, diameter and bending stiffness of the shielded (triaxial) cables result in a large bending radius. This then leads to a larger joint diameter than structurally necessary and therefore too high a mass. It was found that the use of a commercially available sensor significantly impacts the system design.

A new capacitive displacement sensor system is designed [1] and realized to avoid the adverse effects described above. The sensing surface is integrated in the cover of the e-core housing, located inside the air gap thereby meeting the Abbe criterium. The cover is constructed out of two glass parts where a conducting silver layer is sputtered onto the top surface (figure 8 (3)). This silver layer acts as the sensing surface. A pre-processing printed circuit board (PCB)is located inside the carriage. This pre-processing PCB acts as a pre-amplifier and multiplexes all five sensor signals. This makes that only two small diameter coaxial cables are required for connecting the pre-amplifier PCB to the fixed world and greatly simplifying the rotary cable feedthrough in the SCARA arm. The sensor target (stationary iron strip) is connected to the oscillating excitation signal to simplify the design of the sensing surface.

The new capacitive probe is compared to a Heidenhain LIP 281 linear encoder on a dedicated setup containing a precision air bearing straight guide. The encoder absolute accuracy grade is specified as $\pm$ 1 µm with a relative accuracy of

[1] in collaboration with Ron Asjes, SensoRon

0.125 µm over 5 mm stroke. The sensor output was mapped over a range from 0 to 1.0 mm and found to be within ± 0.1 µm of the reference. Data acquisition of the analog sensor output is done using a Speedgoat real-time target and an analog IO104 data acquisition module running at 5kHz sample frequency.

CONCLUSIONS AND FUTURE WORK

A novel linear guide constraining 5 degrees of freedom has been designed (figure 6). The guide contains 7 reluctance based actuators that serve as magnetic bearing modules. Steady-state loads are supported by permanent magnets to minimize steady-state energy dissipation, i.e. heat generation. Mechanical adjustment mechanisms are included to compensate for tolerances in the magnetic and mechanical components. A small mechanical arm is used to feed electrical signals to the moving body and acts as a crank-drive mechanism. A new capacitive sensor has been developed that is integrated with the linear guide to reduce cost and minimize volume. Local signal preprocessing and multiplexing is done to reduce the amount of cables through the system.

A prototype of the linear guide design described in this abstract is currently under construction. When finished and fully operational, a number of performance tests will be performed to evaluate stability, positioning accuracy and energy dissipation.

REFERENCES

[1] A. Peijnenburg, J. Vermeulen, and J. van Eijk, "Magnetic levitation systems compared to conventional bearing systems," *Micro-Electronic engineering*, pp. 1372–1375, Mar. 2006.

[2] L. Z. Jun Young Yoon and D. L. Trumper, "Linear stages for next generation precision motion systems," *Proceedings of the 2019 IEEE/ASME International Conference on Advanced Intelligent Mechatronics*, pp. 241–247, 2019.

[3] X. Lu and I. Usman, "6d direct-drive technology for planar motion stages," *CIRP Annals - Manufacturing Technology*, vol. 61, pp. 359–362, 2012.

[4] D. A. H. Laro, *Mechatronic design of an electromagnetically levitated linear positioning system using novel multi-dof actuators*. phdthesis, Technische Univeriteit Delft, May 2009.

[5] G. Z. A. Angelo C.P. de Klerk and J. van Eijk, "Design of a next generation 6 dof stage for scanning application in vacuum with nanometer accuracy and mgauss magnetic stray field," *Proceedings of the 19th annual ASPE meeting*, 2004.

[6] "Comparative evaluation of lorentz and reluctance actuators," tech. rep., Philips Inovation Services, 2016.

[7] R. T. Meindert L. Norg and J. van Eijk, "Active magnetic bearing controls strategy and calibrations," *Proceedings ASPE spring topical meeting 2008*, 2008.

[8] A. Katalenic, *Control of Reluctance Actuators for High-Precision Positioning*. phdthesis, Eindhoven University of Technology, 2013.

[9] R. Hamelinck, *Adaptive deformable mirror*. phdthesis, Eindhoven University of Technology, 2010.

[10] Micro-Epsilon, "capancdt capacitive displacement sensors and systems." Catalog.

Variable Resolution Fused Filament Fabrication (FFF) Printing Using a Variable Orifice Extruder System

Osama Habbal and Christopher Pannier
Department of Mechanical Engineering
University of Michigan-Dearborn
Dearborn, MI, USA 48128

INTRODUCTION

While additive manufacturing has sped up the production of prototypes [1], the same could not be said of the use of additive manufacturing for serial production [2]. A simple 20 mm^3 cube could take up to 40 minutes of print time using a Fused Filament Fabrication (FFF) printer that extrudes lines of build material. Build times are long because printers must create the objects in successive high-resolution layers as thin as 50 µm. A common alternative to shorten build times is to sacrifice resolution throughout the build by using a larger nozzle orifice for extrusion. A potential solution to reduce build time without sacrificing resolution is a system to vary the nozzle orifice diameter during a print depending on the resolution required for each feature. A variable orifice extruder (VOE) system is designed using coaxial cylinders to vary the orifice diameter; the inner cylinder retracts to leave a larger opening for material flow, but experimental data are not provided in [3]. A VOE system has advantages over the alternative of using a dual (or more) extruder system with two (or more) orifice diameters because the VOE reduces the number of needed extruders and filament feeds to one. This extended abstract presents 1) the design of the novel VOE system with a turret of multiple secondary nozzles to vary the output orifice diameter, 2) test prints with either a single or variable orifice diameter, 3) results of build time measurements and 3D scans of the test prints, and 4) directions for improvement.

DESIGN of the VOE SYSTEM

The design of the VOE system involves modifications to the printhead, microcontroller, and slicer of a desktop FFF printer. The VOE printhead has three unique features: a rotating turret containing several secondary nozzles, a solenoid mechanism for turret raising and lowering, and a secondary nozzle selection mechanism. A stepper motor rotates the turret of secondary nozzles via a gear train. A cam and a snap action limit switch indicate the home position of the turret, which corresponds to the smallest secondary nozzle. The VOE printhead is mounted on the X-axis gantry of a modified desktop FFF printer (Creality Ender-3 Pro, Shenzhen, China).

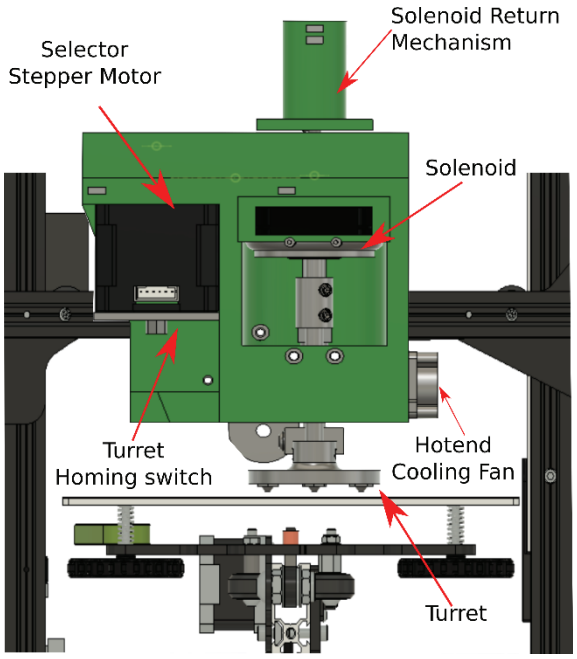

FIGURE 1. CAD model of the VOE printhead with plastic body (green) mounted to the FFF printer gantry (dark gray extruded aluminum profiles). The build plate and its motion system is shown below the turret of secondary nozzles.

A cup and cone surface makes a seal between the primary nozzle and each secondary nozzle. The main body of the assembly is produced using FFF 3D printing and made to be in one piece to provide geometrical stability under successive nozzle change operations. The design of the turret includes the turret disk, into which up to four secondary brass nozzles of various orifice diameters are screwed. The turret material is high strength titanium for two reasons: to reduce deformation under the moment loading by the

solenoid, and to reduce heat loss from the secondary nozzle with the high thermal resistivity of titanium.

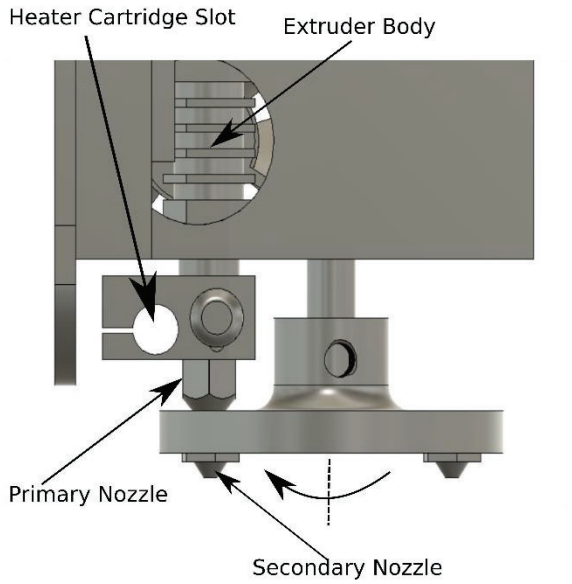

FIGURE 2. CAD model of the hotend and nozzle turret.

A gear train with a final drive ratio of 1:1 provides power transmission between the selector stepper motor and the turret shaft. Precision ground round shafts are used with sintered bronze bushings for all rotating mechanisms within the design. Two fans are used in this design: one fan cools the extruder heat sink, and one fan cools the solenoid. As the solenoid is a pull-type solenoid, a turret return compression spring provides clearance between the primary and secondary nozzle for switching. A microcontroller with a web interface (Duet3D Duet 3 Main Board 6HC, Peterborough, UK) controls the heaters, stepper motors, solenoid and fans with customized G-code for tool change and homing operations.

TESTING

Testing the effectiveness of the VOE system requires a 3D part to print. A small part (2 cm length) allows quick tests. A part with a simple feature (a cylinder) and a complex feature (interposed cylindrical frustra that require printing an overhanging feature) is shown in Figure 5. Three test conditions are assigned: A) a fixed, large orifice extrusion, B) a fixed, small orifice extrusion, and C) a variable orifice extrusion. The test conditions are as follows: A) 0.8 mm orifice diameter and 0.60 mm layer height, B) 0.25 mm orifice diameter and 0.08 mm layer height, and C) two orifice diameters (0.25 mm and 0.8 mm) and two corresponding layer heights (0.08 mm and 0.60 mm).

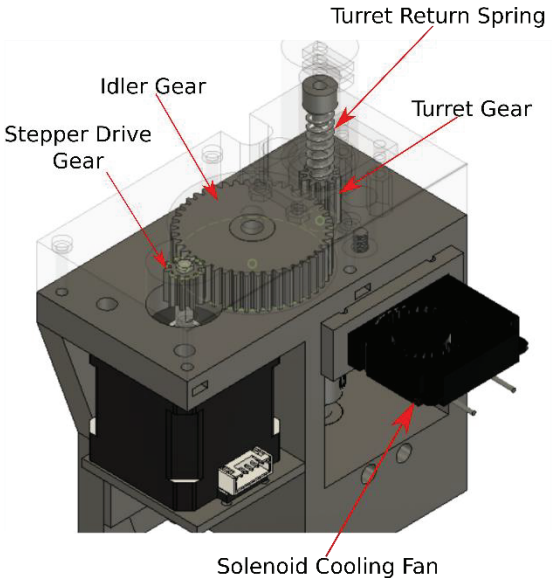

FIGURE 3. Overview of the gear train.

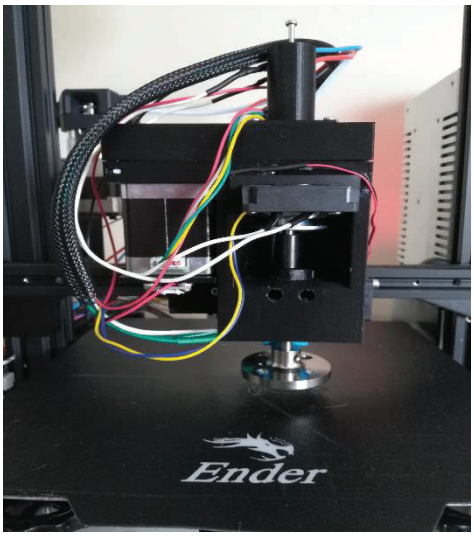

FIGURE 4. Assembled and mounted VOE printhead.

The test piece is segmented into two pieces in the CAD software. Each section is exported individually as an STL file. The STL files are imported into an FFF slicing program (Simplfy3D V4.1, Cincinnati, OH) that has a capability to assign a unique set of slicing settings to each

section as a separate slicing “process”. Different printing profiles corresponding to different nozzle diameters were created as “processes” in the slicing program. Finer sections were allocated to the “processes” with the small orifice diameter while low detail sections were allocated to the process with the large orifice diameter.

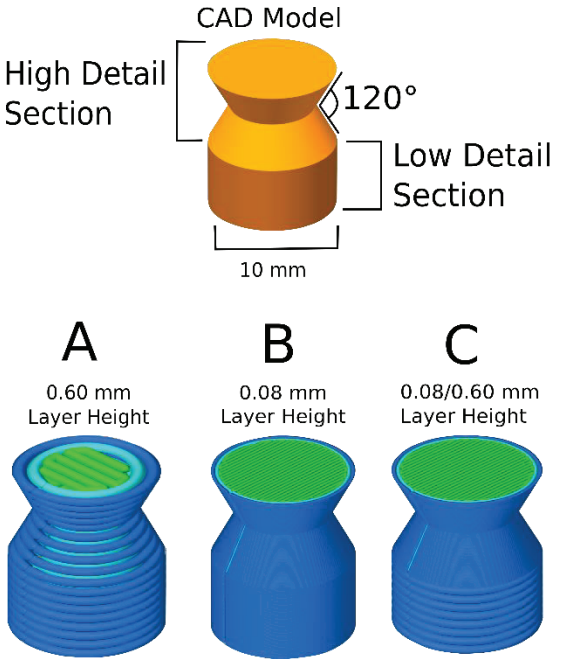

FIGURE 5. CAD model and sliced toolpaths for test conditions A, B, and C. C is sliced using 0.08 mm layer height for the high detail section and 0.60 mm layer height for the low detail section.

RESULTS

The performance of the VOE system is evaluated quantitatively in build time and qualitatively in surface scans for the three test conditions. Build times are predicted in the slicing software, but the predictions do not include nozzle switching and reheating time. Build times are measured for a single print of the test part in conditions A, B, and C. The measured and simulated build times for condition C (variable resolution printing) are less than those of condition A (fixed, high-resolution printing), as shown in Figure 7. As expected, condition A (fixed, low-resolution printing) has a low build time, condition C’s build time is between that of conditions A and B. Build time is feature-size-dependent, so the build time ratios should not be generalized to other part geometries.

Printed pieces are scanned by laser line profiler (LMI3D Gocator 2410, Vancouver, BC) on a motorized axis of another FFF printer (Prusa Research i3 MK3S, Prague, Czech Republic) with an optical encoder (CUI Devices AMT113Q-V, Lake Oswego, OR), as shown in Figure 6.

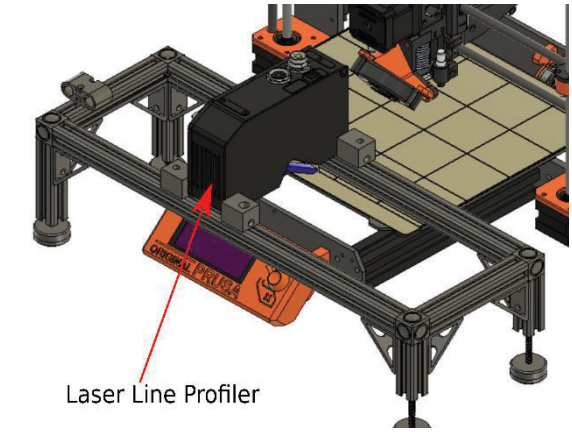

FIGURE 6. 3D scan setup with blue laser line.

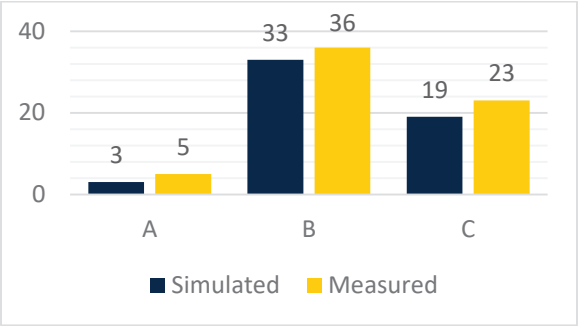

FIGURE 7. Simulated and measured build times.

Test samples are printed using a blue PLA filament. The printing temperatures are found to be 205°C for the hotend and 60°C for the heated build plate. These temperatures reflect the heat loss unique to the VOE printhead. The resulting parts show qualitative similarity to the slicer provided shapes.

The line scan for test sample A show clear stair stepping and loss of resolution on the overhang section of the piece. The transition between the cylindrical section and the overhang section is unclear and feature transitions are smoothed out. Test sample B line scan shows well defined features that are comparable to the CAD design, Transitions between the cylindrical section and the slopped sections are well defined.

While the line scan of test sample C shows the low-resolution layers in the cylindrical section similar to test sample A, the transition from cylindrical to inclined was preserved, as well as

the point of inflection of the slope. This provides an overall part that preserves the required resolution of the CAD design while minimizing the required build time.

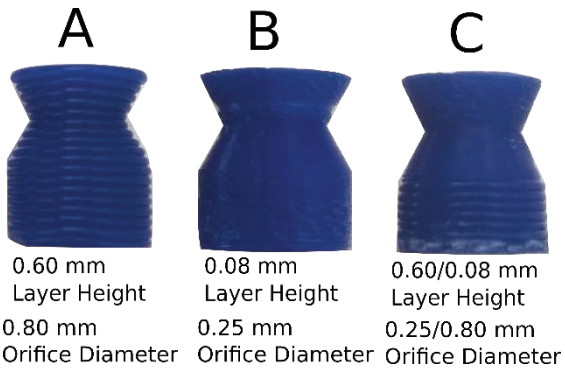

FIGURE 8. Photos of 3D printed test pieces.

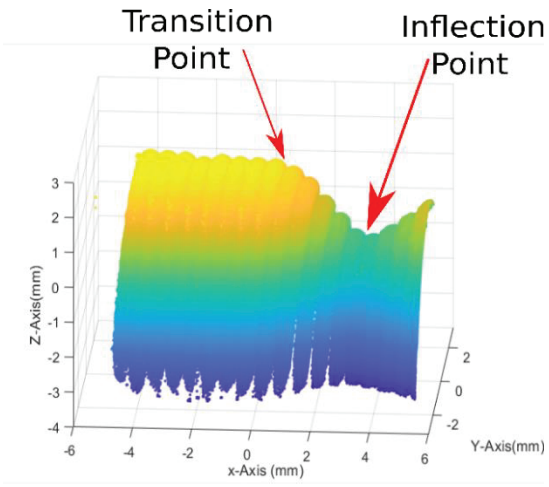

FIGURE 9. Scan of Test Sample A.

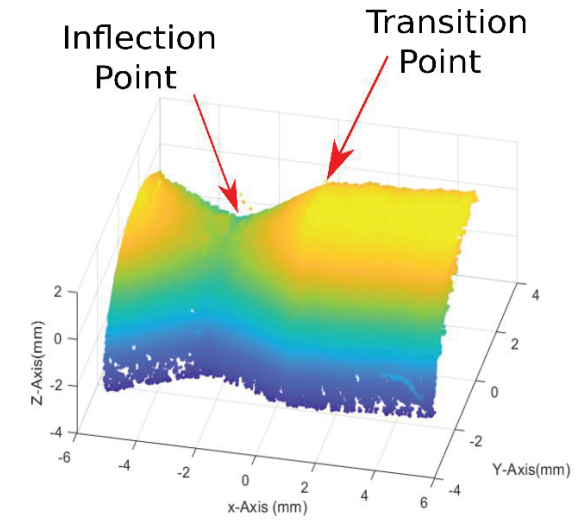

FIGURE 10. Scan of Test Sample B.

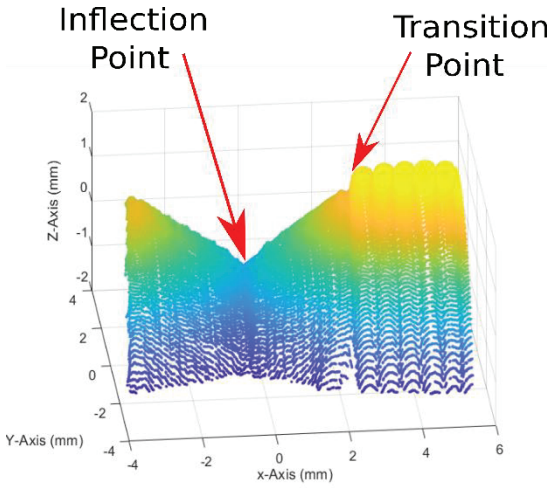

FIGURE 11. Scan of Test Sample C.

CONCLUSION

The VOE system introduces two equally important improvements to the FFF additive manufacturing process. The first improvement is flexibility of resolution within a print, which has implications in design for additive manufacturing. The second improvement is the reduction of build time. As build time is dependent on part geometry, a similar dependence for build time savings with VOE is expected. Lastly, design problems including unequal secondary nozzle height, high printhead mass, and inadequate part cooling are identified for improvement.

REFERENCES

[1] Balletti, C., Ballarin, M., & Guerra, F. 3D printing: State of the art and future perspectives. Journal of Cultural Heritage. 2017; 26, 172-182. doi: 10.1016/j.culher.2017.02.010

[2] Ahuja, Bhrigu, et al. Additive Manufacturing in Production: Challenges and Opportunities. Laser 3D Manufacturing II, 2015, doi:10.1117/12.2082521.

[3] Brooks, H., Rennie, A., Abram, T., Mcgovern, J., & Caron, F. Variable Fused Deposition Modelling – analysis of benefits, concept design and tool path generation. Innovative Developments in Virtual and Physical Prototyping. 2011; 511–517. doi: 10.13140/2.1.2280.2887

DESIGN AND CONTROL OF A THERMAL ACTUATION SYSTEM

Chunjie Fan[1], DJ Hastings[1], and Stuart T. Smith[1]
[1]Center for precision metrology
The University of North Carolina at Charlotte

ABSTRACT

This paper presents the design and control a thermally actuated, single degree of freedom flexure-based translation stage with 200 µm range and capable of operation in the presence of preloads up to 1000 N. The displacement of the thermal actuator is based on the thermal expansion and contraction of the tube actuator, which is controlled by induction heating, and water-mist cooling, Figure 1.

Induction heating is a fast, efficient and contactless method for heating metals by applying a fluctuating magnetic field that, in turn induces eddy currents inside the material. The eddy currents from the induction heater will cause an increase in the temperature of the actuator, which provides the expansion force to actuate the translation stage. Contraction is achieved by decreasing the actuator's temperature using air and water-mist flowing inside of the tube actuator.

The actuator is controlled using a PI controller with feedback via an optical knife-edge displacement sensor. The controller error during steady-state conditions is 17 nm (1σ standard deviation), which means that the mean temperature of the aluminum tube is varying within ±0.0064 °C. The settling time for a step increase in displacement of 40 µm is a relatively constant 25 s under the closed-loop control. For a decrease in displacement of 40 µm, the settling time is between 25 s to 40 s, the longer settling times corresponding to the control temperature approaching that of the mist cooling.

DESIGN AND CONTROLS

The magnitude and distribution of the induced eddy currents can be determined by solving Maxwell's equations in a cylindrical conductive tube [1-4]. The 120 mm long tube has an outside diameter of 10.3 mm and an inner diameter of 6.8 mm. The thermal actuator is secured and thermally isolated between the frame and the stage using glass isolation plates. The heating energy is generated at the outer surface layer of the actuator tube and the cooling is through the inside of the actuator tube using air or water mist (Figure 1).

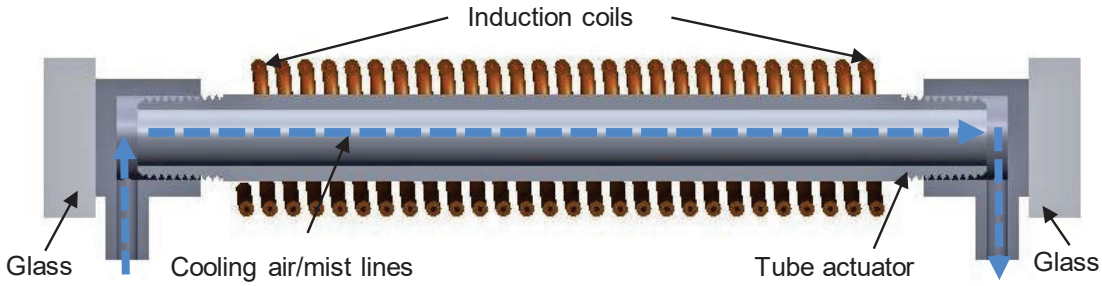

Figure 1: Cross-section of tube actuator indicating the induction coils and the cooling air/mist lines.

The induction coils are wound from hollow copper wire surrounding the aluminum actuator tube. Water is pumped through the hollow wire to prevent overheating of the coil and maintain the induction coil at room temperature. A 220 kHz 43.4 A alternating current is used to generate alternating magnetic fields. The heat generated by the induced eddy currents is diffused throughout the actuator tube and causes an increase in the temperature and therefore the length of the actuator tube.

Energy losses occur through heat conduction from the actuator tube to the connections at each end, heat transfer to the air surrounding the tube, and the heat transfer due to the cooling air or mist flowing through its center.

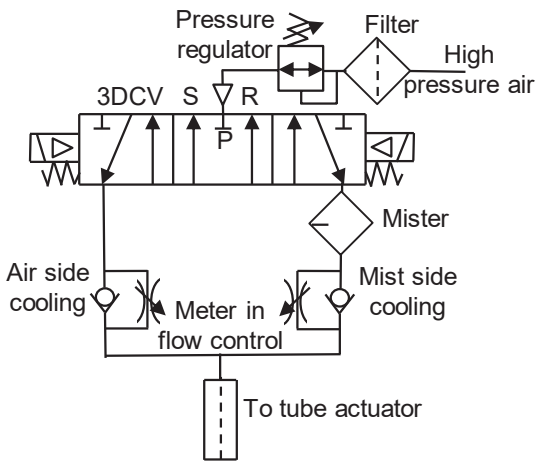

Figure 2: Schematic of the 3 position, solenoid actuated, pneumatic valve.

A three-position, solenoid actuated, pneumatic valve is used to control the cooling air or mist line, shown in figure 2. The return ports on the inlet side (ports S and R) are plugged to prevent unwanted airflow in the opposite direction during a specific cooling type selection. Heat transfer out of the actuator occurs when the high pressure (10 to 20 PSI) cooling air or mist passes through the inside diameter of the tube. The total length of the tube will decrease as the temperature of the actuator tube decreases.

A PI controller is used for the induction heater, and digital on-off signals are used to control the air or water-mist cooling line. During heating and steady-state, the air-line will be turned on, but during the cooling phase the mist line is turned on. A block diagram of the major components of the controller is shown in figure 3 and discussed in more detail in [6]. By changing the duty cycle of the pulse width modulation (PWM) output, the energy input from the induction heater can be controlled. The induction coil driver was a zero-voltage-switching circuit comprising an LC oscillator and power MOSFETs [7]. Cooling in the form of air or mist flowing through the actuator tube is controlled by comparing the previous position and the current measured position: when the previous position is larger than the current measured position, the mist line will be turned on and the air-line will be off; in contrast, when the previous position is equal or smaller than the measured position, the mist line will be turned off and the air-line will be turned on to flush the mist and enable maintaining or heating of the actuator.

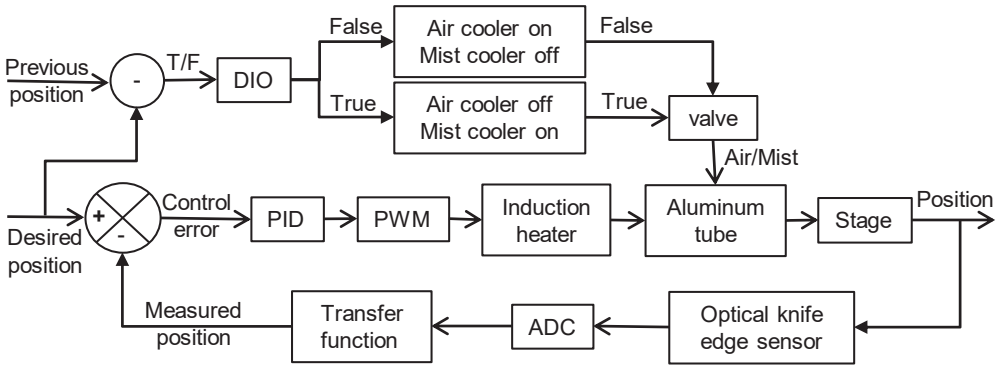

Figure 3: The block diagram of the major components of the controller.

DYNAMICS

During experiments, two 12 V, 10 A DC power supplies are used to build a 240 W power source. This 240 W power source can result in the thermal actuator having a 180 μm displacement using 100 percent duty cycle operation. The first 100 μm movement needs approximately 30 seconds not relying on the preload applied and the final 80 μm for full movement range (180 μm) needs an additional 40 seconds. The thermal time constant is around 60 seconds [5].

The 480 W power source, built by two 24 V 10 A DC power supplies, can produce 200 μm movement using 25 percent duty cycle. The 50 percent duty cycle can produce 200 μm displacement within 50 seconds. The larger displacement was not tested since the sealing glue for the cooling pipe failed when using 50 percent duty cycle for a longer period of time, and the calibrated linear range of the displacement sensor is only 200 μm. The time constant of the 480 W power supply is around 67 seconds as shown in figure 4.

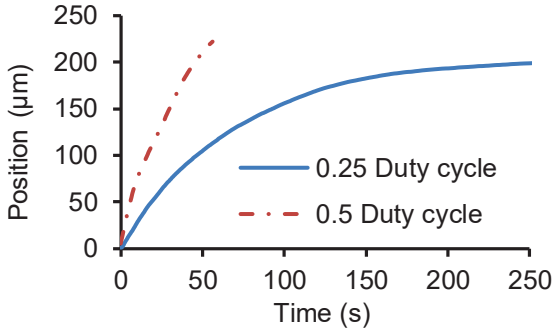

Figure 4: Time constants for 25% and 50% PWM duty cycles when the power supply for the induction heater is 480 W.

To balance the heating and cooling time for 100 µm range, air and water-mist cooling were tested and time-position curves were plotted, as shown in Figure 5. The heating system needs 30 seconds to translate the 100 µm range and the cooling system needs 180 seconds to return to the original position using air cooling alone (left plot). By changing to water mist cooling, the setting time is reduced to 60 s (right plot).

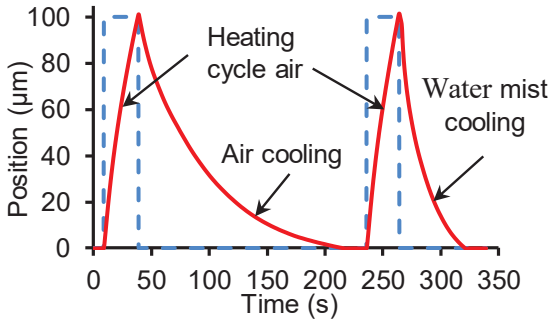

Figure 5: Different settling time using air cooling and water mist cooling methods.

RESULTS

This paper describes the design, modeling, and performance of a thermally actuated translation stage that is simple, rigid, and relatively inexpensive. The high work density of this actuation method enables the positioning of high loads using a relatively compact actuator. For the higher wattage power supply (480 W), it was possible to increase the translation range from 100 µm to 200 µm corresponding to an actuator temperature of approximately 100 °C.

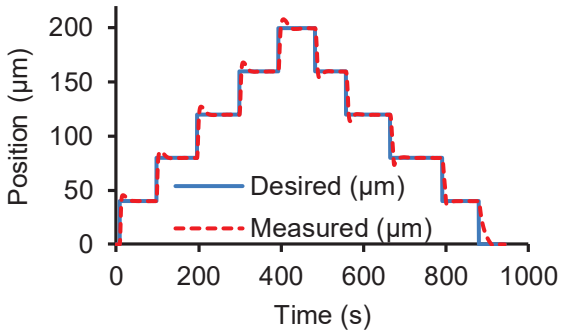

Figure 6: Displacement control test under 1000N load with 40 µm increments up to 200 µm, and 40 µm decrements to initial position.

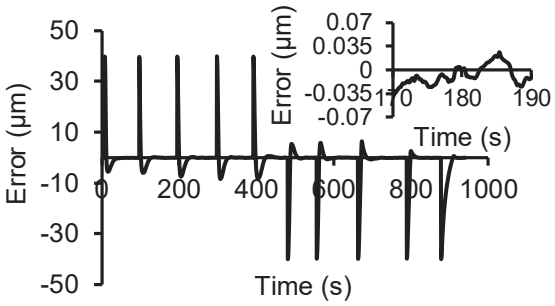

Figure 7: Error in the displacement under 1000N load with 40 µm increments up to 200 µm, and 40 µm decrements to initial position.

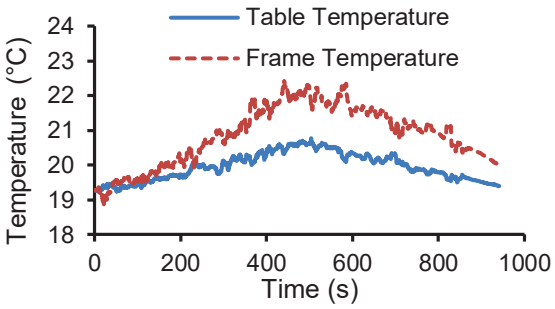

Figure 8: Temperature measurement of the flexure stage and frame.

Figure 6 shows 40 µm heating steps up and 40 µm cooling step down for 200 µm full range and 1 kN preloads are used for this test. The error during steady-state is within ±70 nm (Figure 7). The settling time of the 40 µm increase is around 25 seconds, the settling time of the 40 µm step down will range from 25 seconds to 40 seconds during cooling process. Figure 8 plots the temperatures measured on the frame and

moving table driven by the actuator are varying approximately 21±2 ℃.

The steady-state temperatures within the actuator tube are 100 °C at 25% duty cycle, 162 °C at 50% duty cycle and estimated at 300 °C at 100% duty cycle. This research tried three displacement controls under 0N, 500 N and 1000 N preload. The preload amount has no impact on the settling time and steady-state error of the system. In contrast, the settling time was influenced by the cooling system (i.e., cooling type, temperature difference between the cooling mist and the actuator as shown in Figures 5 and 7).

FUTURE WORK

Future work of the thermal actuator system is multifaceted – there are optimizations to be realized in the electrical system, thermal system, control system, and the overall mechanical design that are currently being explored.

The heating system can be optimized by changing the resonance frequency of the zero-voltage-switching circuit (induction circuit) in an effort to further reduce the time constant. Litz wires will be used as induction coil in the future research to reduce the skin effect loss for high frequency alternating currents. At higher heating power, it is apparent that the stage will need additional cooling to offset the heat input.

There is an ongoing effort to reduce the size of the actuator. With this reduction in size, the goal is for the actuator to continue with the load handling ability of 1000 N as well as a maximum displacement of 10 μm. Possible industrial applications suggest interest in exploring the operation of the actuator at temperature above 200 ºC. Feasibility of the compact actuator in this environment will also be explored.

REFERENCES

[1] J. Huber, N. Fleck, and M. Ashby, "The selection of mechanical actuators based on performance indices," Proceedings of the Royal Society of London. Series A: Mathematical, physical and engineering sciences, vol. 453, no. 1965, pp. 2185-2205, 1997.

[2] S. T. Smith and R. M. Seugling, "Sensor and actuator considerations for precision, small machines," Precision engineering, vol. 30, no. 3, pp. 245-264, 2006.

[3] C. Dodd and W. Deeds, "Analytical solutions to eddy-current probe-coil problems," Journal of applied physics, vol. 39, no. 6, pp. 2829-2838, 1968.

[4] C. Dodd, W. Deeds, and J. Luquire, "Integral solutions to some eddy current problems," International Journal of Nondestructive Testing, vol. 1, pp. 29-90, 1969.

[5] C. Fan, D. Hastings, and S. T. Smith, "Aspects of design and performance of a thermally actuated linear translation stage," 34th American Society for Precision Engineering Conference, vol. 71, pp. 371-374, 2019.

[6] C. Fan, S. T. Smith, and J. Tarbutton, "A linear positioning stage using a thermal actuator," 32nd American Society for Precision Engineering Conference, vol. 67, pp. 451-455, 2017.

[7] L. Grajales, J. Sabate, K. Wang, W. Tabisz, and F. Lee, "Design of a 10 kW, 500 kHz phase-shift controlled series-resonant inverter for induction heating," in Conference Record of the 1993 IEEE Industry Applications Conference Twenty-Eighth IAS Annual Meeting, 1993: IEEE, pp. 843-849.

LOW COST, HIGH DYNAMIC RANGE POSITION SENSING ENABLED BY OVERSAMPLING AND AVERAGING

Brij M. Bhushan[1], David L. Trumper[1]
[1]Department of Mechanical Engineering
Massachusetts Institute of Technology
Cambridge, MA, United States of America

INTRODUCTION

Sensors place a fundamental limit on system performance and stability for mechatronic systems with closed loop feedback. There is a strong correlation between sensor cost and performance resulting in a constant thrust to improve the performance-to-cost metric of sensing systems. One of the ways to improve sensing performance is by oversampling and averaging. With reducing computation costs and the availability of low-cost, high-speed analog-to-digital (ADC) converters, this is becoming a feasible approach even for regular motion control systems.

This paper describes such an approach using Contrinex DW-AS-509-M8-390, a low-cost eddy-current sensor having a measurement range of 2.5 mm and available for about US $100. Measurement with typical connections to a 16-bit ADC converter and no filtering, results in a mid-point resolution (measurement resolution at half the sensor range) of 500 nm−rms which is a dynamic range (range/resolution at a given bandwidth) of 5×10^3 (76 dB) at 500 Hz bandwidth. By implementing anti-aliasing filters, sampling at 20 kHz, and then low-pass filtering with a 500 Hz cut-off, we demonstrate a mid-point resolution of 100 nm−rms resulting in a dynamic range of 2.5×10^4 (88 dB) at 500 Hz bandwidth. Capacitive sensors with high-accuracy amplifiers for a similar measurement range of 2 mm exhibit a mid-point resolution of 10 nm−rms resulting in a dynamic range of 2×10^5 (106 dB) at 500 Hz bandwidth. However, these capacitive sensing systems (probe + amplifier) typically cost upwards of US $3000 per channel. Thus, we are able to achieve $1/10^{\text{th}}$ the performance at about $1/30^{\text{th}}$ of the cost.

The approach described in this paper is translatable to many different kinds of analog sensor measurement systems. Care should be taken to achieve a flat noise power spectrum so that the noise histogram is approximately Gaussian in nature. Enough bit-width must also be maintained in the computation-chain to obtain sufficient accuracy. We also provide links to sample LabVIEW code for implementation using National Instruments (NI) hardware.

BACKGROUND THEORY

Oversampling refers to the process of sampling a signal at a significantly higher rate than the Nyquist frequency [1]. In feedback control applications, oversampling refers to sampling the sensor signal much faster than the control loop rate. Oversampling is capable of improving the resolution and signal-to-noise ratio (SNR) and hence, the dynamic range (DR) within the control loop bandwidth. A high SNR and high DR are important requirements of sensing for mechatronic systems with closed loop feedback.

The impact of oversampling and averaging can be studied from the time-domain and the frequency-domain viewpoints. The core idea is that the sampled analog signal is a summation of the signal and noise components. If the noise is perfectly random (Gaussian probability distribution function (pdf) with variance σ^2), then by taking the average of N such samples, the noise variance reduces to σ^2/N. We sample much faster than the Nyquist rate corresponding to the control-loop bandwidth so that the averaging step does not add significant phase lag to the signal. Further, to minimize phase-drop within the pass-band, we implement an Infinite Impulse Response (IIR) low-pass filter such as Butterworth [2] rather than a moving average filter which has a linear phase drop with frequency.

A good treatment from the time-domain viewpoint of oversampling and averaging is given in application note AN118 by Silicon Laboratories [3]. For the frequency domain viewpoint, we build on the analysis in Chapter-4, Section-8,9 of [4]. The sensor analog output is a summation of signal and noise components. We assume that the noise is perfectly random white noise, i.e. a Gaussian pdf with variance σ^2, with a flat one-sided power spectral density (PSD) stretching from 0 to ∞. ADC sampling practically maps this energy to within 0 to $f_s/2$, where f_s is the sampling frequency, with a flat one-sided PSD, to give almost the same variance. Hence, the signal noise after sampling will have a PSD value of $\sigma^2/(f_s/2)$. The quantizer in an ADC can be modeled as an additive white-noise source (Gaussian) with 0 mean,

and variance of $\Delta^2/12$, where Δ corresponds to the amplitude of the least significant bit, or the quantization level [4]. These noise sources are independent and add together to give 0 mean and variance of $\left(\sigma^2 + \Delta^2/12\right)$, within a bandwidth of $f_s/2$. The noise still looks like white noise with a flat spectral power density amplitude of $(\sigma^2 + \Delta^2/12)/\left(f_s/2\right)$. Now by applying a low-pass filter (ideal) with cut-off frequency, f_{lpf} in the discrete domain on the sampled signal, the noise power beyond f_{lpf} is discarded resulting in a noise spectrum with a variance of $\left(\sigma^2 + \Delta^2/12\right) \cdot 2f_{lpf}/f_s$. The corresponding dynamic range then is the ratio of the maximum signal amplitude (X_m) to the standard deviation of noise $\left(\sqrt{(\sigma^2 + \Delta^2/12) \cdot 2f_{lpf}/f_s}\right)$ within the bandwidth of f_{lpf}.

REQUIREMENTS FOR OVERSAMPLING AND AVERAGING

Oversampling and averaging is effective when the dominant noise sources in the signal chain can be modeled as white noise, having a flat power spectral density (PSD) over the frequency band of interest and a Gaussian histogram, with 0 mean and variance σ^2. Further the noise amplitude must be sufficient the cause the input signal to change randomly from sample to sample by at least the least significant bit (LSB) [3].

To achieve a flat noise spectrum, it is important to carefully ground and shield the circuit components [5] to avoid picking up capacitively- and inductively-coupled noise into the measurement system. Using analog anti-aliasing filters at the ADC input is critical in rejecting high-frequency noise that may be injected from the environment and could potentially alias into the lower frequency signal bands after sampling [4] (Chapter-4).

Another requirement is the ability to sample much faster than the required closed loop feedback bandwidth. The faster sampling relaxes the requirements of cut-off frequency and sharpness of attenuation, for the analog anti-aliasing filter and the digital low-pass filter after sampling. Usually the computations are fixed-point numeric and the computation chain should have enough bit-width, and appropriate range and precision so that no truncation or overflow occurs.

If the noise is correlated or there is some non-linearity, either in the sensor or the ADC, the histogram may not approximate a Gaussian PDF and therefore, the oversampling and averaging may not be helpful in reducing the noise floor [3].

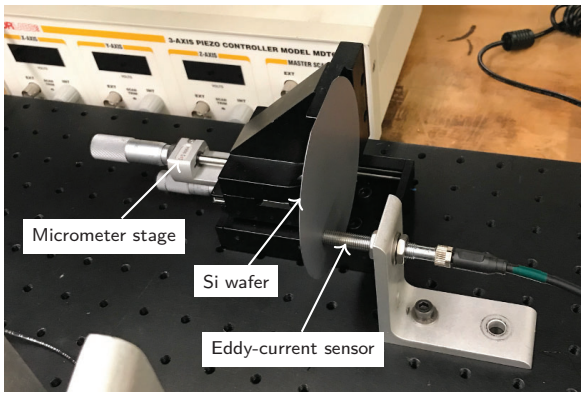

FIGURE 1. Experimental setup: Eddy current sensor measures motion of a Silicon wafer as a thin conductive target.

IIR filter implementations are prone to round-off errors, especially if the filter cut-off frequency is low compared to the sampling frequency [2]. Therefore, sampling speed should be fast to get enough attenuation from anti-aliasing filters, but not greater than 50-times the filter cutoff frequency, as a practical matter. Too high a sampling frequency can severely degrade the filter numerical performance or require more intensive computation which reduces the speed.

IMPLEMENTATION OF OVERSAMPLING AND AVERAGING

To demonstrate the effect of oversampling and averaging, we use a low-cost eddy current sensor, the Contrinex DW-AS-509-M8-390, having a measurement range of 2.5 mm. Measurement with typical connections to a ±10V, 16-bit ADC converter, and no averaging, result in a mid-point resolution (measurement resolution at half the sensor range) of 500 nm—rms, which is a dynamic range (range/resolution at a given bandwidth) of 5×10^3 (76 dB) at 500 Hz bandwidth.

The sensor target is a thin conductive Si-wafer and Figure 1 shows the setup. Using the thin conductor gives a linear response for position vs. voltage which is beneficial for linear feedback control. A precision motion stage with a micrometer is used to calibrate the sensor for its entire working range (Figure 2). This gives us a scaling factor of 3.37 µm/mV.

The sensor output is connected through a shielded twisted pair cable, through the anti-aliasing filter to the differential ADC inputs of the National Instruments, NI-9222 module. The shield of the twisted pair cable is grounded only at the sensor end.

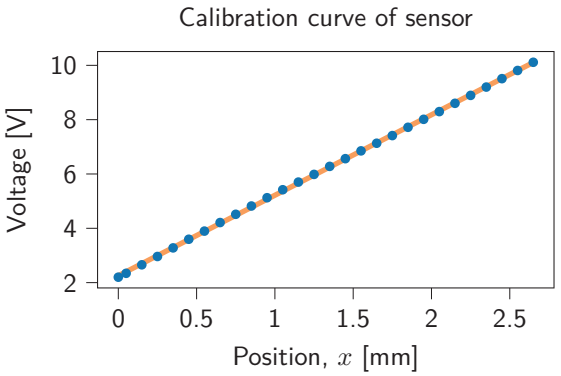

FIGURE 2. Calibration plot of sensor. The target is a conductive Silicon wafer, 0.36 mm thick. The response is linear, with a working range of about 2.5 mm. The fit line has a slope of 2.96 V/mm, an intercept of 2.25 V, and an R^2 of 0.9998. This corresponds to a scaling factor of 0.337 µm/mV

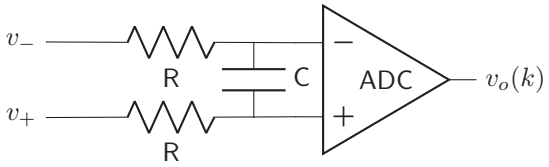

FIGURE 3. Anti-aliasing filter (AAF) schematic: The AAF consists of resistance (R) connected to each of the positive and negative differential inputs of the ADC, with a capacitor (C) connected across them to form a 1st-order differential low-pass filter

The anti-aliasing filter (AAF) is a simple 1st-order differential low-pass filter built of passive components and has a 5 kHz cut-off frequency [6], as shown in Figure 3. The resistance (R) value is based on input and output stage impedance loading. The input impedance should at least be 10-times greater than the output impedance of the sensor and at least $1/10^{\text{th}}$ the ADC input impedance. The sensor has a regulated voltage output and can sink a maximum current of 10 mA. Therefore, at a maximum voltage of 10 V, the anti-aliasing filter should have a resistance greater than 1 kΩ. The input impedance of the NI 9222 is greater than 1 GΩ and a resistance less than 100 MΩ is sufficient. We choose R value of 100 kΩ. The max sampling frequency (f_s) of NI 9222 is 300 kHz and the Nyquist frequency ($f_N = f_s/2$) is 150 kHz. The signals beyond f_N should be attenuated as much as possible so that they are not aliased. We choose a cut-off frequency of 5 kHz to be greater-than 10-times the expected closed loop bandwidth around 100 Hz. We then select the value of the AAF capacitor (C), from the filter cutoff formula $f_{AAF} = 1/(2\pi \cdot 2RC)$, to get a C value of 160 pF. The variations between the two R values may cause a dynamic error in transient measurements. Therefore, we choose matched resistor networks with a matching tolerance of 0.01 % leading to a maximum full-scale error of 0.01 % of 10 V which is 0.1 mV, below the quantization level of the 16-bit ADC input.

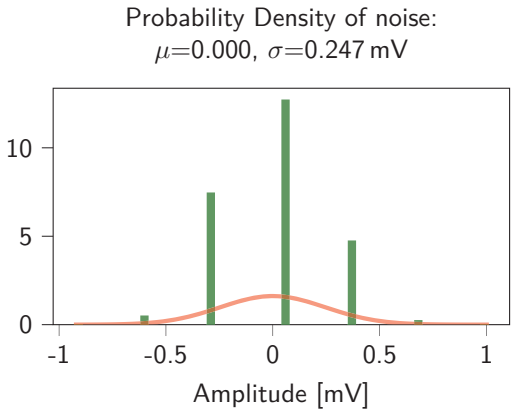

FIGURE 4. Normalized histogram of grounded analog input. Data captured for 10 s, with 5 kHz sample-rate.The quanta corresponding to the least significant bit of the 16-bit ADC, $20/2^{16} = 0.305$ mV. The noise spans approximately 5 bits peak-to-peak

The signals are sampled in the 16-bit NI-9222 module at a desired rate up to 300 kHz, and the signal processing is done on the the NI-FPGA module built into the NI cRIO-9064 controller. The signal then passes through a 4th-order Butterworth low-pass filter with a cut-off frequency of 500 Hz. A fixed-point (FXP) bit-width of 25 is maintained in the signal processing chain to accommodate the increase in resolution due to the low-pass filtering. The value from the low-pass filter is placed in a memory location from which the control-loop can read the values at a lower rate of 5 kHz, which is like a decimation step [4].

RESULTS AND DISCUSSION

The first step is to measure the noise of a grounded Analog Input (AI) measurement as that sets the baseline noise floor. Figure 4 shows the histogram of the captured noise waveform to get the baseline noise-floor of the ADCs. The rms noise of the grounded ADC is 0.247 mV.

Next, we sample at 5 kHz (the loop rate), without any filtering to set the comparison reference. This is referred to as the "Raw" signal. Since the spread of the noise is much greater than that corresponding to the ADC least-significant bit, we can ignore the contribution due to the ADC quantizer noise. Then, we filter the waveform by sampling at 20 kHz, passing through a 4th-order Butterworth filter, and being re-

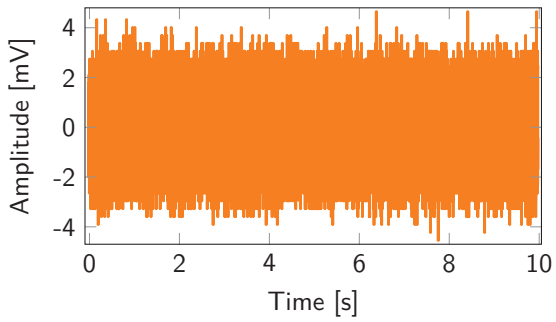

(a) Raw

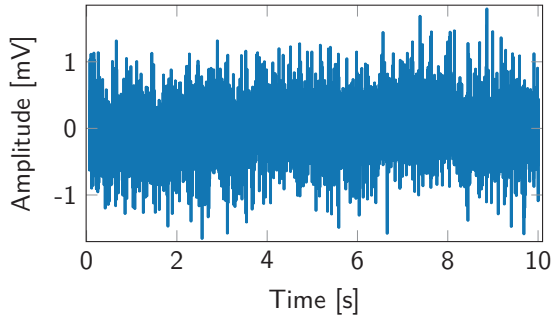

(b) Filtered

FIGURE 5. Time wave-forms of sensor noise, captured for 10 s.(a) Sampled at 5 kHz, no filtering. (b) Sampled at 20 kHz, filtered using 4th-order Butterworth with cut-off frequency of 500 Hz, then re-sampled by the control loop at 5 kHz

sampled by the control-loop at 5 kHz. This is referred to as the "Filtered" signal. Figures 5, 6, 7 show the time-waveforms, histograms, and the power spectral density (PSD) plots for the raw and filtered signals.

The noise level after filtering is 0.30 mV—rms at 500 Hz, which is a sufficiently higher frequency than the required control-loop crossover about 100 Hz. Using the analytical approximation developed in an earlier section and ignoring the noise contribution from the ADC quantizer, we obtain a noise estimate of $1.284 \cdot \sqrt{500/10000} = 0.29$ mV − rms that is close to the measured value. Further increase in sample-rate gives limited noise reduction, primarily because of numerical round-off in the Butterworth filter. Therefore, a practical upper limit of the sample rate is about 200-times the crossover frequency.

A position measurement resolution of 100 nm—rms is obtained by scaling the measured voltage noise level with the position-to-voltage scaling factor of 0.34 µm/mV for the sensor. Thus, the dynamic range of measurement is 2.5×10^4 (88 dB) at 500 Hz bandwidth. This measurement is at the mid-point of the sensor range, i.e.,at 5 V output. We observe that the

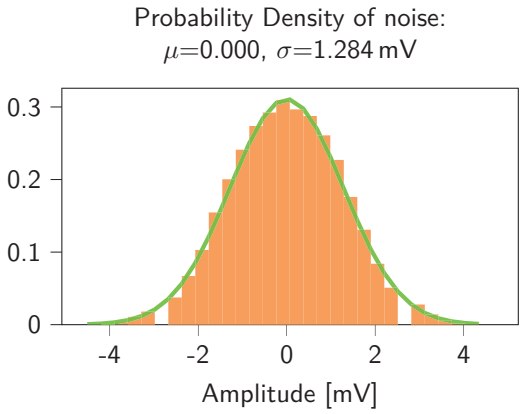

(a) Raw

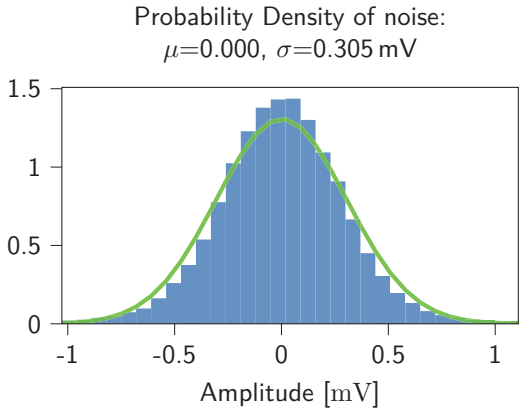

(b) Filtered

FIGURE 6. Normalized histogram of sensor noise, captured for 10s. (a) Sampled at 5 kHz, no filtering. The histogram shape approximates a Gaussian distribution indicating a flat power spectral density and therefore, oversampling and averaging can reduce the noise. (b) Sampled at 20 kHz, filtered using 4th-order Butterworth with cut-off frequency of 500 Hz, then re-sampled by the control loop at 5 kHz

sensor noise level correlates with the output voltage level. At lower voltages of less than 3 V, we obtain a position measurement resolution of about 50 nm—rms at 500 Hz bandwidth.

To optimally utilize the anti-aliasing filter by attenuating all frequencies beyond the Nyquist frequency, we can sample the ADC input at 300 kHz, followed by a 4-point moving average filter. The signal is then resampled at a lower frequency such as 20 kHz (a decimation step), for better numerical accuracy in the Butterworth filter implementation. A moving average filter can be added in the high-frequency sampling loop since it has a minimal phase drop (only 0.2° in this case) at the loop crossover frequency of about 100 Hz and increases the effective-number-of-

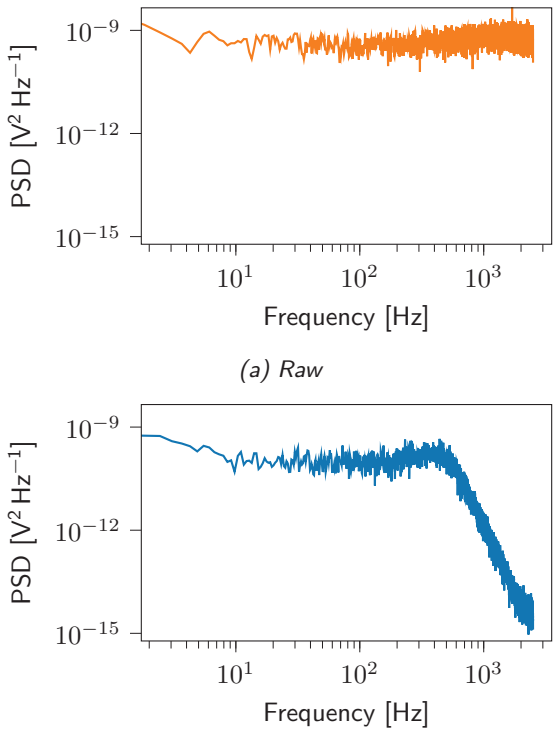

FIGURE 7. Power spectral density (PSD) of sensor noise, captured for 10s. (a) Sampled at 5 kHz, no filtering. The flat power spectrum corresponds to the Gaussian probability distribution. (b) Sampled at 20 kHz, filtered using 4th-order Butterworth with cut-off frequency of 500 Hz, then re-sampled by the control loop at 5 kHz. The PSD drops sharply beyond the Butterworth filter cut-off at 500 Hz

bits after sampling by 1. This mode of operation gives 80 nm—rms noise at 500 kHz bandwidth. In our current setup, we directly sample at 20 kHz followed by the Butterworth filter, which means that the 1st-order anti-aliasing filter at 5 kHz cut-off provides only little attenuation until the nyquist frequency of 10 kHz. We don't notice a significant difference between either of the two modes indicating minimal high-frequency noise pickup. In noisier environments, it may be helpful to sample as fast as possible and also to implement a higher order anti-aliasing filter for a faster roll-off.

SUMMARY

In this paper, we presented an example of obtaining high-precision measurements from low-cost sensors by oversampling and averaging the sensor output. We discussed the theoretical aspects, and implementation details and results using the example of a Contrinex DW-AS-509-M8-390, eddy current sensor demonstrating 100 nm—rms noise at 500 Hz bandwidth. Since most macro-scale mechatronic systems have a crossover frequency of about 100 Hz, this is a cost-effective way to implement sensing for high-precision feedback systems. The approach described in this paper is translatable to many different kinds of analog sensor measurement systems where we are able to obtain a flat noise power spectrum so that the noise distribution is Gaussian in nature.

SOFTWARE

Sample LabVIEW code for implementation and testing oversampling and averaging using National Instruments (NI) Analog-to-Digital Converter (ADC) hardware is provided at [7]. The software can also be used as a tool to characterize the dynamic noise performance of any analog sensor.

REFERENCES

[1] *Oversampling - Wikipedia*. [Online]. Available: https://en.wikipedia.org/wiki/Oversampling (visited on 03/26/2020).

[2] *IIR Filters and FIR Filters*, 2018. [Online]. Available: http://zone.ni.com/reference/en-XX/help/370858P-01/genmaths/genmaths/calc_filterfir_iir/ (visited on 03/26/2020).

[3] "Improving Adc Resolution By Oversampling and Averaging," pp. 1–20, 2013. [Online]. Available: https://www.silabs.com/Support%20Documents/TechnicalDocs/an118.pdf.

[4] A. V. Oppenheim and R. W. Schafer, *Discrete-Time Signal Processing*, 3rd edition. Pearson Education Limited, 2013, p. 647, ISBN: 978-0131988422.

[5] D. L. Trumper, "Grounding and shielding Notes," [Online]. Available: https://pmc.mit.edu/sites/default/files/Grounding_Shielding_Notes.pdf.

[6] R. Andrews, *Three guidelines for designing anti-aliasing filters*. [Online]. Available: https://e2e.ti.com/blogs_/archives/b/precisionhub/archive/2015/11/06/three-guidelines-for-designing-anti-aliasing-filters (visited on 03/26/2020).

[7] B. Bhushan, *Analog Input Noise Characterization*. [Online]. Available: https://github.com/mbrijbhushan/AI_NoiseCharacertization.

IMPROVED CURRENT CONTROL OF INVERTER FED TWO-PHASE BIPOLAR STEPPER MOTORS USING REPETITIVE CONTROL

Boaz Kramer
ACS Motion Control

INTRODUCTION

Three-phase inverters for controlling three phase permanent magnet synchronous motors (so-called "brushless" motors) are widely used in motion control applications. The same three-phase inverters may be used to control two-phase motors, and particularly the very common two-phase bipolar stepper motors [1]. This is a more economical option than the eight-transistors full bridge inverter that is usually used for two-phase stepper control.

One disadvantage is that the two motor phases are no longer individually controlled, as they are tied together and are therefore electrically coupled. This coupling along with the dead-time effect of the power transistors and the stepper motor's own characteristics, such as high harmonics in the Back-EMF waveforms, may cause phase current asymmetry, zero-crossing distortion, and high harmonic distortion. As a result, the stepper operation becomes noisier, vibrations may be induced, the micro-stepping dynamic accuracy is impaired, and the stepper may get hotter. The Proportional-Integral (PI) Controllers that are typically used in the Field-Oriented Control scheme are inadequate to cope with these harmonics because of their limited control bandwidth and the relatively high frequencies of the harmonics.

The paper suggests a Repetitive Control approach to solve these issues and significantly improve the motor current waveforms and overall performance.

SYSTEM CONFIGURATION

Figure 1 describes a two-phase bipolar stepper motor operated by a three-phase inverter fed from a DC voltage supply U_{DC}. Unlike the conventional full H-bridge that uses four power transistors per phase and eight transistors in total, here only six transistors are used to drive the two-phase motor. Phases "T" and "S" of the inverter are used to control the stepper motor windings "A" and "B" respectively. Phase "R" of the inverter is connected as the common of windings "A" and "B" of the motor, and its potential is modified by a space vector modulation algorithm [1],[2]. This increases the available inverter voltage output range by a factor of $\sqrt{2}$ [1],[2].

For micro-stepping control it is desired to have sine and cosine currents in windings "A" and "B", at an excitation frequency that is determined according to the desired speed. The control is typically done in a dq-axis frame that is rotating synchronously with the excitation current [2], where it's typically desired to have constant DC currents.

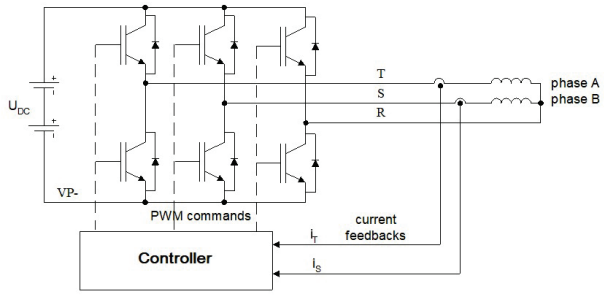

FIGURE 1. Two-phase bipolar stepper motor fed from a three-phase Inverter

MOTOR MODEL

The model of a two-phase bipolar stepper motor can be expressed in a dq-axis frame that is rotating synchronously with the excitation current, as follows [1]:

$$\begin{bmatrix} v_q \\ v_d \end{bmatrix} = \begin{bmatrix} L_q s + R & L_d \omega_e \\ -L_q \omega_e & L_q s + R \end{bmatrix} \begin{bmatrix} i_q \\ i_d \end{bmatrix} + \\ + K_e \frac{\omega_e}{p} \begin{bmatrix} cos(\Delta\theta_e) \\ sin(\Delta\theta_e) \end{bmatrix} \quad (1)$$

Where v_q, v_d, i_q, and i_d are qd-axis voltages and currents, respectively, ω_e is the excitation frequency, R is the motor phase resistance, and L_q and L_d are dq-axis inductances. The last term in (1) denotes the motor back-EMF. $\Delta\theta_e$ is the angle between the d-axis and the rotor electrical position, p is the number of pole-pairs, and K_e is the Back-EMF constant.

For simplicity, we will assume $L_q = L_d = L$ for the rest of this discussion.

Assuming the following vector notation:

$$f_{qd} = f_q - jf_d \qquad (2)$$

where f represents a generic complex vector quantity, and f_q and f_d its qd-axis components, Eq. (1) may be expressed in a more convenient vector form:

$$v_{qd} = (Ls + R + jL\omega_e)i_{qd} + K_e \frac{\omega_e}{p} e^{-j\Delta\theta_e} \quad (3)$$

When excluding cogging torque, the generated motor torque can be expressed as the following dot product:

$$T_e = K_e e^{-j\Delta\theta_e} \cdot i_{qd} \qquad (4)$$

Unlike brushless motors' field-oriented control, the above model is synchronized with the current vector and not the rotor position, as micro-stepper driven systems typically don't have a collocated position sensor (directly coupled to the motor shaft) that allows proper position-based commutation of the motor currents. A non-collocated position sensor (on the load side) may exist, but it is usually inadequate for proper commutation because of backlash effects and the relatively short electrical cycle of the stepper motor.

TYPICAL CURRENT CONTROL

Typically, the current control of the stepper motor is done in the synchronous dq-axis frame, with a Proportional-Integral (PI) regulator for each of the axes. Typically, the zero of each PI filter is chosen to cancel the pole of the controlled plant, $s = -R/L$, when the system is at standstill.
However, the poles of the controlled system (3) in the rotating frame, $s = -R/L - j\omega_e$, migrate along the imaginary axis when the speed increases. This degrades the current loop performance as speed increases.
One way of solving this problem is to eliminate the cross coupling between the q and d axes caused by the $j\omega_e$L term in Eq. (3).
A complex vector block diagram of the current controller with cross-coupling elimination is shown in Figure 2. The term $j\omega_e\hat{L}$ is used for decoupling, where $\hat{L}$ is the estimated motor inductance. The effect of decoupling is to move the pole of the plant from $s = -R/L - j\omega_e$ to $s = -R/L$ in the synchronous reference frame, making the performance of the current regulator independent of the excitation frequency.
The Back-EMF term in Eq. (3) is treated as a disturbance to the current regulators since $\Delta\theta_e$ is a function of the external load force, as seen in Eq. (4).

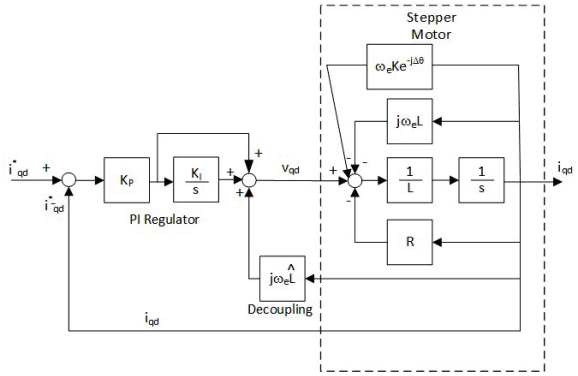

FIGURE 2. Complex vector block diagram of a stepper motor with a synchronous frame PI current regulator and cross-coupling elimination

In general, the commands i_d^* and i_q^* are set to zero and the rated current of the motor, respectively. Additional harmonics may be deliberately added to these commands to compensate for cogging effects [2], however the latter will not be discussed in this paper.

CURRENT WAVEFORM DISTORTIONS

As the speed increases the current waveforms of the two-phase stepper start to get distorted. Undesired harmonics are generated in i_q and i_d currents, and the currents of phases "A" and "B" no longer have the desired waveforms, that in our case are sine and cosine. This is a result of several factors: the dead-time of the inverter (meant to prevent a shoot-through condition) introduces non-linearity and zero crossing distortion [3], the Back-EMF disturbances that usually include higher order harmonics, and the mutual magnetic coupling between the two phases. Though ideally the motor phases are supposed to be magnetically decoupled, in practice some coupling exists. When using the three-phase inverter the problem is more severe, as the motor phases are tied together, and therefore are electrically coupled and no longer independently controlled.
Typical distortions in the current phases of a two-phase stepper motor are shown in Figure 3.

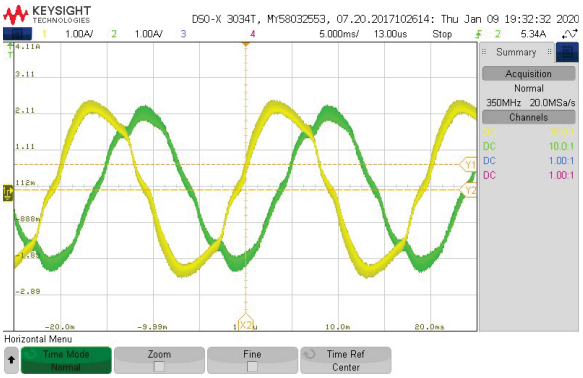

FIGURE 3. Typical current loop distortions observed in a two-phase Stepper motor

As a result of these distortions, the stepper operation becomes noisier, vibrations may be induced, the micro-stepping dynamic accuracy is impaired, and the stepper may get hotter due to the undesired current harmonics.

TIME / FREQUENCY DOMAIN REPETITIVE CONTROL

Since the distortions in the current waveforms appear repetitively every cycle, a Repetitive Controller [4], in parallel with the PI regulator of each axis, may be considered.

The Repetitive Controller is based on the Internal Model Principle, which states that to asymptotically track a reference signal with zero error the generator polynomial (model) of this signal must be included as part of the controller.
For periodic signals a memory loop can be used. The memory loop implementation is based on a cyclic memory buffer (FIFO) with a period equal to the fundamental excitation period of the phase currents. If a positive feedback is put over this FIFO buffer, in steady state no input is needed to generate an output with the given period.
The memory buffer samples data in time domain and uses it iteratively to refine a correction signal.

A possible discrete implementation is shown in Figure 4; this implementation is different from the implementation described in [4], as the Repetitive Controller compensation is added to the output of the PI regulator, denoted in the figure by C(z), and not to its input. This modified implementation achieved faster convergence of the Repetitive Controller. In Figure 4 the Repetitive Controller is implemented by a positive feedback FIFO with size N, that is determined according to the excitation period of the motor T, and the sampling period T_s:

$$N = T/T_s \qquad (5)$$

The Learning Filter L(z) is used to compensate the transfer as seen by the Repetitive Controller. The Robustness Filter Q(z) is used to limit the bandwidth of the Repetitive Controller, to avoid amplification of undesired noise and guarantee the algorithm stability.
Q(z) may be implemented as a symmetrical lowpass FIR filter and its delay maybe compensated by adjusting the delay of the FIFO buffer.

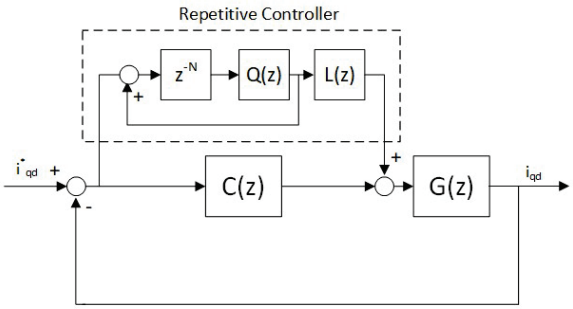

FIGURE 4. Complex vector block diagram of the control loop with a Repetitive Controller

The plant G(z) may be considered as a simple RL model, due to the decoupling that is shown in Figure 2, and consideration of the BEMF as a disturbance. Its Zero-Order Hold discrete equivalent is given by:

$$G(z) = \frac{U_{DC}}{2R}\frac{(1-e^{-RT/L})}{(z-e^{-R\ /L})} \qquad (6)$$

C(z) is a PI regulator, implemented as follows:

$$C(z) = K_P\frac{(K_I T_S+1)z-1}{z-1} \qquad (7)$$

Similar to Iterative Learning Control implementations [5], it can be shown that the required Learning Filter may be calculated as follows:

$$L = (GS)^{-1} \qquad (8)$$

Where S is the loop Sensitivity Function.

Using (6), (7) and (8) the derived Learning Filter will have the following non-causal form:

$$L(z) = z\frac{a_2 z^2+a_1 z+a_0}{z^2-z} \qquad (9)$$

The parameters a_0, a_1, a_2 are determined according to the motor parameters R, L and the PI regulator gains. Roughly speaking, one zero of Eq. (9) corresponds to frequency R/L, while the other one corresponds to loop bandwidth (open loop zero crossing frequency). The non-causal "Z" term may be inserted into the memory loop and compensated from the FIFO size (together with the delay of the filter Q(z)). Therefore, a Causal Learning filter will have the form:

$$L(z) = \frac{a_2 z^2 + a_1 z + a_0}{z^2 - z} \qquad (10)$$

Stability of the learning algorithm will be guaranteed for any FIFO size, if the following inequality is met for all frequencies:

$$\left| Q(z)\left(1 - \mathrm{GS(z)L(z)}\right) \right| < 1 \qquad (11)$$

The above Repetitive Controller has been implemented using an ACS Motion Control controller and tested at various velocities with a standard 1.8^0 stepper. When the memory buffer size was properly selected, it successfully eliminated the undesired distortions.
An example is shown in Figure 5, and may be compared with Figure 3. This is for an excitation frequency of 50Hz corresponding to 1 rev/sec in a 1.8^0 stepper. The same Repetitive Controller is also effective for excitation frequencies that are multiple integers of 50Hz and was tested up to 20 revolutions per second.

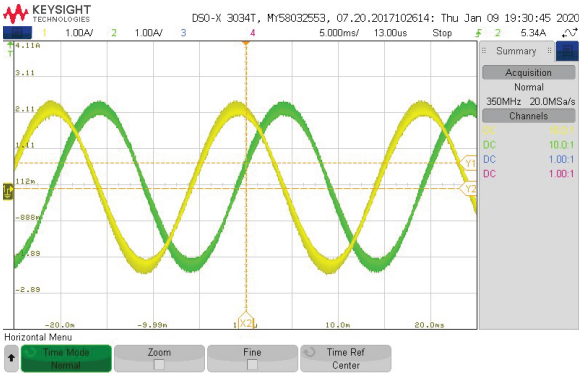

FIGURE 5. Stepper motor currents with Repetitive Control

Figure 6 shows Open-Loop FRF measurement of d-axis current loop measured with white noise excitation. The figure shows the FRF results with (red) and without (blue) a Repetitive Controller that is set for an excitation frequency of 50Hz. It can be seen that the controller has increased gain peaks, and therefore reduced sensitivity, at 50Hz and at its integer multiples. The increased gain peaks continue up to the Q-filter bandwidth, set to 2kHz in this example. It can be also observed that proper stability margins are maintained.

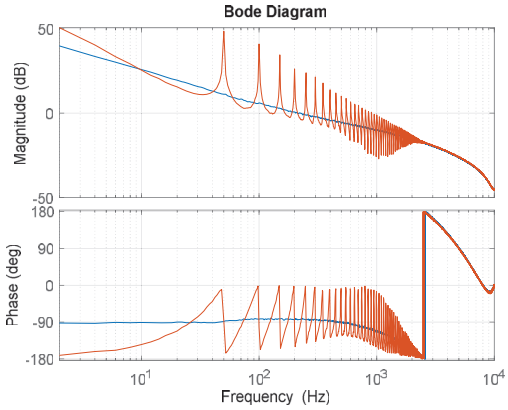

FIGURE 6: Open loop FRF current loop with (red) and without (blue) a Repetitive Controller, set for an excitation frequency of 50Hz.

ANGLE DOMAIN REPETITIVE CONTROL

The proposed Repetitive Controller has one disadvantage: it is not useful when the period of disturbance varies with time. The size of the memory buffer (N) times the sampling frequency must be equal to the desired excitation period, and the Repetitive Control will not work at all for frequencies that are not multiple integers of that excitation frequency.
It is worth noting that the undesired distortions have fixed periods in the angle (or phase) domain. Therefore transforming the Repetitive Controller into an Angle Domain Repetitive Controller merits consideration.
The Angle Domain Repetitive Control [6] is very similar to the Time/Frequency Domain Repetitive Control, except that the excitation period T now is an angle-based period instead of time-based period. Instead of taking samples at fixed time intervals of T_s, they are now taken at angle intervals of $\Delta\theta_S$ and putting a Zero-Order Hold in the angle domain.

This has another advantage over the time domain implementation: In the time domain Repetitive Controller, the memory buffer size is inversely proportional to speed and may get rather large at low velocities; in the angle domain the memory buffer size is fixed and depends on the desired angle resolution $\Delta\theta_S$.

Any time-based model may be transformed to angle-based model [6]. Repetitive Control could

be applied to any model in the angle domain, using a similar methodology that was described in the previous section. In fact, it can be shown that the exact same Repetitive Controller that was designed for the time domain, can be also used in the angle domain, if the filters L and Q are still calculated at period T_s and interpolation is used in between the memory buffer entries.

The angle domain Repetitive Controller was implemented using an ACS Motion Control Controller. It was efficient in eliminating the various distortions at any operating frequency.

Figures 7 and 8 show the motor currents' Lissajous plots at a velocity that is not an integer number of cycles per second, without and with the Angle Domain Repetitive Controller, respectively.

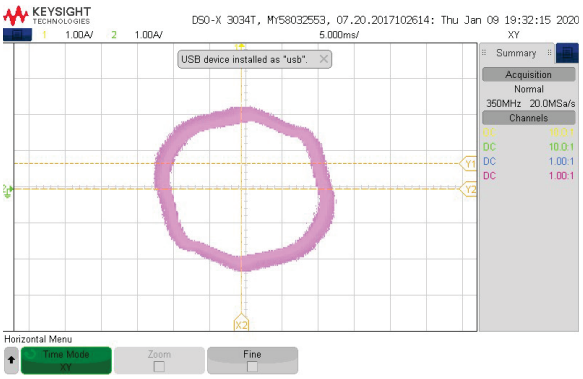

FIGURE 7: Motor currents Lissajous at a velocity of 5.3 rev/sec with just PI Control

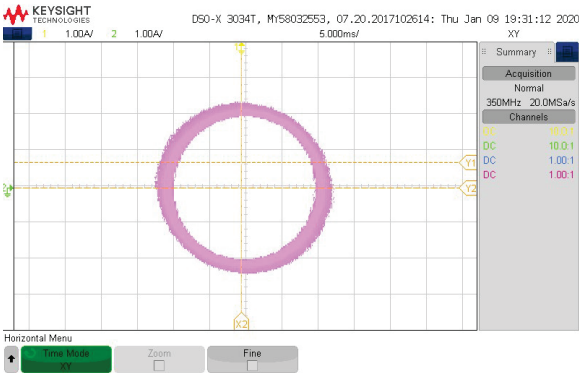

FIGURE 8: Motor currents Lissajous at a velocity of 5.3 rev/sec with the Angle Domain Repetitive Controller

CONCLUSIONS

Repetitive Control can mitigate repetitive disturbances and distortions in the phase currents of a two-phase stepper motor. It can potentially help to achieve smoother motion, higher accuracy, and less motor heat. The Angle Domain Repetitive Controller is insensitive to speed variations and therefore more effective and practical. Such control may be used to improve the waveforms of any polyphase motor type, and is not limited to the specific example of the two-phase stepper motor. In addition, Angle Domain Repetitive Controllers may also be used to eliminate angle (or position) dependent disturbances, such as motor cogging, more efficiently.

REFERENCES

[1] S. M. Yang, F. C. Lin, and M. C. Chen, "Control of a two-phase linear stepping motor with three-phase voltage source inverter," in Proc. IEMDC'03, June 2003, pp. 1720–1725

[2] S. M. Yang, F. C. Lin, and M. C. Chen, "Micro-Stepping Control of a Two-Phase Linear Stepping Motor With Three-Phase VSI Inverter for High-Speed Applications", in IEEE Trans. on Industry Applications, vol. 40, no. 5, September/ October 2004

[3] Bose B. K., "Power Electronics and Variable Frequency Drives", IEEE Press, 1997.

[4] Steinbuch M., van de Molengraft R., "Repetitive Control for Systems with Uncertain Period-Time", Automatica 38, pp. 2103-2109, 2002.

[5] Oomen T., "Learning in Machines", Microniek nr 6, 2018.

[6] Nakano M., She J.-H, Mastuo Y., Hino T., "Elimination of Position-Dependent Disturbances in Constant-Speed-Rotation Control Systems", in Control Eng. Practice, Vol. 4, No. 9, pp. 1241-1248, 1996.

DYNAMICS AND CONTROL OF THE PTB NANOMETER COMPARATOR

P. Köchert[1], R. Köning[1], C. Weichert[1], J. Flügge[1], E. Manske[2]
[1] Physikalisch-Technische Bundesanstalt (PTB), Braunschweig, Germany
[2] Ilmenau University of Technology, Ilmenau, Germany

ABSTRACT
This paper reports on the design, implementation, and experimental results for the control of PTB's Nanometer Comparator. This length comparator is measuring the unidirectional distances of markers on scales and photomasks as well as displacements of encoders and interferometers with sub-nanometer resolution. The machine had been upgraded with a dual-stage drive system. The new setup enables to control the position of calibration objects with sub-nanometer precision over the entire measuring range of 600 mm. We introduce a distributed controller concept using DSP- and FPGA-based equipment. We also present the modeling of our controller design and verify its performance by means of frequency response analysis. The experimentally demonstrated control error exhibits a standard deviation of 0.25 nm at a bandwidth of 145 Hz.

INTRODUCTION
Motion control on the sub-nanometer level is a crucial task in many areas of precision engineering. High-tech manufacturing and inspection machines rely on position sensors with sub-nanometer repeatability over measuring ranges up to 500 mm [1]. To characterize such sensors, photomasks and line scale standards, the national metrology institute of Germany (PTB) developed in cooperation with the company Dr. JOHANNES HEIDENHAIN GmbH a vacuum length comparator, the so-called Nanometer Comparator (NMC). The NMC was designed to comply with fundamental design principles in precision engineering, which have been outlined e.g. by SCHELLEKENS *et al.* [2]. Since this reference measuring machine was put into operation in 2000, the machine structure has continuously been optimized to calibrate length standards, e.g. line scales [3], encoders [4] and laser interferometers [5], more accurately. For that matter the positioning system of the NMC has been ungraded. The goal of this retrofit was to reduce the positioning noise of about 10 nm [6]. The reduction of these unwanted position variations is beneficial for the calibration of customer systems, which cannot be synchronized to the interferometer system of the NMC. Transferring the results of previous investigations of an air-bearing stage [7], the position of systems to be calibrated can now be controlled with sub-nanometer resolution [4].
Inspired by HOCKEN *et al.* [8], the present work focuses on the positioning system and the development of its control algorithm. We are starting with an overview of the motion control concept by introducing the three structural subsystems: drive, sensor and controller system. We continue by describing the development of our control algorithm and finally show experimental results.

SYSTEM DESCRIPTION

Drive System
The original system to drive the positioning table of the NMC consisted of a linear motor with a continuous peak force of 90 N. Between this linear motor and the driving rod of the positioning table a voice coil actuator (VCA) with a continuous peak force of 25.78 N was added (see Fig. 1 for details). Both actuators form a dual-stage drive system. The linear motor and positioning table are guided independently using air bearing systems to avoid friction force characteristics. The old transmission element of the feed mechanism consisting of a rod and two thin places was replaced by a driving rod made of carbon-fiber reinforced polymer (CFRP) with a length of 0.6 m. The new feed mechanism offers an improved mechanical stiffness, minimal drive offset, low weight and a spatially separation of heat sources (motors) from the measurement objects. The VCA represents an actively controlled bearing system between table and drive system. This new setup avoids previously integrated passive connecting elements offered a lower mechanical stiffness. A decoupling is required to allow for relative motions ($Y, Z, \varphi_X, \varphi_Y, \varphi_Z$) of the positioning table and linear motor. But the mechanical thin places limited the control bandwidth to around 25 Hz.
In addition, disturbing cogging forces generated by the linear motor (see Fig. 1) are not transmitted anymore over the actively controlled VCA onto the positioning table.

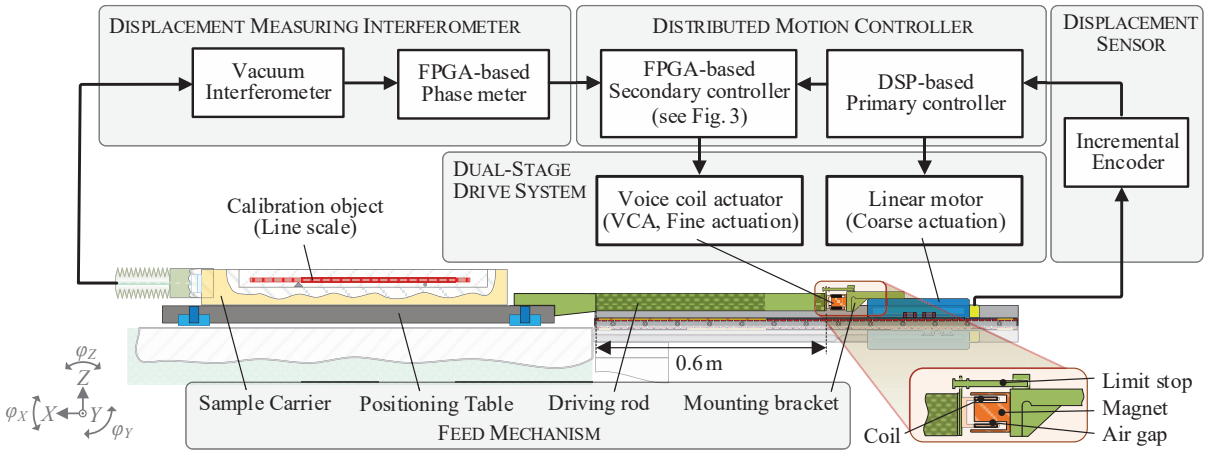

Figure. 1. Schematic representation of the upgraded motion control concept of the NMC. The position of the calibration object placed on the positioning table is controlled by the secondary controller. This FPGA-based controller receives the feedback data of the phase meter and computes a command variable to regulate a VCA.

The drive system moves a mass of 127 kg. The value of the mass was determined with a standard deviation of 0.24 kg using the levitation mass method [9] by relying on the manufacture's specification of the VCA force constant of K_{VCA} = 25.78 N·A^{-1}. The travel range of the dual-stage drive is 600 mm, whereas the maximum speed is limited by the feedback sensor system of the linear motor to 8 mm·s^{-1}. The maximum acceleration during an NMC measurement is typically less than 10 mm s^{-2}, which is equivalent to a driving force of 1.27 N.

Sensor System

The NMC has been designed to ensure length measurements with uncertainties in the single-digit nanometer range. For this purpose, vacuum interferometers were integrated into the machine structure [10]. Interferometric measurements in vacuum do not suffer from uncertainty contributions caused by the variation of the refractive index of air. The heterodyne interferometer setup with custom-made optics [11] was developed based on the principle of spatially separated laser beams [12] to avoid non-linearities due to polarization mixing [13]. The residual periodic non-linearities have an amplitude of less than 10 pm, which has been verified in a comparison measurement with an encoder system [4].

We developed a phase meter to evaluate the interferometric signals by making use of a commercially available FPGA board [15]. The signal processing was adjusted to the operating conditions at the NMC. A band-pass filter at a beat frequency of 2.49 MHz with a bandwidth of 90 kHz was implemented to track maximum speeds up to 8 mm·s^{-1}. The resolving capability of the phase meter was verified to a value of 1 pm by applying nearly ideal synthesizer signals. At an interferometer setup with a similar light source and optical design a standard deviation of 7.4 pm over an observation time of 300 s was demonstrated [15]. For the controller system discussed in the following section, the phase meter was modified to generate feedback position data with a resolution of 1 pm. The position data were then transmitted as absolute values over a 42-bit wide serial data bus to a motion controller unit with a latency of about 2 µs by applying extrapolation techniques [7].

Controller System

The controller system originally consisted of a commercial DSP-based primary controller (Model: PMAC2/VME, Delta Tau Data Systems) and has been enhanced with an FPGA-based secondary controller (PXI system, see [4] for more information) to form a distributed control system. Whereas the linear motor is controlled by the primary controller, the VCA is controlled by the secondary controller. This approach avoided a time-consuming redesign of the control structure but requires a synchronization of both controller units to drive both actuators on identical trajectories. For this purpose, the reference variables are generated by the DSP-based primary controller with a resolution of 1.27 pm. They are transmitted with an update rate of 4.5 kHz over a 24-bit wide parallel bus to the FPGA-based secondary controller.

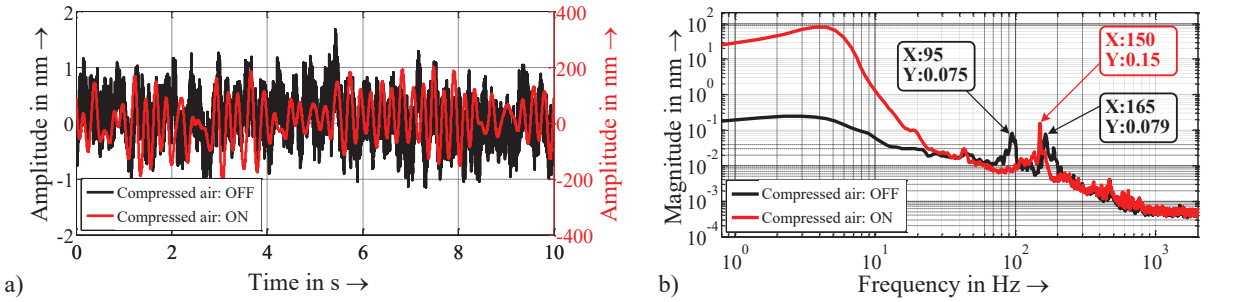

Figure 2. Measurement results to characterize the open-loop behavior of the positioning table (settled and lifted by the air bearing system) to be controlled in (a) time and (b) frequency domain. The data in the time domain were scaled differently due to its large discrepancy.

CONTROL DESIGN

The presented subsystems of the motion control concept avoid disturbances arising from non-linear system behavior, such as friction (drive system) or polarization mixing (sensor system). Conversely, controllers with high computing capacity are not required to perform sophisticated compensation methods, e.g. as demonstrated with KALMAN filtering [16], [17] or HEYDEMANN correction [18]. The subsystems' linearity allows the use of relatively simple linear control methods, which are technologically feasible on FPGA units offering enhanced real-time capabilities and low latencies. Another aspect is associated to the upgrade of the drive system: the stiffness of the proposed dual-stage drive has been increased since the mechanical transmission element with two thin places in the driveline was replaced by the driving rod made and the VCA. This option delivers advantages to shape a feedback loop such that the closed-loop gain and bandwidth could be increased by a factor of 5 to attenuate higher frequent disturbances [19].

Our single-input single-output control design relies in general on classical linear control theory, in which fundamental trade-offs have to be taken into account [20]. We intended to reduce the control error to the single-digit nanometer range during in-position and dynamic motion procedure by finding a compromise in practice which will be discussed in the following subsections.

Other groups [21] have already demonstrated that an air-bearing positioning system can be controlled and set in the sub-nanometer regime over 300 mm using voice coil actuators. We have achieved such results with a single VCA and a simple PD control using a demonstrator setup with 6.5 mm travel range [7]. The obtained knowledge and developed principles on that setup were then transferred to the NMC and will be evaluated in three classical steps represented by the following subsections.

Open-loop Validation

The open-loop operation was examined in two steps with modified air bearing characteristics. Moreover, the dual-stage drive was deactivated, and the vacuum chamber of the interferometer was flooded with air to avoid influences due to external forces caused by the compensation mechanisms [11] during this experiment.

In the first measurement, compressed air was provided to the air bearing of the position table to be controlled. In this state, maximum deviations of the positioning table of about ±200 nm were observed (red curve in Fig 2.a). As already shown by LEE AND KIM [22] the behavior of such a weakly damped system is determined by its bearing system, especially in the frequency range below 10 Hz (red curve in Fig. 2.b).

In the second measurement, the compressed air was disconnected from the air bearings and the table was settled down on the 4.8 t granite block. In this state, the stage was subject of frictional force and the position deviations (black curve in Fig. 2.a) were reduced significantly to a maximum value of ±1.5 nm and a standard deviation of 0.35 nm.

Control Synthesis

The position table of the NMC exhibited a position variation with a peak-to-peak value of 15 nm over an observation time of 10 s if, instead of the VCA, a mechanical connection element was applied. For the introduced dual-stage setup, we aimed to develop a control strategy for the VCA to reduce the peak-to-peak value in closed-loop operation down to a value of ±1.5 nm, which was achieved while the table was settled down. The final control method based on two parallel controls is shown in Fig. 3. It was developed in two stages, which will be described below.

In the first stage the PD control settings (K_{P1}, K_{D1}) were empirically adapted such that the positioning table was held in position. This could be

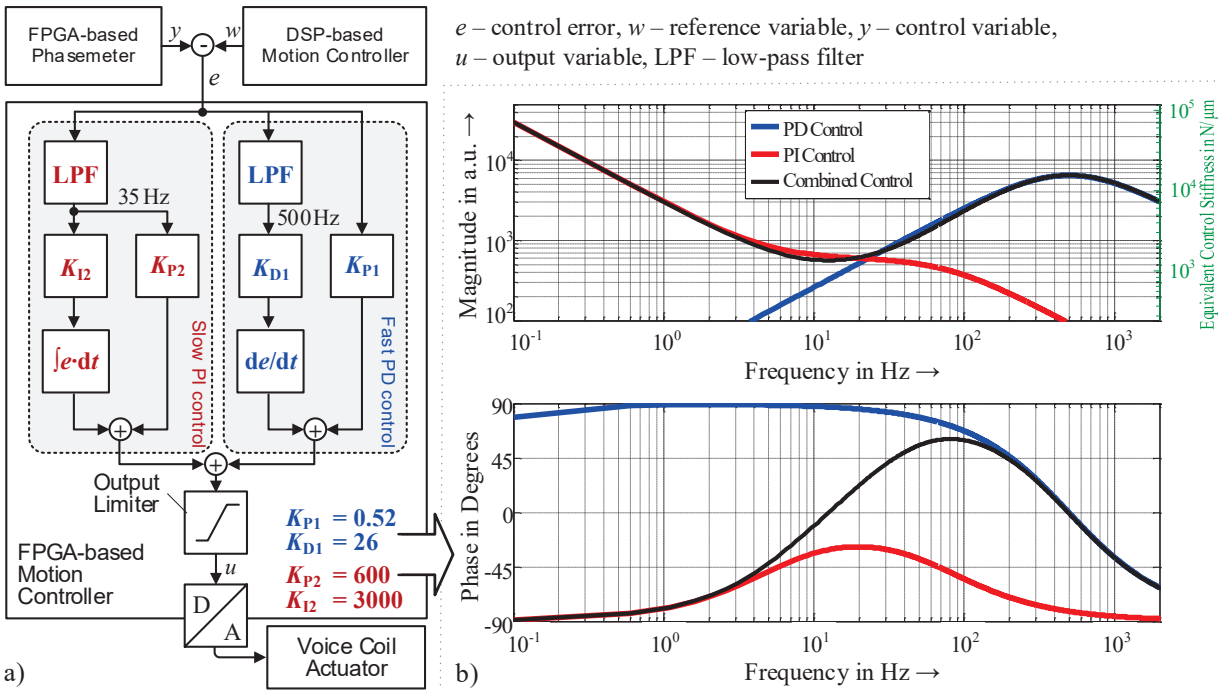

Figure 3. (a) Block diagram of the control algorithm to regulate the voice coil actuator, which is part of the dual-stage drive system. (b) Bode plot of the control algorithm derived from the control settings in (a).

achieved without considering an integral part (K_{I1}) because of the nearly frictionless bearings. However, the derivative action comes with the drawback that an ideal derivative part has high gain for high-frequency signals [23]. To suppress such high-frequency disturbances, e.g. arising from feedback noise [24] the derivative control part (K_{D1}) was tamed with a low-pass filter (LPF) featuring a bandwidth of 500 Hz. The poles and zeros, deduced from the parameter setting, produce the transfer function of the proposed PD control, which is shown in blue color in the double logarithmic scaled Bode diagram in Fig. 3.b).

In the next stage, an additional PI controller was integrated parallel to the PD controller to reduce the low-frequency disturbances even further. The control variables sampled with a data rate of 160 kHz were averaged over a window length of 2048 reducing the data rate to 78 Hz. Subsequently, the control parameters (K_{P2}, K_{I2}) were set to enable optimal disturbance rejection. The transfer function of the PI control is shown in red color in the Bode diagrams of Fig. 3.b) and the poles and zeros were derived from the selected control parameters. The addition of both PD and PI control resulted in the combined transfer function, which is shown in black color in the same diagram.

The described implementation is the result of an iterative controller synthesis, in which the least square method [25] was used as a quality criterion. The control parameters of the underlying controls were adapted such that the quadratic deviation of the control error reached a minimum. This procedure finally resulted in a parameterization, which agrees to a large extent with independently published results of VCA-equipped positioning systems [24], [26].

Closed-loop Validation

We have evaluated the closed-loop behavior with respect to two transfer functions: complementary sensitivity function $T(s)$ and sensitivity function $S(s)$. This frequency response design method provides in-sights into the potential to gain control stiffness that allows to achieve an optimum response to reference signals ($|T(s)| \approx 1$) and disturbances ($|S(s)| \approx 0$).

We enhanced our FPGA-based controller to stimulate disturbances. Gaussian white noise was added via digital test signals to reference and control signals. The measurement values required to process transfer function $T_{closed}(s)$ were sampled on the FPGA controller with an acquisition rate of 2 kS·s^{-1}. The sensitivity function $S(s)$ was determined by processing the ratio between the transfer functions $T_{open}(s)$ and $T_{closed}(s)$ representing the feedback system behavior in closed-loop and open-loop operation.

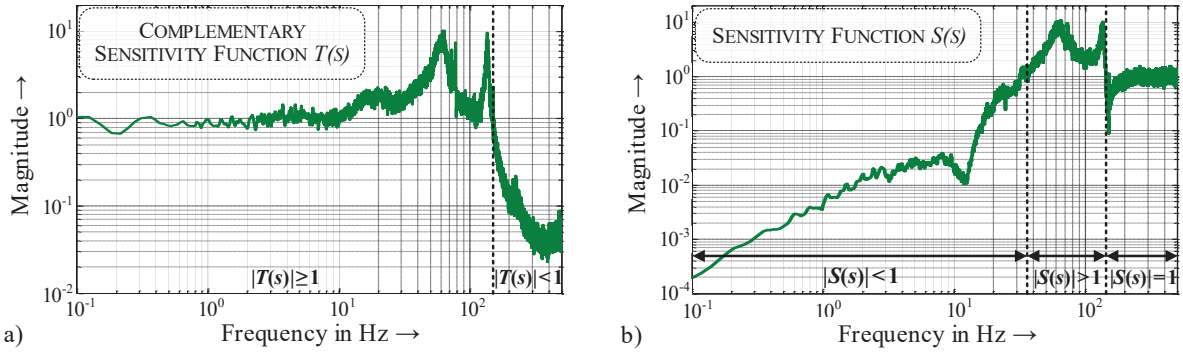

Figure 4. Magnitude curves for Bode plots of the (a) complementary sensitivity function T(s) and (b) sensitivity function S(s).

The behavior of the reference transfer function is characterized by $T(s)$. For motion control applications in general and the NMC in particular, this transfer function is a measure of the system's sensitivity to measurement noise and slow reference signal changes during motion and in-position sequences. The servo mechanism can attenuate disturbances with a bandwidth of up to 145 Hz, because $T(s)$ illustrated in Fig. 4.a) drops below one ($|T(s)| < 1$) at this frequency.

The sensitivity function $S(s)$ is used to validate the disturbance attenuation of the feedback system in the presence of process variations. At the NMC, these disturbances were mainly caused by its air bearings. The resulting behavior deduced from $S(s)$ can be divided in three typical characteristic regions [27], which are related to each other following BODE's integral formulae. There is a fundamental limitation to what can be accomplished by linear control since the integral remains constant. Thus, if the sensitivity function at the NMC is decreasing for lower frequencies, there must be an increase at other frequencies. This means an improvement of disturbance attenuation in one frequency range is associated with a decline in another, a property sometimes also called "waterbed effect". For a more detailed discussion we refer to the work of WESTCOTT [28], who extended the basic considerations of BODE concerning feedback amplifier circuits to feedback control systems. In control systems of positioning systems in general and the NMC in particular, disturbances occur predominantly in the low-frequency range. Therefore, the control accuracy improved to a greater extent than by minimizing disturbances in the positive feedback region ($|S(s)| > 1$).

EXPERIMENTAL RESULTS

The performance of the control system has been evaluated during a sub-nanometer motion sequence. The figure of merit to characterize the control behavior is the standard deviation (STD) at a certain bandwidth [29]. The measurement data were acquired with a sampling rate of 48.828 kHz during a continuous sinusoidal motion with an amplitude of 1 nm. Then the data was processed with two FIR filters featuring a bandwidth (BW) of 145 Hz and 1 Hz, respectively (see Fig. 5.a). The difference of both filtered data sets demonstrates a positioning noise of 0.25 nm at the maximum control rate of 145 Hz (see Fig. 5.b). An analysis with respect to the spectral density of the unfiltered data shows that no spectral component exceeds 25 pm/√Hz. In the final step, the cumulative representation was calculated from the spectral data shown in Fig. 5.c) and is according to PARSEVAL's theorem in agreement with the 0.25 nm RMS value at a bandwidth of 145 Hz, which has been shown in Fig. 5.b).

CONCLUSION

The control and dynamics of the Nanometer Comparator's air bearing guided table are presented. The positioning system, consisting of drive, sensor and control subsystems, is characterized via open-loop and closed-loop measurements. The control algorithm based on simple linear control is described by frequency response analysis. During a quasi-stationary measurement in the principal X-axis, a standard deviation of 0.25 nm was achieved under servo control at a bandwidth of 145 Hz.

ACKNOWLEDGMENT

The authors thank Arvid Amthor for careful reading of the manuscript and valuable references.

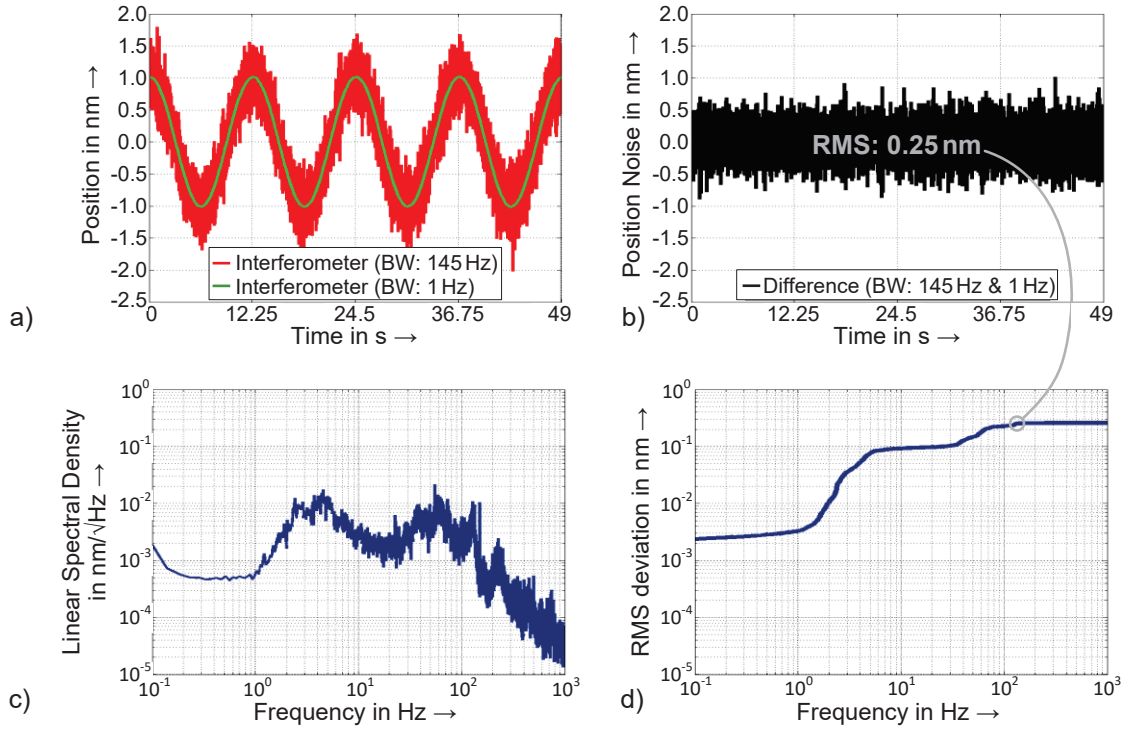

Figure 5. Measurements results of a continuous sinusoidal motion with an amplitude of 1 nm.

REFERENCES

[1] W. Gao *et al.*, *CIRP Ann. Manuf. Technol.*, vol. 64, no. 2, pp. 773–796, 2015.

[2] P. Schellekens *et al.*, *CIRP Ann. Manuf. Technol.*, vol. 47, no. 2, pp. 557–586, 1998.

[3] I. Tiemann et al., *Prec. Eng.*, vol. 32, no. 1, pp. 1–6, 2008.

[4] P. Köchert *et al.*, in *Proc. ASPE – Spring Topical Meeting*, Golden, CO, USA, 2015, pp. 61–66.

[5] P. Köchert *et al.*, *Proc. 16th EUSPEN*, Nottingham, UK, 2016, pp. 51-52.

[6] J. Flügge *et al.*, in *Proc. SPIE 5190*, San Diego, CA, USA, 2003, pp. 391–399.

[7] P. Köchert *et al.*, in *Proc. ASPE – Spring Topical Meeting*, Cambridge, MA, USA, 2013, pp. 39–44.

[8] R. J. Hocken *et al.*, *CIRP Ann. Manuf. Technol.*, vol. 50, no. 1, pp. 373–376, 2001.

[9] Y. Fujii and H. Fujimoto, *Meas. Sci. Technol.*, vol. 10, pp. 362–366, 1999.

[10] J. Flügge *et al.*, in *Proc. SPIE 7133*, Shenyang, China, 2008.

[11] J. Flügge and R. Köning, in *Proc. SPIE 4401*, München, Germany, 2001, pp. 275–283.

[12] M. Tanaka *et al.*, *IEEE Trans. Instrum. Meas.*, vol. 38, no. 2, pp. 552–554, 1989.

[13] C. M. Wu and R. D. Deslattes, *Appl. Opt.*, vol. 37, no. 28, pp. 6696–6700, 1998.

[14] P. Köchert *et al.*, *Meas. Sci. Technol.*, vol. 23, no. 7, p. 074005, 2012.

[15] C. Weichert *et al.*, in *Proc. 10th IMEKO TC14*, Braunschweig, Germany, 2011, pp. 243–250.

[16] A. Amthor *et al.*, in *Proc. 34th Annu. Conf. IEEE Ind. Electron.*, Orlando, 2008, pp. 2568–2573.

[17] C. Wang *et al.*, *Precis. Eng.*, vol. 48, pp.133–143, 2017.

[18] P. L. M. Heydemann, *Appl. Opt.*, vol. 20, no. 19, pp. 3382–3384, 1981.

[19] M. Weck *et al.*, in *Int. J. of Mach. Tools and Manufacture*, vol. 41, no. 1, pp. 65–88, 2001.

[20] M. M. Seron et al., "Fundamental Limitations in Filtering and Control," 1997.

[21] H. Shinno *et al.*, *CIRP Ann. Manuf. Technol.*, vol. 60, no. 1, 2011, pp. 403–406.

[22] C.-W. Lee and S.-W. Kim, *Prec. Eng.*, vol. 21, no. 2–3, pp. 113–122, 1997.

[23] K. J. Åström and T. Hägglund, in *Advanced PID Control*, ISA - The Instrumentation, Systems and Automation Society, 2006, ch. 3, sec. 3.

[24] R. Munnig Schmidt *et al.*, *The Design of High Performance Mechatronics*, Delft University Press, 2011.

[25] J. Lunze, *Regelungstechnik 1*, 2007, p. 433.

[26] E. Csencsics *et al.*, in *IEEJ J. Ind. Appl.*, vol. 8, no. 2, pp. 207–217, 2019.

[27] J. M. L. Janssen, in *Frequency Response*, 1956, pp. 131–140.

[28] J. H. Westcott, in *Automatic and Manual Control,* 1952, pp. 45–64.

[29] P. de Groot *et al.*, in *Proc. ASPE – Spring Topical Meeting*, Tucson, AZ, April, 2017, pp. 72–76.

HEURISTICALLY OPTIMIZAED H-INFINITY SYNTHEIS FOR THE REAL-TIME POSITIONING OF A TIP-BASED MEASUREMENT DEVICE

Liam G. Connolly, Obehi G. Dibua, and Michael Cullinan
Walker Department of Mechanical Engineering
The University of Texas at Austin
Austin, TX, USA

ABSTRACT

This work leverages a heuristic, multi-objective optimization process, Direct MultiSearch, to procedurally generate a control system for the real-time positioning of an atomic force microscope (AFM) probe for process measurement in roll-to-roll nanomanufacturing. To achieve this, the system must regulate probe trajectory to match web velocity in order to enable measurement without costly web stoppage. This high demand for controller performance would typically mandate the use of a more traditional optimal control technique such as iterative learning control (ILC) or finite-horizon linear quadratic programming, but as a-priori knowledge of the precise trajectory required is not available, H-infinity control is chosen. The various parameters used to define the high- and low-pass, 1st order filters used as the weights which drive mixed sensitivity H-infinity control synthesis are chosen by the optimization algorithm. Through varying the high and low frequency magnitudes, and cutoff frequency of these weighting functions, this optimization process attempts to minimize both controller error and effort in order to achieve the best possible closed-loop system performance which, as a result of the robust nature of H-infinity synthesis, is also resistant to varying parameters such as moving mass, flexure strain hardening and fabrication defects, or varying actuator sensitivity. A set of optimal controller candidates is thereby generated, and the advantageous performance of this method compared to traditional, loop-shaped, H-infinity design is shown, all without the need for a traditional, experience driven trial-and-error process of choosing weighting functions.

INTRODUCTION

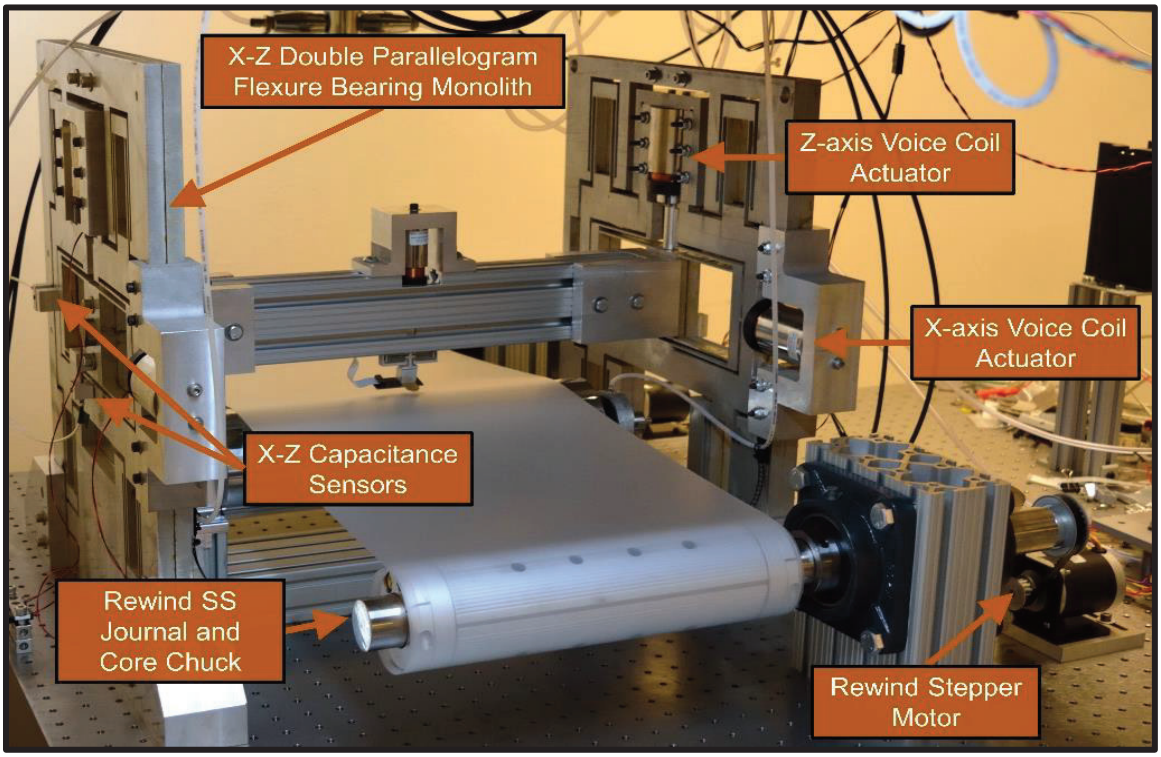
X-Z Double Parallelogram Flexure Bearing Monolith
Z-axis Voice Coil Actuator
X-axis Voice Coil Actuator
X-Z Capacitance Sensors
Rewind SS Journal and Core Chuck
Rewind Stepper Motor

FIGURE 1. Roll-to-Roll, Tip-based Measurement System Proof-of-concept Prototype

Research into manufacturing processes for the roll-to-roll (R2R) nanofabrication of various products has ballooned considering the perceived economic and design benefits to shifting products which are either traditionally manufactured on silicon wafers, or impossible to manufacture at scale today, to R2R [1]–[4]. However, for these efforts to be successful, new capabilities in nano-scale accurate measurement are required. In applications where fast and precise measurement of nanostructures is necessary, high-speed positioning of a metrology probe or device is critical to achieving the throughputs required for use in such an environment [5]–[7]. A variety of traditional and optimal feedback control strategies have been applied to mechatronic systems comprised of flexure mechanism bearings and Lorentz force actuators, ranging from the ubiquitous proportional-integral (PI) control to both finite- and infinite-horizon linear quadratic programming approaches, like linear quadratic regulation (LQR) based control schemes. However, in situations where stability despite potentially time-variant system parameters is required in addition to high bandwidth in comparison to the open loop system, a robust optimal control framework has been successfully applied to nanopositioning systems [8]–[14]. The mixed sensitivity H-Infinity synthesis most often used is driven by weighting functions, typically chosen as first or second order low- and high-pass filters, which can be used to account for constraints like desired reference following and disturbance rejection performance, sensor quantization, and actuator force and slew limits in the controller synthesis [15]. While previous work has demonstrated impressive performance results, there is a significantly steep learning curve and subjective "nuance" to the precise selection of the weighting functions.

SYSTEM MODEL

To accurately drive simulation-based controller design, a system model which correctly describes the plant dynamics is required. While

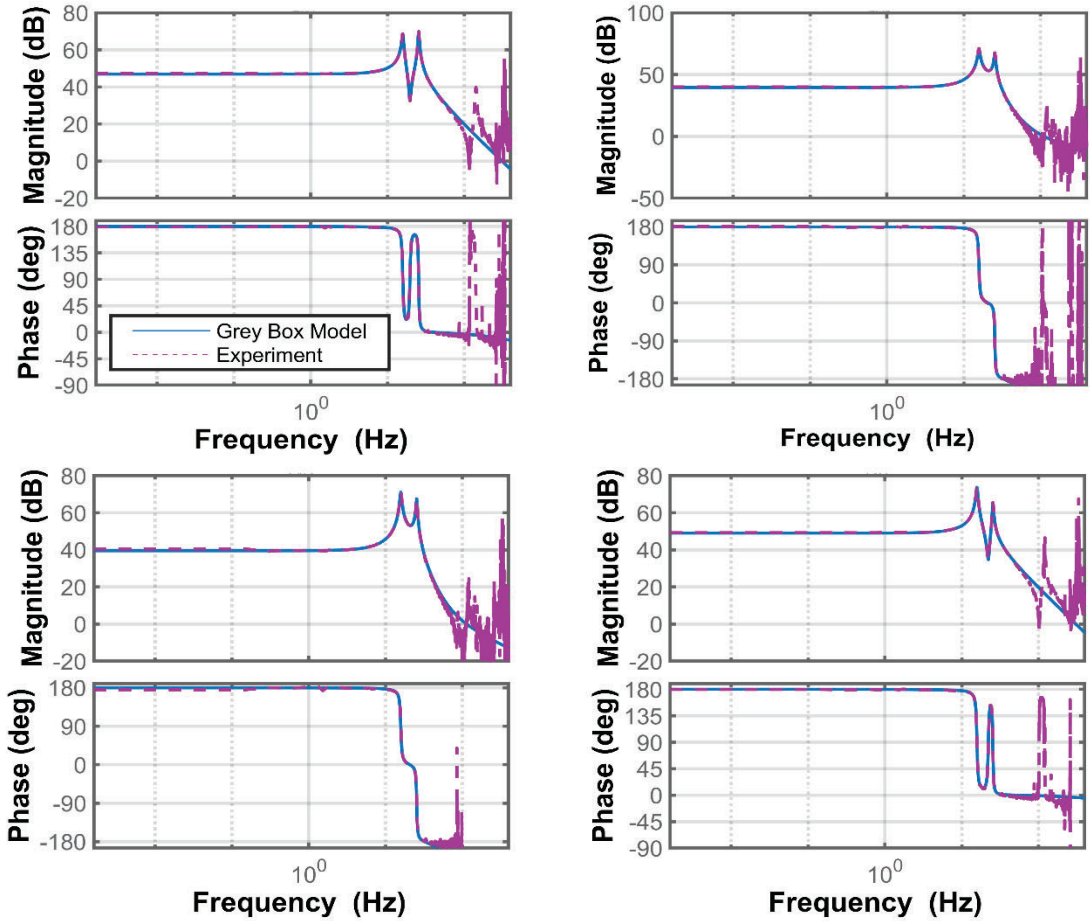

FIGURE 2: Frequency Response of White Noise System ID Periodogram Estimate and 4th Order Model

such a model could be constructed from parameters such as design stiffness, actuator sensitivity, and bearing geometry, due to as-fabricated variations in the system, a grey-box model is chosen as shown in Fig 3. To identify this model, a 1 kHz white noise signal is fed to each input of the system in succession, and a Welch averaged periodogram estimate is then used to fit a multiple-input-multiple-output (MIMO) frequency response function to this data. Then, using the same input-output data, a 4th order transfer function with 4 poles and 3 zeros, as would be proper for the identified dyanmics model, is estimated. The frequency response of both models is shown in Fig. 2.

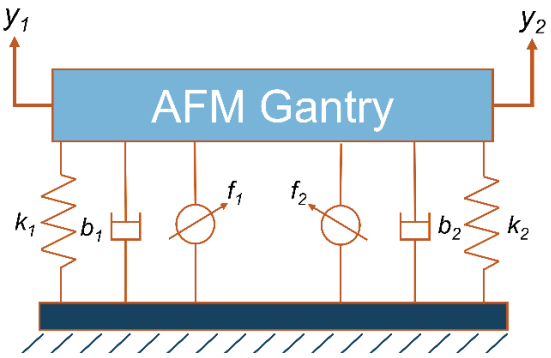

FIGURE 4: Schematic of 4th order coupled flexure dynamic system.

H-INFINITY CONTROL SYNTHESIS

Outlined in Fig. 4 is the control block diagram for a typical H-infinity implementation. In this layout *K* is the stabilizing controller which minimizes the H-infinity norm of Eq. 1 where S and T are the sensitivity and complementary sensitivity functions and R is a measure of control effort [16], [17].

$$\boldsymbol{T} = \begin{bmatrix} W_1 S \\ W_2 R \\ W_3 T \end{bmatrix} \quad (1)$$

$$\boldsymbol{S} = (1 + GK)^{-1} \quad (2)$$

$$\boldsymbol{R} = K(1 + GK)^{-1} \quad (3)$$

$$\boldsymbol{T} = GK(1 + GK)^{-1} \quad (4)$$

As such, the inverse of W_1 and W_3 influence the control bandwidth and disturbance attenuation respectively. W_1 is most often taken to be a low pass filter and W_2 and W_3 high pass filters in order to provide good tracking performance and robustness to higher frequency noise. In the loop-shaping method, these weights are chosen

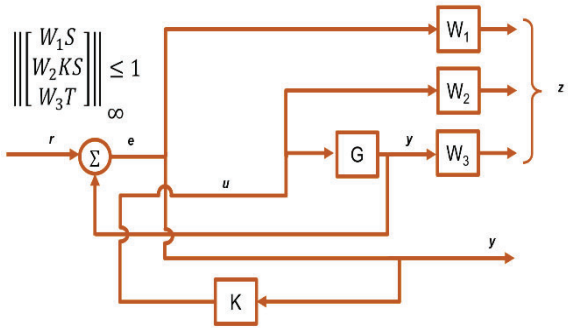

FIGURE 3: Control diagram of H∞ stabilized controller K of system G.

algorithmically in order to optimize T such that it matches a desired closed loop behavior goal in the frequency space: high bandwidth in the desired access and suppressed coupling behavior.

Optimization Architecture

Unlink traditional loop shaping, the heuristic optimization method implemented in this work, a Direct Multisearch algorithm, is leveraged to minimize two objectives. This fitness function is derived from a linear simulation of a typical system operating procedure, a 5 Hz sawtooth wave, conducted for each evaluation of the fitness function. The cumulative, absolute value of controller error and controller effort is then recorded for each generation of design

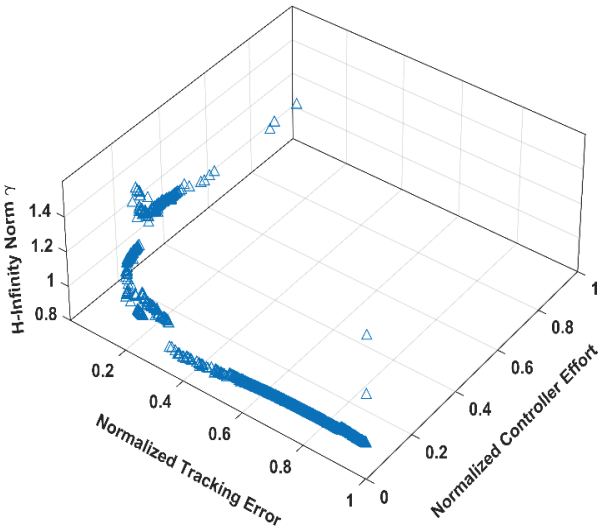

FIGURE 5: Pareto Front of Generated H-infinity Controllers from the Direct MultiSearch Algorithm Plotted with the H-infinity Norm (γ)

TABLE 1: H-Infinity Optimization Parameters

Objectives	*Implementation*
Minimize Error	$\sum abs(\text{LinearSim}(\text{Reference} - \text{Output}))$
Minimize Controller Effort	$\sum abs(\text{LinearSim}((\text{Reference} - \text{Output}) * \text{K}))$
Design Variables	*Implementation*
W_1(Low Freq Mag, Crossover, High Freq Mag)	$\text{MakeWeight}(W_{11}, W_{12}, W_{13})$
W_2(Low Freq Mag, Crossover, High Freq Mag)	$\text{MakeWeight}(W_{21}, W_{22}, W_{23})$
W_3(Low Freq Mag, Crossover, High Freq Mag)	$\text{MakeWeight}(W_{31}, W_{32}, W_{33})$
Constraints	*Implementation*
W_1(Low Freq Mag, Crossover, High Freq Mag)	Low Pass (1st Order)
W_2(Low Freq Mag, Crossover, High Freq Mag)	High Pass (1st Order)
W_3(Low Freq Mag, Crossover, High Freq Mag)	High Pass (1st Order)

candidates [18]–[22]**.** A summary of the parameters used in the optimization can be seen in Table 1. To map the solution space, a pareto curve was constructed of 1000 optimal solutions. In order to better visualize the relative tradeoff in robust stability when compromising between trajectory tracking and control effort, each optimal solution is plotted against the H-infinity norm gamma in Fig. 6. When comparing to previous work's loop shaped H-infinity controller, a clear improvement in tracking performance can be seen, as shown in the 5 Hz sawtooth tracking simulation shown in Fig. 6 [23]. That said, among controller candidates, the tradeoff between tracking error and effort is strictly proportional.

In order to visualize the solution space in more traditional control terms, and given the focus on fast reference tracking for the application of the control system, the frequency response of the stabilizing controller, K, for the 250 designs with the smallest controller error is plotted in Fig. 7. Here the previously generated controller in addition to a subset of solutions are simulated (where Sol. 1, the first pareto optimal solution, exhibits the smallest controller error).

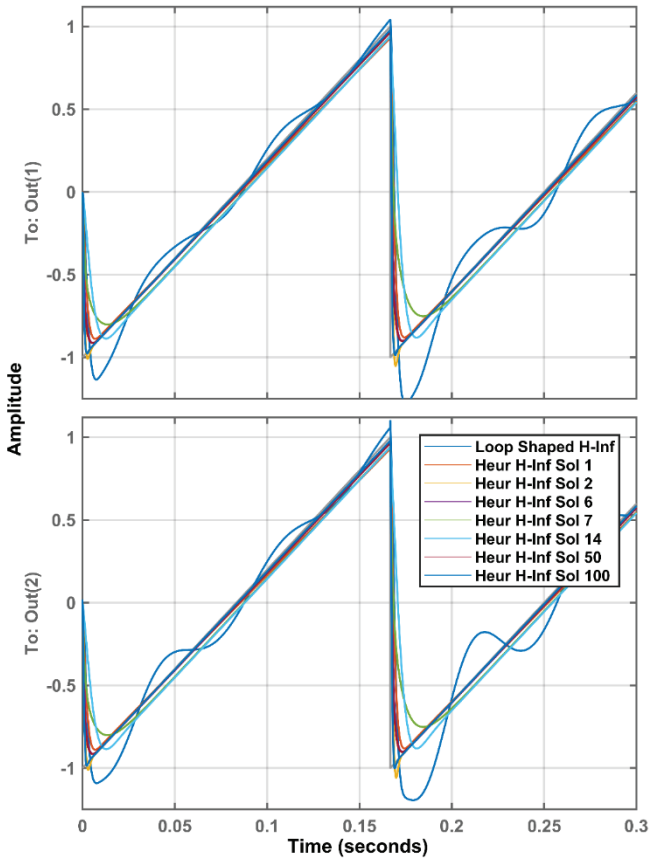

FIGURE 6: Reference Tracking Performance of Previous Loop-shaped H-infinity Controller and Various Candidate Solutions from the Generated Pareto Curve

FUTURE WORK

To confirm the performance of the optimal controller candidates generated in this work, and inform best practice in selecting a design

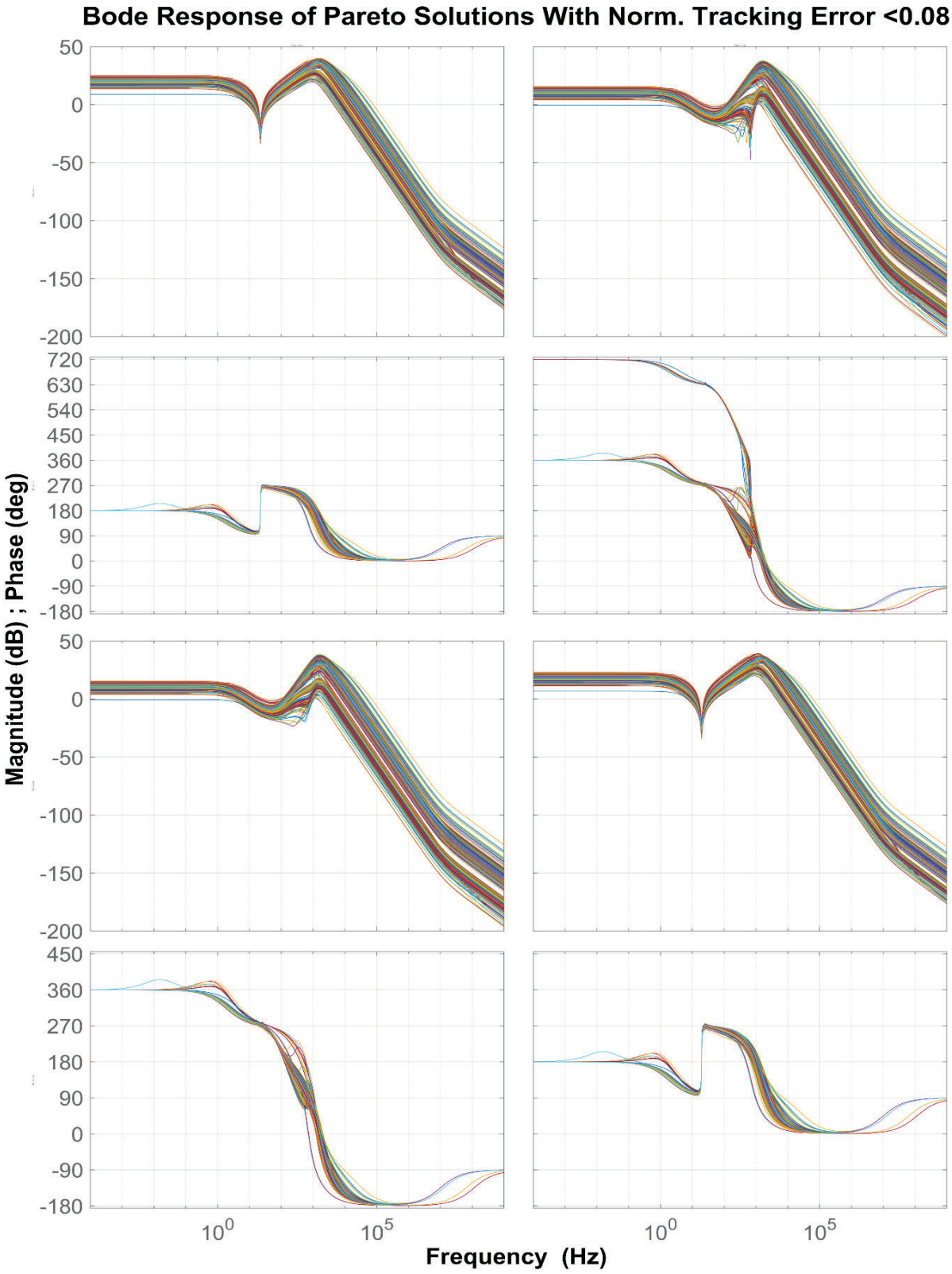

FIGURE 7: Bode Plot of H-Infinity Stabilizing Controller (K) for 250 Identified Pareto Optimal Controllers with the Lowest Tracking Error

from the set of pareto solutions, and the balance between controller effort, stability, and disturbance rejection when selecting a design candidate, an additional optimization must be conducted with a hardware-in-the-loop architecture. This will allow for evaluation of the fitness function on the physical prototype tool as opposed to a linear simulation – granting a much more reliable picture of final controller performance. Furthermore, the same set of fitness experiments will be carried out using a traditional infinite horizon, LQR full-state feedback controller to better benchmark the overall effectiveness of the generate H-infinity designs and their real-world performance tradeoff in order to guarantee robustness.

REFERENCES

[1] H. Lan, "Large-Area Nanoimprint Lithography and Applications," *Micro/Nanolithography - A Heuristic Asp. Endur. Technol.*, 2018, doi: 10.5772/intechopen.72860.

[2] M. Smolka *et al.*, "Roll-to-Roll pilot line for large-scale manufacturing of microfluidic devices," 2017.

[3] N. Palavesam, S. Marin, D. Hemmetzberger, C. Landesberger, K. Bock, and C. Kutter, "Roll-to-roll processing of film substrates for hybrid integrated flexible electronics," *Flex. Print. Electron.*, vol. 3, no. 1, 2018, doi: 10.1088/2058-8585/aaaa04.

[4] S. Ahn *et al.*, "Roll-to-roll nanopatterning using jet and flash imprint lithography," 2012, vol. 8323, no., pp. 83231L-8323–7, [Online]. Available: https://doi.org/10.1117/12.918040.

[5] L. G. Connolly, T.-F. Yao, A. Chang, and M. Cullinan, "A tip-based metrology framework for real-time process feedback of roll-to-roll fabricated nanopatterned structures," *Precis. Eng.*, Apr. 2019, doi: 10.1016/J.PRECISIONENG.2019.04.001.

[6] T.-F. Yao, L. G. Connolly, and M. Cullinan, "Expanded area metrology for tip-based wafer inspection in the nanomanufacturing of electronic devices," *J. Micro/Nanolithography, MEMS, MOEMS*, vol. 18, no. 03, p. 1, Sep. 2019, doi: 10.1117/1.JMM.18.3.034003.

[7] S. H. Ahn *et al.*, "High-performance wire-grid polarizers using jet and Flash^{TM} imprint lithography," *J. Micro/Nanolithography, MEMS, MOEMS*, vol. 12, no. 3, p. 031104, Aug. 2013, doi: 10.1117/1.JMM.12.3.031104.

[8] N. K. Roy and M. A. Cullinan, "Fast Trajectory Tracking of a Flexure-Based, Multiaxis Nanopositioner With 50-mm Travel," *IEEE/ASME Trans. Mechatronics*, vol. 23, no. 6, pp. 2805–2813, Dec. 2018, doi: 10.1109/TMECH.2018.2871162.

[9] S. Salapaka, A. Sebastian, J. P. Cleveland, and M. V. Salapaka, "High bandwidth nano-positioner: A robust control approach," *Rev. Sci. Instrum.*, vol. 73, no. 9, p. 3232, 2002, doi: 10.1063/1.1499533.

[10] S. T. Mashrafi, C. Preissner, and S. M. Salapaka, "The velociprobe: Pushing the limits with fast and robust control," in *Proceedings - 32nd ASPE Annual Meeting*, 2016, vol. 67, pp. 468–473.

[11] C. Li, J. Wang, and S. C. Chen, "Flexure-based dynamic-tunable five-axis nanopositioner for parallel nanomanufacturing," *Precis. Eng.*, vol. 45, pp. 423–434, 2016, doi: 10.1016/j.precisioneng.2016.04.002.

[12] X. Zhou, D. Wang, J. Wang, and S. C. Chen, "Precision design and control of a flexure-based roll-to-roll printing system," *Precis. Eng.*, vol. 45, pp. 332–341, 2015, doi: 10.1016/j.precisioneng.2016.03.010.

[13] R. A. Braker and L. Y. Pao, "Fast setpoint tracking of an Atomic Force Microscope X-Y stage via optimal trajectory tracking," *Proc. Am. Control Conf.*, pp. 2875–2881, 2017, doi: 10.23919/ACC.2017.7963387.

[14] S. T. Mashrafi, C. Preissner, and S. M. Salapaka, "Countering Sensor Drift in X-ray Microscopy with Fast and Robust Optimal Control," *Proc. Am. Control Conf.*, vol. 2018-June, pp. 5119–5124, 2018, doi: 10.23919/ACC.2018.8431093.

[15] R. W. Beaven, M. T. Wright, and D. R. Seaward, "Weighting function selection in the H∞ design process," *Control Eng. Pract.*, vol. 4, no. 5, pp. 625–633, May 1996, doi: 10.1016/0967-0661(96)00044-5.

[16] R. Y. Chiang and M. G. Safonov, "H∞ synthesis using a bilinear pole shifting transform," *J. Guid. Control. Dyn.*, 1992, doi: 10.2514/3.20957.

[17] K. Glover and D. Mcfarlane, "Robust Stabilization of Normalized Coprime Factor Plant Descriptions with H∞-Bounded Uncertainty," *IEEE Trans. Automat. Contr.*, 1989, doi: 10.1109/9.29424.

[18] Y. Boughari, R. M. Botez, G. Ghazi, and F. Theel, "Flight control clearance of the Cessna Citation X using evolutionary algorithms," *Proc. Inst. Mech. Eng. Part G J. Aerosp. Eng.*, vol. 231, no. 3, pp. 510–532, 2017, doi: 10.1177/0954410016640821.

[19] Y. K. Yong, K. Liu, and S. O. R. Moheimani, "Reducing cross-coupling in a compliant XY nanopositioner for fast and accurate raster scanning," *IEEE Trans. Control Syst. Technol.*, vol. 18, no. 5, pp. 1172–1179, 2010, doi: 10.1109/TCST.2009.2033201.

[20] I. B. Tijani, R. Akmeliawati, A. Legowo, M. Iwan, and A. G. A. Muthalif, "Robust H-infinity controller synthesis using multi-objectives differential evolution algorithm (MODE) for two-mass-spring system," *2011 4th Int. Conf. Model. Simul. Appl. Optim. ICMSAO 2011*, pp. 0–6, 2011, doi: 10.1109/ICMSAO.2011.5775610.

[21] H. I. Ali, S. B. Mohd Noor, M. H. Marhaban, and S. M. Bashi, "Design of H-inf controller with tuning of weights using particle swarm optimization method," *IAENG Int. J. Comput. Sci.*, vol. 38, no. 2, pp. 103–112, 2011.

[22] A. L. Custódio, J. F. A. Madeira, A. I. F. Vaz, and L. N. Vicente, "Direct Multisearch for Multiobjective Optimization," *SIAM J. Optim.*, vol. 21, no. 3, pp. 1109–1140, Jul. 2011, doi: 10.1137/10079731X.

[23] L. G. Connolly and M. Cullinan, "Towards Embedded High-Speed Control For Dynamic Tip-Based Nanometrology In Roll-To-Roll Manufacturing", ASPE 35th Annual Meeting, Nov. 2019.

MODEL AND CONTROLLER DESIGN FOR HIGH-SPEED ATOMIC FORCE MICROSCOPE IMAGING AND AUTOTUNING

Fangzhou Xia[1], Chen Yang[1], Yi Wang[1] and Kamal Youcef-Toumi[1]
[1] Mechatronics Research Lab in Department of Mechanical Engineering
Massachusetts Institute of Technology
Cambridge, Massachusetts, U.S.

INTRODUCTION

Atomic Force Microscopy (AFM) has been widely used in nanotechnology researches for sample surface characterization since its invention [1]. In its basic form, AFM generates 3D topography images by controlling the probe deflection or oscillation. AFM can characterize sample surfaces with a wide range of properties, conduct imaging in different environments, and be combined with various measurement techniques.

Although AFM has a history over thirty years, its operation still depends heavily on operator experience. For novice users, controller tuning is mostly a trial and error process with risks of damaging the probe or the sample. Therefore, it would be beneficial to provide a comprehensive simulation environment for operator training and controller investigation. In recent years, significant research efforts have been placed on increasing the imaging throughput of the AFM system. The in-plane scanning bandwidth has been increased to over tens of kilohertz with range over tens of microns with new generation scanner design [2] and control algorithm optimization [3]. By utilizing smaller size cantilever probes with specialized optical setup, the out-of-plane tracking bandwidth of the AFM system can also be increased [4]. The development in high-speed AFMs opens up the possibility of observing reaction dynamics on the sample surface. However, the controller tuning procedure becomes more complicated to enable high-speed operation. In addition, the high scanning rate makes the original manual tuning unsuitable since improper controller parameters can damage the sample or the probe in a short time.

To reduce operation overhead and meet the controller tuning demand for high-speed AFM, automated parameter tuning can be a suitable solution. For offline AFM PID controller gain selection, previous research has demonstrated a semi-automated method for parameter adjustment [5]. If a raster scanning pattern is utilized, an iterative learning controller can be trained by scanning over the initial line for several times until convergence [6]. However, these methods are utilized offline and cannot adapt to sample property variation during imaging.

In this work, we propose a unified model and controller investigation framework for contact mode high-speed AFM imaging performance improvement. The paper is organized as follows. First, we create a lumped parameter model including the cantilever probe, the scanner, and the sample for simulation. Second, we propose imaging parameter tuning algorithms with a relay-based PID auto-tuner and a deflection error based scanning speed auto-tuner. Third, we investigate three methods to improve the performance of high-speed imaging. Fourth, we present a single neuron PID controller to adapt to variation of sample material properties. Performance improvements of the proposed methods are evaluated in simulation with the model to demonstrate their effectiveness. Finally, the investigated models and control methods are organized into a unified framework with switching conditions provided.

AFM SYSTEM MODEL

A number of AFM models with focus on atomic level interaction for physical understanding have been developed in previous research [**sim˙contact˙molecular˙hert**, 7]. However, instrument level dynamics (e.g. scanner) and controller interfaces are often not available in these efforts. The model developed in this work aims to capture the essential dynamics in contact mode AFM operation with a simplified lumped parameter model in Matlab Simulink for efficient control algorithm investigation.

Out-of-plane Dynamics

The AFM out-of-plane Z-axis dynamics mainly has three components, namely, the cantilever probe, the scanner and the sample. For the cantilever probe, a second-order mass-spring-damper model is sufficient to capture the first resonance. More complex models for higher frequency resonance can be used for other modes

of operation [8]. For the scanner Z-axis, another mass-spring-damper system is used with dynamics matching a scanner previously designed for a high-speed AFM system in our lab. The frequency responses of both the cantilever probe and the scanner are shown in Fig. 1(b). We notice that the cantilever dynamics is faster than the scanner dynamics such that the control loop bandwidth for probe deflection regulation is limited primarily by the sample or the scanner. In addition, the piezo hysteresis non-linearity in the Z-axis is neglected as it can be compensated electrically with charge control methods [9].

The full dynamics of the AFM probe and sample interaction is complicated with the presence of multiple interactions such as the Lennard Jones potential, capillary forces, Van der Waals forces, etc. The tip geometry of the AFM probe can typically be modeled by Hertzian, Johnson-Kendall-Roberts (JKR) or Derjaguin-Müller-Toporov (DMT) models at different levels of complexity. However, even the simplest model has several parameters that are necessary to know but difficult to measure or control. Since lumped parameter models of the sample have proven effective in capturing the dominant dynamics matching the experiment observation for jumping mode AFM [8], the sample is modeled as another mass-spring-damper system with adjustable height and parameter vales.

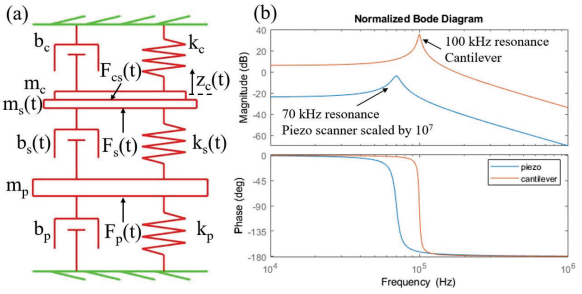

FIGURE 1. (a) Lumped parameter model of out-of-plane dynamics, (b) Simulated displacement output versus force input frequency response of the scanner (scaled by 10^7) and the probe

An illustration of the overall lumped parameter model is shown in Fig. 1(a). In the figure, m_c, b_c and k_c are the cantilever probe mass, damping and stiffness coefficients. Similarly, the subscripts s and p represent the sample and the piezo scanner with (t) indicateing time dependency. $F_{cs}(t)$ is the cantilever-sample interaction force, $F_s(t)$ is the disturbance force from sample variation, and $F_p(t)$ is the piezo actuator force input. $z_c(t)$ is the cantilever deflection. For contact mode operation with sufficiently large reference deflection, the probe and the sample remain in contact and share an added mass. This modular Matlab Simulink model captures the main dynamics for efficient simulation with easy configuration of its sub-components.

In-plane Scanning Model

For the in-plane scanning model, maps for topography height, sample mass, stiffness, and damping with pixel resolution are generated first. A scanner with Preisach hysteresis model and controller previously developed in [10] is used to generate the in-plane location. Bi-linear interpolation based on the scanner position is utilized to compute the time dependent parameters.

AUTOMATIC PARAMETER TUNING

With the complex probe-sample interaction in the AFM probe deflection regulation loop, a PID controller is conventionally used as a generic approach. In this section, we propose an automatic tuning procedure for controller parameter and scanning speed adjustment for AFM imaging.

Automatic PID Tuning

With the modeling complexity and potential variation across sample properties, model-free tuning methods that do not rely on system identification are more suitable. With this requirement, the widely used Ziegler–Nichols (Z-N) tuning method can be utilized for its good disturbance rejection property. For the controller shown in Eq.(1), the Z-N tuning rule of a classic PID controller is $K_p = 0.6K_u$, $K_i = 1.2K_u/T_u$ and $3K_uT_u/40$.

$$u(t) = K_p e(t) + K_i \int_0^t e(\tau)d\tau + K_d \frac{d}{dt} e(t) \quad (1)$$

where $u(t)$ is the control effort, $e(t)$ is the error, K_p, K_i, and K_d are the proportional, integral, and derivative gains respectively, K_u is the ultimate gain when the system started to have stable oscillation with only the proportional gain in the loop, and T_u is the oscillation period.

To automatically determine K_u and T_u without risking unstable oscillation, a relay is used to replace the PID controller as shown in Fig. 2(a). The relay switches between two values with equal magnitude d, which limits the controller output to avoid large amplitude oscillation. As shown in Fig. 2(b), with the relay, a sinusoidal steady oscillation

$e(t) = A\sin(\omega t + \phi)$ can be observed in the error signal similar to the case when ultimate proportional gain is reached. Based on describing function analyses [11], the ultimate gain K_u and the period T_u can be calculated as in Eq.(2).

$$K_u = \frac{4d}{\pi A}, \quad T_u = \frac{1}{2\pi\omega} \tag{2}$$

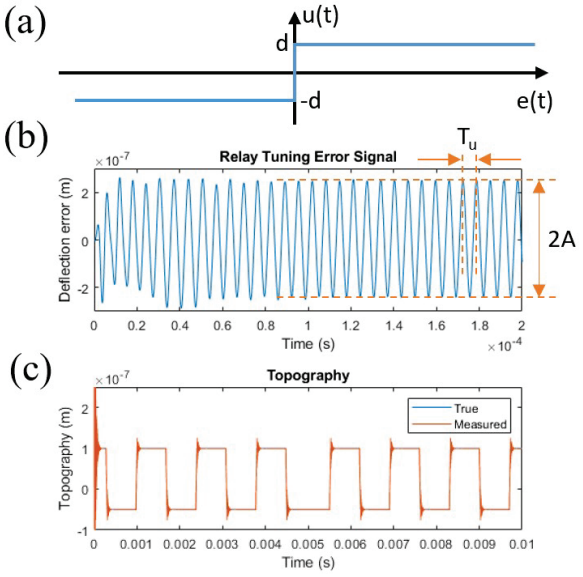

FIGURE 2. (a) Relay with magnitude d (b) Relay tuning error signal with amplitude A and period T_u (c) Simulated tracking of step topography.

At this point, measuring the amplitude A and frequency ω of the sine wave in the error function $e(t)$ will solve the tuning problem. By finding the second maximum peak in the auto-correlation function of the error $e(t)$ or the relay control effort $u(t)$, the frequency ω and period T_u can be determined. To extract the amplitude A, the formula of a digital lock-in amplifier can be used with the known ω as shown in Eq.(3).

$$\begin{cases} A_{sin} = \frac{1}{T}\int_0^T e(\tau)\sin(\omega\tau)d\tau \\ A_{cos} = \frac{1}{T}\int_0^T e(\tau)\cos(\omega\tau)d\tau \\ A = \sqrt{A_{sin}^2 + A_{cos}^2} \end{cases} \tag{3}$$

where T is the sampling time, A_{sin} and A_{cos} are the averaged sine and cosine components during the lock-in process to compute the amplitude. The integration will be replaced by summation due to discrete sampling. The relay based Z-N rule of automatic PID tuning procedure can be summarize in seven steps. First, engage the AFM probe and disable scanning. Second, set relay amplitude d below maximum allowed probe deflection. Third, deactivate the PID controller and activate the relay unit. Fourth, record the error data $e(t)$ for multiple periods. Fifth, extract the frequency from $e(t)$ with auto-correlation. Sixth, obtain the amplitude with lock-in amplification principle. Seventh, compute K_u, T_u and derive K_p, K_i, K_d.

The simulated step tracking of the PID controller tuned automatically with this procedure is shown in Fig. 2(c). The controller provides good tracking with slight overshoot. Other formula for parameter estimation from K_u and T_u can be used to reduce overshoot with slower response time. Parameter retuning can also be implemented when the line error exceeds the user specified threshold.

Scanning Speed Tuning

A suitable in-plane scanning speed is important to get a good tracking performance and avoid excitation of scanner resonance. To initialize a suitable scanning speed, the sample RMS roughness defined by $R_q = \sqrt{\frac{1}{n}\sum_{i=0}^{n} z_{topo}^2(i)}$ can be estimated to produce an initial guess based on previous operation records. During imaging, the root mean square (RMS) tracking error of a line defined by $e_{RMS} = \sqrt{\frac{1}{n}\sum_{i=0}^{n} e^2(i)}$ with n being the pixel resolution in X direction. It can be used to adjust the scan speed to be as fast as possible while maintaining e_{RMS} to be smaller than the user defined error threshold. This method can even be applied inline for sample with large roughness variation [12].

HIGH-SPEED IMAGING IMPROVEMENT

In this section, we discuss three methods to improve topography tracking and image generation, which are especially helpful for high-speed imaging. These methods can be used together with the automatic PID tuning procedure.

Location Based Sampling

In a conventional AFM system, the image pixels are sampled at a constant frequency. For trajectories with varying in-plane X-direction scan speed such as a sine wave, this would cause the sampled points to spread unevenly as shown in the top half of Fig. 3. As sine waves are preferred for high-speed scanning to avoid excitation of the scanner dynamics, equal spacing based sampling is needed. For implementation, an in-plane scanner location tracking module is designed with a lookup table.

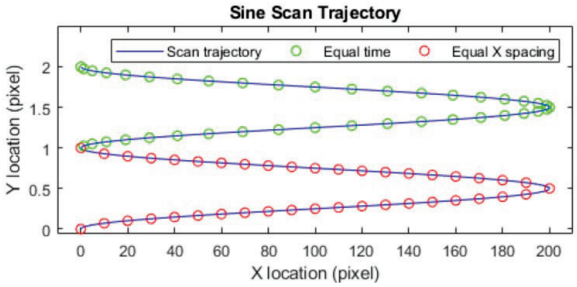

FIGURE 3. Sine wave scan in fast scanning X direction and constant speed in Y. Equal X spacing sampling yields more uniformly distributed pixels.

Error-corrected AFM Image Generation

For early-stage AFM systems without probe deflection regulation, the topography is measured directly from probe deflection. With regulation of the probe deflection, the scanner control command is recorded as the topography variation. If the proportional constant between the probe deflection signal and the physical height is obtained from calibration, adding the deflection error signal to the scanner command helps to obtain more accurate topography tracking. As shown in Fig. 4, even the tracking performance of the PID controller is poor, the corrected image scan line still matches well with the simulated true topography. The small error remained from the corrected tracking line originates from the deformation of the sample itself. This method has also proven to be useful in imaging experiments [13].

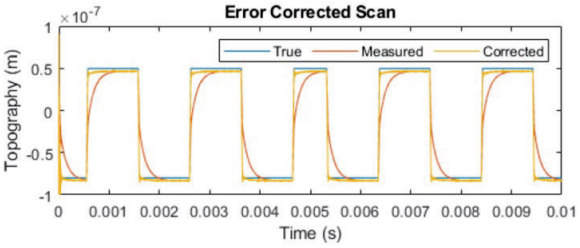

FIGURE 4. Topography feedforward method demonstrates good image generation even with non-ideal tracking due to poorly tuned controller.

Topography Feedforward

With raster scan, the topography variation between adjacent line scans is usually small in common imaging applications. Using the collected data points from the previous line as a feedforward signal can be helpful to reduce the tracking error. Due to different controller responses when scanning from different directions, the trace and retrace lines should be used separately. With discrete sampling, the bi-linear interpolation method is used again to interpolate the estimated upcoming topography based on the last scanned line. For evaluation, the simulated sample has a sinusoidal topography variation with constant material properties. As shown in Fig. 5, the tracking error decreases significantly after the feedforward controller is turned on starting from the third line scan. The initial transient error peak diminishes after several line scans. Compared to iterative learning controllers [14], this method is significantly easier to implement and does not require system identification procedure.

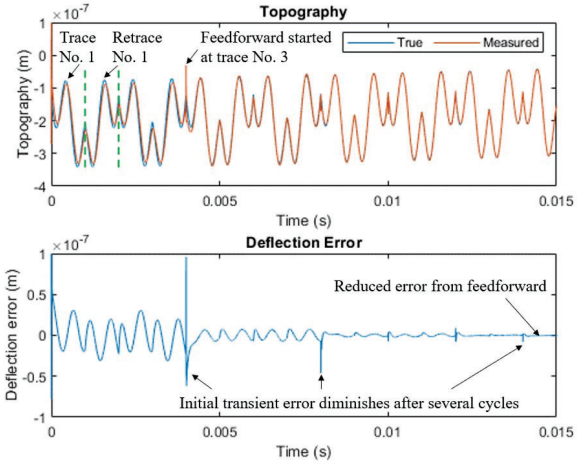

FIGURE 5. Topography feedforward starting at line 3 reduces the RMS error by an order of magnitude for sample with pattern $Z = (Ysin(X/500) - Xcos(Y/500))/25$ *with* X, Y, Z *units in* nm.

ADAPTIVE LEARNING ALGORITHM

The aforementioned automatic controller tuning algorithms and AFM imaging performance improvement methods can handle most of the imaging cases. In this section, we discuss the limitations in handling specialized samples and propose an adaptive algorithm to solve the problem.

Limitation of PID and Potential Alternatives

Since the PID controller is tuned each time based on a single location of the sample, if the material properties vary significantly during a line scan, the controller performance can become poor or even unstable. As shown in Fig. 6, the tuned controller can track the topography well with identical material property while becomes unstable when the sample stiffness varies in a step pattern by 20%. With unknown sample properties, it would be difficult to anticipate the variation to retune the PID controller so that an adaptive algorithm other than a simple PID controller is needed.

Robust control, adaptive control, and fuzzy logic control techniques are commonly utilized to han-

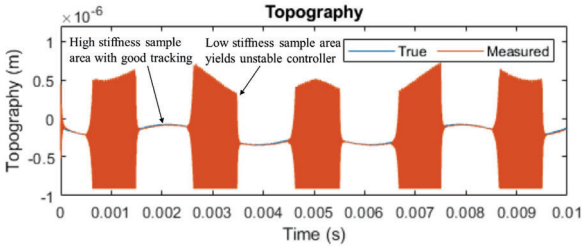

FIGURE 6. Imaging the sample with identical topography as Fig. 3 but with 20% step variation in the sample stiffness map. Properly tuned PID controller can track high stiffness area well but becomes unstable at low stiffness area.

dle modeling parameter uncertainties and changing system properties. As the complex contact mechanics is difficult to model, system identification based controller tuning is needed. As an alternative, data-driven methods such as deep reinforcement learning have demonstrated their capability in handling complex model-free control problems. However, with high bandwidth signal processing running on Field Programmable Gate Arrays (FPGA), the real-time computation of deep neural networks can be challenging.

Single Neuron Adaptive PID

Among various algorithms, the Single Neuron PID (SNPID) controller is a suitable solution to resolve this problem with its good balance between algorithm complexity and adaptive performance. The adaptive algorithm is based on the Hebb learning rule and is computationally inexpensive due to its simple structure [15]. We present the discrete-time implementation of the SNPID controller.

The controller architecture of the single neuron PID is shown in Fig. 7(a). The inputs of the neuron $x_P(n)$, $x_I(n)$ and $x_D(n)$ are given in Eq.(4).

$$\begin{cases} x_P(n) = e(n) - e(n-1) \\ x_I(n) = e(n) \\ x_D(n) = e(n) - 2e(n-1) + e(n-2) \end{cases} \tag{4}$$

where $e(n)$ is the error signal of sample n. The neuron output $u(n)$ is updated at each cycle with the increment Δu as shown in Eq.(5).

$$\begin{cases} \Delta u(n) = \frac{K(w_P(n)x_P(n)+w_I(n)x_I(n)+w_D(n)x_D(n))}{w_P(n)+w_I(n)+w_D(n)} \\ u(n+1) = u(n) + \Delta u(n) \end{cases} \tag{5}$$

where K is a constant gain, $w_P(n)$, $w_I(n)$, $w_D(n)$ are weights at sample n updated with Eq.(6).

$$\begin{cases} w_P(n+1) = w_P(n) + \eta_P e(n)u(n)x_P(n) \\ w_I(n+1) = w_I(n) + \eta_I e(n)u(n)x_I(n) \\ w_D(n+1) = w_D(n) + \eta_D e(n)u(n)x_D(n) \end{cases} \tag{6}$$

where η_P, η_I, η_D are positive constant learning rates. It can be proven by stochastic approximation theory that the formula has a form similar to that of the classic gradient descent method. With sufficiently small learning rates, the weights of the neurons converges to a steady state value [15].

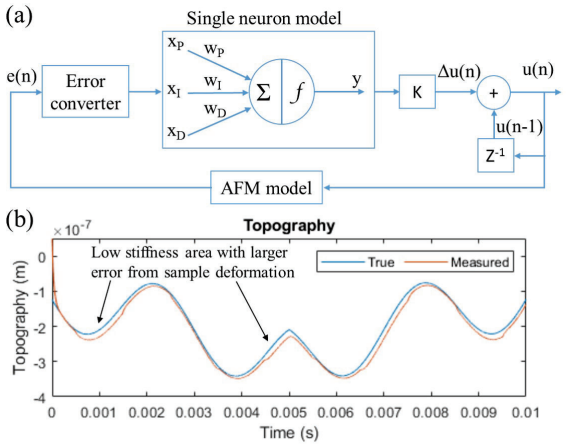

FIGURE 7. Single neuron PID controller: (a) architecture for weight update (b) good tracking performance for sinusoidal sample topography with step variation in the sample stiffness map

Similar to the neurons in artificial neural networks, the SNPID controller weights are adjusted with new data. A total of seven constants are initialized by the operator. For convergence, the gain K is set to a small value of 0.1. The learning rates η_P, η_I, η_D are set all to 1 and initial values of $w_P(0)$, $w_I(0)$, $w_D(0)$ all set to 0.1. The simulation results using the SNPID controller is shown in Fig. 7.

Compared to a classic PID controller as shown in Fig. 6, the SNPID controller remains stable regardless of the varying material property. The weight adjustment capability of the SNPID controller allows it to adapt to the parameter variation online. With this capability, AFM imaging of samples with significant property variations can be conducted without operator intervention. One minor drawback of this method is that the learning rate might need some manual tuning to ensure the convergence of the weights.

CONTROLLER AUTOMATION FRAMEWORK

With the proposed controller architecture in Fig. 8, three image level improvement methods can be activated at all time. The system performs automatic PID and line speed parameter initialization and start imaging. To handle samples with large material property and topography variation, the roughness R_q and the relative error

$e_{relative} = e_{RMS}/R_q$ is computed online. If percentage variation within a single line exceeds a predefined threshold, the controller switches into adaptive mode with online parameter updates based on the user initialized learning rates.

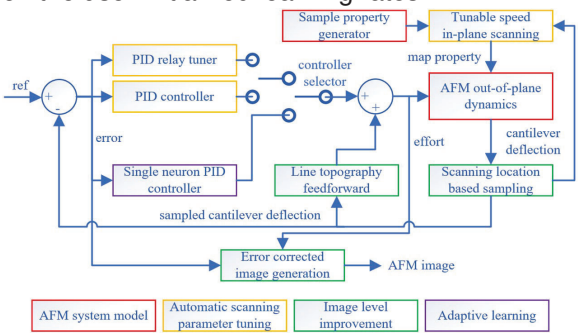

FIGURE 8. Framework of the proposed controller

CONCLUSION

In this work, we modeled the AFM imaging dynamics and proposed an automatic tuning method for PID controller with scanning speed adjustment. Location based sampling, topography feed-forward, and error-corrected AFM image generation methods are evaluated for their ability to improve high-speed imaging performance. To handle imaging of samples with varying properties, a single neuron PID controller is proposed with criteria for controller switching. For future work, a graphical interface of the simulation for education purpose is under development. Algorithm implementation on custom AFM systems and extension to other modes of operation are also interesting directions to pursue.

ACKNOWLEDGMENT

The authors would like to thank Synfuels Americas for funding this research.

References

[1] G. Binnig et al. “Atomic Force Microscope”. In: *Phys. Rev. Lett.* 56 (Mar. 1986), p. 930.

[2] C. Yang et al. “Design and Control of a Multi-Actuated Nanopositioning Stage with Stacked Structure”. In: *ACC’19*. July 2019, pp. 3782–3788.

[3] F. Xia et al. “Bandwidth Based Repetitive Controller Design for a Modular Multi-actuated AFM Scanner”. In: *ACC’19*, pp. 3776–3781.

[4] I. Soltani Bozchalooi et al. “Design and control of multi-actuated atomic force microscope for large-range and high-speed imaging”. In: *Ultramicroscopy* 160 (2016), pp. 213–224. ISSN: 0304-3991.

[5] D. Y. Abramovitch, S. Hoen, and R. Workman. “Semi-automatic tuning of PID gains for Atomic Force Microscopes”. In: *ACC’08*. June 2008, pp. 2684–2689.

[6] “Intelligent tuning method of PID parameters based on iterative learning control for atomic force microscopy”. In: *Micron* 104 (2018), pp. 26–36.

[7] Horacio V Guzman, Pablo D Garcia, and Ricardo Garcia. “Dynamic force microscopy simulator (dForce): A tool for planning and understanding tapping and bimodal AFM experiments”. In: *Beilstein journal of nanotechnology* 6.1 (2015), pp. 369–379.

[8] F. Xia et al. “Induced vibration contact detection for minimizing cantilever tip-sample interaction forces in jumping mode atomic force microscopy”. In: ACC’17, pp. 4141–4146.

[9] C. Yang et al. “Charge Controller With Decoupled and Self-Compensating Configurations for Linear Operation of Piezoelectric Actuators in a Wide Bandwidth”. In: *IEEE Transactions on Industrial Electronics* 66.7 (July 2019), pp. 5392–5402.

[10] F. Xia et al. “Design and Control of a Multi-actuated High-bandwidth and Large-range Scanner for Atomic Force Microscopy”. In: *2018 Annual American Control Conference (ACC)*. June 2018, pp. 4330–4335.

[11] K.J. Astrom and T. Hagglund. “Automatic tuning of simple regulators with specifications on phase and amplitude margins”. In: *Automatica* 20.5 (1984), pp. 645–651.

[12] Yudong Zhang et al. “Note: A novel atomic force microscope fast imaging approach: Variable-speed scanning”. In: *Review of Scientific Instruments* 82.5 (2011).

[13] James L Bosse and Bryan D Huey. “Error-corrected AFM: a simple and broadly applicable approach for substantially improving AFM image accuracy”. In: *Nanotechnology* 25.15 (Mar. 2014), p. 155704.

[14] Ying Wu, Qingze Zou, and Chanmin Su. “A Current Cycle Feedback Iterative Learning Control Approach for AFM Imaging”. In: *IEEE Transactions on Nanotechnology* 8 (2009), pp. 515–527.

[15] Liyi Li et al. “High precision position control of voice coil motor based on single neuron PID”. In: *ISPEMI* 8759 (2013).

IMPLEMENTATION OF LENGTH CONTROL OF AN OPTICAL CAVITY USING SECOND-ORDER TRANSVERSE MODES

Alvaro Fernandez-Galiana[1*], Jens Arnbak[2*], Matthew Evans[3] and Nergis Mavalvala[3]
[1]**Department of Mechanical Engineering**
Massachusetts Institute of Technology
Cambridge, MA, USA
[2]**Department of Physics**
The Technical University of Denmark
Lyngby, Denmark
[3]**Department of Physics**
Massachusetts Institute of Technology
Cambridge, MA, USA

INTRODUCTION

Optical cavities are used in a variety of applications due to their ability to enhance the optical field [1]. However, this enhancement is only present when the optical length of the cavity is stabilized (*locked*) to an integer number of half-wave lengths of the input field, $L = n\lambda/2$, which causes the input field to resonate. Typically, the cavity is kept *locked* using a feedback control scheme to drive a piezoelectric transducer (PZT) that actuates on the cavity length.

Several techniques can be used to generate the error signal used to drive the PZT. The purpose of this paper is to further develop and test a method that is based on higher-order Laguerre-Gaussian (LG) modes of order two (first excited mode) to generate the error signal, thereby extending the work performed in Ref. [2]. The interest of this *locking* scheme, which relies only on an imperfect mode-match to the cavity, is its simplicity combined with the capability of locking at the peak of the cavity resonance. The combination of these two factors is not achievable with other more prevalent *locking* techniques, such as the Pound–Drever–Hall [3] or the side-fringe lock [4]. The presented technique is of special interest to compact applications, since the number of components required is minimal.

THEORETICAL DEVELOPMENT

The Miller-Evans (ME) technique uses the interference between the fundamental cavity mode and the second order LG mode, where the later serves as a stable phase reference. This mode is generated by deliberately mismatching the input beam mode and the cavity mode (see fig. 1). When the input field does not perfectly spatially overlap with the cavity mode, the intra-cavity field can be described as the superposition of the TEM_{00} mode of the cavity and a second order mode:

$$u(z,r) \approx u_{0,0}(z,r) + \epsilon_w u_{0,1}(z,r), \qquad (1)$$

where $\epsilon_w = \epsilon_{w,0}\exp(i\phi_\epsilon)$ is a complex number representing the level of mismatch and $u_{l=0,p}$ is the mode function of the LG mode (with mode order $N = l + 2p$). To generate the error signal, the reflected light from the cavity is split into two beams. The first beam goes directly into Photodiode A (PD-A), whereas the second beam is cut on the edge using an iris before reaching Photodiode B (PD-B), as shown in Figure 2. This breaks the orthogonality of the fundamental and excited modes, hence generating the error signal. It can be shown that, for a cavity with complex amplitude reflectivities for the N^{th} order LG mode defined as $\mathfrak{r}_{\mathrm{N}} = r_{\mathrm{N}}\exp(\phi^r_{\mathrm{N}})$; and an input intensity of $|E_0|^2$, subtracting the amplified signal of PD-A

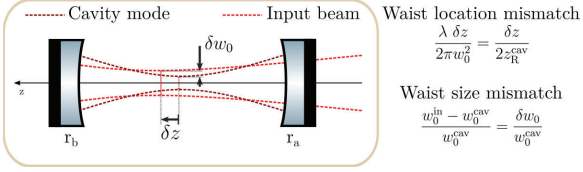

FIGURE 1. Cavity mode mismatch. The level of mismatch between the incoming beam and the cavity mode can be decomposed into waist location mismatch and waist size mismatch.

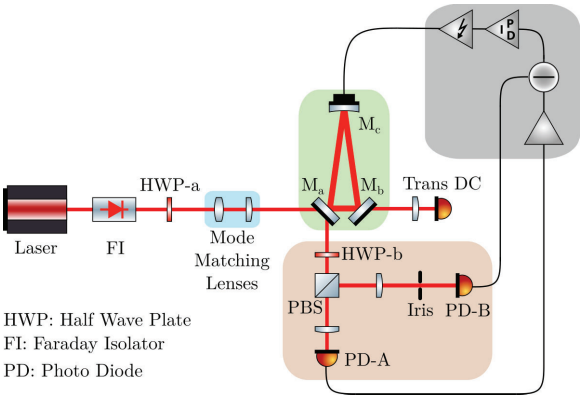

FIGURE 2. Experimental setup used to test the ME locking scheme. The error signal is generated using the reflected light from the cavity an splitting it into two beams. The first beam goes directly into PD-A, while the second is sent through an iris of radius $R_{\rm ir}$ before reaching PD-B. In our particular setup, the splitting ratio is controlled using a half wave plate and a polarization beam splitter. In a practical application this could be replaced with a regular beam splitter. The degree of mismatch is controlled with the mode matching lenses. The cavity has a Free Spectral Range (FSR) of $f_{\rm FSR} = 714$ MHz and a finesse of approximately 400.

from the signal of PD-B leads to:

$$i_- = 4|E_0|^2 \left[\frac{R_{\rm ir}}{w(z_{\rm ir})}\right]^2 \exp\left(-2\left[\frac{R_{\rm ir}}{w(z_{\rm ir})}\right]^2\right) (1-\eta)^2 r_0 r_2 \epsilon_{w,0} \cos\left(2\phi_0(z_{\rm ir}) + \phi_\epsilon + \phi_2^r - \phi_0^r\right) \quad (2)$$

where η is the splitting ration between PDs, $R_{\rm ir}$ is the radius of the iris, $w(z_{\rm ir})$ is spot size (radius) of the beam at the iris, $\epsilon_{w,0} = \left|\frac{\delta w_0}{w_0^{\rm cav}} + i\frac{\delta z}{2z_{\rm R}^{\rm cav}}\right|$ is the mode mismatch parameter, $\phi_\epsilon = \arg\left[\frac{\delta w_0}{w_0^{\rm cav}} + i\frac{\delta z}{2z_{\rm R}^{\rm cav}}\right]$ is the mode mismatch phase, and $\phi_0(z_{\rm ir})$ is the Gouy phase of the TEM_{00} mode at the iris. Figure 3 presents the computed error signal for different values of the Gouy phase at the iris, using the parameters of our cavity. In the example, a position of the iris where the phase $\Phi = 0°$ provides a good error signal, whereas for $\Phi = 45°$ the linear region does not allow locking of the cavity at the peak. Thus, in practice, to obtain a large linear error signal around the cavity resonance the iris has to be carefully positioned to match some Gouy phase condition. Figure 3 also shows that, as expected, this locking scheme also generates an error signal around the second order LG mode. Nevertheless, it is not difficult to lock into the desired mode by applying the correct initial offset. Equation 2 shows that the peak-to-peak amplitude of the error signal is dependent on the mismatch amplitude and on the position and radius of the iris (see Figure 4).

TEST SETUP

We implement the ME locking technique in an experimental test setup, presented in Figure 2, to demonstrate its feasibility with different levels of mismatch and splitting ratios, and to verify the theoretical predictions of Ref. [2]. For this test we use a triangular cavity with round-trip length $L_{\rm rt} = 420$ mm and a finesse $\mathscr{F} \approx 400$ [5]. Using a triangular cavity has the advantage that the incoming and reflected beam do not overlap. For linear cavities an unbalanced beam splitter can be placed before the cavity to pick-up the signal in the reflected light. Two mode-matching lenses

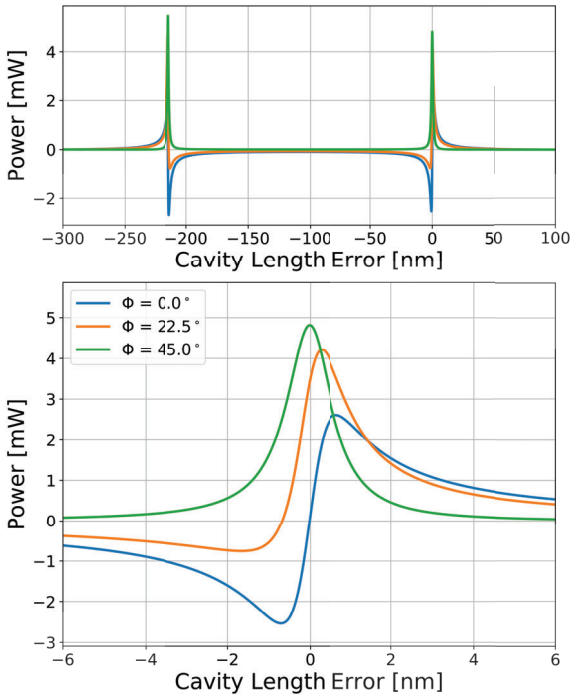

FIGURE 3. Simulated error signal around the resonance position as a function of $\Phi = 2\phi_0(z_{\rm ir}) + \phi_\epsilon$. The second resonance corresponds to locking the second-order mode. In this example, where optimal $R_{\rm ir}$ is assumed, $\Phi = 0°$ provides a good error signal, whereas for $\Phi = 45°$ the linear region does not allow locking of the cavity.

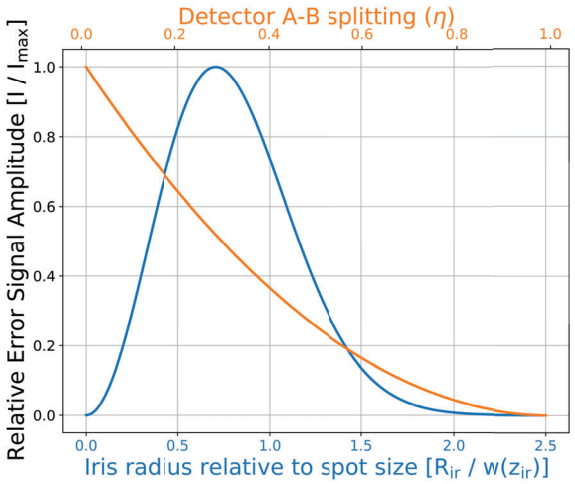

FIGURE 4. Effect of iris radius and detector splitting in error signal amplitude. To maximize the signal amplitude the iris radius must be such that $R_{\mathrm{ir}} = w(z_{\mathrm{ir}})/\sqrt{2}$. This figure also shows the effect of changing the splitting ratio between PD-A and PD-B. However, it does not take into account the limitations in amplification of the signal from PD-A nor the noise re-injected.

control the degree of mode-matching into the cavity. In the presented work, we have a mode-matching into the cavity of 90 %. The splitting ratio between PD-A and PD-B is controlled by the combined action of the half wave plate (HWP) and a polarization beam splitter (PBS). In general, a fixed splitting is sufficient. Thus, and a regular beam splitter could be used, specially for birefringent cavities such as the one used in our setup.

CAVITY LENGTH CONTROL

The more general form of controller scheme is to use a feedback control from the generated error signal into the PZT. A simplified version of the cavity length control scheme is presented in Figure 5. The cavity mechanical response $H_m(s)$ can be modelled as a second order system with resonance at the first longitudinal mode. This first resonance can be analytically estimated approximating our cavity to an elastic bar of length , which results in:

$$f_0^{\mathrm{cav}} = \frac{1}{2}\sqrt{\frac{E_{\mathrm{cav}}}{\rho_{\mathrm{cav}}}} = 16.2\ \mathrm{kHz} \tag{3}$$

where E_{cav} and ρ_{cav} are, respectively, the Young modulus and density of the cavity material (silica in our experiment). Figure 6 shows the estimated cavity mechanical response. A finite element analysis can better predict this resonance.

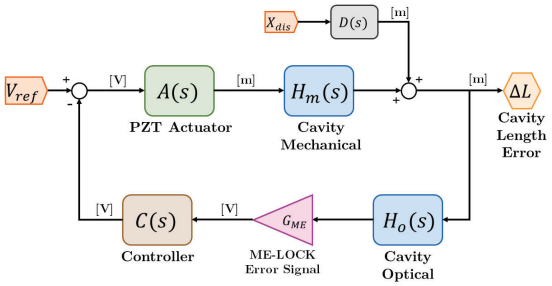

FIGURE 5. Simplified cavity length control scheme. The scheme is a classical feedback control, where the PZT acts as the actuator and the cavity mechanical response is the plant. The cavity optical response, combined with the ME scheme detectors and electronics, act as sensor. Assuming the cavity is kept within the linear region of the error signal, this can be simplified into a gain. For completeness, we have included an external disturbance, which could account for thermal fluctuations or seismic motion. For simplicity, all the electronic noises have been neglected.

This figure also presents the modelled PZT response. In our experiment, the PZT is a Noliac NAC2125 [6] of thickness $h = 2$ mm. The frequency constant (N_3) of this piezoelectric material (NCE51F) is 1320 Hz·m [6], from which we can estimate the first free elongation resonance as:

$$f_0^{\mathrm{PZT}} = \frac{N_3}{h} = 660.0\ \mathrm{kHz} \tag{4}$$

This can be corrected for our assembly, where the PZT of mass m is fixed on one side and attached to a mirror of mass M on the other as:

$$f_{\mathrm{res}}^{\mathrm{PZT}} = \frac{1}{2} f_0^{\mathrm{PZT}} \sqrt{\frac{m}{m+3M}} = 19.0\ \mathrm{kHz} \tag{5}$$

Using the information, along with the reported radial frequency of ≈ 80.0 kHz, the estimated PZT response is presented in Ref. 6. Since we are using the cavity reflection to generate the error signal, the cavity response for the electromagnetic field corresponds to:

$$H_{\mathrm{ME}}(s) = \frac{(1-r_0)\exp\left[-s/f_{\mathrm{FSR}}\right]}{1-r_0\exp\left[-s/f_{\mathrm{FSR}}\right]} \tag{6}$$

This can be simplified as a low pass filter with unity DC value and a pole at $f_c = \frac{f_{\mathrm{FSR}}}{4\mathscr{F}}$, which in our case corresponds to 446 kHz. In our

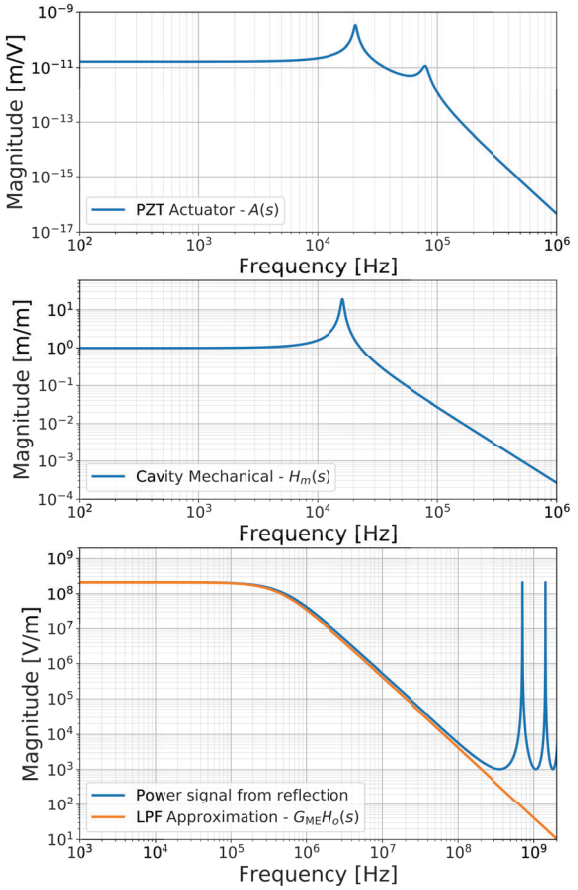

FIGURE 6. (Top) Modelled piezoelectric response based on information from the vendor. The first elongation and radial modes are predicted at 19 kHz and 80 kHz, respectively. (Mid) Modelled cavity mechanical response. Only the first longitudinal mode (≈16 kHz) has been considered. (Bottom) Modelled optical sensing response. The blue line present the exact response in power, including the extra resonances one FSR apart. The orange line is the equivalent low pass filter, with a cavity pole of 446 kHz. The DC value corresponds to the gain of the ME lock (0.209 V/nm in our case).

case, we are interested in the power transmission, which is simply: $H(s) = |H_{\mathrm{ME}}(s)|^2$. Figure 6 presents the optical sensing power transfer function ($G_{\mathrm{ME}}H(s)$), as well as the equivalent low pass filter used for the modeling.

Using the presented models and neglecting the effect of the disturbances, we can estimate the system's open loop (see Figure 7) and design the corresponding controller. In our particular case, the system is simple enough where a few hundred

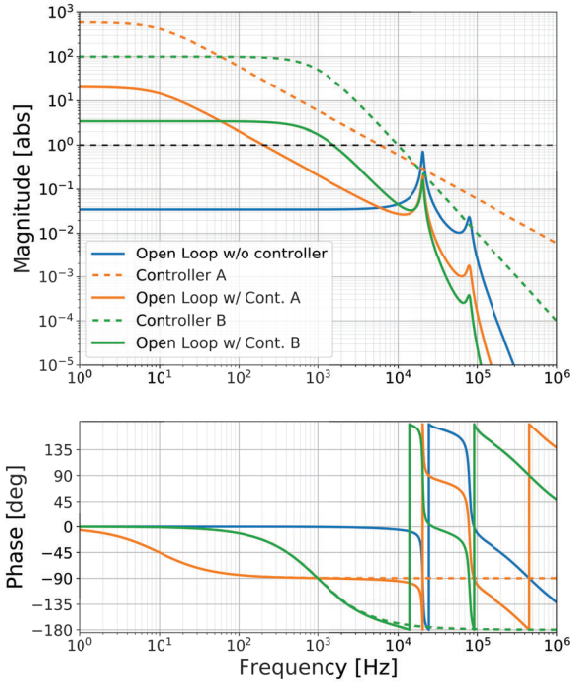

FIGURE 7. Modelled open Loop of the system. The blue line corresponds to the projected open loop of the system, with C(s) = 1. The orange dashed and solid lines correspond, respectively, to a first order low pass filter with cutoff at 10Hz and gain of 600 and the corresponding projected open loop. The blue dashed and solid lines correspond, respectively, to a second order low pass filter with cutoff at 1kHz and gain of 100.

Hertz of bandwidth can be achieved by applying a first order low-pass filter (Controller A in Figure 7). The limitation in bandwidth comes from the resonances of the PZT and the cavity mechanics. In order to increase the bandwidth, a more aggressive controller roll-off can be used, which results in an increase of an order of magnitude in the bandwidth (Controller B in Figure 7). In order to increase it further, or in order to increase the gain margin, a notch filter could be used around the frequency. Alternatively, the PZT and the cavity assemblies could be redesigned to mechanically damp the resonances.

All the data presented in this section has been generated using models. Although this models are valuable to generate an initial controller, the system's dynamic response must be experimentally measured in order to achieve the highest performance.

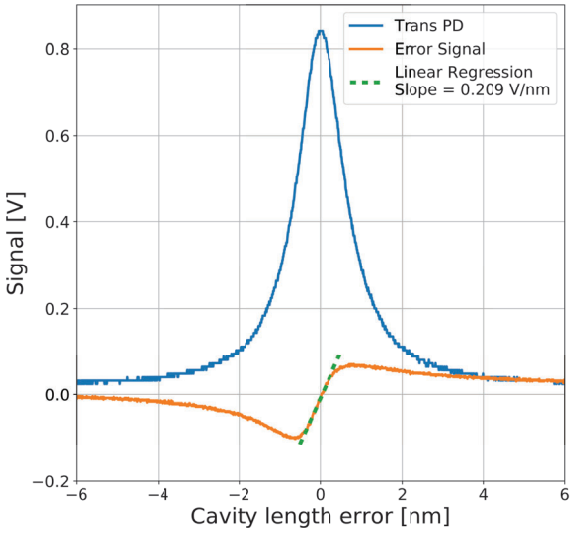

FIGURE 8. Measured error and transmission PD signals. The error signal is symmetric and centered around the resonance. The linear region of the signal has a dynamic range of approximately $\pm$0.25nm and a slope of 0.209 V/nm.

EXPERIMENTAL RESULTS

The control scheme was implemented using a high speed servo controller (NewFocus LB1005-A), low noise voltage preamplifier (Stanford Research Systems SR-560 [7]) and a high-voltage amplifier (Thorlabs MDT693A). The result is the error signal presented in Figure 8. To maximize the dynamic range of the error signal and obtain a symmetric signal we had to minimally adjust the iris position and aperture, after which we applied a small DC offset. This signal corresponds to the case of a balanced splitting ratio ($\eta = 0.5$).

Using the SR-560 voltage preamplifier we implemented the control scheme applying a first order low pass filter with a cutoff frequency of 10 Hz as the controller $C(s)$. The lock was stable and kept the cavity at the resonance in a relatively quiet environment for over 6 hours. Unfortunately, at this time we cannot report the phase and gain margin of the implemented lock.

The next steps are to further test the performance of this scheme and its long term reliability, and to measure the frequency response of the system and compare it to our predictions. This will refine our *a priori* controller design. On the other hand, moving into a Field-Programmable Gate Array controller will simplify and reduce the cost of implementation of this scheme.

CONCLUSIONS

The ME locking technique is a low cost and simple to implement cavity locking scheme. In our experimental realization this was used simply to actuate on one of the mirrors to keep the cavity at lock, but it could be used in any system requiring precise relative position between their elements. In the reported work, a low pass filter is sufficient to keep the cavity stably for several hours. The bandwidth of the controlled system is ultimately limited by the resonances of the piezoelectric actuator and the mechanical cavity assembly.

ACKNOWLEDGEMENT

This work has been possible thanks to the support of the National Science Foundation (NSF), grant PHY1707840. LIGO was constructed by the California Institute of Technology and Massachusetts Institute of Technology with funding from the NSF, and operates under cooperative agreement PHY0757058. Advanced LIGO was built under award PHY0823459. Finally, we wish to thank Dr. Slawek Gras LIGO-MIT for his help.

REFERENCES

[1] Ye J, Lynn T W. Applications of optical cavities in modern atomic, molecular, and optical physics. In Advances in Atomic, Molecular, and Optical Physics. 2003; 49: 1-83.

[2] Miller J, Evans M. Length control of an optical resonator using second-order transverse modes. Optics letters. 2014; 39(8): 2495-2498.

[3] Black E D. An introduction to Pound–Drever–Hall laser frequency stabilization. American journal of physics. 2001; 69(1): 79-87.

[4] Barger R L, Sorem M S, and Hall J L. Frequency stabilization of a cw dye laser. Applied Physics Letters. 1973; 22(11): 573-575.

[5] Willke B, et al. Spatial and temporal filtering of a 10-W Nd: YAG laser with a Fabry–Perot ring-cavity premode cleaner. Optics letters. 1998; 23(21) : 1704-1706.

[6] NAC2125 - Noliac. http://www.noliac.com/products/actuators/ring-actuators/show/nac2125/, Noliac-CTS.

[7] SR-560 Low Noise Preamplifier. https://www.thinksrs.com/products/sr560.html, Stanford Research Systems.

ACTIVE OPTICAL MODE MATCHING FOR THE QUANTUM SQUEEZING CAVITIES AND UPCOMING LIGO UPGRADES

Minkyun Noh[1,2], Huy Tuong Cao[3], Sebastian Ng[3], Varun Srivastava[4], Wenxuan Jia[1], Georgia Mansell[1], Don Griffith[5], Calum Torrie[5], Richard Abbott[5], Aidan Brooks[5], Stefan Ballmer[4], Peter Veitch[3], Peter Fritschel[1], and Fabrice Matichard[1,5]

[1]LIGO Laboratory, MIT, Cambridge, MA, US
[2]The University of British Columbia, Vancouver, BC Canada
[3]The University of Adelaide, Adelaide, AUSTRALIA
[4]Syracuse University, Syracuse, NY, US
[5]LIGO Laboratory, Caltech, Cambridge, MA, US

INTRODUCTION

The two LIGO detectors use 4km Michelson interferometers to detect gravitational waves emitted by astrophysical events [1]. The sensitivity of the detectors is limited by optical quantum noise at most frequencies of the observation bandwidth, in the form of shot noise in the upper portion of the gravitational wave band [>100Hz], and transitioning to radiation pressure noise [<50Hz]. Optical squeezing is used to reduce the impact of shot noise on the sensitivity [2]. Filter cavities [3] are planned to be implemented starting in mid-2020 to reduce the effect of radiation pressure.

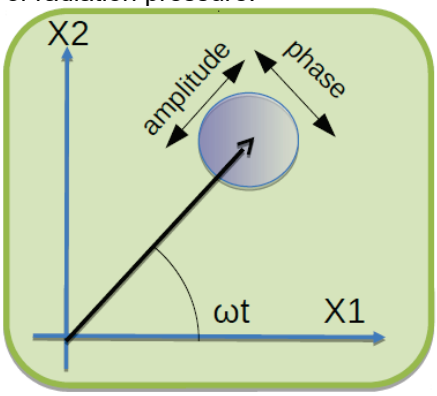

FIGURE 1. Picture illustrating the quantum noise of the carrier. It results in radiation pressure noise at low frequencies, and shot noise in the optical readout at higher frequencies.

Squeezing techniques are primarily limited by optical loss. To optimize the performance of these enhanced interferometers, the fields circulating from an optical cavity to the next must be mode matched at the 95% level minimum, and up to 99% on certain optical paths.

To reach these goals, we have developed deformable optics for active mode matching between the optical fields and the squeezer cavities. This active wavefront control upgrade is planned for deployment in the LIGO interferometer in 2020.

The presentation associated with this extended abstract will give an overview of the quantum noise limitations, the technology implemented for reduction, and the crucial role of optical mode matching for performance optimization. It will present and focus on the adaptive optics developed for active mode matching and the system level implementation.

QUANTUM NOISE, SQUEEZING AND OPTICAL MODE MATCHING

Figure 2 illustrates the principle of quantum squeezing. In this example, phase noise is reduced at the expense of amplitude noise. This is achieved in the LIGO detectors using an optical parametric oscillator generating correlation between side-bands noise.

Filter cavities are used to rotate the ellipse as a function of frequency. The frequency dependence is tuned to reduce radiation pressure noise at low frequency and shot noise at higher frequencies.

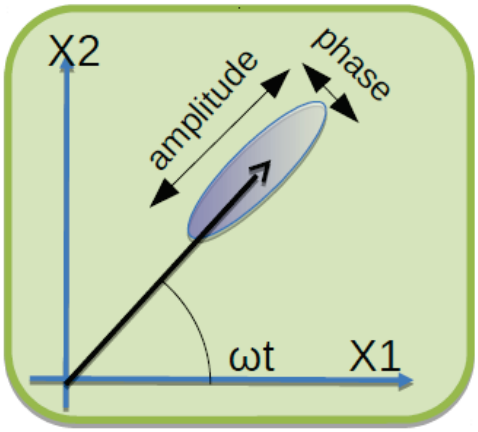

FIGURE 2. Picture illustrating the squeezed state of the quantum noise.

Every loss on the optical path between the optical parametric oscillator and the interferometer degrades the squeezer performance. Mismatch of the radius of curvature and waist location of the squeezed beam with respect of the filter cavities and interferometer, referred as mode-matching defect, is one of the dominant losses.
The next section presents a device developed to actively improve the mode matching, thus reducing the optical loss, improving the LIGO sensitivity, and the rate of detection.

ACTIVE PIEZO-DEFORMABLE OPTICS

Design

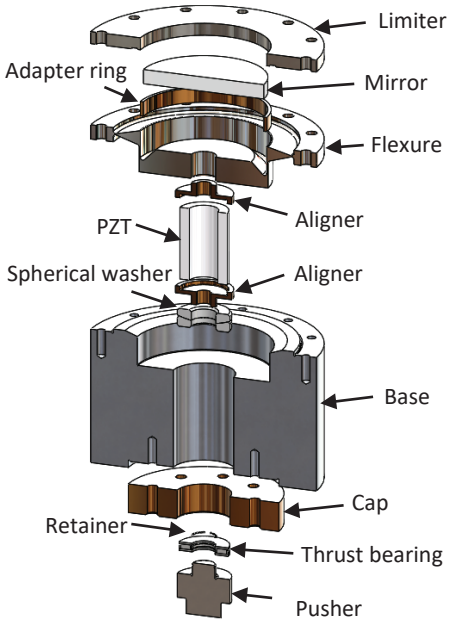

FIGURE 3. Exploded view of the piezo deformable mirror. The flexure converts the PZT displacement into mirror curvature.

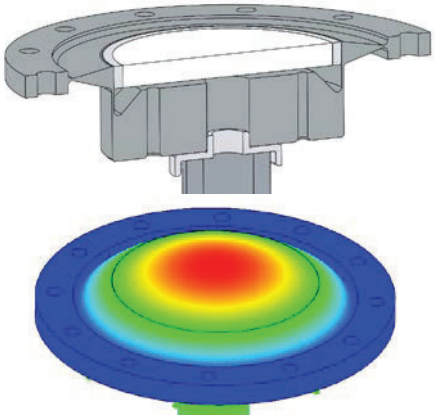

FIGURE 4. Top, cross section of the flexure mechanism. Bottom, simulation of the deflection at full range, a 44 µm sag across the 50 mm mirror, for a change of optical power of 225 mD.

The device is based on an innovative flexure mechanism that translates displacement of a piezo-ring actuator into curvature of a mirror.
The mirror is compressed inside the flexure. The assembly is performed at high temperature to generate a difference of thermal expansion between the fused silica and the metal parts. After cool down, the shrink-fit generates a compression bias of the same order as the tension stress induced by the bending of the mirror during operations. This ensures the brittle mirror mostly operate under compressed state.

Testing

Testing to qualify this adaptive optics for operation includes measurement of actuation range (curvature), higher order aberrations, and piston motion at the level of 10^{-15} m/√ Hz. The presentation will present details of the test set-ups and test results.

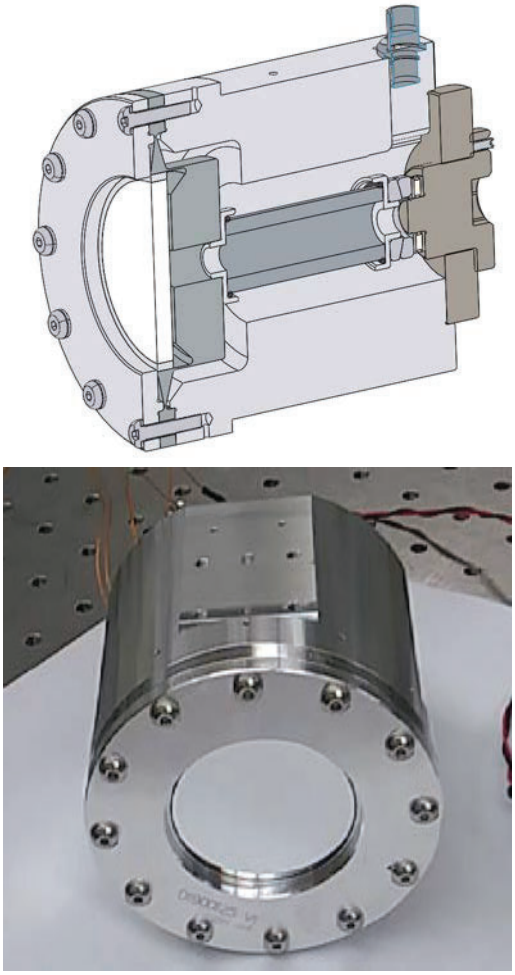

FIGURE 5. CAD picture of the piezo-deformable optics assembly (top), and prototype (bottom)

SUSPENDED STAGE AND SYSTEM LAYOUT

The adaptive optics is integrated into a double stage suspension that provides vibration isolation and mirror steering functionalities. The presentation will also give an overview of the overall system layout.

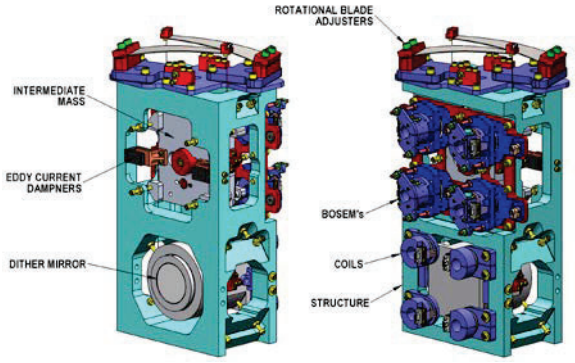

FIGURE 6. Suspension assembly for seismic isolation, resonance damping, steering and dithering of the piezo-deformable optics assembly

REFERENCES

[1] Abbott B, et al. Gw150914: The advanced ligo detectors in the era of first discoveries. Phys. Rev. Lett. 2016. 116: 131103

[2] Tse M, Yu H, Kijbunchoo N .et al. Quantum-enhanced advanced ligo detectors in the era of gravitational-wave astronomy. Phys. Rev. Lett. 2019, 123: 231107

[3] Kwee P, Miller J, Isogai T, Barsotti L & Evans M. Decoherence and degradation of squeezed states in quantum filter cavities. Phys. Rev. D90, 062006 (2014)

ACKNOLEDEGEMENTS

LIGO was constructed by the California Institute of Technology and Massachusetts Institute of Technology with funding from the National Science Foundation, and operates under Cooperative Agreement No. PHY-0757058. Advanced LIGO was built under GrantNo.PHY-0823459. This paper carries LIGO document number P2000027.

Figures 1 & 2 are courtesy of Eric Oelker reference document LIGO-G1600680-v1 Tutorial on squeezing and quantum noise

REDUCED THERMO-MECHANICAL MODEL OF A ROTARY TABLE OF A 5-AXIS PRECISION MACHINE TOOL

Pablo Hernández-Becerro[1,2], Josef Mayr[1] and Konrad Wegener[2]
[1]**inspire AG Technoparkstrasse 1, 8005 Zürich, Switzerland**
[2]**Institute of Machine Tools and Manufacturing (IWF)**
ETH Zürich, Switzerland

INTRODUCTION

Precise manufacturing processes require accurate and repeatable machine tools. Among the different error sources, Mayr et al. [1] stated that thermally induced deviations are the major contributor to geometrical errors in manufactured parts. The heat losses of the machine elements and external devices lead to an inhomogeneous, time-varying temperature distribution. The temperature gradients result in a structural deformation, inducing position and orientation errors between the tool center point (TCP) and the workpiece. Thermal errors can be understood as variation of the reference geometry of the machine tool and the workpiece, measured at a homogeneous reference temperature. Bryan [2] outlined the different heat sources in production machines and measurement systems and classified the sources as either internal (e.g. drives, bearings) or external (environment, process, cutting fluid, and people).

Thermo-mechanical models, based on the Finite Element (FE) discretization of the heat transfer and elasticity equations, describe the temperature distribution and the associated structural deformation. These models enable testing the feasibility of design modifications and are a useful tool to optimize the performance of the system. However, evaluating thermo-mechanical models is computationally expensive, limiting applications that require a large amount of model evaluations, as well as the possibility of real time predictions. Therefore, this work develops surrogate models by means of projection-based Model Order Reduction (MOR). MOR techniques project the high fidelity model into a lower dimensional space, which contains the most relevant information about the response of the system. The main advantage of projection-based model reduction is that it retains the system structure and allows the traceability of the dynamical evolution. Projection-based reduction use the underlying structure of the system enabling the derivation of error bounds of the surrogate model, as explained by Benner et al. in [3]. The MOR techniques are an intrusive method, as they require the access and modification to the system matrices. MOR is increasingly used both in academia and industry enabling applications such as parameter identification, uncertainty analysis, design optimization, and real-time control of systems.

MODEL ORDER REDUCTION OF THERMO-MECHANICAL MODELS

The different MOR methods define the reduced-order subspace, and its projection basis, according to some criteria to minimize the error between the response of the original and the reduced system. Antoulas [4] reviewed the MOR techniques for linear time invariant (LTI) systems. Thermo-mechanical models of mechatronic systems, such as machine tools, have a certain characteristic behavior compared to other general first order systems. Firstly, the amplitude of the thermal response of the system decays at higher excitation frequencies. Therefore, the reduced system only needs to approximate the thermal response of the system at low frequencies. Secondly, the steady state response is relevant in order to describe the behavior of the system. Thus, the reduced system needs to match the steady state temperature field of the original system for the different input and output combinations. This paper uses the Krylov Modal Subspace (KMS) reduction method developed by Spescha [5] for structural dynamic problems. The KMS method approximates the static part of the response using a moment matching Krylov subspace method with a expansion point at a low frequency. Additionally, the projection basis includes the eigenvectors of the thermal system in the frequency range of interest. The main advantage of the KMS method is that there is an a-priori error estimator, which is an upper bound of the error between the response of the original and reduced-order system.

MORe [6] is a simulation framework to analyze the static, dynamic, and thermo-mechanical be-

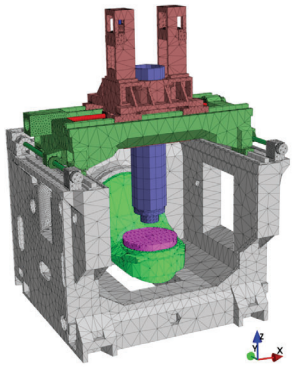

FIGURE 1. FE model of a precision 5-axis machine tool in MORe

havior of machine tools, where the reduction methods are implemented. It offers an efficient workflow to develop FE models of machine tool assemblies. MORe imports the geometrical information and the system matrices from a commercial FE-software, Ansys. The software platform enables the definition of the boundary conditions and the connections between the different structural components. MORe provides specialized analysis tools as well as a postprocessor with interactive results visualization.

DEVELOPMENT OF THE THERMO-MECHANICAL MODEL

This paper investigates the thermo-mechanical behavior of a precision 5-axis machine tool, shown in Figure 1. The kinematic configuration according to ISO 10791-1:2015 adapted for machining centers with vertical spindles is

V [w C2' B' b [Y1 Y2] X [Z1 Z2] (C1) t]

The working volume is 730x510x510 mm, with a table of 500 mm of diameter. The linear axes are arranged in a box-in-box design, ensuring the thermal symmetry of the machine tool. The investigated machine tool has a rotary table, C-axis, providing the possibility to perform turning operations with a maximal rotational speed of 1200 rpm. The heat losses due to the rotation of the C-axis results in thermally induced deviations, which have a direct impact on the geometrical errors of the manufactured parts. This paper concentrates on the thermo-mechanical response of the machine tool during the rotation of the C-axis.

The heat losses at the machine elements determine the thermo-mechanical behavior during the

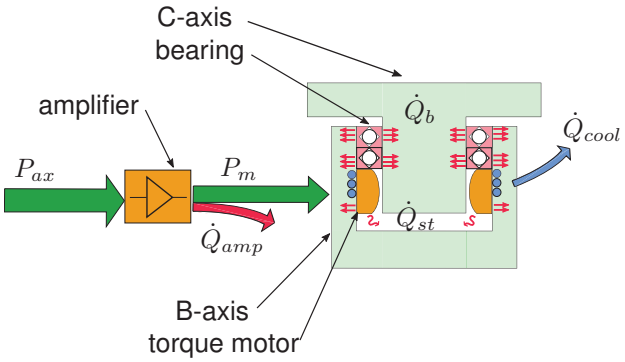

FIGURE 2. Energy flow due to the rotation of the C-axis. Green represents electrical power, red thermal power, and blue hydraulic power

rotation of the C-axis. A thermo-energetic model enables the estimation of the heat losses and provides the boundary conditions for the thermo-mechanical model. Mohammadi et al. [7] developed a thermo-energetic model of the investigated machine tool. The authors presented a model to predict the different energy flows, i.e. mechanical, electrical, hydraulic, and thermal, for different operational points. The model was developed in the EMod, a simulation framework developed by Züst [8] for thermo-energetic models.

Figure 2 illustrates the energy flows of the rotary table unit. The supplied electrical power to the motor, P_m, can be decomposed as

$$P_m = P_{mech} + \dot{Q}_{ag} + \dot{Q}_{rt} + \dot{Q}_{st} + \dot{Q}_b \quad (1)$$

where $\dot{Q}_{st}$ are the losses at the stator, $\dot{Q}_{rt}$ the losses at the rotor, $\dot{Q}_{ag}$ the losses at the air gap, $\dot{Q}_b$ the losses at the bearing, and P_{mech} the mechanical power required to rotate the axes. At a constant rotational speed, the mechanical torque and therefore mechanical power, P_{mech}, is zero. The losses at the air gap can be expressed according to Saari [9] as a function of the shear stress τ_{ag} at the air gap as

$$\dot{Q}_{ag} = \pi \cdot \tau_{ag} \cdot \omega \cdot D_{ro} \cdot l_{ro} \quad (2)$$

Züst [8] developed a meta model to determine the shear stress τ_{ag} as a function of the rotational speed and the Reynolds number. For the dimensions of the motor of the axis under investigation and a maximal rotational speed of 1200 rpm, the losses at the air gap are 1.3 W. Therefore, the

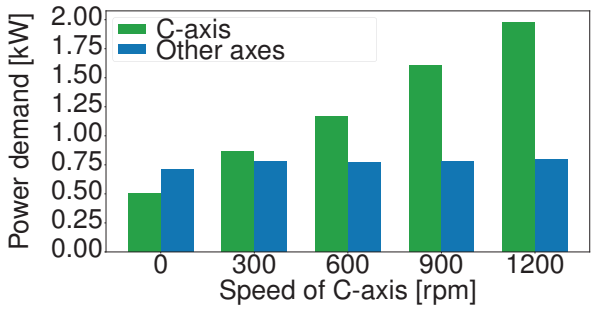

FIGURE 3. Energy demand of the C-axis and other components (linear axes, spindle, and B-axis) of the machine tool for different values of the rotational speed of the C-axis

heat losses at the air gap are considered negligible in comparison with the other heat inputs to the system, i.e. $\dot{Q}_{ag} \approx 0$. The axis depicted in Figure 2 uses a torque motor, which is a type of motor with winding exclusively in the stator. Thus, heat losses at the rotor are zero, i.e. $\dot{Q}_{rt} = 0$. Therefore, only two terms of Equation (1), namely $\dot{Q}_{st}$ and $\dot{Q}_b$, need to be determined.

The losses at the stator $\dot{Q}_{st}$ can be calculated in terms of the rotational speed ω and the current of the motor I, provided several characteristics of the motor are known. However, the required information about the torque motor is not available. Therefore, the estimation of the heat losses at the stator and bearing rely on the parameter η_{mot}, describing the efficiency of the torque motor as

$$\dot{Q}_b = \eta_{mot} \cdot P_m \tag{3}$$

$$\dot{Q}_{st} = (1 - \eta_{mot}) \cdot P_m \tag{4}$$

In order to quantify the heat losses, the energy demand of the machine tool for different rotational speeds of the C-axis is measured. Figure 3 shows the power demand measured at a constant rotational speed. The electrical power of the B-axis, linear axes, and spindle is around 750 W. The power consumption of the C-axis ranges from 504 W for standing still to 1977 W for 1200 rpm, which corresponds to the maximal rotational speed.

An internal cooling system removes part of the heat introduced by the machine elements. A pump located outside the machine tool working space supplies pressurized cooling fluid from a tank. An external unit controls the temperature of the fluid to a reference temperature provided by a sensor located in the machine tool bed. The heat removed by the structural cooling $\dot{Q}_{cool}$ is

$$\dot{Q}_{cool} = c_p \cdot \rho \cdot \dot{V} \cdot (T_{out} - T_{in}) \tag{5}$$

where c_p is the heat capacity, ρ is the fluid density, $\dot{V}$ is the volumetric flow, T_{out} is the outlet temperature, and T_{in} is the inlet temperature.

After estimating the heat losses and the heat removed by the cooling system of the rotary table, the thermo-mechanical contacts between the different structural parts of the machine tool need to be defined. Among the different thermal contacts, the heat transfer at the bearing of the C-axis plays an important role due to its proximity to the heat source. Weidermann [10] proposed an empirical correlation for the thermal contact conductivity (TCC) of bearings based on the geometry and rotational speed. The TCC λ_{TCC} in $\frac{\mathrm{W}}{\mathrm{K}}$ can be expressed as

$$\lambda_{TCC} = Z \frac{d_b^2}{2400} \sqrt{14 + 2\ln(v_p) - 2\ln(d_b)} \tag{6}$$

where Z is the number of rolling elements, d_b is the diameter of the rolling elements in mm, and v_p is defined as

$$v_p = \frac{d + d_p}{19099} n_r \tag{7}$$

being d the mean diameter of the bearing in mm, and n_r the rotational speed of the bearing in rpm. According to Weidermann [10], a value of $v_p = 0.1$ is considered for stationary bearings.

The convective boundary conditions are relevant in order to describe the thermo-mechanical behavior of the system. The rotation of the C-axis modifies the air flow inside the machine tool enclosure, enhancing the circulation of the air inside the working space. The mechanical enhancement of the airflow results in a more efficient heat exchange between the air inside the enclosure and the structure, leading to forced convection. Cardone et al. [11] proposed a correlation for the Nusselt (Nu) of a rotating disk for turbulent flow

corresponding to values the Reynolds (Re) number above 320,000 as

$$Nu = 0.0163 \cdot Re^{0.8} \tag{8}$$

The Reynolds number is defined as

$$Re = \frac{r^2 \cdot \omega}{\nu_0} \tag{9}$$

where ω is the rotational speed in rad/s, r is the radius of the disk, and ν_0 is the kinematic viscosity of the air. The Nusselt number is defined as

$$Nu = \frac{h \cdot r}{\lambda} \tag{10}$$

where h is the HTC and λ is the conductivity of the air.

After the definition of the boundary conditions, MOR transforms the original thermal system of 508,462 degrees of freedom (DOF) to a reduced system of 392 DOF, capturing all relevant thermal information up to 0.01 rad/s. Additionally, the reduced-order thermo-mechanical system has 1,164 DOF, from an original model of 1,525,386 DOF.

VALIDATION OF THE THERMO-MECHANICAL MODEL

The validation of the thermo-mechanical model requires the comparison between the simulated and measured thermally induced deviations. The R-Test, developed by Weikert [12], evaluates the deviations between a displacement sensor in the spindle and a precision sphere located on the table. Gebhardt et al. [13] used the discrete R-Test, which measures the deviations at 4 indentations of the rotary axis, namely 0°, 90°, 180°, and 270°. The average value of the measured deviations provides the position error of the C-axis in X-, Y-, and Z-direction. For the validation of the thermo-mechanical model, the thermally induced deviations are measured every 5 min.

During the rotation of the C-axis, several temperature signals are recorded. Figure 4 shows the air temperature inside the machine room (MR) enclosure during the rotation of the C-axis at 600 rpm over 6 h. The heat dissipated at the bearing and torque motor is transferred to the air inside the machine tool enclosure, increasing its temperature 1 °C over the first 3 hours. The recorded temperature data is used as an input signal for the thermo-mechanical model.

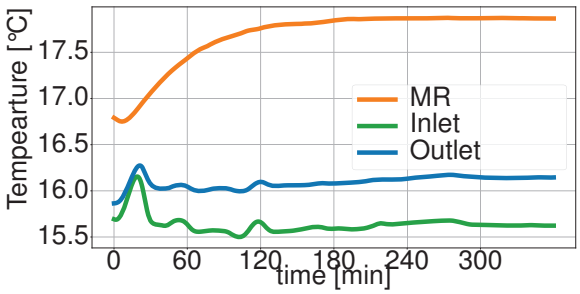

FIGURE 4. Measured temperature of the environment inside the machine room (MR), inlet of the cooling, and outlet of the cooling during the rotation of the C-axis at 600 rpm over 6h

According to Equation (5), the heat dissipated by the cooling system depends on the difference between the inlet and outlet cooling temperature. Figure 4 shows the measurement of the inlet and outlet temperature during the rotation of the C-axis. The control system of the cooling unit establishes the inlet temperature after the first 30 min, ensuring afterwards a constant cooling power. The thermo-mechanical model uses the difference between the inlet and the outlet temperature as an input signal to estimate the cooling power.

Figure 5 compares the measured and simulated thermally induced deviations in X-, Y-, and Z-direction during the rotation of the C-axis at a constant speed of 600 rpm over 6 h. The sampling time of the simulated thermo-mechanical deviations is 5 min. Due to the symmetric design of the machine tool, the thermal deviations in X-direction are close to zero during the rotation of the C-axis. The thermo-mechanical model shows a good quantitative agreement with the measured thermal deviations in Y- and Z-direction.

The validation of the thermo-mechanical model needs to be extended to other rotational speeds. Therefore, the load case of Figure 6 is investigated. The rotational speed of the C-axis ranges from 300 rpm to 1200 rpm with steps every hour over a total measurement time of 6 hours. Figure 7 shows a comparison between the simulated and measured thermo-mechanical response of the system in X-, Y-, and Z-direction.

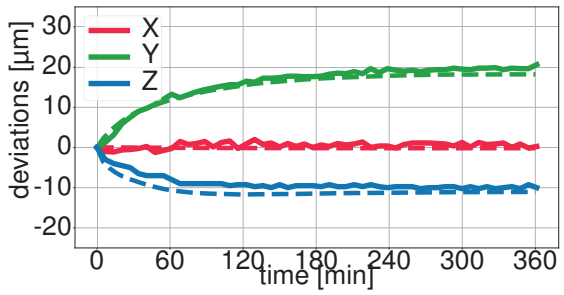

FIGURE 5. Comparison of the measured (full line) and simulated (dashed) transient response in X-, Y- and Z-direction for the rotation of the C-axis at 600 rpm over 6 h

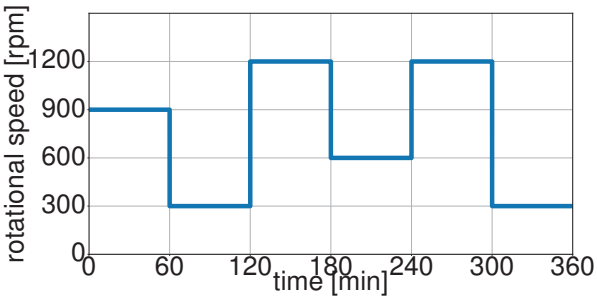

FIGURE 6. Speed profile of the C-axis over 6 h

There is a good match between the experimental and model data, confirming that the thermo-mechanical model can capture the response of the machine tool at different rotational speeds of the C-axis. The main discrepancies between model and simulation appear in Z-direction, which can be attributed to measurement uncertainty and model inaccuracies.

ANALYSIS OF THE THERMO-MECHANICAL DESIGN

After validating the thermo-mechanical model with experimental data, the physical model is a good resource to analyze the response of the machine tool during the rotation of the C-axis. Figure 8 depicts the thermo-mechanical response in frequency domain, illustrating the characteristic behavior of the system in the frequency range of interest. The input of the frequency response function (FRF) is the variation of the temperature of the air inside the machine tool enclosure and the outputs are deviations in X-, Y-, and Z-direction. The FRF is evaluated in a frequency range between 10^{-6} to 0.01 rad/s. Figure 8 shows that the variation of the temperature inside the working space has an impact on the deviations in Y-

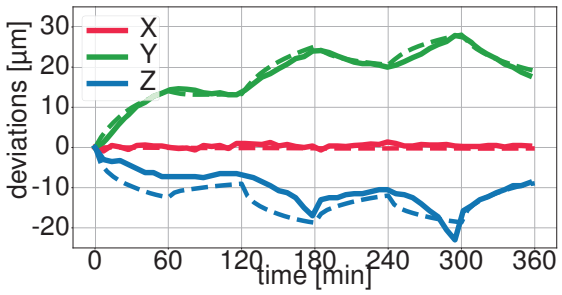

FIGURE 7. Comparison of the measured (full line) and simulated (dashed) transient response in X-, Y- and Z-direction for the rotation of the C-axis over 6 h with rotational speeds shown in Figure 6

direction, with a static gain of 2.8 $\frac{\mu m}{K}$. The increase of the air temperature inside the machine enclosure results in a thermal expansion of the structure of the B- and C-axis, leading to thermally induced deviations in Y-direction.

In order to reduce the effect of the thermally induced deviations on the manufactured part, it is customary to develop compensation models based on experimental data. The compensation models predict the thermal deviations during the rotation of the C-axis, as explained by Mayr et al. [14]. The tool-sided axes offset the predicted errors, assuming that the structural deformation of the workpiece-sided axes are the only cause of the thermal deviations. However, the temperature inside the machine enclosure increases during the rotation of the C-axis, affecting both the tool- and workpiece-sided axes. The validated thermo-mechanical model can be used to estimate the magnitude of the thermal deviations of the tool-sided axes. During the rotation of the C-axis at maximal speed, i.e. 1200 rpm, the model predicts deviations up to -2.4 µm in Z-direction of the tool-sided axes, corresponding to 12% of the relative deviations in Z-direction. Due to the symmetric design, the deviations in Y-direction of the tool-sided axes remain close to zero. This information needs to be considered during the design of thermal error compensation models at different indentations of the B-axis.

CONCLUSIONS AND OUTLOOK

This paper develops a thermo-mechanical model of a precision 5-axis machine tool to investigate its response during rotation of the C-axis. In oder to reduce the computational effort required to evaluate the thermo-mechanical model,

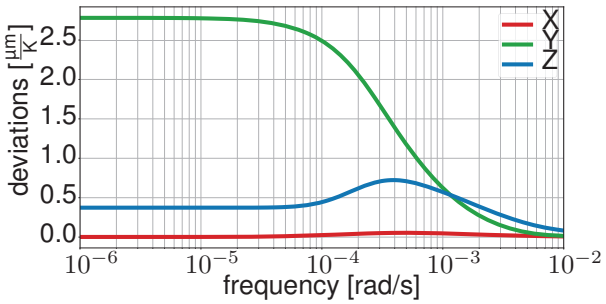

FIGURE 8. FRF response of the machine tool of Figure 1. Input: variation of the air temperature in the machine room. Output: TCP deviations relative to the workpiece for the X-, Y- and, Z-direction.

this work develops a surrogate model by means of MOR with the simulation environment MORe. After estimating the thermal boundary conditions, the outputs of the model are compared to the measured thermal deviations. The thermo-mechanical model shows a good quantitative agreement to the measured thermal deviations during the rotation of the C-axis at different rotational speeds. The validated thermo-mechanical model is a useful tool to separate the effect of the different inputs on the thermally induced deviations. Furthermore, the model enables the separation between tool- and workpiece-sided deviations. This information is important for the design of thermal error compensation models at different orientations of the B-axis.

Future work will concentrate on the investigation of the thermal response of the machine tool to other load cases as well as using the information of physical models to improve current thermal error compensation models.

ACKNOWLEDGMENTS

The authors would like to thank the Swiss Innovation Agency (Innosuisse) and the Machine Tool Technologies Research Foundation (MTTRF) for their financial support.

REFERENCES

[1] Mayr J, Jedrzejewski J, Uhlmann E, Donmez MA, Knapp W, Härtig F, et al. Thermal issues in machine tools. CIRP Annals - Manufacturing Technology. 2012;61(2):771 – 791.

[2] Bryan J. International Status of Thermal Error Research (1990). CIRP Annals - Manufacturing Technology. 1990;39(2):645 – 656.

[3] Benner P, Gugercin S, Willcox K. A survey of projection-based model reduction methods for parametric dynamical systems. SIAM review. 2015;57(4):483–531.

[4] Antoulas AC. Approximation of large-scale dynamical systems. Society for Industrial and Applied Mathematics; 2005.

[5] Spescha D. Framework for efficient and accurate simulation of the dynamics of machine tools. TU Clausthal; 2018.

[6] inspire AG. MORe; 2020. Available from: `https://www.more-simulations.ch`.

[7] Mohammadi A, Züst S, Mayr J, Blaser P, Sonne MR, Hattel JH, et al. A methodology for online visualization of the energy flow in a machine tool. CIRP Journal of Manufacturing Science and Technology. 2017;19:138 – 146.

[8] Züst SD. Model Based Optimization of Internal Heat Sources in Machine Tools. ETH Zurich; 2017.

[9] Saari J. Thermal analysis of high-speed induction machines [G4 Monografiavitskirja]. Helsinki University of Technology; 1998.

[10] Weidermann F. Praxisnahe thermische Simulation von Lagern und Führungen in Werkzeugmaschinen. In: 19th CAD-FEM Users Meeting; 2001. .

[11] Cardone G, Astarita T, Carlomagno G. Heat transfer measurements on a rotating disk. International Journal of Rotating Machinery. 1997;3(1):1–9.

[12] Weikert S. R-Test, a New Device for Accuracy Measurements on Five Axis Machine Tools. CIRP Annals - Manufacturing Technology. 2004;53(1):429 – 432.

[13] Gebhardt M, Cube Pv, Knapp W, Wegener K. Measurement set-ups and -cycles for thermal characterization of axes of rotation of 5-axis machine tools. In: Proceedings of the 12th euspen International Conference, Stockholm, June 2012; 2012. .

[14] Mayr J, Blaser P, Ryser A, Hernandez-Becerro P. An adaptive self-learning compensation approach for thermal errors on 5-axis machine tools handling an arbitrary set of sample rates. CIRP Annals. 2018;67(1):551 – 554.

DYNAMIC ERROR BUDGETING IN THE DEVELOPMENT OF THE HIGH-DYNAMIC DOUBLE- CRYSTAL MONOCHROMATOR FOR SIRIUS LIGHT SOURCE

Renan R. Geraldes [1,2], Marcelo A. L. Moraes[1], Ricardo M. Caliari[1] and Gert Witvoet[2]
[1]**Brazilian Synchrotron Light Laboratory (LNLS)**
Brazilian Center for Research in Energy and Materials (CNPEM)
Campinas, São Paulo, Brasil
[2]**Control Systems Technology Group, Department of Mechanical Engineering**
Eindhoven University of Technology (TU/e)
Eindhoven, The Netherlands

INTRODUCTION

This work presents the Dynamic Error Budgeting (DEB) workflow in the High-Dynamic Double-Crystal Monochromator (HD-DCM) [1], which has been developed since 2015 for X-rays beamlines of Sirius 4th-generation Light Source at the Brazilian Synchrotron Light Laboratory (LNLS) [2]. Being the first DCM to implement a low-stiffness mechanical design concept with high closed-loop mechatronic performance, its development was based on predictive design to realize it "first time right" and deliver positioning performance improvements by factors of 4 and 100 with respect to state-of-the-art DCMs, in fixed and scanning modes, respectively. The DEB methodology is demonstrated via a 6-degree-of-freedom (DoF) mechatronic model with special attention to the disturbance models and the predicted performance, which can finally be compared with experimental results.

CONCEPT

A DCM in an X-rays beamline is defined by an arrangement of two crystals (typically, pure blocks of silicon or germanium) that can filter a given incoming beam with a large wavelength distribution into a monochromatic outgoing beam. The desired wavelength is defined by the incidence angle of the beam with respect to the surface of the crystals according to Bragg's law of diffraction [3], while the monochromatic beam is kept at a fixed offset H by adjusting the gap g between the two crystals. This concept is depicted in Figure 1 for Bragg angles θ_{B_i} and θ_{B_f}, and gaps g_i and g_f.

In the HD-DCM, the operational angular range is $3° < \theta < 60°$ and the nominal offset is $H = 18\,\text{mm}$, so that the operational gap is $9\,\text{mm} < g < 18\,\text{mm}$. In operation, at fixed wavelength or during scanning, the maximum root mean square (RMS)

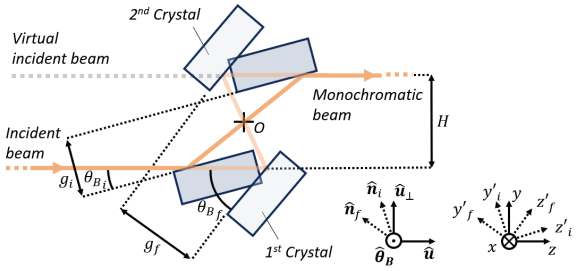

FIGURE 1. DCM concept with a symmetric arrangement of crystals at two incidence angles.

errors, of the beam incidence angle Rx on the first crystal, and of the gap y' and the parallelism Rx' and Rz' (pitch and roll, respectively) between crystals, are specified as 150 nrad, 300 nm, 10 nrad and 90 nrad, respectively. The system operates in ultra-high vacuum (UVH) at 1×10^{-9} mbar and the crystals are cryocooled with liquid nitrogen (LN_2) for thermal requirements.

DESIGN

The HD-DCM and its mechanical schematics are shown in Figure 2. The most fundamental design choice in this project was turning the traditionally passive performances of gap y', pitch Rx' and roll Rz' DoF into servo error specifications of a high-bandwidth closed-loop control system. Then, with a control bandwidth in the range of 200 to 250 Hz, for sufficient noise suppression and trajectory following capacity during scans, the overall dynamics of the instrument was pushed to the kHz range, whereas innovative actuation and metrology schemes were needed.

Given the demanding dynamic requirements, a mechanical design concept with only the essential DoF was envisioned. The main rotation function Rx is implemented by means of a high-quality

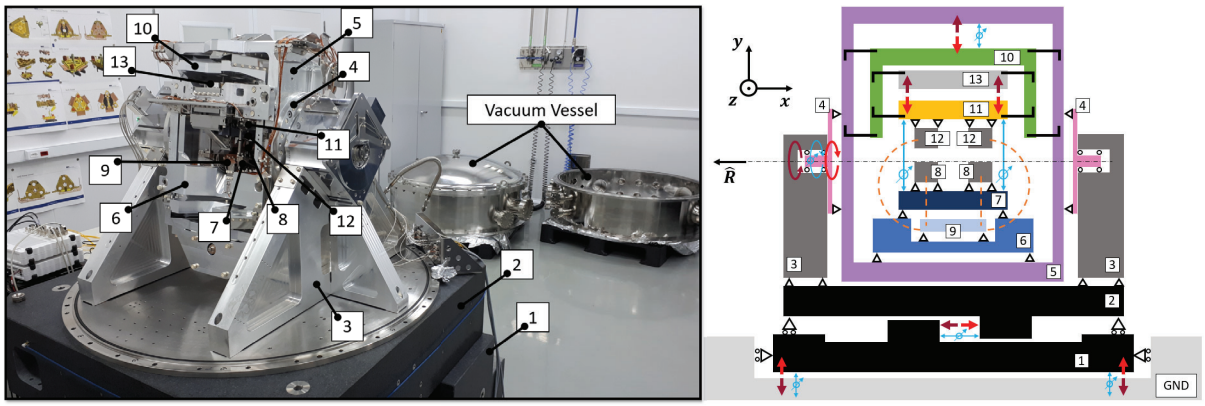

FIGURE 2. Left: HD-DCM with open vessel in the cleanroom. Right: Mechanical schematics.

in-vacuum double-side mechanical bearing with a direct drive (3 and 4). Then, the first crystals (2 of different types) (8) are mounted to a first metrology frame (7), which, in turn, is directly fixed to the main rotating frame (5) via a an auxiliary mounting frame (6). This auxiliary frame also holds the cooling manifold (9), from where LN_2 is derived for the first crystals and where braids are connected for cooling the second crystals (2 corresponding crystal types) (12). For the second crystals three voice-coil actuators and three laser interferometers are sufficient to control the position of the short-stroke module (second metrology frame) (11) in y', Rx' and Rz' with respect to the first metrology frame over an arrangement of three folded leaf-spring. Then, to avoid the excitation of reaction dynamics, a balance mass (13) is used. An additional low-bandwidth long-stroke module (10) driven by a stepper motor and measured by an absolute optical encoder complements the full gap stroke y' of the second crystals. Concerning the alignment of the system with respect to the beam, a two-level granite bench is implemented (1 and 2). At the interface with the floor (GND), a system with levelers allows for the alignment of the height y, tip Rx and tilt Rz. Between granite blocks, via air-bearings, the alignment of the perpendicularity of the rotation axis with respect to the beam Ry can be done, as well as the lateral shift x of the instrument.

DYNAMIC ERROR BUDGETING

The design process of the HD-DCM followed the DEB methodology [4] shown in Figure 3. Thus, by weighing the contribution of the Power Spectral Density (PSD) of the disturbances on the closed-loop dynamics of a mechatronic model of the instrument, the mechanical design and controllers may be iteratively refined until the predicted performances meet the requirements. Formally, the DEB approach requires the disturbance sources to be stationary, stochastic and independent. In the HD-DCM, this is a reasonable approximation for the considered control noise sources, whereas for the plant disturbances it is sufficient to work with averaging.

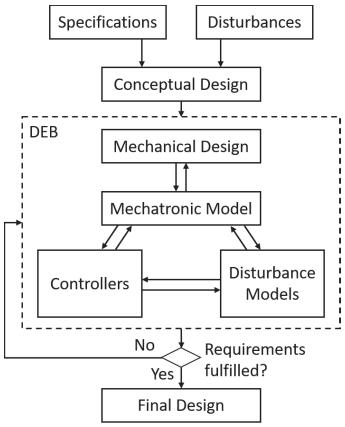

FIGURE 3. HD-DCM design process within the Dynamic Error Budgeting (DEB) methodology [4].

Machine disturbances are often divided into two groups, namely environmental and operational. The first comprises floor and acoustic vibrations, as well as temperature changes, among others. Fortunately, due to fine environment control inside the beamline hutches and to the fact that most of its sensitive parts are in vacuum, the HD-DCM is relatively immune to acoustics and ambient temperature effects. The floor, on the other hand, is a permanent point of attention. Indeed,

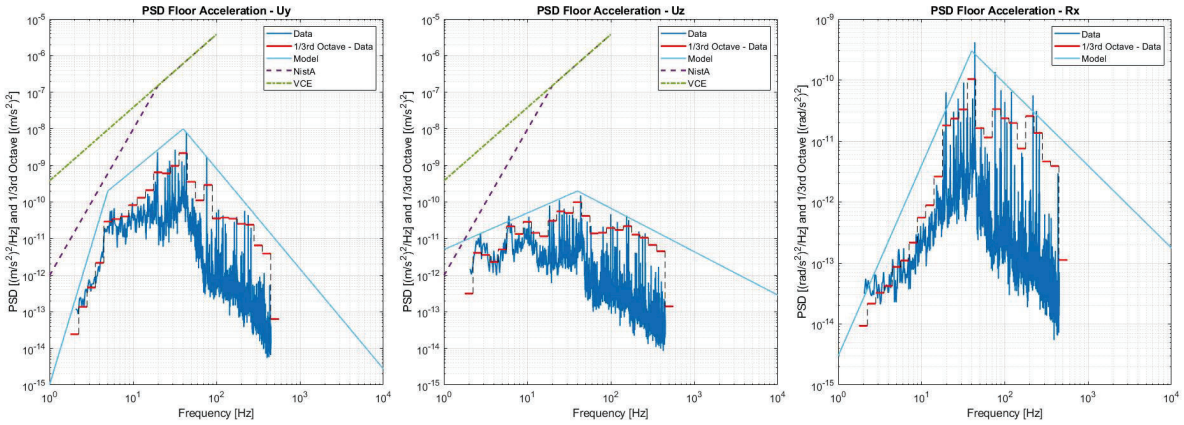

FIGURE 4. Floor disturbances in the HD-DCM.

many high-precision machines are isolated from the floor, hence filtering most of its excitation. At beamlines, however, there must be positional correlation between the instrument and the beam source, which makes decoupling a more complex subject. For the HD-DCM, the current choice is using high-stiffness levelers and relying on the natural damping of the floor and the exceptional stability levels of the experimental floor, as described in the next section.

Regarding operational disturbances, the flow-induced vibrations (FIV) are inevitable and one of the most detrimental influences in DCMs. Next, motion related disturbances may be more or less significant depending on the choices of actuators and guiding mechanisms. In DCMs they occur as a result of the change of the Bragg angle and the adjustment of the gap. Thus, they become a major point of attention in *fly-scan* operation. This is where an important innovation step takes place in the HD-DCM, since it replaces most of the rolling elements and stepping actuators by smooth flexural bearings and force actuators with metrology in closed-loop. In this way, broadband motion disturbances can be minimized, whereas the noise of sensors, amplifiers, digital-to-analog (DA) and analog-to-digital (AD) converters, as well as nonlinearities can be easily modeled for predictive performance and partly mitigated by feedback.

It is worth noticing that, regarding control, the main rotary system and the short-stroke module, the so-called crystal cage, are the two relevant components in the HD-DCM. Indeed, the bench and the long-stroke module (as long as driven by the stepper motor) can be seen as passive elements. In the following sub-sections, each disturbance source is individually addressed, then, an updated mechatronic model is explained, and, finally, the DEB results are presented.

Disturbance Models

In a more control-oriented perspective, the disturbances may be conveniently grouped into plant and control disturbances, as described below.

Plant Disturbances

Starting with the plant disturbances, on the one hand, the floor spectra are readily available from measurements with accelerometers and seismometers. Figure 4 shows floor acceleration PSDs measured at the experimental hall of Sirius and the used models in *Uy*, *Uz* and *Rx* axes, which are the most sensitive ones for the instrument. Although the model frequency range spans from 1 Hz to 10 kHz, floor measurements have more limited bandwidth due to instrumentation limitations. Remarkably, *Uy* and *Uz* are significantly below VC-E and NIST-A standards, highlighting the excellent levels of the floor of the experimental hall.

On the other hand, FIV experimental measurements have proven to be extremely challenging, not only due to the complexity of flow effects alone, but also because of the cryogenic conditions and vacuum-compatibility requirements of the setup. According to preliminary results, the current best guestimate for the model is a white-noise PSD with a second-order low-pass characteristic with a corner frequency of 250 Hz. For the dedicated cooling blocks on the crystals and the manifold, integrated RMS values of 1 and 10 mN,

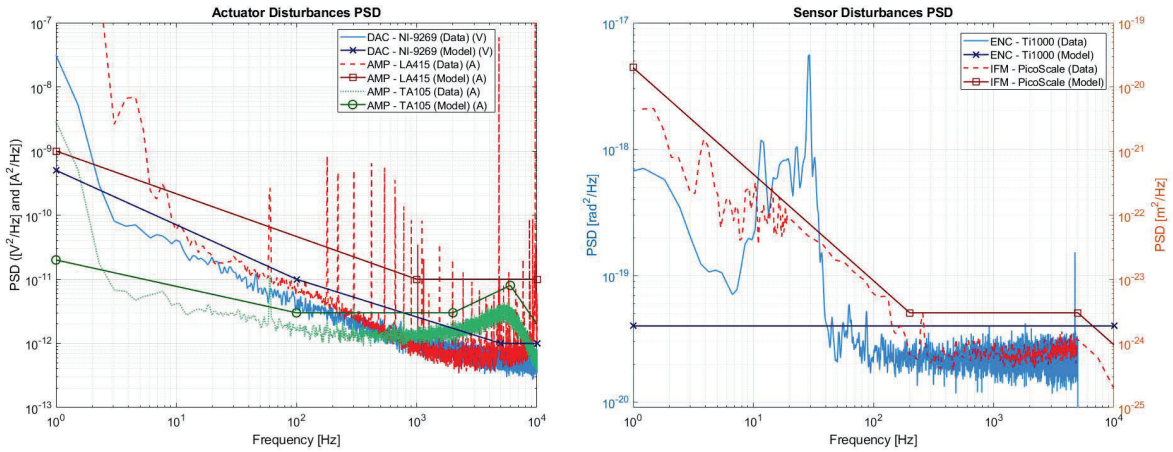

FIGURE 5. Actuators and sensors disturbances in the HD-DCM.

respectively, are considered. New experimental setups and computational fluid dynamics (CFD) simulations in both acoustics and turbulence domains are ongoing for future analyses.

Control Disturbances

Control disturbances can also be divided in two groups, namely, actuators and sensors. The first act on the process sensitivity transfer functions of the control-loop, whereas the latter on the complementary sensitivity transfer functions. As the HD-DCM runs at 20 kHz in the National Instruments CompactRIO (cRIO) control platform [5], its control disturbances result essentially from the noise levels of the DAC boards in this controller and of the third-party amplifiers.

All actuators are controlled via the 16-bit NI-9269 DAC. The Aerotech APR260 S-240-83 rotary stage uses the Varedan LA-415-SA-T linear amplifier, whereas the Akribis AVM 40-HF-6.5 voice-coils use Trust Automation TA105 linear drives. Figure 5 shows the experimental results, obtained with dedicated setups using a NI-9239 ADC at 50 kHz (where the first few points in the PSD can be neglected due to the characteristic Hann windowing effect), and the respective models of all these noise levels. The NI board and the Trust amplifier show smooth curves, whereas the Varedan amplifier shows several sharp peaks that could result from switching electronics in the hardware or pick-up noise. Actually, the Trust amplifiers, as provided by the supplier, also showed similar peaks. The source of the problem was tracked back to its fan, and those harmonic disturbances were eliminated by switching the fan to an external power supply. Work is currently in progress to track and eliminate Varedan's harmonic disturbances as well, but, for the moment, its disturbance model has simply been made at a significantly higher level than its noise floor. Finally, for the rotary stage, the corresponding torque disturbances are found using the amplifier and motor gains: 0.3 Arms/V and 7.09 Nm/Arms, respectively. And, analogously, the force noise in the voice-coils is also found using the amplifiers and force gains: 0.05 A/V and 19.15 N/A.

As for the sensors, the rotary stage uses a high-resolution Renishaw TONIC optical rotary encoder with 32768 encoder lines and additional interpolation to deliver a quadrature signal with about 25 nrad/count. The crystal cage uses SmarAct PicoScale C01 fiber-based Michelson interferometers, which also deliver quadrature signals with 0.1 nm/count at 10 MHz. Both quadrature signals are read by NI-9753 board in cRIO, where downsampling is eventually made in the FPGA. Figure 5 also shows the experimental results and the respective models for the noise levels of both electronic parts. The encoder was measured already with the HD-DCM, such that the peaks below 40 Hz result from mechanical resonances in the system. Its white-noise model over the full range was assumed from previous experience with optical encoders, with the level being determined by the high-frequency content. Finally, the RMS value of this model over the radius of the rotor of 0.1 m agrees with publicly available data from Renishaw estimating the jitter of TONIC encoders around $0.5\,\mathrm{nm_{RMS}}$. The interferometer noise was measured in a dedicated static setup.

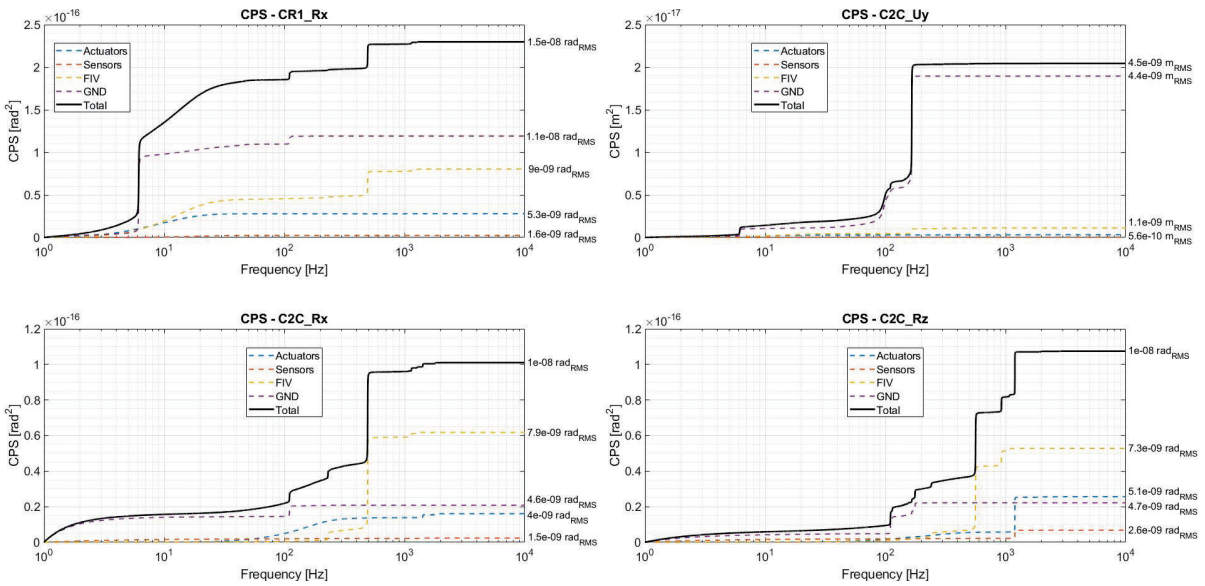

FIGURE 6. DEB output for beam incidence angle (CR1) and relative position between crystals (C2C) in the HD-DCM 11-body model. Disturbances grouped as: actuators, sensors, FIV and floor vibrations (GND).

Mechatronic Model

The mechatronic model presented in this work is built with a DEB toolbox that has just recently been developed by the authors to improve the predictive modeling capabilities at LNLS. With this toolbox, CAD drawing properties can be directly exported from Autodesk Inventor and loaded into Matlab, where: the mechanical plant is built (based on dynamic substructuring methods), animated mode shapes may be created, modal damping is included, the controllers are designed, the disturbances are modeled, and, finally, the cumulative power spectra (CPS) are calculated.

The model has 11 lumped masses in 6 DoF. Referring once again to Figure 2, elements 1, 2 and 3 have been put together as one lump, forming the bench, as well as elements 5, 6 and 9, which form the main rotating structure. All the remaining elements have been modeled individually. Regarding the design of the controllers, as shown in [6], the HD-DCM was designed in a way that the DoF of interest are sufficiently decoupled to have the controllers designed with individual single-input-single-output (SISO) techniques. Thus, four control loops are created, namely BRG, GAP, PTC and RLL, for the Bragg angle, by the main rotary stage, and for gap, pitch and roll in the crystal cage, respectively. Defining the closed-loop bandwidth as the frequency in which the open-loop transfer function crosses the unit gain, the BRG has a bandwidth of 20 Hz, whereas the remaining loops in the crystal cage 250 Hz. All of them are simply designed with a second-order low-pass filter in the high-frequency range, an integrator in the low-frequency range, a lead filter around the bandwidth frequency for phase margin and a proportional gain. All control loops are stable and for the purposes of DEB additional notch filters have been unnecessary.

DEB Results

In addition to their predictive potential, DEB models also allow the system architect to access and explore elements of the mechatronic system that are not available in the real world. Thus, in Figure 6 it is possible to investigate the in-position performance of the HD-DCM, not simply by the control error of the feedback loops, which rely on indirect metrology of the rotor of the rotary drive and of the metrology frames that actually hold the crystals, but rather, by the absolute incidence angle of the beam on the first crystal (CR1_Rx) and the relative position between crystals (C2C_Uy, C2C_Rx and C2C_Rz). For readability, the plots show the disturbances arbitrarily grouped as actuators, sensors, FIV and GND, and the total budget for each output.

On the one hand, the incidence angle, gap and roll outputs are within their specifications by a

large margin, i.e. one or two orders of magnitude. Indeed, gap and roll superior performances are a natural fallout of the architecture developed for pitch. The incidence angle and gap are dominated by floor vibrations, whereas roll is dominated by FIV. The pitch between crystals, which is the most stringent parameter, on the other hand, just meets its specification of $10\,\mathrm{nrad_{RMS}}$. It is also dominated by FIV, particularly as a result of the excitation of the first rocking mode of the first metrology frame at 500 Hz. To improve this, changes in the design to shift this resonance to a higher frequency and tuned mass dampers are currently under investigation. Yet, the contributions of the floor vibrations and the actuators are not negligible. The first might be addressed in the future with different suspension concepts, the latter, by replacing the current linear amplifier by a lower-noise model.

At this point, we may also compare the DEB results with experimental data that was just recently taken from the first HD-DCM installed at the Manacá beamline in Sirius. Two experimental data sets are shown for reference, namely, with and without liquid nitrogen flow. It can be seen that the model is in good agreement with the experimental data up to 500 Hz. Indeed, the most surprising element in both data sets is the large contribution at 1 kHz, because it corresponds to the second rocking mode of the first metrology frame and no significant disturbance source on the first metrology frame was expected in such high frequency. One possible explanation for this, that shall be investigated shortly, is one of the current peaks of the Varedan amplifier in Figure 5 matching this specific mechanical resonance of the crystal cage and finally limiting the dynamic performance of the HD-DCM. By comparing the pitch model outputs of Figure 6 and Figure 7, i.e. true value versus control error, one may indeed assume that the true mechanical stability between crystals must currently be a few percentage above the specifications in the real cryocooled system.

CONCLUSIONS

From the beginning, the DEB methodology proved to be an essential tool in the development of the HD-DCM, the first high-bandwidth control-based beamline DCM. Now, updated models have just proved to have good correlation with experimental data. Finally, in the near future, these models will support system upgrades, and new

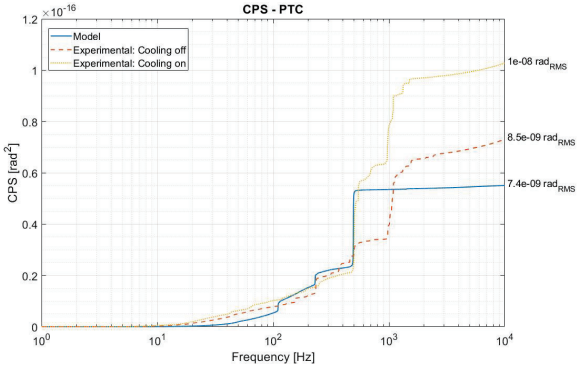

FIGURE 7. Comparison between DEB model and experimental data in the error of the pitch control loop in the HD-DCM.

models will be developed for a broader family of high-dynamic DCMs.

ACKNOWLEDGEMENTS

The authors would like to acknowledge the contributions of the LNLS staff group, in particular Cassiano Bueno and Mauricio Donatti for the measurements of the disturbances, and MI-Partners over the course of this project. This work is supported by the Brazilian Center for Research in Energy and Materials (CNPEM) under contract with the Brazilian Ministry of Science and Technology and Innovation and Communication (MCTIC).

REFERENCES

[1] Geraldes R R, et al. The Status of the New High-Dynamic DCM for Sirius. Proc. 10th Mechanical Engineering Design of Synchrotron Radiation Equipment and Instrumentation. 2018; 147-152.

[2] Rodrigues A R D, et al. Sirius Status Update. Proc. 10th International Particle Accelerator Conference. 2019; 1381-1384.

[3] Ashcroft N W. Solid State Physics. Thomson Press, (India) Ltd. 2003.

[4] Jabben L. Mechatronic design of a magnetically suspended rotating platform. 2007.

[5] Moraes M A L, et al. The FPGA Control Implementation of the High-Dynamic Double-Crystal Monochromator at Sirius Light Source. This conference. 2020.

[6] Caliari R M, et al. Loop-Shaping Controller Design in the Development of the High-Dynamic Double-Crystal Monochromator at Sirius Light Source. This conference. 2020.

LOOP-SHAPING CONTROLLER DESIGN IN THE DEVELOPMENT OF THE HIGH-DYNAMIC DOUBLE-CRYSTAL MONOCHROMATOR AT SIRIUS LIGHT SOURCE

Ricardo M. Caliari[1], Renan R. Geraldes[1,2], Marcelo A. L. de Moraes[1], Gert Witvoet[2]
[1]Brazilian Synchrotron Light Laboratory (LNLS)
Brazilian Center for Research in Energy and Materials (CNPEM)
Campinas, SP, Brazil
[2]Control Systems Technology Group, Mechanical Engineering Department
Eindhoven University of Technology (TU/e)
Eindhoven, The Netherlands

INTRODUCTION

This work presents the system identification, the closed-loop controller design by loop-shaping and control performance results of the High-Dynamic Double-Crystal Monochromator (HD-DCM) [1], which has been developed since 2015 for X-rays beamlines of Sirius 4th-generation Light Source at the Brazilian Synchrotron Light Laboratory (LNLS) [2]. Being the first DCM to implement a low-stiffness mechanical design concept with high closed-loop mechatronic performance, its development was based on predictive design to realize it “first time right“ and deliver positioning performance improvements by factors of 4 and 100 with respect to state-of-the-art DCMs, in fixed and scanning modes, respectively. The system identification techniques presented here focus on the high-performance module of the machine, a 3-degree-of-freedom (DoF) sub-nanometer resolution positioning stage, using well known MIMO identification approach. The controller was designed for each individual DoF separately, according to well-established control design targets and criteria, by means of loop-shaping through frequency domain analysis.

MECHANICAL DESIGN

A DCM at a synchrotron beamline is an optical component that selects the desired photon energy/wavelength for a given experimental analysis related to materials characterization. In this case, the desired outgoing wavelength is selected according to Bragg‘s law of diffraction, by controlling the incidence angle of a broad-band incident beam with respect to the surface of two crystals, which must remain parallel to each other, but with variable gap to keep a constant beam offset. Operational ranges and more details about this implementation are shown in [3].

Figure 1 shows the downstream view of the core of the HD-DCM, whereas Figure 2 depicts the mechanical schematics with its main elements. Because of complex cryocooling solutions to handle high power loads, the first crystals (8) were chosen to be rigidly fixed to its metrology frame (7) and, finally, to the main rotating frame (5) via the auxiliary mounting frame (6). Then, all the relative DoF that are necessary for fine positioning between crystals are limited to the second crystals (12), which can be cryocooled with more compliant copper braids, and their metrology frame (11). Therefore, aiming at the highest repeatability and mechanical stability performance, only the essential motion DoF were implemented in the so-called crystal cage, namely: the translation for the gap between the crystals; and two rotations, pitch and roll, for parallelism tuning.

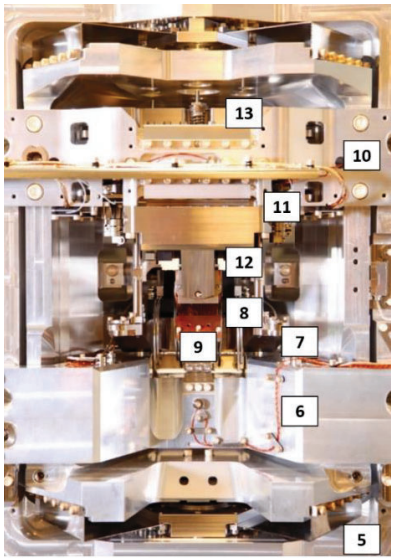

FIGURE 1. Core of the HD-DCM (sharing the part description of Figure 2).

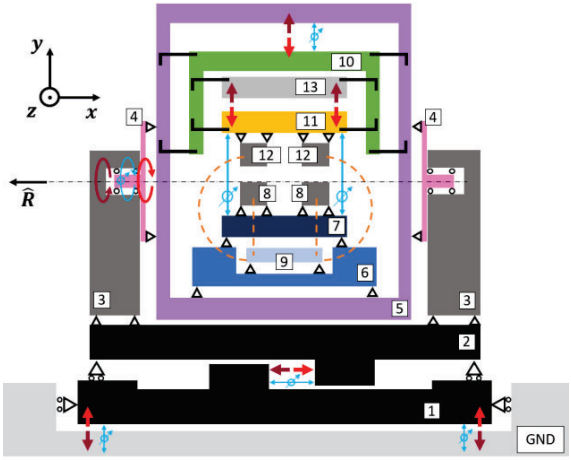

FIGURE 2. HD-DCM schematics: GND; bottom granite block (1); top granite block (2); towers with the stators of the two rotary bearings (3); rotors of the two bearings (4); main rotating frame (5); auxiliary mounting frame (6); metrology frame of 1st crystals (7); 1st crystals (8); cooling manifold (9); long-stroke frame (10); metrology frame of the 2nd crystals (11); 2nd crystals (12); and balance mass (13).

Since a mechanism with several millimeters of range and nanometer-level performance as a single motion stage may find severe practical concretization limitations, a concept using long-stroke and short-stroke stages was implemented. The first is an auxiliary stage (10) with sub-micrometer resolution and $10\ \mathrm{mm}$ gap range in a low-bandwidth closed-loop control. It is guided by an arrangement of six leafsprings, driven by a stepper motor and measured by an absolute encoder. The latter is the high-bandwidth module, consisting of the short-stroke frame, i.e. the metrology frame of the second crystals, and a reaction mass, the so-called balance mass (13). Both are equally guided by an arrangement of three leafsprings with respect to the long-stroke stage, providing the piston-tip-tilt DoF for the second crystals with the ranges of $\pm 2\ \mathrm{mm}$ and $\pm 2\ \mathrm{mrad}$. So, the high-performance closed-loop control of the crystal cage is realized by means of three voice-coil force actuators between the short-stroke frame and the balance mass, and an embedded interferometric system that measures the position between the metrology frames.

Finally, it is worth mentioning that, due to the cryogenic boundary conditions and beam interaction issues, the system must operate in ultra-high vacuum (UVH) of $10^{-9}\ \mathrm{mbar}$.

PERFORMANCE SPECIFICATIONS

Among the 3 high-bandwidth control loops of the crystal cage, i.e. gap, pitch and roll (also referred to as *Y*, *Rx* and *Rz*, according to the rotating coordinate system of the instrument), pitch is of particular attention. Indeed, it may affect not only the outgoing photon flux and energy bandwidth, but, with geometric lever-arms of tens of meters, also the position of the beam on the sample and the beam spot size due to vibration-related blurring effects. Because of that, the main target of this system is to hold the control error of the pitch within $10\ \mathrm{nrad_{RMS}}$ (root mean square) in the frequency range between $1\ \mathrm{Hz}$ and $2.5\ \mathrm{kHz}$. This target is put both for in-position operation mode, in which the experiments are performed with a fixed energy, and scanning operation mode, in which the energy varies over the experiment, requiring the main rotation and the gap to follow coordinated setpoints. For roll, there is a forgiveness factor of nearly 10 with respect to pitch requirements, thus, $90\ \mathrm{nrad_{RMS}}$ is defined as a target. For the gap, as much as $300\ \mathrm{nm_{RMS}}$ could be accepted. In practice, in meeting the requirements for pitch, the performances of roll and gap stay well below their specifications without additional effort.

SYSTEM IDENTIFICATION

The Frequency Response Function (FRF) of the *Shs* Multiple-Input-Multiple-Output (MIMO) plant must be experimentally determined to better design the controller for the real application and to check if all the design effort to build a high-dynamic machine succeeded.

The first step is to impose a White Noise broadband signal to the plant input in open loop. As the Shs has three inputs and three outputs, the identification is done by exciting each of the inputs and reading all outputs. Then, the FRF are given simply by the division of the Fourier Transformation of the output by the input signals.

Although straightforward, this method has the disadvantage that the static position is not kept by a feedback controller during the identification. So, drifts may occur, and the identified signal may contain lower-frequency disturbances. Even though, having the first identified plant, the controller designer has an idea of the system resonances and of the magnitude of the plant FRF. Then, with this information, one can derive a preliminary low-bandwidth controller essentially to hold position for a subsequent identification.

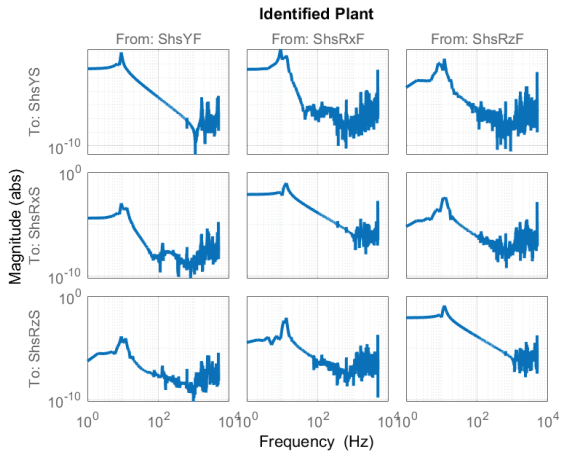

FIGURE 3. MIMO plant identification using single sine method.

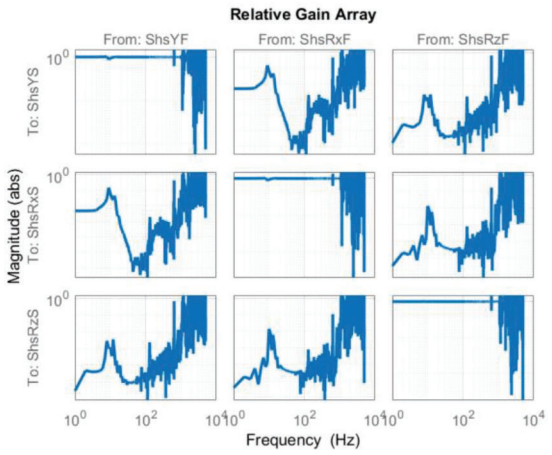

FIGURE 4. Relative gain array plot for MIMO coupling analyses.

At this point, the loop can be closed, and the position error can be stabilized to a certain extent. This is desired because a sufficient Signal-to-Noise Ratio (SNR) is necessary to draw a more reliable plant FRF, which, in turn, requires the excitation signal power to be increased.

Next, a more well-defined excitation signal can be further used. One alternative is the *multisine* method, which consists of a simultaneous sum of sines in a finite number of frequencies, with specifically chosen phases and amplitudes. This excitation signal introduces a specific number of periods in the plant and excites the system just in those given frequencies, improving determinism and SNR. Another alternative is using just a sequence of sines with different frequencies and pre-determined amplitudes, the so-called *single sine* method. This is the method used here to derive the MIMO identified plant depicted in Figure 3. This decision was made to achieve a clearer identification of magnitude and phase of some peaks that proved to be critical in designing the controller.

With the plant identified, additional analyses can be done. In particular, the Relative Gain Array (RGA) analysis indicates how well decoupled a MIMO system is over frequency. The closer the RGA is to the identity matrix, the more decoupled the system. Then, if sufficiently decoupled, the MIMO system can be addressed separately with *Single-Input-Single-Output* (SISO) techniques, which considerably simplifies the controller design effort. Indeed, as it can be seen in Figure 4, by comparing the magnitudes in the rows and the columns of the matrix plot, the Shs is well decoupled up to about $1\,\mathrm{kHz}$.

CONTROLLER DESIGN USING THE LOOP-SHAPING METHOD

The loop-shaping controller design method [4] consists in explicitly shaping the magnitude and the phase of the open-loop Transfer Functions (TF) towards specific control targets. Here, the plant TF is the result of the system identification, such that actuators, sensors and data acquisition dynamics are already included. Then, the control engineer must add enough control elements to the open-loop TF to achieve the desired closed-loop system performance, which here is defined as follows:

1. Phase Margin of $30°$, for robustness;
2. Gain Margin of $8\,\mathrm{dB}$, for robustness;
3. High low-frequency gain, for high trajectory following capacity;
4. Low high-frequency gain, for noise disturbance suppression.

All the controllers in the Shs have been designed as follows: a second-order low-pass filter with a corner frequency around $1000\,\mathrm{Hz}$ reduces the magnitude at high frequencies; one integrator with a cut-off frequency around $50\,\mathrm{Hz}$ increases the low frequency gain and trajectory following capacity; a lead filter increases the phase margin around the bandwidth frequency; notch filters reduce the magnitude of (otherwise bandwidth-limiting) poorly damped peaks; and, finally, the proportional gain meets the unit gain at the target bandwidth of $250\,\mathrm{Hz}$. In the Shs, all the high-frequency and high-magnitude peaks were extensively characterized, in order to guarantee that their positions would not change during operation, which might compromise the system performance and stability.

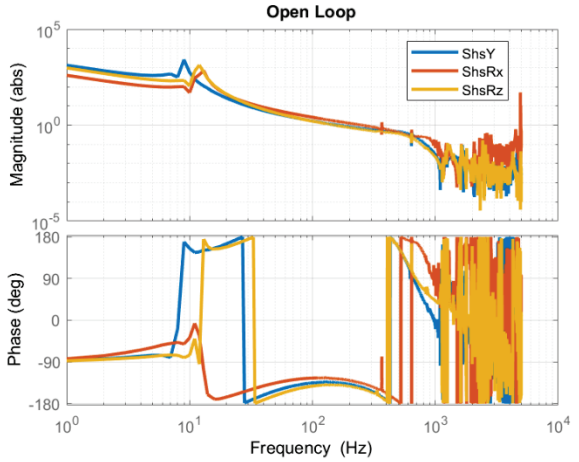

FIGURE 5. Open-loop plots of magnitude and phase of the 3-DoF Shs SISO system.

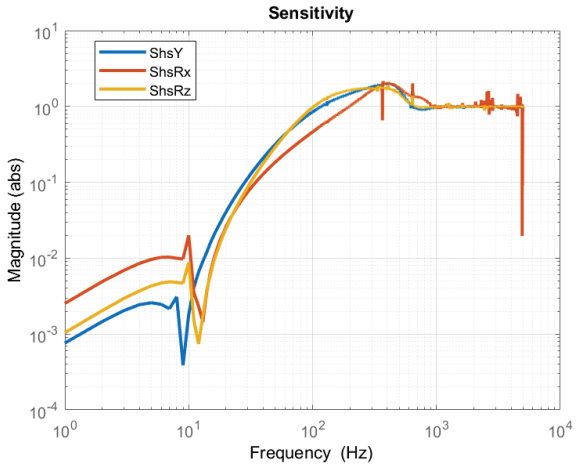

FIGURE 6. Sensitivity plot of the 3-DoF Shs SISO system.

This procedure consists of an iterative process in which the open-loop transfer functions are shaped and reshaped after calculating the required stability, robustness and performance indicators. Furthermore, considering that there are different operation modes with conflicting performance priorities, in addition to these standard controllers, multiple controllers may be designed, in which the designer may play with different bandwidths and/or low frequency gains.

Figure 5 shows the open-loop Bode diagram of each individual DoF for the Shs system. The phase-margin can be seen at the bandwidth frequency on the phase plot, as well as the higher gain in the low frequency range and suppressed amplitude for the high frequency range. Figure 6 presents the sensitivity plot, which is designed not to exceed the magnitude of 2 for robustness and noise amplification purposes.

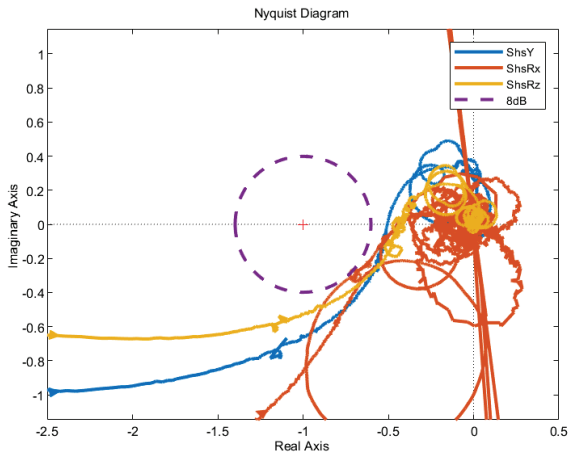

FIGURE 7. Nyquist plot of the 3-DoF Shs SISO system, with the robustness target circle of 8dB.

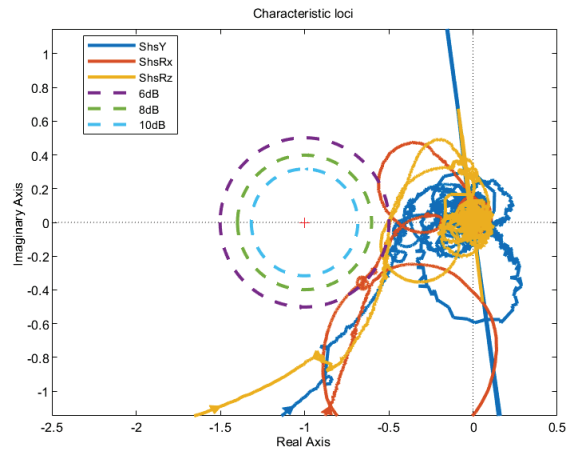

FIGURE 8. Characteristic loci of the 3-DoF Shs system, analyzing the MIMO stability.

Next, the final result of the SISO standard controller design by the loop-shaping method can be verified by the Nyquist diagram, depicted in Figure 7. It attests not only for the stability of the individual controllers, but also for their robustness margins, in this case, better than $8\ \mathrm{dB}$ for all 3 loops. Finally, Figure 8 shows the *characteristic loci*, or *eigenvalue loci*, diagram. Defined as the eigenvalues of the frequency response of the open-loop transfer function, this graph provides a generalization of the Nyquist plot from SISO to MIMO systems. Thus, it states the MIMO stability.

RESULTS

The following subsections present control performance results for the pitch (ShsRx) control loop, which is the most demanding and relevant DoF in the HD-DCM. These results were partly obtained with the machine in a test laboratory, but already under completely operational conditions,

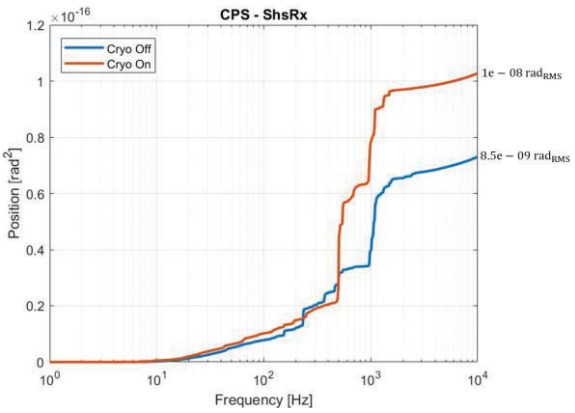

FIGURE 9. In-position control error CPS for pitch (ShsRx), with and without cryogenic cooling.

including cryogenics and vacuum, and partly obtained in its final environment at Macaná beamline in Sirius.

In-position Performance

Analyzing the performance of the system as a function of frequency is essential not only to understand how the machine behaves to the different disturbance sources, but also to evaluate the impact of this spectral signature at the user's end. Therefore, the cumulative power spectrum (CPS) provides a convenient output format for performance analysis, with the partial integrated RMS value simply given the square root of the data points.

Figure 8 shows the in-position control error for pitch (ShsRx) under the standard controller running at $20\,\mathrm{kHz}$ in National Instruments CompactRIO platform (see [5]). Data sets of two different experimental conditions, namely, with and without liquid nitrogen flow, are shown for comparison. The error within the bandwidth is kept below $5\,\mathrm{nrad_{RMS}}$ and changes little between data sets, attesting that the additional flow disturbances are well suppressed in this range. At $1\,\mathrm{kHz}$, a significant contribution is present in both sets. As detailed in [3], this corresponds to the second rocking mode of the metrology frame of the first crystals, which might be excited by electronic noise in the linear amplifier of the main rotary driver. Finally, the main difference between data sets lies in the contribution around $500\,\mathrm{Hz}$, which, as also detailed in [3], corresponds to the first rocking mode of the metrology frame of the first crystals being excited by the flow-induced vibrations. As this is currently in the sensitivity peak of this control loop (see Fig. 6), the disturbance effect is amplified, rather than suppressed. So, even though the system already meets its requirements, this is just the beginning for this machine and many aspects have already been mapped for improvements.

Trajectory Following Performance

Considering the dynamic concept of the HD-DCM, more interesting than the achieved in-position performance is the scanning capacity of the instrument, as compared to existing DCMs. The scanning performance is here evaluated considering the complete functional setpoint requirements, which include: the main rotary stage, driven by a direct drive with a closed-loop bandwidth of 20 Hz; the Shs system; and, optionally, the long-stroke stage. Indeed, thanks to the two-level design, two energy-scan modes are available, namely: standard scanning mode and high-performance scanning mode.

In the standard mode, the Bragg angle is a setpoint to both the long-stroke and the short-stroke modules, which move together to adjust the nominal gap while the references for pitch and roll are generally fixed. Thus, scans of any range within the operational boundaries of the instrument can be made. However, the stepper-driven long-stroke actuator introduces significant mechanical disturbances in the system, lowering the control performance. Naturally, larger motion ranges and velocities, which are related to lower photon energies, i.e. energies between 3 and $10\,\mathrm{keV}$, create more intense disturbances. In the high-performance scanning mode, on the other hand, the long-stroke is kept still while the Bragg setpoint is send to the short-stroke only. Then, although the scanning ranges become limited to feasible gap ranges within the short-stroke capabilities, the control errors can be equivalent to those of in-position performance. At, $3\,\mathrm{keV}$ feasible scanning ranges are very limited and even at $5\,\mathrm{keV}$, scans in high-performance mode are limited to $500\,\mathrm{eV}$ scans, only. Fortunately, for scans at energies above $10\,\mathrm{keV}$, the boundaries imposed by the high-performance mode bring no additional limitation.

This is shown in Figure 10, with the control error RMS values for the ShsRx in scans in standard and high-performance modes. As cases of interest, $1\,\mathrm{keV}$ scans were made around different energy values for different speeds, so that every point in the graph corresponds to the total RMS value between $1\,\mathrm{Hz}$ and $2.5\,\mathrm{kHz}$ for a full scan at constant speed in eV/s. At speeds below $1\,\mathrm{keV/s}$, it can be seen at one energy end, i.e. above

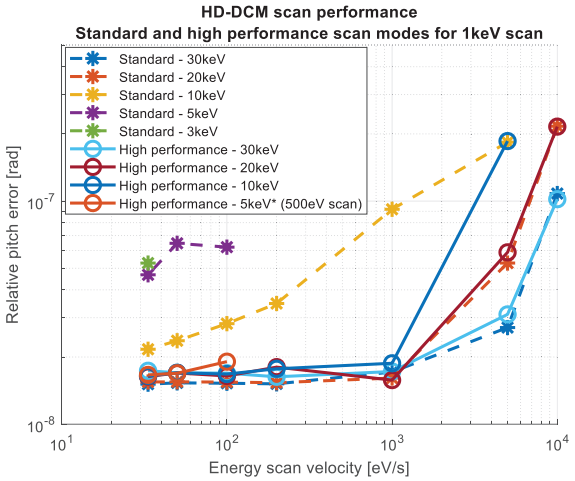
HD-DCM scan performance
Standard and high performance scan modes for 1keV scan
Standard - 30keV
Standard - 20keV
Standard - 10keV
Standard - 5keV
Standard - 3keV
High performance - 30keV
High performance - 20keV
High performance - 10keV
High performance - 5keV* (500eV scan)
Relative pitch error [rad]
Energy scan velocity [eV/s]

FIGURE 10. Scanning control error RMS for pitch (ShsRx) in standard and high-performance modes: 1 keV scans, 30 to 10.000 eV/s.

$20\ \mathrm{keV}$, the angular and gap motions are so small that the performance is equivalent to that of in-position errors even in standard mode. At the opposite end, as the energy is reduced, however, the stroke and the speed of the long-stroke actuator increase, and the disturbing effects are clear, reaching as much as $80\ \mathrm{nrad_{RMS}}$ at $3\ \mathrm{keV}$. Above $1\ \mathrm{keV/s}$, high speeds and accelerations are present, and the error levels increase. Nonetheless, significant improvement can be expected once feedforward control, which has not been implemented yet, is introduced.

In this study, the RMS value is taken for the frequency band between $1\ \mathrm{Hz}$ and $2.5\ \mathrm{kHz}$, because this covers typical detection time scales of beamline experiments. Furthermore, it must be said that this study was carried in the test lab with an xPC prototyping control platform running at $10\ \mathrm{kHz}$ (see [5]). This explains why the smallest numbers in Figure 10 do not meet the cryocooled performance displayed in Figure 9.

To conclude, it is worth noticing that at 3 and $5\ \mathrm{keV}$ the scanning speeds are limited to 30 and $100\ \mathrm{eV/s}$, respectively. This is due to a practical operational limit of about $1\ \mathrm{mm/s}$ in the variation of the gap between the crystals, which is partly given by the current speed limitations in the acquisition rate of the interferometers, but also related to acceleration levels and heat dissipation issues in the mechanics and actuators, respectively. For the future, this boundary is expected to be extended as well.

CONCLUSIONS

The complete controller design methodology for the high-bandwidth module of the HD-DCM has been described. SISO feedback controllers were designed with loop-shaping after extensive MIMO plant identifications and RGA decoupling analyses. Stability and robustness have been attested according to well-established control diagrams and, finally, performance has been experimentally demonstrated in operational conditions. In particular, the control error performance of the pitch between crystals has proven to meet its specifications, not only in in-position operation mode, but also under demanding scanning conditions. Yet, there are still opportunities for control upgrades and performance improvement. In the near future, feedforward control shall be implemented to reduce trajectory following errors.

ACKNOWLEDGEMENTS

The authors would like to gratefully acknowledge the funding by the Brazilian Ministry of Science, Technology, Innovation and Communication, and the contributions of the LNLS staff group and MI-Partners team.

REFERENCES

[1] Geraldes R R, et al. The Status of the New High-Dynamic DCM for Sirius. Proc. 10th Mechanical Engineering Design of Synchrotron Radiation Equipment and Instrumentation. 2018; 147-152.

[2] Rodrigues A R D, et al. Sirius Status Update. Proc. 10th International Particle Accelerator Conference. 2019; 1381-1384.

[3] Geraldes R R, et al. Dynamic Error Budgeting in the Development of the High-Dynamic Double-Crystal Monochromator for Sirius Light Source. This conference. 2020.

[4] Skogestad S, Postlethwaite I. Multivariable feedback control analysis and design. John Wiley and Sons, Inc. New York: 2001.

[5] Moraes M A L, et al. The FPGA Control Implementation of the High-Dynamic Double-Crystal Monochromator at Sirius Light Source. This conference. 2020.

THE FPGA CONTROL IMPLEMENTATION OF THE HIGH-DYNAMIC DOUBLE-CRYSTAL MONOCHROMATOR AT SIRIUS LIGHT SOURCE

Marcelo A. L. Moraes[1], Ricardo M. Caliari[1], and Renan R. Geraldes[1,2]
[1]**Brazilian Synchrotron Light Laboratory (LNLS)**
Brazilian Center for Research in Energy and Materials (CNPEM)
Campinas, São Paulo, Brasil
[2]**Control Systems Technology Group, Mechanical Engineering Department**
Eindhoven University of Technology (TU/e)
Eindhoven, The Netherlands

INTRODUCTION

This work presents the Field-Programmable Gate Array (FPGA) control implementation of the High-Dynamic Double-Crystal Monochromator (HD-DCM) [1], which has been developed since 2015 for X-rays beamlines of Sirius 4th-generation Light Source at the Brazilian Synchrotron Light Laboratory (LNLS) [2]. Being the first DCM to implement a low-stiffness mechanical design concept with high closed-loop mechatronics performance, its development was based on predictive design to realize it "first time right" and deliver positioning performance improvements by factors of 4 and 100 with respect to state-of-the-art DCMs, in fixed and scanning modes, respectively. The development workflow is discussed from the architecture definition to beamline commissioning, including control platform benchmarking, numeric quantization errors, and FPGA resources optimization.

BACKGROUND

In the recent years it has become clear to the synchrotron community that the stability performance of DCMs would turn out to be one of the main bottlenecks in the overall performance of many X-ray beamlines, particularly for the new 4th generation machines, the so called Diffraction Limited Storage Rings (DLSR) [3]. Indeed, over time DCM performances have become limited by well-known vibration sources, as the cooling systems, the experimental floor and vacuum pumps in the surroundings. Even though some incremental progress has been achieved in mitigating such disturbances, examples from applications in other industries showed that the new requirements could hardly be achieved with incremental upgrades of the common architecture. Therefore, a fundamentally different overall system approach was considered necessary to successfully design and realize such an ultra-precision system.

HD-DCM DESIGN

The concepts applied in the design of the HD-DCM (Figure 1) aim at a high-bandwidth closed-loop control system, reaching a control bandwidth of the inter-crystal parallelism around 200 to $250\,\mathrm{Hz}$. Then, the disturbance rejection capacity of the control loop should be able to suppress the positioning errors to the required $10\,\mathrm{nrad_{RMS}}$ level, both in stand-still and during flyscan operation.

To achieve such a high closed-loop control bandwidth, a well designed mechanical system, based on a fundamentally different dynamic architecture, is applied, and the use of force actuators is crucial. Whereas common DCM systems typically use piezo actuators or other inherently stiff actuator systems (like spindle drives), the use of inherently compliant actuators, as voice-coils (VC), allows for the required change of paradigm in the dynamic architecture. By this principle, the dynamics of the system can be designed to reach a significantly higher closed-loop bandwidth, as only the essential mechanical parts are included in the control loop. Indeed, by means of a mechanical filter, established by a so-called reaction mass, or balance mass, the non-essential so-called reaction path dynamics can be filtered and, as such, eliminated from the close-loop dynamics in the sense of control stability and disturbance amplification.

Starting with the right overall architecture and taking all the essential requirements into account, predictive modeling, error-budgeting and proper design principles based on experience were essential for a successful design of such a high-end system. With respect to dynamics, both lumped-mass and finite element method (FEM) models have been used to derive transfer functions that guided the conceptual choices and the mechanical design towards the required perfor-

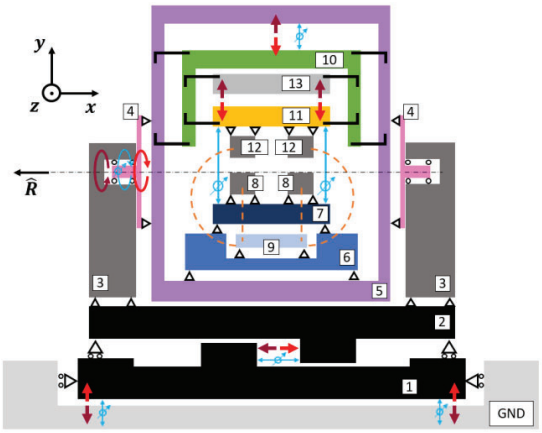

FIGURE 1. HD-DCM schematics: GND; bottom granite block (1); top granite block (2); towers with the stators of the two rotary bearings (3); rotors of the two bearings (4); main rotating frame (5); auxiliary mounting frame (6); metrology frame of 1st crytals (7); 1st crystals (8); cooling manifold (9); long-stroke frame (10); metrology frame of the 2nd crystals (11); 2nd crystals (12); and balance mass (13).

mance. Using power spectral densities (PSD) of modeled and measured disturbances, quantitative error budgeting has been extensively applied to predict the expected performance [4].

PROTOTYPING ARCHITECTURE

The prototyping phase in the HD-DCM project was used to validate both the mechatronic concept, developed with the forementioned predictive modeling techniques, and the required plant identification techniques and control loop-shaping estrategies [5]. This was achieved by means of a rapid control prototyping tool in a real-time target machine from Speedgoat [6]. As illustrated in Figure 2, the control architecture was composed of: input and output drivers in FPGA layer (for encoder decoding and motor control signals); a controller in the real-time operating system (RTOS) layer; and a user interface in a host computer.

Once the HD-DCM control prototyping phase was concluded, the system was able to keep the control errors under the specifications even during relatively high-speed scans in the time frame of a few hundred milliseconds up to a few tens of seconds [7]. However, the rapid control prototyping platform is not intended to run in a "production environment". Its kernel is not stable enough for running critical embedded control loops, but it

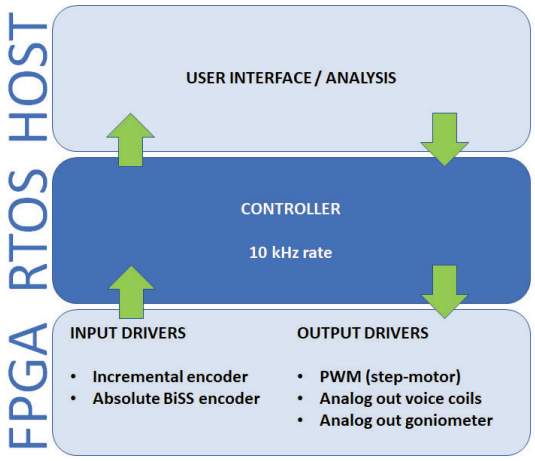

FIGURE 2. HD-DCM prototype control architecture diagram.

is, instead, intended to perform laboratory tests. Hence, the next challenge was to deploy the application to a rugged platform, more adequate to the beamline environment and long-term execution. The chosen platform was the National Instruments CompactRIO (cRIO-9039), which also combined FPGA and RTOS [8].

CRIO-9039 BENCHMARKING

The natural deployment strategy would be to reconstruct the same architecture used in the prototyping phase. Nevertheless, even though the Speedgoat and National Instruments platforms used in this project have equivalent FPGA boards (Xilinx Kintex 7), there is an important difference between them: the processor. The prototype was controlled with a Speedgoat Performance Real-Time Target Machine with an Intel Core i7 3.5 GHz Quad Core, whereas the cRIO-9039 had an Intel Atom E3845 1.91 GHz Quad Core. Then, due to lack of information about control loop rates achievable with cRIO-9039 RTOS [9], a benchmark test was performed with an empty model.

Two main criteria were considered in the tests: firstly, CPU usage should not exceed 75 % [10]; next, determinism was required, so that the maximum jitter should not exceed the iteration time [11]. The first test was performed with an empty loop at 20 kHz. As a result, the average CPU usage was 90 %, violating the first criterion. Slowing down the loop rate to 10 kHz, a second test that was carried over one weekend produced the jitter-occurrence histogram depicted in Figure 3.

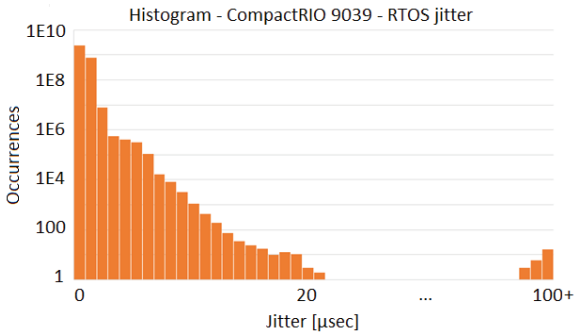

FIGURE 3. Benchmark test: jitter occurrences for an empty 10 kHz *loop.*

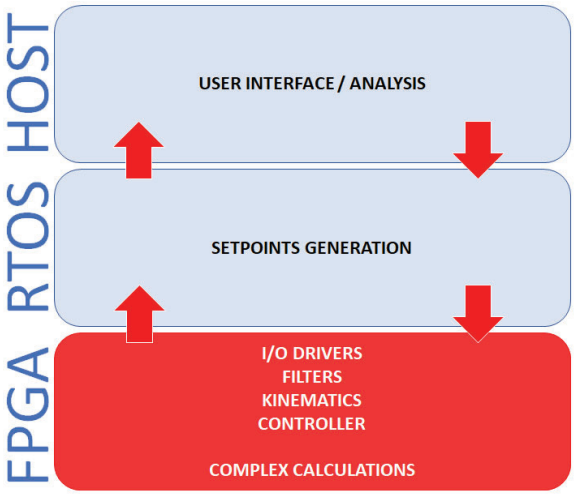

FIGURE 4. FPGA-based control architecture for the HD-DCM in cRIO-9039.

Although no occurrences were found between 22 and 97 µs, seventeen determinism violations occurred with jitters above 100 µs (last histogram bar). So, regardless of the application complexity, the cRIO-9039 RTOS was classified as Soft Real-Time for 10 kHz loop rate applications [11].

Consequently, the HD-DCM control system would not fit into cRIO-9039 RTOS. So, the final architecture using cRIO was defined with FPGA FIFOs (*First-In-First-Out*) for the communication between RTOS and FPGA, and EPICS (*Experimental Physics and Industrial Control System*) [12] for the communication between RTOS and the host computer, as summarized in Figure 4.

MATLAB-LABVIEW INTEGRATION TOOLBOX

The platform portability started with a Matlab library, developed by the authors, to export dynamic systems – either in state-space or transfer-

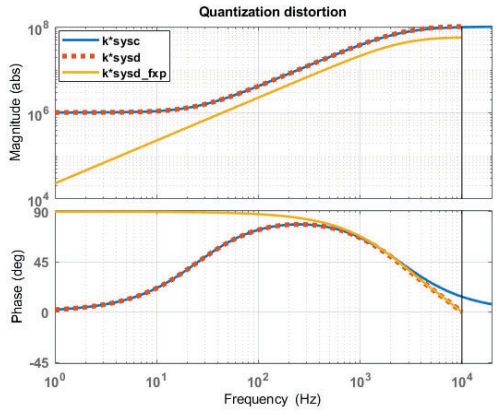

FIGURE 5. Quantization error example with a lead filter described as continuous and discrete systems, and as the discrete system with insufficient fixed-point numeric representation.

function representations – with lossless numeric precision. Then, considering the FPGA limitations about numeric representation (where double-precision floating point is a very limited and expensive resource), a second feature was developed in Matlab to check frequency domain distortions due to quantization errors (as exemplified in Figure 5) and calculate minimum numeric representations which guarantee the dynamic system integrity. Finally, the integration is completed with LabVIEW VIs (*virtual instruments*), developed to import the dynamic systems, convert the numeric representations and deploy to real-time application or FPGA.

CRIO FPGA IMPLEMENTATION

The work of implementation of the controller of the HD-DCM in the FPGA of the cRIO included the following steps: development of input and output drivers, solutions on numeric representation, decisions of the overall architecture and, finally, resource optimization. These topics are addressed in details in the following subsections.

Drivers

Encoder signals are acquired with NI-9753 modules, which have proven to be reliable options for general purpose fast digital differential I/O (*input/output*) signals. Absolute BiSS (serial encoder protocol) and incremental quadrature encoders drivers were developed and all position feedbacks (three interferometers, one BiSS encoder, and two incremental encoders with index) can be read with two modules. Output drivers

were also developed to perform brushless motors commutation (NI-9269), step-motor pulse-frequency modulation (NI-9401) and VC amplifiers' current setpoints (NI-9269).

Numeric Representations

Complex calculations such as matrix multiplications and large data handling should be avoided in the FPGA layer. Indeed, beyond the steep learning curve required to perform complex calculations in FPGAs, some calculations consume way too many resources. Hence, fixed-point numeric representation is the natural choice in FPGA applications. In the HD-DCM, multiple controllers include a lead filter, integrators, a second-order low-pass filter and notch filters, which may reach 16 states per controller. Besides that, the Matlab-LabVIEW Integration tool pointed that up to 52 bits would be required to represent some of the transfer function coefficients in fixed-point representation.

Most of the FPGA control implementation examples found in the LabVIEW community refer to much lower-order systems. And, indeed, LabVIEW FPGA native fixed-point blocks present practical limitations in working with large systems, such as the HD-DCM. Firstly, the LabVIEW native Discrete Transfer Function Direct block has a 32-bit fixed-point numeric representation, which would mean a lossy representation for this application. Secondly, the LabVIEW native Transfer Function control block type definition is limited to 9 states. Next, LabVIEW native FPGA math blocks are limited to 64 bits. Finally, increasing the numeric representation and array sizes to implement higher order controllers consumes too many digital signal processing elements (DSPs). Attempts to modify the native libraries resulted in about 70 DSPs per transfer function calculation VI, and the bitgrowth easily overcame the maximum native numeric representation of 64 bits.

Hence, the implementation effort shifted from fixed-point to single-precision floating point numeric representation, so that an extended numeric domain could be covered and DSP resources saved. Nonetheless, with the Matlab-LabVIEW Integration toolbox it was found that even the single-precision representation would not be enough for a lossless implementation of the complete transfer functions of the controllers of the the HD-DCM in the FPGA. Then, the solution was to divide the controller into smaller blocks and serialize their calculations, which is possible

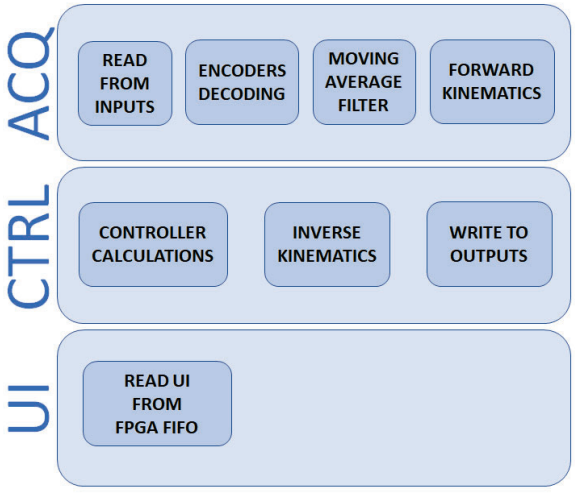

FIGURE 6. FPGA structure where each block, namely: acquisition, control and user interface, is a parallel loop at a different rate.

thanks to the FPGA high clock rate of 40 MHz. In this process, no DSPs were required in the calculations of the control effort with single-precision numeric representation, and the amount of FPGA slices did not increase much as compared with fixed-point solutions in equivalent applications.

Architecture

Thus, the FPGA architecture can be finally summarized according to Figure 6. The moving average filter, the forward kinematics calculations, the readout from inputs and the decoding of encoders are performed inside the acquisition loop at 40 MHz; controller calculations, the inverse kinematics and writing outputs, in turn, are performed at the control loop rate of 20 kHz.

During the project, cRIO-9039 became legacy and the development was eventually migrated to cRIO-9049. Fortunately, this migration between models was trivial, because the FPGA models are the same. It would probably not be the case in an extremely demanding real-time application, since the processor of the new model has lower clock frequency, namely, 1.6 GHz against 1.91 GHz.

Resources Optimization

Five single-input-single-output (SISO) high-order controllers with pre and post-processing from and to I/O drivers build an application that is complex enough to easily overflow the FPGA capacity if best saving practices are not applied. Taking NI FPGA developer's guide [13] as a baseline,

the main optimization rules developed within this project were:

- FPGA settings should be implemented as variables only when strictly necessary; otherwise, as constants.
- Although using arrays is not expected to save resources [13], the standardization of codes using arrays can be beneficial: less control loops, less different loop rates, and less FIFOs to RTOS.
- Front-panel controls should be avoided.
- Timing violations should be avoided with pipelines, particularly around time-demanding blocks (e.g. read from register or I/O node). Oftentimes, the debugging tools available for timing errors are not clear.
- Type definition should be avoided in host-to-target and target-to-host communications. It is useful in small applications where Read/Write control is used, but FPGA FIFO is very limited about data types, making data cast necessary (which it is time consuming because there is no tool for this).

RESULTS

Figure 7 shows the performance of the HD-DCM at room-temperature under both the prototyping and the final control platforms via the cumulative power spectrum (CPS) of the control error of the pitch parallelism between crystals. It does not necessarily attest for a superior performance of one or another, because the results where obtained at different times and, eventually, in different experimental conditions. Yet, it does prove that the target specification of $10\,\mathrm{nrad_{RMS}}$ was met with both systems and that the alternative FPGA-based control could be successfully implemented. The first HD-DCM has recently been installed with the cRIO-9049 platform at the Manacá beamline in Sirius and the integrated commissioning is expect to take place in the second quarter of 2020.

CONCLUSIONS

Within the scope of the project of the HD-DCM, CompactRio has proven to be a rugged control platform whose FPGA is capable of running five SISO control loops, with up to 16-state controllers each, at a control rate of $20\,\mathrm{kHz}$. Regarding the next control-related steps for the HD-DCM at the

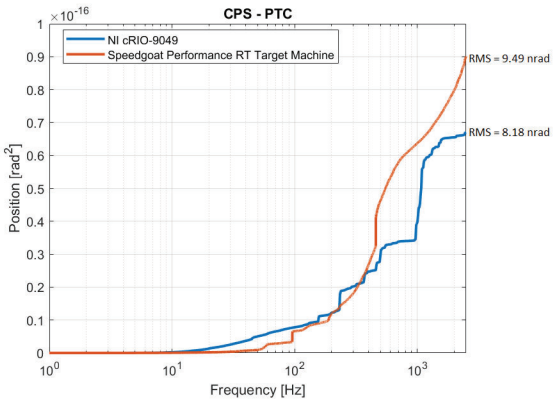

FIGURE 7. CPS error of the pitch control loop in the HD-DCM for the Speedgoat prototyping platform and the cRIO final control platform.

beamline, the following can be highlighted: development of the interface with the EPICS control system up to the user level; coordinated motion with the undulator photon source for scanning experiments; and feedforward control for higher performance in motion setpoints.

Furthermore, the workflow consisting of rapid control prototyping followed by deploy to an industry-certified platform is now solid and, together with the developed libraries, is expected to be constantly used in future beamline projects.

ACKNOWLEDGEMENTS

The authors would like to acknowledge the contribution of the LNLS staff group and the funding by the Brazilian Center for Research in Energy and Materials (CNPEM) under contract with the Brazilian Ministry of Science and Technology and Innovation and Communication (MCTIC).

REFERENCES

[1] Geraldes R R, et al. The Status of the New High-Dynamic DCM for Sirius. Proc. 10th Mechanical Engineering Design of Synchrotron Radiation Equipment and Instrumentation. 2018; 147-152.

[2] Rodrigues A R D, et al. Sirius Status Update. Proc. 10th International Particle Accelerator Conference. 2019; 1381-1384.

[3] Double Crystal Monochromator Workshop. European Synchrotron Radiation Facility. 2014

[4] Geraldes R R, et al. Dynamic Error Budgeting in the Development of the High-Dynamic

Double-Crystal Monochromator for Sirius Light Source. This conference. 2020.

[5] Caliari R M, et al. System Identification and Contol for The Sirius High-Dynamic DCM. Proc. 16th International Conference on Accelerator and Large Experimental Control Systems. 2017; 997-1002.

[6] Moreno G B Z L, et al. Rapid Control Prototyping Tool for The Sirius High-Dynamic DCM Control System. Proc. 16th International Conference on Accelerator and Large Experimental Control Systems. 2017; 1941-1946.

[7] Caliari R M, et al. Loop-Shaping Controller Design in the Development of the High-Dynamic Double-Crystal Monochromator at Sirius Light Source. This conference. 2020.

[8] Moraes M A L, et al. A Control Architecture Proposal for Sirius Beamlines. Proc. 16th International Conference on Accelerator and Large Experimental Control Systems. 2017; 1947-1952.

[9] National Instruments documentation. Available at: http://www.ni.com/pdf/manuals/375697d_03.pdf

[10] National Instruments knowledge base. Available at: https://knowledge.ni.com/KnowledgeArticleDetails?id=kA00Z0000004BT2SAM

[11] National Instruments white papers. Available at: https://www.ni.com/en-us/innovations/white-papers/12/do-i-need-a-real-time-system-.html#section–280088352

[12] Experimental Physics and Industrial Control System. Available at: https://epics-controls.org/

[13] National Instruments documentation. Available at: https://www.ni.com/content/dam/web/product-documentation/labview_high-perf_fpga_v1.1.pdf

Delta Robot Combining Millimetre Travel with Nanometre Performance

Jon H. Kelly
The Diamond Light Source
Harwell Science Campus
Oxfordshire, UK

INTRODUCTION

Sample motion stages for Synchrotron X-ray microscopy are usually built from a stack of coarse, large travel stages and fine, flexure based scanning stages. The coarse stages are actuated by stepper motors via a ball screw and the fine stages by a piezo stack, where the fine stage is mounted directly on top of the course stage. Both are driven in closed loop using a common laser interferometer feedback. This concept is not mechanically optimal because the stacked stages bring about relatively low resonant frequencies compromising the overall system bandwidth. Typically the mechanical fundamental vibration mode is < 100 Hz. The stack design also causes control complexity and compromise because of two stages using one feedback signal. The stack may be configured so that both axes are enabled and moving together in a coordinated move in the X direction for example and in this mode the fine axes is used to reduce motion errors from the course stage or to run separately as isolated coarse and fine. In the latter mode the data sets taken over the small range must be “stitched” together during post processing. The stages are used in a scan where motion triggers a detector using its feedback source. The velocity of the scan is limited by the data rate allowed by the detector to 1 - 10 µm/s.

This paper details the design of a parallel kinematic three axis stage (Delta Robot) which combines millimetre travel with nanometre performance. This mechatronic design eliminates many of the control and implementation issues found with the existing technology. This idea has been published in the literature[1][2][3][4] but this project was to develop and optimize a design for this specific Synchrotron application.

DESIGN PROCESS

Mechatronics design principles were employed for this project. First a specification was defined which enabled a calculation of the desired bandwidth (See Table 1). A design could then be developed to achieve the required mechanical resonant frequency. The process was then an iterative loop of finite element analysis to acquire stiffness data, dynamic modelling to look at the performance in both the frequency and time domains and mechanical/electrical design.

TABLE 1. Given below is the initial stage specification and the final, measured values.
** Using absolute encoders*
*** Using Trust Automation Inc. TA105 Amplifier*

Property	Specification	Measured
Range of motion in XYZ	3 mm	3 mm
Position Stability	< 10 nm Peak-Peak 1-1000Hz	± 10 nm**
Max Speed	1 mm/s	10 mm/s*
Max Acceleration	1 mm/s^2	500 mm/s^2
Mechanical Resonant Frequency	> 150 Hz	600 Hz

MECHANICAL DESIGN

The parallel kinematic concept is three orthogonal voice coil actuated, parallelogram flexures, coupled to a sample platform via flexure arms. See Figures 1 & 2 below. The voice coils and linear encoders are aligned on the XYZ motion axes to minimize Abbe errors and maximize stiffness. The voice coils and magnets may be swapped to either have the much lighter but heat generating coil on the moving or fixed side. This allows the choice to prioritize high resonant frequency or low thermal drift. Only components with vacuum compatible versions where selected, as the intended application was within a vacuum envelope. As this was a proof of concept stage it was designed with two feedback options for comparison. Incremental linear optical encoders on the actuators were selected to give close to co-location feedback, separated from the parasitic sample platform resonance motion.

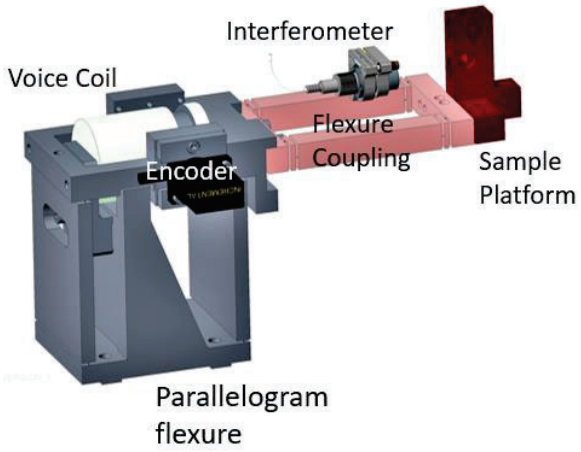

FIGURE 1. Given above is one of the three voice coil, actuator assemblies. The Titanium parallelogram flexure is coupled to the sample platform via the flexure arms.

Absolute protocol laser interferometers were chosen to measure the sample platform position, which was the point of interest, thus minimising the effect of the thermal expansion and parasitic motion errors of the flexure coupling arms.

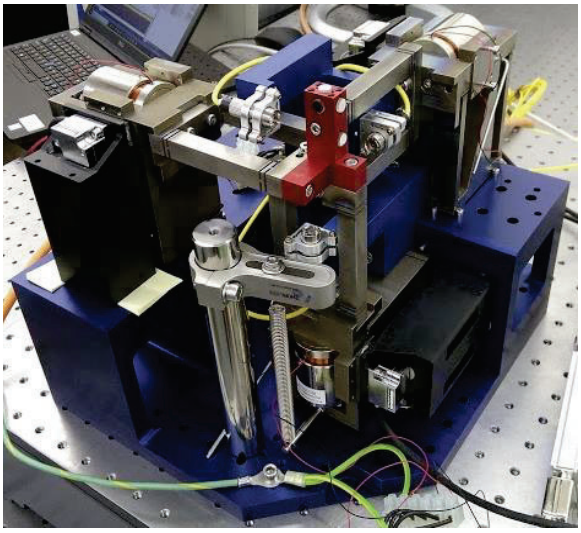

FIGURE 2. The operational proof-of-concept Delta Robot stage.

The Heidenhain linear encoders with a fine, 2 µm scale period were used with high interpolation factor Renishaw x2000 interpolators to give 1 nm resolution. The Heidenhain encoder was selected for its factor of 10 smaller scale period i.e. it required less interpolation. Attocube IDS 3010 laser interferometers were selected due to their compact size, BiSS C absolute protocol and vacuum option. The incremental vs. absolute feedback was chosen based on two competing factors;

- Existing microscope scanning instruments require an incremental signal
- Absolute encoders enable faster more robust control without risk of step loss

FINITE ELEMENT ANALYSIS

Titainium (Ti-6Al-4V) was chosen for the flexure material due to its favorable yield stress to Young's modulus ratio. A fatigue life of 100,000 cycles was selected giving a stress limit of 460 MPa[5]. The notch-flexure dimensions were optimised with a number of competing criteria:

- To give the minimum stiffness in the desired actuation direction and hence required voice coil force constant
- To block the rotational degrees of freedom of the sample platform which is critical for data quality
- To reach a maximum stress of ~460 MPa at the extremes of travel
- To have a low moving mass and hence high resonant frequency
- To stay within a compact space envelope (0.3 x 0.3 x 0.3 m)

ANSYS 17 was used to perform static structural and modal analysis of a simplified assembly model.

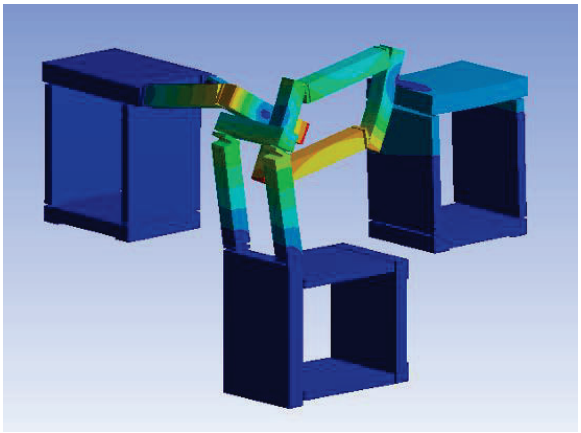

FIGURE 3. ANSYS Modal analysis result showing the first undesirable vibration mode at 677 Hz.

The first three resonant frequencies of the system were the desired XYZ sample platform

motions at 12 Hz. The fourth resonant frequency was at 677 Hz, see Figure 3 below. The encoder mounts and support structures were designed to have a 1 kHz fundamental resonant frequency.

DYNAMIC MODELLING

A single degree of freedom Mathworks® Simulink model was created to inform the design. The model was used to investigate the effects of:

- Flexure & encoder mount stiffness
- Moving masses
- Additional damping
- Higher order resonant modes
- Voice coil force constant & back EMF
- Encoder resolution
- Amplifier current ripple
- Amplifier resolution
- PID frequency
- PID tuning
- External vibration

The model included additional spring, mass, damper systems to represent the 677 Hz and 840 Hz higher order vibration modes predicted by the ANSYS modal analysis. Without these the control gains could be increased to unrealistic values. The higher order damping values were adjusted later to limit the bandwidth to the actual measured value and hence the presented bode plot has the same Bandwidth as the experimental value. The bode plot is given below in Figure 4.

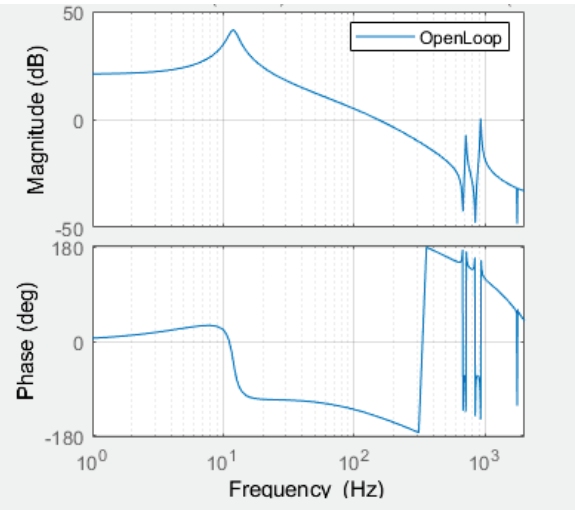

FIGURE 4. Open-loop bode plot from the 1 degree of freedom Simulink Model

It was found that the position stability was not strongly dependent on the encoder resolution, amplifier resolution nor PID frequency. Clearly the achievable Bandwidth was critical for vibration rejection which was limited by the mechanical resonances; However, because this stage is designed to operate in a low vibration, non-industrial environment the defining factor was the amplifier current ripple.

VIBRATION TEST RESULTS

The vibration frequency response function was measured using a triaxial accelerometer and an impact hammer to compare with the theoretical ANSYS modal analysis.

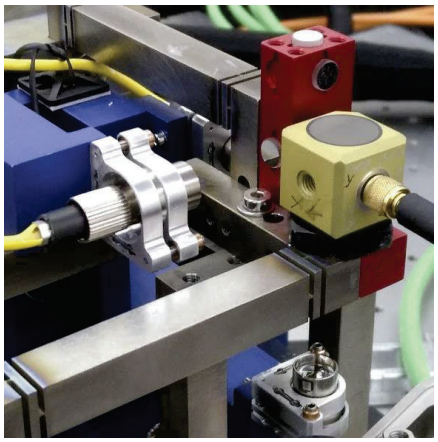

FIGURE 5. Location of the tri-axial accelerometer for the experimental modal analysis

The accelerometer was held on the sample platform using wax (See Figure 5).

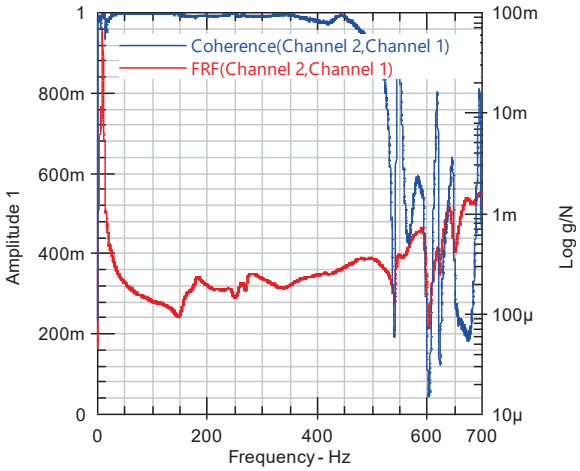

FIGURE 6. Measured Delta Robot frequency response function

The table upon which the Delta Robot was bolted was impacted in alignment with the horizontal X actuator axis. The hardest hammer tip available gave a force spectrum whose reduction with frequency caused poor coherence above 550 Hz. Although experimental data is less reliable above 550 Hz there is a good qualative agreement with the FEA that the undesirable resonances are above 600 Hz (See Figure 6).

MOTION TEST RESULTS

The Delta Robot was tested with three motion control set-ups to measure the position stability. The Delta Tau Power Brick LV-IMS gave a ± 200 nm stability, the Aerotech A3200 Npaq Controller ± 20 nm and the Delta Tau Brick Controller with a Trust Automation Inc. TA105 external drive ± 10 nm Peak to Peak. The lack of friction meant that the position stability didn't change from standstill to the data capture scanning velocity of 10 µm/s. The Aerotech controller has tools that will allow you to tune the system in the frequency domain while the DeltaTau was tuned using the time domain only. The Bode plot obtained using Aerotech gave a direct comparison with the Simulink model. The Aerotech controller was tuned to have a Bandwidth of 144 Hz with a Phase margin of 33º and a Gain margin 5.4dB. A screenshot of the interface is given in Figure 7.

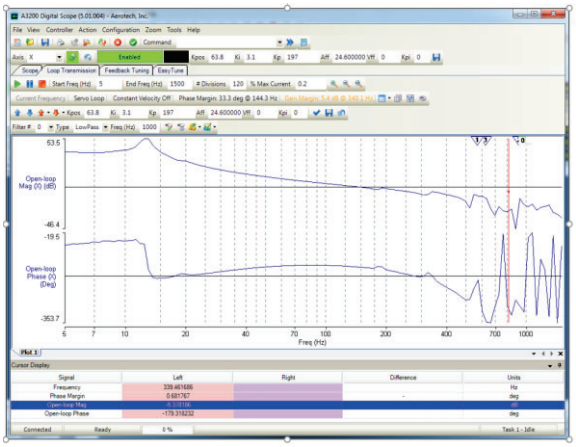

FIGURE 7. Aerotech 3200 controller screenshot

This may be compared with the Simulink bode plot in Figure 4. The amplitude and phase curves largly agree. However, one clear difference is that the Aerotech controller automatically applied notch filters to the mechanical resonances, so they are not visible.

CONCLUSION

A voice coil actuated parallel kinematic flexure stage was designed, built and tested. The theoretical FEA and Simulink modelling broadly agreed with the measured system which validated the design process. The position stability didn't quite meet the specification. However, a new development project is underway to take this proof of concept stage to an operational design. This new project is a combination of further Simulink analysis, control hardware tests and mechanical design. For example a lever to demagnify the voice coil actuation can make the current ripple in the motor be less of a movement at the point of interest although this improvement may have a detrimental effect in the bandwidth because of the introduction of extra linkages and masses that may bring new resonant frequencies.

REFERENCES

[1] Richard M, Clavel R. Concept of modular flexure-based mechanisms for ultra-high precision robot design. Mechanical Sciences. 2011. 2. 99-107.

[2] Bacher J. Conception De Robots De Très Haute Précision À Articulations Flexibles: Interaction Dynamique-Commande. École Polytechnique Fédérale De Lausanne. 2003.

[3] Shan G, Li Y, et.al. Application of voice coil motors in high-precision positioning stages with large travel ranges. Review of Scientific Instruments. 2015. 86, 101501

[4] Shang J, Tian Yanling et.al. A novel voice coil motor-driven compliant micropositioning stage based on flexure mechanism. Review of Scientific Instruments. 2015. 86, 095001

[5] Boyer R, Welsch G, Collings E. W. Materials Properties Handbook: Titanium Alloys. ASM International, Materials Park, OH 1994.

THERMALLY STABLE PRECISION MOTION AND POSITIONING MECHANISM

Heebum Chun[1], Hyo-Young Kim[2], and ChaBum Lee[1]
[1]J. Mike Walker 66' Department of Mechanical Engineering
Texas A&M University
College Station, TX, 77843, USA
[2]Manufacturing System R&D Group
Korea Institute of Industrial Technology
Cheonan-si, Chungnam-do, 31056, South Korea

ABSTRACT
This paper introduces a novel mechanism to control motion and thermal issues of nanopositioning systems that use flexure mechanisms by flowing fluid (compressed air or water) into the internal fluidic channels of the flexures. The nanopositioning system was additively manufactured of stainless steel. The rectangular fluidic channels were created on both sides of the flexure mechanisms that applied double compound type. The motion behavior of the flexure mechanism was evaluated by measuring the stiffness as well as frequency responses by impact hammering test while the different compressed air and the fluid flowing in each side of fluidic channels. The behavior in thermal properties was analyzed by measuring the heat distribution and the displacement caused by heat over the flexure system under various conditions of compressed air and water flowing. Also, dynamic behaviors in nanopositioning systems under various conditions of pressure or fluid-fed were characterized by the Finite Element Method (FEM) and validated with experiment results. As a result, under the various compressed air or water-fed mechanisms accompanied following characteristics: (1) the existence of fluid in the internal channels in shows increase in damping, (2) the compressed air-fed mechanism has the ability to move the stage within nanometer precision with fast response time, and (3) the media flowing through fluidic channels lower the increased temperature and reduce the error in thermal displacement caused by heat generation.

INTRODUCTION
In precision engineering, thermal stability has always been important for achieving high precision[1-4] in the mechanical, electrical or chemical systems. Nonetheless, most of the precision systems, such as atomic force microscopes (AFM), scanning electron microscopes (SEM), semiconductor manufacturing systems or precision machine tools, are used in temperature-controlled and vibration-isolated environments since the most of motor-driven motion mechanisms generate heat in motion systems[5-7], the performance of systems highly depend on thermal stability. For instance, the power consumption of a laser-based sensor could also be the source of heat generation in the precision machine systems. Achieving high precision in the mechanical system is prohibited by the generated heat because the components in the machine system: machine frames, guides, feedback sensors, control systems, or the motors are susceptible to thermally deform. Although temperature sensors might directly monitor the variation in temperature and enable the motion controller to compensate errors, the heat sources are prone to unpredictable and hence even a relatively small heat source may have a dramatic impact on the stability of precision system[8-10]. Therefore, the novel methods are required for the precision machine systems to sustain the environment to be most thermally stable.

The flexure (or compliant) mechanisms are among the most commonly used for precision motion systems[9,10]. At present, the mechanisms consisting of metals, polymers, composites, silicon or glass can be fabricated by traditional machining processes[8-11] (wire electric discharge machining, milling, water jet machining), semiconductor lithography processes[12,13], or additive manufacturing processes[14-21], and those processes are driven by thermal, electrostatic, piezoelectric actuation, or magnetic, even microscale gears[22]. The flexure joints, so-called springs or hinges, are articulates the compliant mechanisms. The mechanisms take advantage

of stictionless, frictionless, configuration of backlash-free and compact design through elastic bending or torsional motion. On the other hand, the small deflection of flexure joint, fatigue, and low load capacity limit the motion of flexure mechanisms[23]. As discussed above, as long as the motion of mechanisms driven by motors which are the heat source, the instability induced by thermal effects is inevitable. Most studies on flexure mechanisms have been focused on system modeling, design, actuation, control of motion, and long-stroke with high-speed manipulation methods to improve the positioning performance although its dynamic and motion characteristics are highly sensitive to the variation in temperature and furthermore, the issues arising from the temperature variation cannot be fully eliminated by compensation or calibration.

The significant contribution of the proposed study is a new and proper method for thermal management with avoiding any additional attachments to system structure at a low-cost manner, to provide high accuracy and precision motion quality as well as a novel actuation method driven by pneumatic pressure for flexure mechanisms.

MECHANISM DESIGN

The rectangular internal fluidic channels (2.5 mm × 2.5 mm) with the flexure mechanism that applied double compound-type was designed and fabricated by additive manufacturing that made out of stainless steel as shown in Figure 1

The designed flexure mechanism can hold a piezoelectric actuator (5 × 5 × 10 mm^3) and the fluidic channels are bilateral symmetry.

To monitor the pressure difference of inlet and outlet (pressure level) in the internal fluidic channels, pressure gauges are mounted at the inlet and outlet of internal channels.

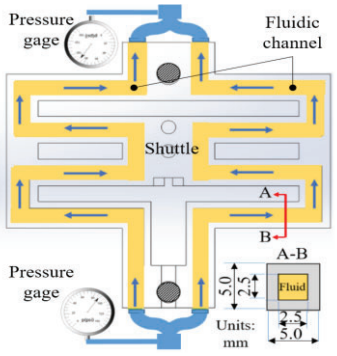

FIGURE 1. Configuration of the pressure-fed flexure mechanism.

SYSTEM CHARACTERIZATION

The pressure or fluid-fed flexure mechanism was simulated using Finite Element Method (FEM) for modal analysis. The simulation used the condition of 304 Stainless Steel material properties (elastic modulus 193 GPa, density 8,000 kg/m^3, Poisson's ratio 0.29), compressed air properties (density of 1.2 kg/m^3 at ambient, 4.0 kg/m^3 at 50 psi, 6.4 kg/m^3 at 80 psi, and bulk modulus of 101 kPa), and water properties (density of 998.2 kg/m^3 at ambient, 996.7 kg/m^3 at 50 psi, 996.7 kg/m^3 at 80 psi, and bulk modulus of 2.2 GPa). The Tetra type mesh was formed for simulation with 155,766 of nodes and 87,382 elements.

As a result that shown in Figure 2, the stiffness of the fluid-fed flexure mechanism shows a similar tendency with any other reference to the pressure levels and fluid media; however, in high-frequency vibration modes, it shows somewhat inconsistency when the various compressed-air filled. The natural frequencies of fundamental and the following mode were found out to be approximately 3,030 Hz and 3, 050 Hz, respectively.

The experimental validation had been carried out in restricted conditions. The internal fluidic channels were fully filled with water and the water flowed at a certain rate since the compressed water requirements in a laboratory setting are somehow different.

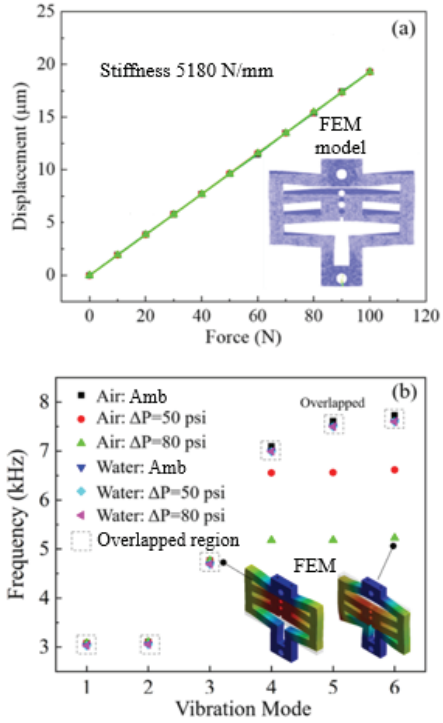

FIGURE 2. Stiffness curves (a) and vibration modes (b) of the flexure stage calculated by FEM.

As described in Figure 3, the pressure difference colored in blue was monitored by pressure gauges placed at the inlet and outlet of the fluidic channels. The capacitive sensor (CS) was used to measure the displacement when applying force at the shuttle part of flexure. The result of the stiffness measurement showed that the discrepancy between experimental and FEM results was approximately 5%.

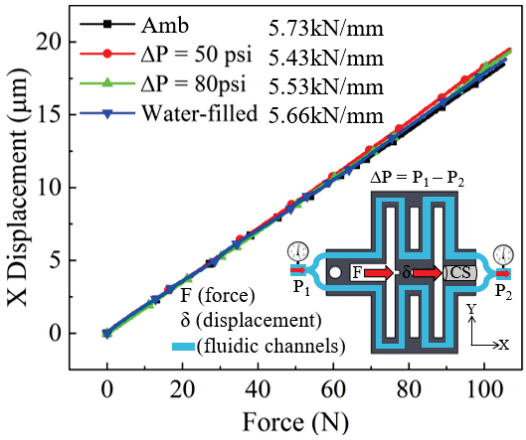

FIGURE 3. Experimental results of stiffness curve with varying conditions

EXPERIMENT

Motion Behavior

The CS measured the displacement of the shuttle part of flexure by applying different pressure levels (ΔP) between the inlet and outlet of the fluidic channels as shown in Figure 4. It demonstrated that the flexure mechanism can move up to about 160 nm at the pressure level of 75 psi condition. Although the displacements at various pressure conditions did not linearly increase because of manually manipulated air pressure and the open-loop control, the flexure mechanism showed prompt responses to the pressure difference.

Considering the experiment was performed by manually raising and decreasing the different pressure at the inlet of the channels every 5 minutes, this research was limited to acquire the exact characteristics of response (settling time, rising time, and steady-state error). However, the result revealed that this motion mechanism driven by compressed air can be integrated with piezoelectric (PZT) actuation coarse-fine stages for precise motion control.

For better performance, the solenoid-based compressed air pressure controller may be implemented for proper characterization of the compressed air-driven motion mechanisms and for employing a closed-loop positioning control method.

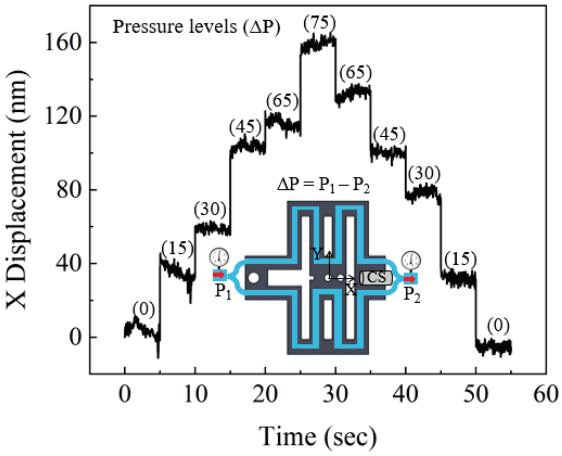

FIGURE 4. Open-loop stepwise motion driven by varying pneumatic pressure.

Thermal Behavior

The experiment for the characterization of thermal behavior was set up as shown in Figure 5. The cartridge heater was mounted at the center of the flexure shuttle and five thermocouples (TC) were attached on the top surface of the flexure stage. The CS was used to measure the thermal displacement as the temperature rises and to measure the corresponding variances in displacement with respect to the varying compressed air or water flow into the fluidic channels.

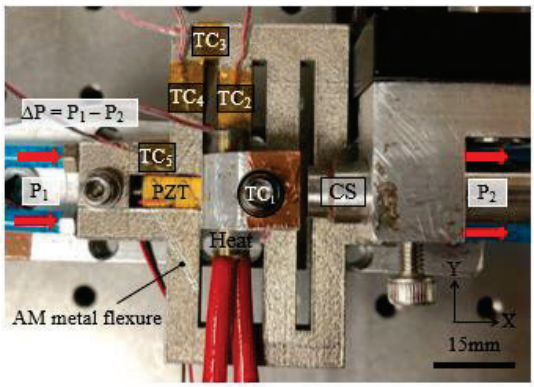

FIGURE 5. Schematic of Experiment setup for Characterization of Thermal management

The PZT actuator was not included in this experiment. The variation in temperature measured at TC_1 and collected the data for 30

minutes with seven different cases (Ambient condition; ΔP of 10, 20, 50 and 80 psi; and water flow rates of 113 mm/s and 530 mm/s) as shown in Figure 6.

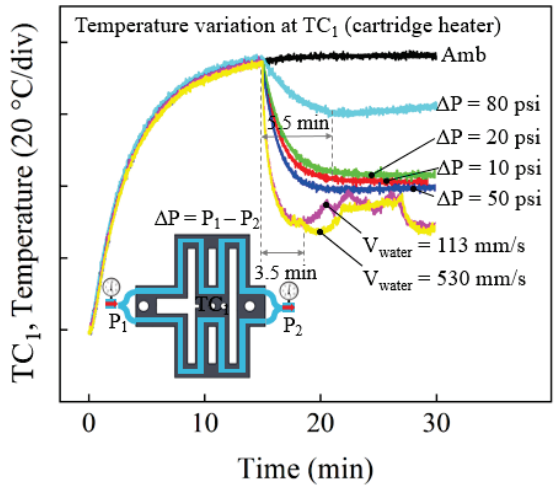

FIGURE 6. Temperature distribution at the location of TC_1 according to the media and pressure conditions.

When the thermal management plan was not applied to the flexure stage, the cartridge heater increased the temperature of the flexure stage up to 76 °C at TC_1 from room temperature and the temperature was saturated within 15 min. The seven different cases of compressed air and water started to flow at 15 min when the rising temperature was saturated. Among seven different treatments, the water case has demonstrated the best effects of cooling performance. While the temperature fell to 50 °C in 3.5 min when water started to flow, the compressed air of 10, 20 and 50 psi showed the temperature dropped to 30~35 °C within 5.5 min. In water cases, the temperature variations exhibited some fluctuation because the flow rate of water is comparatively slower than in the cases of compressed air. Moreover, interestingly, the compressed air of 80 psi showed only 17 °C temperature decreasing. It was assumed that the compressed air 80 psi may surpass the critical fluidic flow rate so that the transfer of heat from convection and the growth in a thermal boundary layer could hamper the heat transfer. More investigation by FEM will be taken up in the near future.

Thermal Management

While the piezoelectric actuator operated and moved the flexure mechanism, the thermal behavior at TC_5, nearest to the PZT actuator, was examined under four different cases (ambient, ΔP of 20 psi, and water flow V 350 mm/s). A similar trend when comparing the results of Figure 7, the temperature at the shuttle of the flexure stage increased exponentially by the heat dissipation of the actuator for motion up to 7 °C. The fluidic flows of compressed air and water could significantly reduce the increased temperature to approximately 5 °C and 7 °C, respectively, as seen in Figure 8. Furthermore, the temperature dropped to semi-equilibrium conditions in 6.2 min for compressed air conditions and 2.6 min for water case. Temperature fluctuation existed in the case of water flow. It was considered that the flow rate of water is low to properly dissipate the heat.

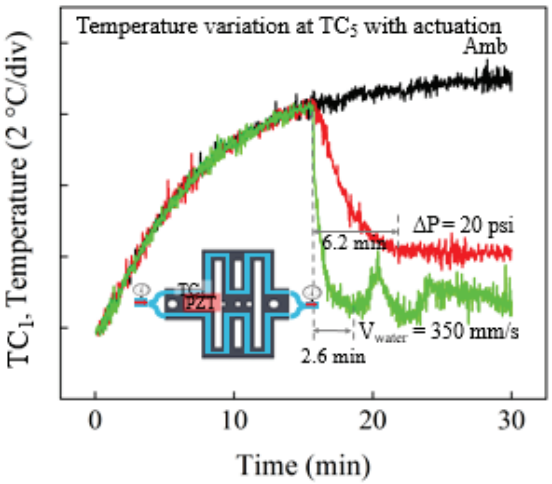

FIGURE 7. Thermal management performance comparison at TC_5 when the motion occurred by motor.

CONCLUSION

Here the motion mechanism driven by pneumatic pressure with a novel method for thermal management was presented and preliminarily examined the manufactured flexure stage with internal fluidic channels under various medium and pressure conditions for achieving high precision motion quality. The thermal behavior was then identified by measuring the heat dissipation over the flexure mechanism and corresponding thermal behavior under the various flow conditions of compressed air and water. As a consequence, the heat-induced by the piezoelectric actuator can be conveniently dissipated via internal fluidic channels by flowing compressed air or water through the internal channels, and additionally, these fluidic flows allow the dynamic motion systems to increase its damping. The variation in temperature

variation has negative effects on the positioning accuracy and control long-term effectiveness in precision motion devices. Therefore, the proposed method can be applied for proper thermal management techniques in many applications, especially for nanopositioning systems. The developed technology is expected to meet the growing need for accuracy and precision in nanometer motion control and achieve the environments that are thermally stable in an effective, low-cost, convenient way.

ACKNOWLEDGMENTS

This work was supported by the Texas A&M University and partially the Technology Innovation Program (20000748, Development of 1,000mm/s class laser dicing machine for ultra-thin silicon wafers less than 50 ㎛ using low thermal expansion ceramics) funded By the Ministry of Trade, Industry & Energy(MOTIE, Korea). Similarly thank researchers at Korea Institute of Industrial Technology (KITECH) for computational efforts.

REFERENCES

1. M. Weck, P. McKeown, R. Bonse, U. Herbst, Reduction and compensation of thermal errors in machine tools, CIRP Annals, Vol. 44, Iss. 2, pp. 589-598 (1995).
2. Sun-Kyu Lee, Jae-Heung Yoo, Moon-Su Yang, Effect of thermal deformation on machine tool slide guide motion, Tribology International, Vol. 36, Iss. 1, pp. 41-47 (2003).
3. Sun-Min Kim, and Sun-Kyu Lee, Prediction of thermos-elastic behavior in a spindle-bearing system considering bearing surroundings, International Journal of Machine Tools and Manufacture, Vol. 41, Iss. 6, pp. 809-831 (2001).
4. Brian S. Salmons, Daniel R. Katz, Matthew L. Trawick, Correction of distortion due to thermal drift in canning probe microscopy, Ultramicroscopy, Vol. 110, Iss. 4, pp. 339-349 (2010).
5. Jianguo Dai, Jingjing Xia, Cheng Wang and Shanzhen Xu, Thermal analysis of an electromagnetic linear actuator, Advances in Mechanical Engineering, Vol. 9(12), pp. 1-12 (2017).
6. A. Boglietti, A. Cavagnino, D. Staton, M. Shanel, M. Mueller, and C. Mejuto, Evolution and modern approaches for thermal analysis of electrical machines, Industrial Electronics, IEEE Transactions on, Vol. 56, pp. 871-882 (2009).
7. Y. Bertin, E. Videcoq, S. Thieblin, and D. Petit, Thermal behavior of an electrical motor through a reduced model, Energy Conversion, IEEE Transactions on, Vol. 15, pp. 129-134 (2000).
8. Alain C. Diebold, Handbook of Silicon Semiconductor Metrology, CRC Press, 2001.
9. L. Howell, Compliant mechanisms, John Wiley & Sons Inc, 2001.
10. S. T. Smith, Flexures, Gordon and Breach Science Publishers, ISBN 90-5699-261-9, 2000.
11. David J. Guckenberger, Theodorus E. de Groot, Alwin M. D. Wan, David J. Beebe, and Edmond W. K. Young, Micromilling: A method for ultra-rapid prototyping of plastic microfluidic devices, Lab Chip, Vol. 15, No. 11, pp. 2364-2378 (2015).
12. Herminso Villarraga-Gómez, ChaBum Lee, and Stuart T. Smith, Dimensional metrology with X-ray CT: a comparison with CMM measurements on internal features and compliant structures, Precision Engineering, 51, pp. 291-307 (2018).
13. ChaBum Lee, Christopher K. Stepanick, Sun-Kyu Lee, and Joshua A. Tarbutton, Cross-coupling effect of large range XY nanopositioning stage fabricated by stereolithography process, Precision Engineering, Vol. 46, pp. 81-87 (2016).
14. ChaBum Lee, Sun-Kyu Lee and Joshua A Tarbutton, Positioning control effectiveness of optical knife edge displacement sensor-embedded monolithic precision stage, Sens. Actuators A. Vol. 233, pp. 390-396 (2015).
15. ChaBum Lee and Joshua A Tarbutton, Compliance and control characteristics of an additive manufactured-flexure stage, Rev. Sci. Instrum. 86(4) 045107 (2015).
16. M. Aliakbari, Additive Manufacturing: State-of-the-Art, Capabilities, and Sample Applications with Cost Analysis, Master of Science Thesis, Department of Industrial Production, KTH, June 2012.
17. Valmik Bhavar, Prakash Kattire, Vinaykumar Bapuso Patil, S. M. Khot, Kiran Gujar, Rajkumar Raju Singh, A review on power bed fusion technology of metal additive manufacturing, Additive Manufacturing Handbook DOI:10.1201/9781315119105-15 (2017).
18. S. V. Sreenivasan, Nanoimprint lithography steppers for volume fabrication of leading-edge semiconductor integrated circuits, Microsystems & Nanoengineering, Vol. 3, 17075 (2017).
19. Byoung Hun Kang, John Ting-Yung Wen, Nicholas G. Dagalakis, Jason J. Gorman, Analysis and design of parallel mechanisms with flexure joints, IEEE Transactions on Robotics, Vol. 21, No. 6 (2005).

20. Heebum Chun, Jaemin Han, Lesley Wright, Alaa Elwany, Herminso Villarraga-Gomez, and ChaBum Lee, Pressure-fed mechanism to compensate for motions and dynamic characteristics of compliant nanopositioning stage, Precision Engineering, Vol. 63, pp. 33-40 (2020).
21. Jaemin Han and ChaBum Lee, Dynamic and thermal characterization of additively manufactured pressure-fed flexures with internal fluidic channels, Smart Materials and Structures, 28, 105032 (2019).
22. Zeyi Wu and Qingsong Xu, Survey on recent designs of compliant micro-/nano positioning stages, Actuators, Vol. 7 (1), 5 (2018).

Authors Index

Aarnoudse, Leontine 16
Abbott, Richard 110
Arnbak, Jens 105
Baade, Rick 63
Badrawy, Sinan 43
Ballmer, Stefan 110
Barati Farimani, Amir 12
Bhushan, Brij M. 77
Brooks, Aidan 110
Caliari, Ricardo M. 119, 125, 131
Cao, Huy Tuong 110
Cao, Zhonglin 12
Chabot, Joshua 31
Chun, Heebum 141
Connolly, Liam G. 93
Cullinan, Michael 93
Dibua, Obehi G. 93
Dumanli, Alper 43
Enengl, Patrick 27
Evans, Matthew 105
Fan, Chunjie 73
Fernández-Galiana, Álvaro 105
Flügge, Jens 87
Fritschel, Peter 110
Fyler, Donald C. 37
Geraldes, Renan R. 119, 125, 131
Griffith, Don 110
Gruber, Wolfgang 27
Habbal, Osama 69
Hakvoort, W.B.J. 58
Hamer, Tyler T. 31
Hastings, DJ 73
Hernández-Becerro, Pablo 113
Jabben, Leon 54
Jia, Wenxuan 110
Kelly, Jon H. 137
Kim, Heejin 49
Kim, Hyo-Young 141
Köchert, Paul 87
Köning, Rainier 87
Kramer, Boaz 82
Lee, ChaBum 141
Lowe, Jeff 43
Luijten, Fons 54
Mansell, Georgia 110
Manske, Eberhard 87
Matichard,Fabrice 110
Mavalvala, Nergis 105
Mayr, Josef 113
Mooren, Noud 1
Moraes, Marcelo A.L. 119, 125, 131
Ng, Sebastian 110
Noh, Minkyun 110
Okwudire, Chinedum E. 6, 49
Oomen, Tom 1, 16
Pannier, Christopher 69
Peijnenburg, Ton 63
Sencer, Burak 43
Smith, Stuart T. 73
Sokolov, Maksim 27
Spanjer, S.T. 58
Srivastava, Varun 110
Steinbuch, Maarten 63
Stokkermans, Joep 1
Strijbosch, Nard 16
Torrie, Calum 110
Trumper, David L. 21, 31, 37, 77
van der Veen, Gijs 1
Veitch, Peter 110
Verschueren, Edwin 16
Wang, Yi 99
Wang, Yuyang 12
Wegener, Konrad 113
Weichert, Christoph 87
Weinreb, Benjamin S. 37
Witvoet, Gert 119, 125
Xia, Fangzhou 99
Yang, Chen 99
Youcef-Toumi, Kamal 99
Zhou, Lei 21